Monte Carlo and experimental small-field dosimetry applied to spatially fractionated synchrotron radiotherapy techniques

DOCTORAL DISSERTATION

Immaculada Martínez-Rovira

Supervisors
Dr. Yolanda Prezado
Dr. Josep Sempau

March 2012

PhD in Nuclear Engineering and Ionising Radiations

Universitat Politècnica de Catalunya

A la meva família

Oficina de Doctorat
UNIVERSITAT POLITÈCNICA DE CATALUNYA

Acta de grau de doctor/doctora

Curs acadèmic:

Nom i cognoms

DNI / NIE / Passaport

Programa de doctorat

Unitat estructural responsable del programa

Resolució del Tribunal

Reunit el Tribunal designat a l'efecte, el doctorand / la doctoranda exposa el tema de la seva tesi doctoral titulada

_____

_____.

Acabada la lectura i després de donar resposta a les qüestions formulades pels membres titulars del tribunal, aquest atorga la qualificació:

☐ APTA/E ☐ NO APTA/E

(Nom, cognoms i signatura) President/a		(Nom, cognoms i signatura) Secretari/ària
(Nom, cognoms i signatura) Vocal	(Nom, cognoms i signatura) Vocal	(Nom, cognoms i signatura) Vocal

_____, _____ d'/de _____ de _____

El resultat de l'escrutini dels vots emesos pels membres titulars del tribunal, efectuat per l'Oficina de Doctorat, a instància de la Comissió de Doctorat de la UPC, atorga la MENCIÓ CUM LAUDE:

☐ SI ☐ NO

(Nom, cognoms i signatura) Vicerectora de Recerca Presidenta de la Comissió de Doctorat	(Nom, cognoms i signatura) Cap de l'Oficina de Doctorat Secretària de la Comissió de Doctorat	(Nom, cognoms i signatura) Secretari/ària del tribunal (o membre del tribunal de la UPC)

Barcelona, _____ d'/de _____ de _____

Diligència "Internacional del títol de doctor o doctora"

Com a secretari/ària del tribunal faig constar que la tesi s'ha defensat en part, i com a mínim pel que fa al resum i les conclusions, en una de les llengües habituals per a la comunicació científica en el seu camp de coneixement i diferent de les que són oficials a Espanya. Aquesta norma no s'aplica si l'estada, els informes i els experts externs provenen d'un país de parla hispana.

(Nom, cognoms i signatura) Secretari/ària del tribunal

Abstract

Two innovative radiotherapy (RT) approaches are under development at the ID17 Biomedical Beamline of the European Synchrotron Radiation Facility (ESRF): microbeam radiation therapy (MRT) and minibeam radiation therapy (MBRT). The two main distinct characteristics with respect to conventional RT are the use of submillimetric field sizes and spatial fractionation of the dose. This PhD work deals with different features related to small-field dosimetry involved in these techniques. Monte Carlo (MC) calculations and several experimental methods are used with this aim in mind. The core of this PhD Thesis consisted of the development and benchmarking of an MC-based computation engine for a treatment planning system devoted to MRT within the framework of the preparation of forthcoming MRT clinical trials. Additional achievements were the definition of safe MRT irradiation protocols, the assessment of scatter factors in MRT, the further improvement of the MRT therapeutic index by injecting a contrast agent into the tumour and the definition of a dosimetry protocol for preclinical trials in MBRT.

Keywords: microbeam radiation therapy, minibeam radiation therapy, small-field dosimetry, Monte Carlo simulation, treatment planning system, dosimetry protocols, clinical trials, synchrotron radiation

Immaculada Martínez-Rovira
***Contact*: immamartinez@gmail.com**

Preface

Radiotherapy (RT) is the use of ionising radiation to treat cancer or other types of benign lesions. Along with surgery and chemotherapy, RT is one of the most effective methods for cancer treatment. Furthermore, around 70% of all cancer patients will receive RT at some stage during the course of their illness [IAEA-TRS-461 2008]. Since radiation does not attack cancer cells specifically, it also produces deleterious effects in the surrounding healthy tissue. Despite intensive research and development during the last few decades, there are still some radioresistant tumours for which radical treatment is not feasible at hospitals. In the quest for ways to improve the therapeutic index for such tumours, new approaches have been explored. Intensity-modulated radiation therapy (IMRT), hadrontherapy and synchrotron radiation therapies are some examples.

Within this context, three new RT techniques are under development at the ID17 Biomedical Beamline of the European Synchrotron Radiation Facility (ESRF): synchrotron stereotactic radiation therapy (SSRT), microbeam radiation therapy (MRT) and, more recently, minibeam radiation therapy (MBRT). The last two techniques possess very distinct features with respect to conventional RT methods. They combine submillimetric field sizes and spatial fractionation of the dose. The resulting biological effects appear to challenge many of the current paradigms in RT. Remarkable healthy tissue resistance to very high doses in one fraction was observed in several MRT biological investigations performed during the last two decades. In addition, MRT rendered significant tumour growth delay and, in some cases, complete tumour ablation. The success of the preclinical studies has paved the way for clinical trials, which are currently in preparation at the ESRF. The first step includes the treatment of large animals as a milestone before implementation in human beings.

Thin microbeams (and their associated small beam spacing) demand high dose rates, which are nowadays only available at synchrotrons. Since microbeams are closely packed, it is important that the patient does not move during irradiation. Even cardiosynchronous motion effects might be an issue. The therapeutic dose should thus be delivered in a fraction of a second. The thicker beams employed in MBRT might represent a compromise between having high tissue sparing and the ease of implementing this technique with cost-effective equipment at hospitals. For this reason, a new method to produce minibeam patterns was recently developed and tested at the ESRF Biomedical Beamline. The different beam widths and spacings used in MRT and MBRT might lead to a dissimilar biological response. In the light of the advantages of MBRT over MRT, preclinical trials in MBRT need to be performed

in order to evaluate the healthy tissue sparing capability of MBRT and (possible) distinct biological effects.

This PhD thesis is framed within medical physics developments aimed at the preparation of forthcoming clinical trials in MRT and preclinical studies in MBRT. To this end, both Monte Carlo (MC) simulations and experimental dosimetry studies were performed for the dose assessment of the micrometre-sized fields used in these two innovative techniques.

The dissertation is divided into three parts: *i)* the first part provides an introduction of the main topics to be addressed in this thesis, *i.e.*, the use of RT to treat cancer and its limitations, fundamentals of synchrotron radiation and third-generation sources, such as the ESRF, and the basis of spatially fractionated synchrotron RT techniques from the biological and physical point of view; *ii)* the second part contains a compendium of several original investigations reported in six papers published in (or submitted to) peer-reviewed journals. In the first paper, safe irradiation protocols for forthcoming MRT clinical trials are defined. The second article assesses how much the MRT therapeutic index can be further improved by enhancing dose deposition in the tumour when loading it with high-atomic-number contrast agents. The third and fourth papers report the development and commissioning of the MC-based calculation engine for a dedicated treatment planning system (TPS) in MRT. In line with this, the fifth article deals with one of the most challenging issues in MRT: the assessment of absolute dose in such extremely small field sizes by means of scatter factors. The sixth paper consists of the development of a dosimetry protocol to guide preclinical trials in MBRT; *iii)* finally, the main conclusions of this work and some reflections on future developments are presented.

Table of Contents

List of Abbreviations

AAPM	American Association of Physicists in Medicine
AP	Anterior-Posterior
BNCT	Boron Neutron Capture Therapy
BNL	Brookhaven National Laboratory
c-t-c	centre-to-centre
CRT	Conformal Radiation Therapy
CT	Computer Tomography
DEF	Dose Enhancement Factor
DICOM	Digital Imaging and Communication in Medicine
DNA	DeoxyriboNucleic Acid
DOPL	Degree Of Linear Polarisation
DTPA	Diethylene Triamide Pentaacetic Acid
EPDL	Evaluated Photon Data Library
ESRF	European Synchrotron Radiation Facility
FWHM	Full Width at Half Maximum
GOS	Generalised Oscillator Strength
HU	Hounsfield Units
HVL	Half Value Layer
IAEA	International Atomic Energy Agency
IC	Ionisation Chamber
ICRU	International Commission on Radiation Units and measurements
ID	Insertion Device
IGRT	Image-Guided Radiation Therapy
IMRT	Intensity-Modulated Radiation Therapy
IR	Ionising Radiation
LAC	Large Area Chamber
linac	LINear ACcelerator
LLNL	Lawrence Livermore National Laboratory
LQ	Linear-Quadratic
MBRT	MiniBeam Radiation Therapy

MC	Monte Carlo
MLC	Multi-Leaf Collimator
MOSFET	Metal-Oxide-Semiconductor Field-Effect Transistor
MRI	Magnetic Resonance Imaging
MRT	Microbeam Radiation Therapy
MSLC	MultiSLit Collimator
NSLS	National Synchrotron Light Source
NTCP	Normal Tissue Complication Probability
NTD	Normalised Total Dose
OD	Optical Density
OFHC	Oxygen-Free High Conductivity
PD	Pen Deflection
PDD	Percentage Depth-Dose
PET	Positron Emission Tomography
PMMA	PolyMethyl MethAcrylate
PSF	Phase-Space File
PVDR	Peak-to-Valley Dose Ratio
RF	Radio-Frequency
RGB	Red-Green-Blue
RIA	Relativistic Impulse Approximation
RMS	Root Mean Square
ROI	Region Of Interest
RT	RadioTherapy
SBRT	Stereotactic Body Radiation Therapy
SR	Synchrotron Radiation
SRS	Stereotactic RadioSurgery
SSRT	Stereotactic Synchrotron Radiation Therapy
TCP	Tumour Control Probability
TL	ThermoLuminescence
TPS	Treatment Planning System
TRS	Technical Reports Series
VMAT	Volumetric Modulated Arc therapy
VR	Variance-Reduction

CHAPTER 1

Introduction

Contents

1.1 Radiotherapy

1.1.1 Cancer incidence and treatment

Cancer is a large group of diseases characterised by uncontrolled growth of abnormal cells, which leads to the formation of malignant tumours. Cancerous cells can invade nearby tissue and spread out to distant parts of the body through the bloodstream and lymphatic system. Both external factors (tobacco, infectious organisms, chemicals and radiation) and internal factors (inherited mutations or mutations generated from metabolism, immune conditions and hormones) can initiate carcinogenesis [ACS 2011].

Cancer is considered to be responsible for one out of four deaths in Europe. In particular, it is the cause of approximately 40% of deaths of people between the age of 45 and 74 [Niederlaender 2006]. The incidence and mortality of different types of cancer (in Europe) is represented in figure 1.1. More details on cancer epidemiology worldwide can be found elsewhere [Ferlay 2010, ACS 2011, CBTRUS 2011].

The 5-year survival rate for all cancers diagnosed in 1999–2006 was 68% [ACS 2011]. This value has been largely improved with respect to the value of 50% in the period 1975–1977 due to advances in early diagnosis and cancer treatment [ACS 2011].

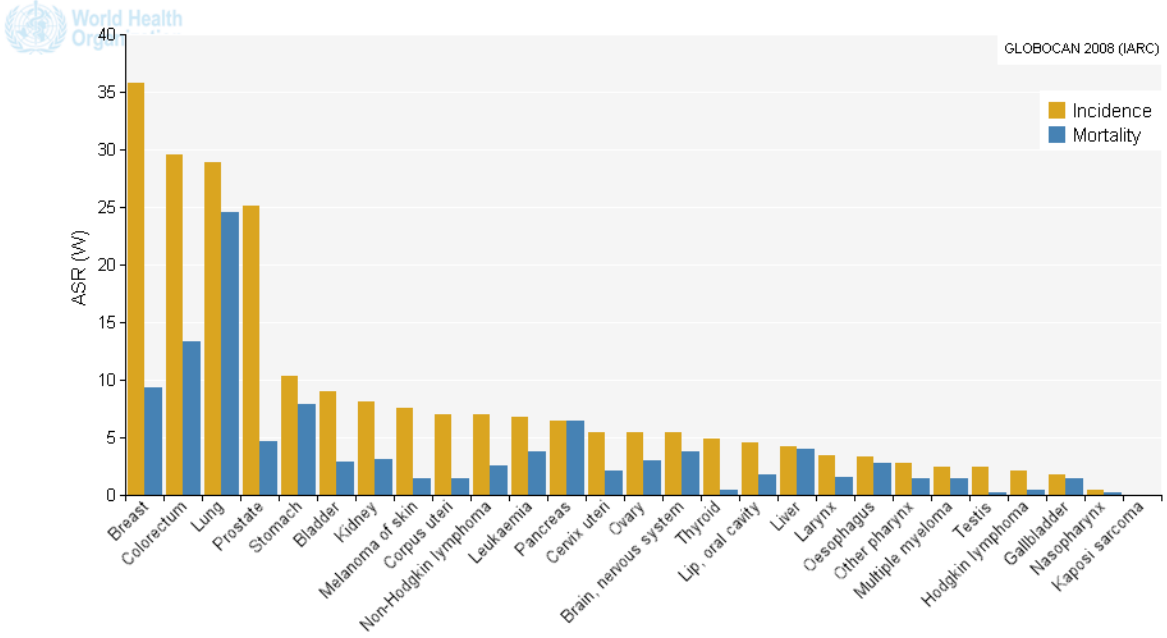

Figure 1.1: *Age-standarised rate (ASR) for world (W) standard population on incidence and mortality of different types of cancer in Europe in 2008 (both sexes, all ages). Extracted from [Ferlay 2010].*

However, despite the great improvements in the treatment of cancer, the outcome of some tumours remains unsatisfactory [Niyazi 2011]. This is the case of high-grade gliomas (glioblastomas), a cancer of glial cells, which is the most frequent and aggressive type of brain tumour. The median survival time of these patients is approximately one year and the survival rate five years after treatment is only about 5% [CBTRUS 2011]. Although the annual incidence of malignant primary brain and central nervous system tumours is low, these cancers entail extremely high morbidity and mortality. This is especially dramatic in children, as brain tumours are the second most common paediatrics malignancy, after leukaemia [ACS 2011], and the treatment options are very limited due to the high risk of complications in the development of the central nervous system.

Cancer treatment highly depends on tumour type, location and stage. Surgery, radiotherapy (RT) and chemotherapy are the most frequent options. It is common to combine all or several of these techniques. Among them, RT has a key role since a high percentage of patients (about 70%) will receive RT at some point during their illness [IAEA-TRS-461 2008].

1.1.2 Radiotherapy: concept and brief history

Radiotherapy is the medical use of ionising radiation (IR) to treat tumours and some benign lesions such as nodules, vascular problems, etc. IR is able to damage cells either by direct

break-up of DNA chains, or indirectly, as a result of the free radicals generated from the ionisation of water followed by DNA oxidation. The latter process is the dominant in conventional RT. The basis of RT lies in the fact that, compared to healthy cells, cancerous cells possess a reduced capability to repair DNA [Joiner 2009].

The first RT treatment was performed less than a year after W. C. Roentgen discovered the x-rays in 1895; E. H. Grubbe irradiated a patient that was suffering postoperative recurrence of breast cancer with x-rays. Despite the fact that first attempts were limited by primitive available x-ray generators, the therapeutic use of x-rays became widespread very quickly and 3134 cases of malignancies were treated from 1896 to 1909 [Kazem 1995].

In parallel, the discovery of radioactivity by H. Becquerel in 1986 and of polonium and radium in 1898 by M. Curie and P. Curie remarkably advanced the methods used for the treatment of cancer. Radium was initially used in several ways to treat different types of tumours until 1950, when cobalt-60 units started to come into use. This last step represented a big boost in the quest for higher photon energies for the treatment of deep-seated tumours. Additionally, the discovery of new isotopes and improved techniques for dose delivery expanded the idea of shrinking tumours through direct exposure to radioactive materials.

Thus, RT was soon split into two main divisions: external beam RT and brachytherapy [Khan 2010]. In the first case, the radiation source is external to the patient and radiation is delivered to the tumour in a non-invasive way. At present, this modality, which is mainly based on linear accelerators (also named linacs), accounts for almost 90% percent of RT treatments [Gerber 2008]. Instead, in brachytherapy, the radiation source (usually contained in radioactive seeds, rods or liquid) is located inside the patient in direct contact with the tumour. Hereafter, we will only refer to external beam RT. More information on brachytherapy can be found elsewhere [Thomadsen 2005, Polgár 2009, Crook 2011].

Cobalt therapy units have been at the forefront of external RT for a number of years. However, the reliability, flexibility, accuracy and the possibility of reaching higher energies given by linacs partially supplanted cobalt therapy as a treatment tool. Nevertheless, cobalt-60 is still in use for certain tumour sites. Both gamma and electron RT beams are produced by modern linacs, which accelerate electrons to kinetic energies from 2 to 25 MeV using microwave radio-frequency (RF) fields. Thanks to their characteristic dose fall-off in depth, direct electron beams are used to treat tumours that are not very deep. They are also employed to boost photon treatments to increase the dose deposited in the tumour while sparing nearby healthy tissue. Photon beams (6–18 MV) are produced by the rapid deceleration of electrons in a high-density target (bremsstrahlung). See figure 1.2 for a schematic representation of a linac. More details about their working principle can be found in [Podgorsak 2005]. Superficial and orthovoltage units (50–500 keV x-rays) are also employed for treatment of

superficial cancers [Amdur 1992]. Other accelerators such as microtrons have also been explored as electron accelerators for medical applications due to their reduced dimensions [Brahme 1981].

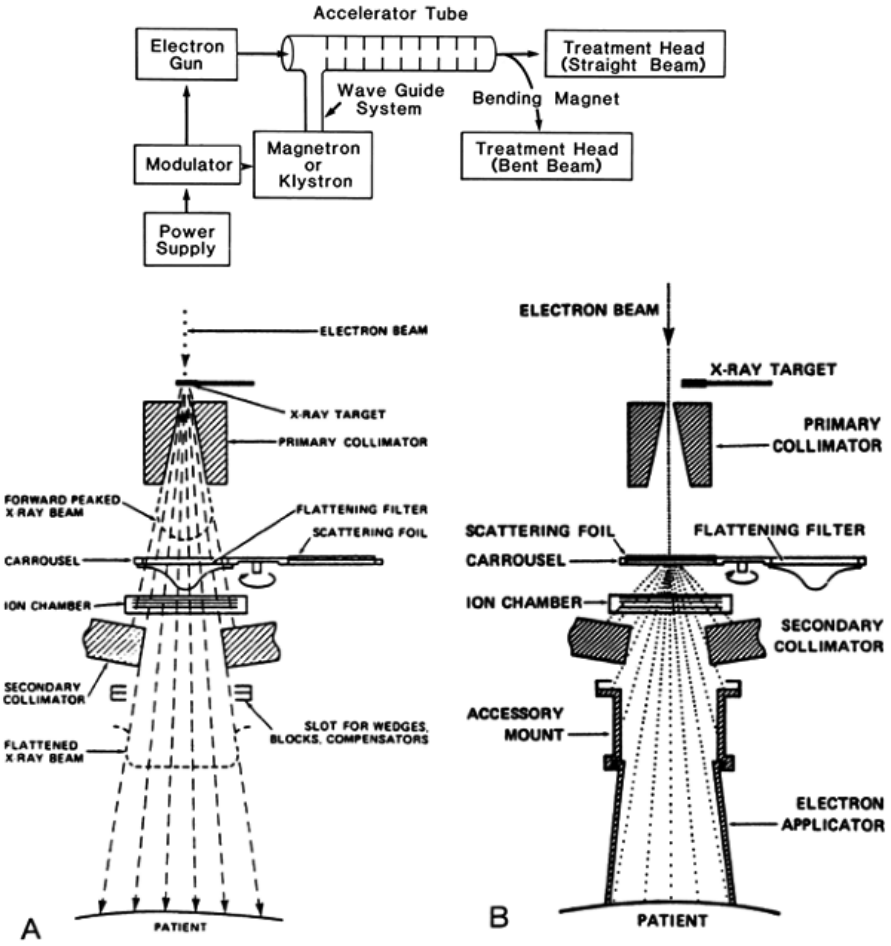

Figure 1.2: *A block diagram of a typical medical linear accelerator (top) and schematic images showing the basic components of the head of a modern linac for x-ray (A) and electron (B) therapy (bottom). Extracted from [Khan 2010].*

A series of technological advances have improved the targeting of external beam RT by moving from 2D rectangular treatment fields to four-dimensional conformal RT (4D-CRT) techniques. In particular, advanced imaging technologies such as computer tomography (CT), magnetic resonance imaging (MRI) and positron emission tomography (PET) have enabled the direct 3D visualisation, definition and characterisation of the tumour and surrounding healthy tissue. This, along with the use of an increased number of fields and multi-leaf collimators (MLC) allowed high, homogeneous and conformed doses to be delivered to the

tumour with minimal irradiation of normal tissue. Intensity-modulated radiation therapy (IMRT) is the most modern and sophisticated high-precision 3D-CRT, with the ability to fit complex shapes in treatment volumes. This is obtained by modulating the number of fields, their shape and intensity distribution of each beam, which is constituted by multiple small and adjustable 'beamlets' [Elith 2011, IMRTGroup 2001]. The high level of dose conformity encouraged the development of new imaging capabilities in real time or during the course of the treatment in order to improve precision on dose delivery (4D-CRT or image-guided radiation therapies, IGRT [Dawson 2006]).

Historically, fractionation of the dose in small daily doses of radiation (1.8–4 Gy) over several weeks has been applied in order to permit healthy cells to recover between sessions while causing cumulative damage to the tumor cells [Coutard 1934]. The high precision delivery methods mentioned above and advances in radiobiology enabled a move towards different dose-escalation schemes for some types of tumours [Papiez 2008]. For instance, stereotactic radiosurgery (SRS) delivers a high radiation dose to the tumour in one or a few fractions by converging multiple radiation beams on an intracranial lesion [Phillips 1994]; or stereotactic body radiation therapy (SBRT), which also uses hypo-fractionated scheme, employs robotic guidance technologies [Martin 2010]. As a result, the impact of tumour cell repopulation is diminished. Both techniques can be delivered by using adapted linacs or specialised systems such as the Gamma Knife® [ELEKTA® 2012] or CyberKnife® [ACCURAY® 2012].

There are other RT methods available or in development nowadays. For instance, hadrontherapy, which is an advanced external RT technique that uses charged particles such as protons, alphas, C, Ne, etc. [Brahme 2004]; or boron neutron capture therapy (BNCT), where the patient is exposed to neutron irradiation which causes the activation of boron compounds (previously injected and mostly concentrated in tumour cells) to emit alpha particles and lithium nuclei from the disintegration of ^{11}B, which deposit the dose locally within the tumour [Barth 2005]. The combination of enhanced radiobiological properties and localised dose deposition of such particles have overcome some of the inherent dosimetric and biological shortcomings of photons and electrons [Halperin 2006]. Additionally, new delivery and dose deposition methods are being explored by synchrotron RT techniques, which will be thoroughly explained in the following sections.

1.1.3 The therapeutic index

IR induces cell damage both in the tumour and in adjacent normal tissue. The rationale of RT lies in the fact that, in general, healthy tissue presents a higher recovery capability than tumour tissue. In addition, the tumour control probability (TCP) follows a sigmoid curve in

function of dose. As the radiation dose is increased, the TCP rapidly escalates until a plateau is reached. The same is true for the probability of inducing deleterious effects in normal tissue, which is represented by the normal tissue complication probability (NTCP) curve. The balance between the TCP and NTCP is a measure of the therapeutic index of the treatment [Joiner 2009]. This concept was introduced in 1936 by H. Holthusen [Holthusen 1936] and is illustrated in figure 1.3. The term therapeutic window corresponds to the range of doses for which TCP is much higher than NTCP, that is to say, a tumour can be effectively treated while staying within the safety range for healthy tissue.

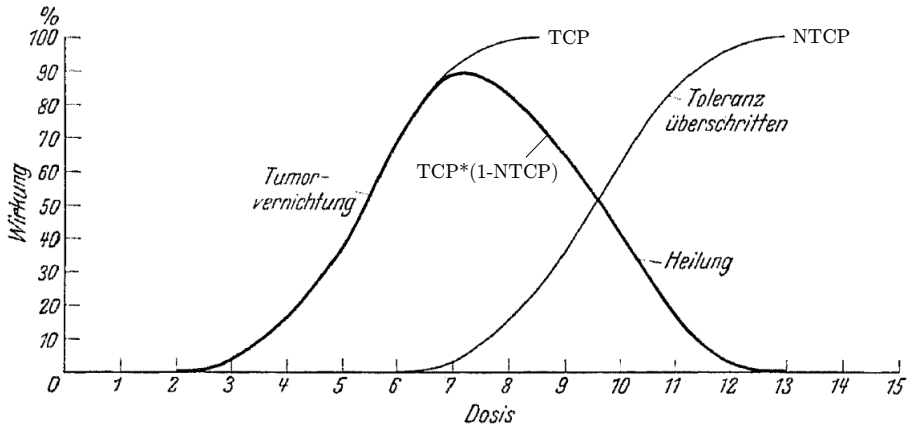

Figure 1.3: *Illustration of the therapeutic index concept. TCP curve represents the probability of tumour control and NTCP indicates the normal tissue complication probability. TCP*(1-NTCP) is the probability of cure without deleterious effects in terms of the dose deposited to the tumour (arbitrary units). Extracted from [Holthusen 1936].*

The dose-response curves lie in close proximity for very radioresistant tumours such as gliomas. In these cases, the risk of serious damage to normal tissue is not compatible with the possibility of reaching curative doses. In order to widen the therapeutic window, either the effect on the tumour needs to be increased (for example, by achieving a higher gradient in TCP) or the dose received by the healthy tissue is reduced (the NTCP curve needs to shift to the right) or both [Joiner 2009].

The beam type (photons, electrons, protons, etc.), beam quality, dose delivery methods (temporal fractionation scheme, dose rate, spatial distribution, etc.) have a direct impact on the therapeutic index [Willers 2006, Kim 2008, Joiner 2009]. Thus, the modification of any of these parameters implies a different biological response. This might lead to a shift of the NTCP dose-response curve to higher doses, opening the therapeutic window for highly aggressive tumours.

The response of gliomas to variations of some of these parameters has been already explored [Combs 2005, Fuller 2007, Wen 2008, Yamamoto 2008], as well as biological optimisation by using chemotherapy drugs (concomitant and adjuvant temozolomide) together with RT [Stupp 2005, Stupp 2009]. Despite the fact that a significant prolongation of the survival probability was observed in the latter case, tumour recurrence is still important [Niyazi 2011]. This is the reason behind the interest in prospecting new RT approaches.

1.1.4 Exploring new paths in RT at the ESRF: synchrotron RT techniques

The application of synchrotron radiation in RT at the European Synchrotron Radiation Facility (ESRF) was first suggested by Larsson [Larsson 1983]. Nowadays, the quest for a curative treatment of gliomas is at the origin of the development of three RT techniques at the ID17 Biomedical Beamline of the ESRF: contrast-enhanced synchrotron stereotactic radiation therapy (SSRT), microbeam radiation therapy (MRT) and minibeam radiation therapy (MBRT).

Contrast-enhanced SSRT consists of loading the brain tumour with a high-atomic-number (Z) element, such as iodinated contrast media, and irradiating it with monochromatic x-rays from a synchrotron source (tuned at an optimal energy) in stereotactic conditions. The highly conformal irradiation geometry and the increase in the photoelectric cross section produce localised dose enhancement in the tumour. This leads to improved dose distributions when compared to conventional high energy RT treatments [Mesa 1999, Boudou 2005, Adam 2008].

The other two techniques, *i.e.*, MRT and MBRT, are the most exotic ones. Both approaches combine submillimetric field sizes (25–100 μm and 500–700 μm-wide beams in MRT and MBRT, respectively) with the spatial fractionation of the dose (interbeam separation of 200–400 μm in MRT and 1200 μm in MBRT). At present, they are restricted to synchrotrons, despite the fact that MBRT has the potential to be extended to hospitals with cost-effective equipment. Further details on these techniques will be given in sections 1.4, 1.5 and 1.6.

1.2 Synchrotron radiation and third-generation sources

In this section, the fundamentals of SR will be presented. Afterwards, a brief overview of the different components of third-generation synchrotrons, such as the ESRF, will be described, with especial emphasis on insertion devices used to generate SR.

1.2.1 Synchrotron radiation

Charged particles emit electromagnetic radiation when accelerated [Jackson 1998]. In particular, synchrotron radiation (SR) is generated when a charge moving at a relativistic speed follows a curved trajectory. A non-relativistic particle produces radiation with the characteristic pattern shown in figure 1.4 (left). The relativistic speed changes the observed frequency by the Lorentz factor, $\gamma = 1 + E/(mc^2)$, where E is the kinetic energy of the electron, m is the rest mass of the electron and c is the speed of light in vacuum. In particular, the radiation pattern is distorted from an isotropic dipole into an extremely narrow cone of radiation with an opening angle equal to $2\gamma^{-1}$ (in rad). See figure 1.4 (right). A higher electron energy implies a smaller opening radiation angle, and thus, brighter SR [Wille 2001].

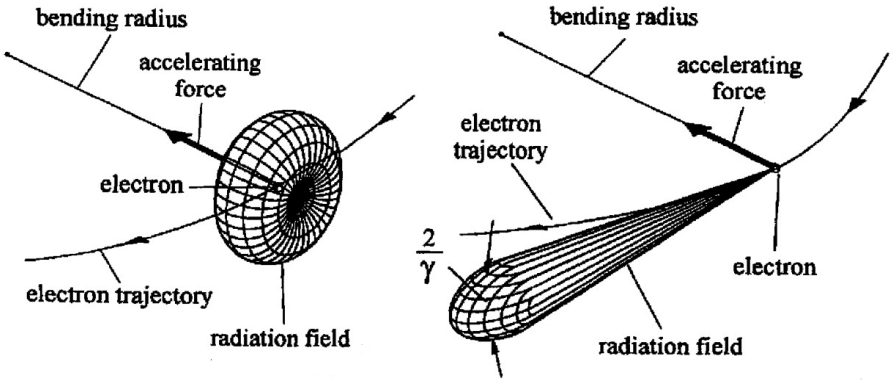

Figure 1.4: *Angular distribution of the radiation emitted by non-relativistic (left) and relativistic (right) charged particles following a curved trajectory. Extracted from [Wille 2001].*

SR can be generated by astronomical structures or in specialised particle accelerators. In the latter case, SR can occur as an undesired energy loss or produced on purpose for certain applications. The widespread usefulness of SR in material science, biology, etc. has led to the building of special facilities devoted to SR generation, which are named synchrotrons. These facilities accelerate charged particles (typically, electrons) and confine them in a circular orbit by means of electromagnetic fields. Figure 1.5 shows a scheme of the different parts constituting a synchrotron (left) and a storage ring (right).

Electrons are generated by heating a cathode (typically made of tungsten) and then they are pulled out by a strong electric field through a hole at the end of a gun. These electrons are first accelerated in a linear accelerator. Subsequently, bunches of electrons are transmitted into a circular accelerator (booster), where they are speeded up to operational energies. At

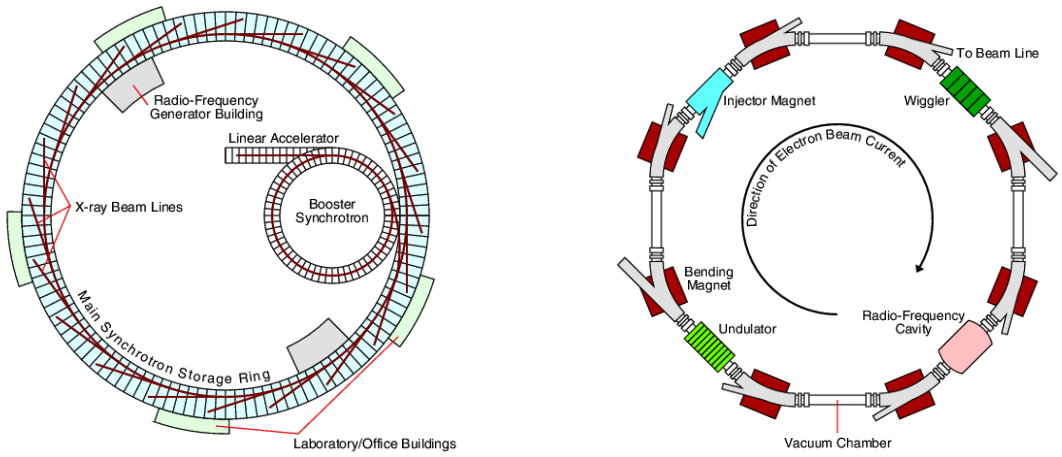

Figure 1.5: *Scheme of the different parts constituting a synchrotron (left) and a storage ring (right). Extracted from [Barnes 2012].*

this point, electrons are injected into a large storage ring, where they circulate in vacuum for many hours.

Storage rings comprise both straight and curved sections under ultra-high vacuum (less than 10^{-8} mbar). Dipole magnets (bending magnets) are located in the curved sections to bend the electrons trajectory in order to maintain them in a closed orbit and/or produce SR with a continuous spectrum. The electron beam is steered and focused by quadrupoles and sextupoles in order to keep the beam within a defined orbit.

In third-generation synchrotron radiation sources, specialised devices called insertion devices (ID) are located in the straight sections, between dipole magnets. They consist of an array of magnets which are used to generate a spatially periodic magnetic field along the electron beam path (see figure 1.6). There are two types of IDs at synchrotron facilities: wigglers and undulators. They both produce significantly higher brightness SR than bending magnets. Details on the properties of the SR emitted by an ID will be given in section 1.2.2.

RF cavities compensate the energy loss of the electrons on their trip along the storage ring. The presence of RF accelerating fields and radiation damping result in variations in the electron beam dimension and in the angular divergence with respect to the ideal position. Let us denote the standard deviation of the dimensions of the electron beam in the horizontal and vertical directions by σ_x and σ_z, respectively. Similarly, the divergence of the electron beam is expressed as σ'_x and σ'_z. See the coordinate system in figure 1.6 (right). The deviation of the electron beam position and angle are correlated by the emittances, $\varepsilon_x = \sigma_x \sigma'_x$ and $\varepsilon_z = \sigma_z \sigma'_z$, which remain invariant (Liouville's theorem). Beam size and emittance are related

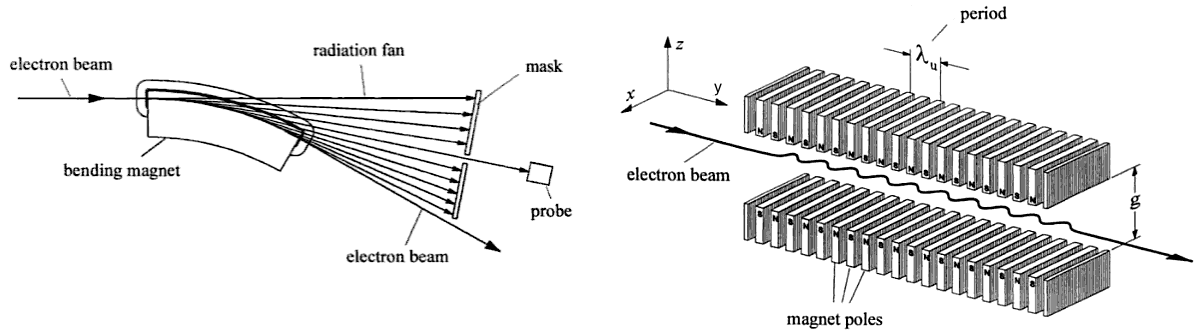

Figure 1.6: *Electron beam crossing a bending magnet (left) and an ID (right). Both systems are used to produce extremely bright SR. IDs (undulators and wigglers) are present in third-generation synchrotron sources and they consist of periodic magnetic structures. Extracted from [Wille 2001].*

through the beta parameters, defined as $\beta_x = {\sigma_x}^2 \varepsilon_x$ and $\beta_z = {\sigma_z}^2 \varepsilon_z$. Low β sections of the synchrotron correspond to a small source size and a high divergent beam while a high β section corresponds to the opposite situation [Wille 2001].

As has been explained, the SR is generated in the storage ring and it is channelled into the beamlines through the front-end sections. A beamline is composed of several parts: the optical hutch(es), the experimental hutch(es) and the control room(s). The first part is devoted to tuning the photon beam to the desired characteristics by means of monochromators, slits, filters, etc. The second part is where the experiment is carried out. Several photon beam modifiers, detectors and sample holders are also present in this hutch. The final part is where scientists control the experiment remotely and acquire data.

The final characteristics of the photon beam depend on the device used to generate the SR and on the beam modifiers interposed in the beam path. Key features of SR are:

- Wide energy range, ranging from infrared to hard x-rays. Experiments can be conducted with white radiation or with monochromatic beams.
- The beam has a small angular divergence (of the order of a few mrad) and possesses a low emittance, *i.e.*, the product of the source cross section and the solid angle of emission is small.
- High intensity and brightness. This enables measurements to be conducted at a high speed and with better statistics.
- Highly tunable due to the small natural divergence and the high beam intensity (monochromators, optical systems, filters, etc.).

- High linear polarisation degree in the plane of the electron orbit. Above and below this plane, the beam is elliptically polarised. This is of particular interest in the study of magnetic systems.
- Pulsed light emission (pulse durations of or below one nanosecond), that can be effectively used for research applications that are highly demanding in terms of time resolution.
- High temporal coherence (it is possible to have a small relative bandwidth by using undulators or/and monochromators) and spatial coherence (low emittance). These properties are used, for instance, in synchrotron imaging techniques.

1.2.2 Insertion devices

The two types of ID, *i.e.*, wigglers and undulators, are distinguished by the deflection parameter (K), which characterises the electron motion inside the ID. For a sinusoidal magnetic field, this dimensionless parameter is related to the deflection angle for half a wiggler pole (δ) as $K = \gamma\delta$. In practical units, K is expressed as

$$K = 0.934\, B[\mathrm{T}]\lambda_{\mathrm{u}}[\mathrm{cm}], \tag{1.1}$$

where B is the peak magnetic field (in T), which depends on the wiggler gap (g), and λ_{u} is the magnetic field period (in cm) [Als-Nielsen 2001].

If $K \leq 1$, the flight of the electron beam is inferior or equal to the natural opening angle of SR ($2\gamma^{-1}$). Moreover, SR from different periods interfere coherently and the resulting spectrum is constituted by quasi-monochromatic peaks at specific harmonics. The on-axis brightness increases as N^2, where N is the number of magnetic periods. In this regime, the device is called an undulator [Brown 1983].

In the particular case of spatially fractionated techniques, the photon source is generated by a wiggler. For these IDs, K is large (typically from 10–60). Thus, the horizontal beam divergence ($2K\gamma^{-1}$) is much larger than the natural opening angle of SR and the radiation produced at each pole adds incoherently. The spectrum of photons exiting a wiggler is essentially emitted in a continuum of energies from the infrared to the x-ray region and it is characterised by the critical energy ε_{c}, for which the radiated power is divided into two equal parts. This energy is given by

$$\varepsilon_{\mathrm{c}}(\theta) = \varepsilon_{\mathrm{c,max}}\sqrt{1-(\theta/\delta)^2}, \tag{1.2}$$

where θ is the observation angle in the horizontal plane and $\varepsilon_{\mathrm{c,max}}$ is

$$\varepsilon_{\mathrm{c,max}}[\mathrm{keV}] = 0.665\, B^2[\mathrm{T}^2] E^2[\mathrm{GeV}^2]. \tag{1.3}$$

From equations (1.2) and (1.3), it can be derived that high energy photons are concentrated on the central part of the beam.

Interference effects are still present in wigglers, especially at long wavelengths and in devices with many periods. Since wigglers are typically used at short wavelengths, these effects produce small variations about the normal continuous spectrum and the SR generated by a wiggler approximates the superposition of the SR from $2N$ bending magnets of alternating curvature. However, this enhancement depends on the design of the wiggler and on the emittance of the electron beam [Brown 1983].

More information on the physical properties of SR generated by IDs can be found elsewhere [Brown 1983, Als-Nielsen 2001, Clarke 2004, Thompson 2009].

1.3 The ESRF and the ID17 Biomedical Beamline

A general overview of the ESRF is presented in this section, with special emphasis on the technical description of the ID17 Biomedical Beamline. In particular, the characteristics of the beam modifiers used for spatially fractionated synchrotron RT techniques will be described.

1.3.1 European Synchrotron Radiation Facility (ESRF)

The ESRF [ESRF 2012] is one of the largest and most powerful synchrotrons in the world. It was founded in 1988 in Grenoble (France) and, nowadays, the ESRF is the result of an international consortium of nineteen countries devoted to cutting-edge science with photons. Figure 1.7 shows a satellite view of the ESRF (left) and a photograph taken inside the storage ring (right).

The ESRF is a third-generation synchrotron composed of: *i*) a linac that accelerates electrons up to 200 MeV; *ii*) a booster with a circumference of 300 m and a repetition rate of 10 Hz; and *iii*) a 6.04 GeV electron storage ring (844.4 m of perimeter). The beam is guided by 64 bending magnets and focused by 320 quadrupoles and 224 sextupoles [ESRF 2012]. The main features of the machine are listed in table 1.1.

The 40 beamlines available at the ESRF are used for a wide variety of scientific topics: material science, structural biology, extreme conditions science, x-ray imaging, etc. In particular, ID17 is one of the few synchrotron beamlines in the world entirely used for biomedical research.

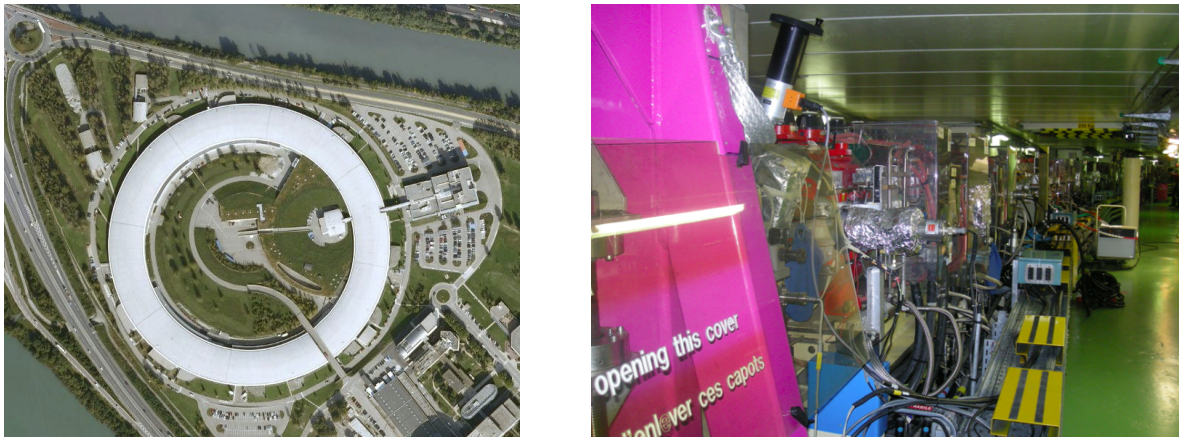

Figure 1.7: *Satellite view of the ESRF, from Google Maps (left), and a photograph of the ESRF storage ring (right).*

Table 1.1: *ESRF storage ring electron beam parameters (*RMS: Root Mean Square) [ESRF 2012].*

ESRF electron beam parameters	
Electron energy E	6.04 GeV
Maximum intensity $I_{\max}$	0.2 A
Horizontal emittance ε_x	3.9 nm
Vertical emittance ε_z	0.039 nm
Revolution frequency	355 kHz
Number of bunches	1 to 992
Time between bunches	2816 to 2.82 ns
Lifetime (992 bunches)	75 hours
RMS* bunch length (0.2 A)	20 ps
RMS* energy spread (0.2 A)	0.11%

1.3.2 ID17 Biomedical Beamline

ID17 is one of the two longest beamlines at the ESRF. The three main working areas are medical imaging, radiation biology and radiation therapy [Suortti 2003, Thomlinson 2005, Baruchel 2008, Bravin 2011]. Nowadays, large efforts are focused on RT programs, especially on the preparation of clinical trials in MRT and SSRT [Renier 2008, Requardt 2010, Adam 2011].

ID17 possesses two experimental hutches and their corresponding optical hutches (see figure 1.8). The first one, named the 'MRT hutch', is located at around 40 m from the wig-

gler source and is used for spatially fractionated RT techniques (MRT and MBRT) and brain microsurgery. In this case, the irradiations are performed with the white-beam coming from the wiggler after some filtering. The second station is located at about 150 m from the source and it uses monochromatic x-rays for SSRT [Adam 2011] or for medical imaging (absorption, time-resolved, K-edge subtraction, phase contrast, analyzer-based and diffraction-enhanced modes) [Baruchel 2008].

The photon source at ID17 is composed of two planar wigglers with periods of 15 cm (named w150) and 12.5 cm (w125). In spatially fractionated synchrotron RT techniques, only the first wiggler (w150) is used. The second wiggler (w125) was constructed to further increase the photon beam flux in other applications such as SSRT.

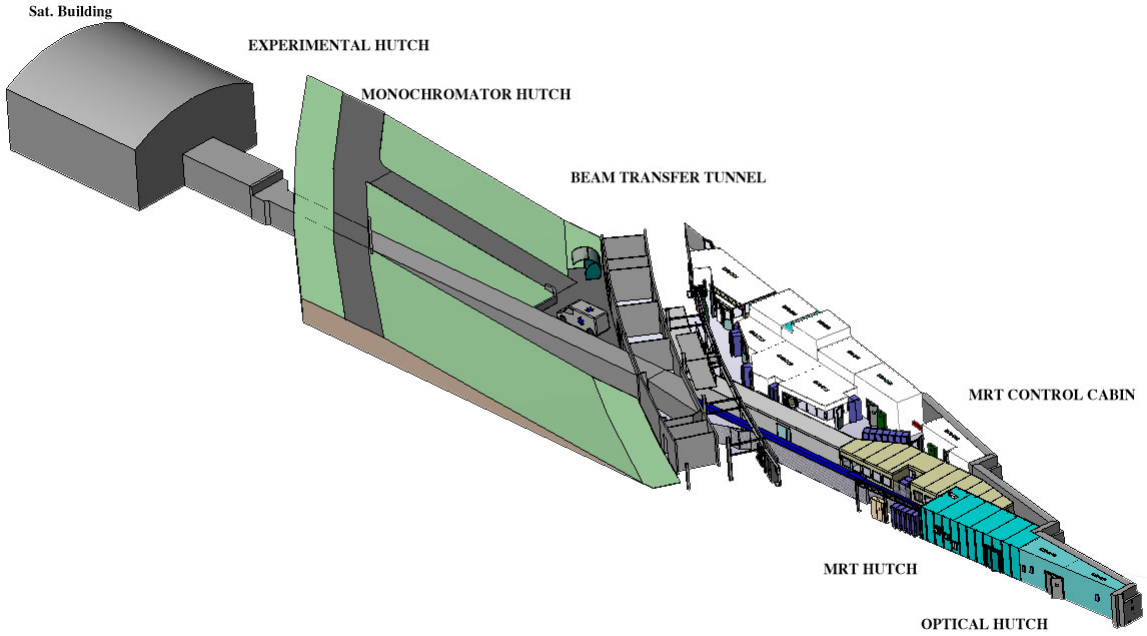

Figure 1.8: *ID17 Biomedical Beamline layout. Extracted from [ESRF 2012].*

After exiting the wiggler, the beam is directed to the front-end sections and then to the optical hutches, where it will encounter a series of beam modifiers that will tune the beam following the particular requirements of each experiment. Specific details of the set-up used in spatial-fractionated RT techniques (MRT and MBRT) will be given in following sections. Additional information on the other parts of the beamline can be found elsewhere [Elleaume 1999].

1.3.3 ID17 w150 wiggler

The main characteristics of the ID17 w150 wiggler are listed in table 1.2. This wiggler is located in a low β section (small source size and a high divergent electron beam) and it is composed of 21 poles. The magnetic field and the deflection parameter depend on the wiggler gap in a complex way, as represented in figure 1.9. The maximum magnetic field is approximately 1.6 T for the minimum permitted gap of 2.48 cm. This corresponds to a maximum total power of approximately 19.3 kW.

Table 1.2: *ID17 wiggler (w150) characteristics (*RMS: Root Mean Square) [ESRF 2012].*

ESRF electron beam parameters at the ID17 wiggler position	
RMS* horizontal source size	57 μm
RMS* vertical source size	10.3 μm
ID17 wiggler parameters	
Magnetic field period λ_u	15 cm
Number of poles	21 total, 19 equivalent
Number of periods N	11
Gap g (for the MRT irradiation conditions)	2.48 cm
Peak magnetic field $B(g = 2.48$ cm)	1.592 T
Deflection parameter $K(g = 2.48$ cm)	22.30
Critical energy $\varepsilon_c(g = 2.48$ cm)	38.6 keV

The full width at half maximum (FWHM) of the spatial distributions of photons at the wiggler exit along the horizontal and vertical axis are 0.280 and 0.018 cm, respectively. The vertical divergence corresponds to the natural opening angle of SR, $2\gamma^{-1}$=0.17 mrad, while the horizontal divergence is equal to $2K\gamma^{-1}$=3.77 mrad. Photons are emitted in a continuum of energies with a critical energy (ε_c) of 38.6 keV for MRT and MBRT irradiation conditions (g=2.48 cm). The emitted SR is linearly polarised in the orbital plane. Above and below this plane, elliptical polarisation is observed. Since photons emitted by successive poles have opposite sense of helicity, the net helicity is zero and the resulting beam is partially (linearly) polarised. In particular, the total degree of linear polarisation of the SR emitted by the ID17 wiggler is 0.660 [Martínez-Rovira 2012a].

Detailed information on the phase-space distributions (position, direction of flight, spectrum and polarisation state) of the beam was assessed in this work and it will be presented in

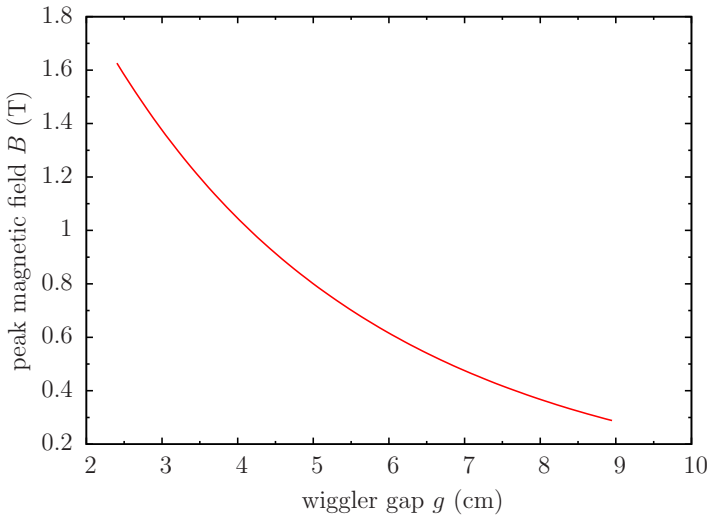

Figure 1.9: *Peak magnetic field (B) versus wiggler gap (g) for the w150 wiggler. The curve follows a complex trend:* $B = 2.78e^{-0.02535g} + 0.8425e^{-0.07538g} - 0.087e^{-0.081g} - 0.487e^{-0.16g}$. *The dependence between both magnitudes has been measured experimentally and then fitted by a sum of exponential curves (courtesy of J. Chavanne, ESRF).*

section 2.5. Results were obtained with the SHADOW code [Lai 1986, Sánchez del Río 2011].

1.3.3.1 ID17 wiggler modelling: the SHADOW code

SHADOW is a widely used synchrotron radiation ray-tracing program [Lai 1986, Lai 1988, Chapman 1989, Sánchez del Río 2011]. It is able to model synchrotron sources (bending magnets, undulators and wigglers) and to trace the generated SR beam along complex optical systems based on a phase ray-tracing approach.

SHADOW considers wigglers as a series of pseudo-bending magnets with no interference effects between the different bends in the trajectory [Lai 1988]. Wiggler modelling involves the calculation of the electron trajectory and the generation of the photon source by using MC methods. Firstly, the electron trajectories in a sinusoidal magnetic field perpendicular to the wiggler axis are calculated [Chapman 1989]. The resulting electron motion is also sinusoidal and lies on the horizontal plane. Secondly, the total emitted number of photons at each point of the trajectory is computed [Jackson 1998]. Most photons are produced in regions of high curvature and only few of them in the region between the poles. The distribution probability of photon emission is used to select the point (and its associated radius of curvature ρ) where the photon is generated. Subsequently, the source is treated as a conventional bending magnet with a radius of curvature ρ.

The divergence and position of electrons are computed by taking into account their emit-

tances, *i.e.*, the fact that the electrons are not all moving on the ideal central orbit but rather distributed around two double-Gaussian distributions in the phase-space. Since the photon emission is aligned to the electron direction, the photon energy and angle can be generated independently from the electron direction [Green 1976, Chapman 1989]. The final photon direction is then computed by shifting the emission angles along the real orbit of the electron.

SHADOW describes the state of polarisation of electromagnetic radiation by means of the Stokes parameters [Fano 1954]. They are calculated from the electric field of the propagating wavefront and the phase difference between the parallel and perpendicular (to the plane of incidence) components [Hetch 2001].

1.3.4 Front-end section and MRT optical hutch

The beam exiting the wiggler travels in vacuum inside a long stainless steel pipe. Several valves and Be windows (300–500 μm-thick) allow isolation between different vacuum sections. Along the way, ionisation chambers (IC) are used to monitor the beam.

In its path, the beam encounters several beam modifiers. Firstly, some diaphragms limit the beam aperture to reduce the heat load in the downstream optical elements. The diaphragm that effectively limits the maximum irradiation field size is located at 21.6 m from the wiggler centre, in the so-called front-end section. It is made of oxygen-free high conductivity (OFHC) copper and its horizontal (H) $\times$ vertical (V) apertures are 2.4$\times$0.15 cm^2. This leads to a fixed maximum H and V dimensions at the patient position of 4.1 cm and 0.25 cm, respectively.

The beam is directed towards the first optical hutch, whose layout is shown in figure 1.10. After traversing an additional diaphragm, the beam finds a Kr gas filter (at a pressure of 85 mbar without the beam and of about 160 mbar for the maximum electron beam current). This filter helps to further attenuate the beam intensity in order to protect the downstream components in case of failure. The field size at the patient position is then defined by the aperture of the primary slits. They consist of four motorised blocks of OFHC Cu (left, right, up and down). Five water-cooled attenuators (1.42 mm of C, 0.28 + 1.24 mm of Al and 0.35 + 0.69 mm of Cu), which are located after the primary slits, progressively eliminate the low energy part of the spectrum.

The 'fast shutter' and the photon absorber are key elements since they are responsible for stopping the radiation in less than 5 ms, after the irradiation process has been completed. The fast shutter consists of two 15-mm-thick tungsten carbide blades coupled to two actuator magnets. During the closing time of the 'fast shutter', the beam is absorbed by the photon absorber (cooled 40-mm-thick Cu block), which has a longer reaction time (about 1 s). More

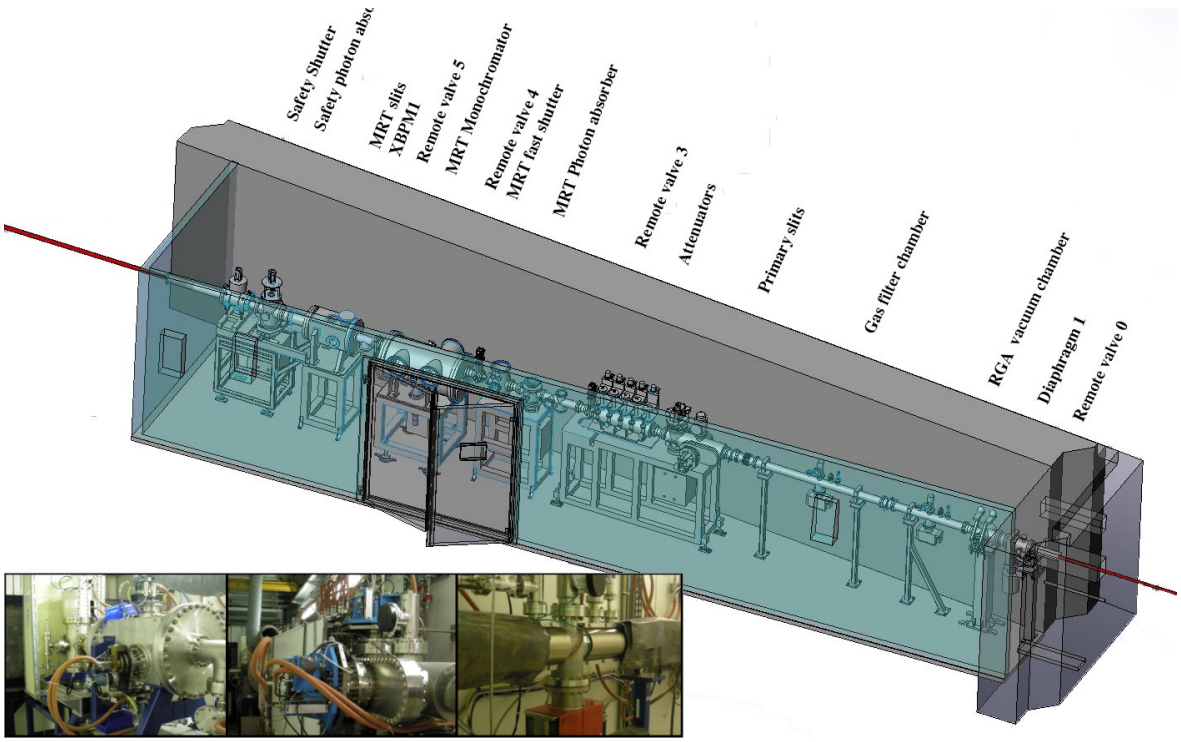

Figure 1.10: *MRT optical hutch layout (extracted from [ESRF 2012]). The photographs are taken at several points in the optical hutch: at the monochromator, at the attenuators and at the gas filter position (from left to right).*

information on this system can be found in the work of Renier *et al.* [Renier 2002].

There are other elements placed out of the beam path in RT experiments or not used nowadays. For instance, the double-Si (111) crystal Laue-type monochromator (energy range: 30 to 80 keV), which is used to perform CT imaging prior to irradiation to ensure good positioning, or the MRT slits, which consist of a couple of additional slits that were used to further define the field size at the patient position.

1.3.5 MRT experimental hutch

The beam leaves the vacuum when it crosses the final Be window, which constitutes the boundary with the experimental area. An Al foil acts as a separator between vacuum and air. Figure 1.11 shows a schematic representation and a picture of the beam modifiers present in the experimental hutch. An IC is located just after the vacuum section in order to monitor the beam. The next three elements are out of the beam path in RT experiments and they are only used for specific purposes. For instance, the plexiglass blocks act as photon absorbers

during imaging, the rotary shutter is employed for some radiobiology MRT experiments and the horizontal slit is only used for beamline alignment. The vertical slit (V slit) is present in all MRT irradiations. It consists of a small aperture made of tungsten carbide and has several available sizes (50, 100, 500 or 800 μm). Its function is very important since it allows only the homogeneous central part of the beam to be selected for the irradiation.

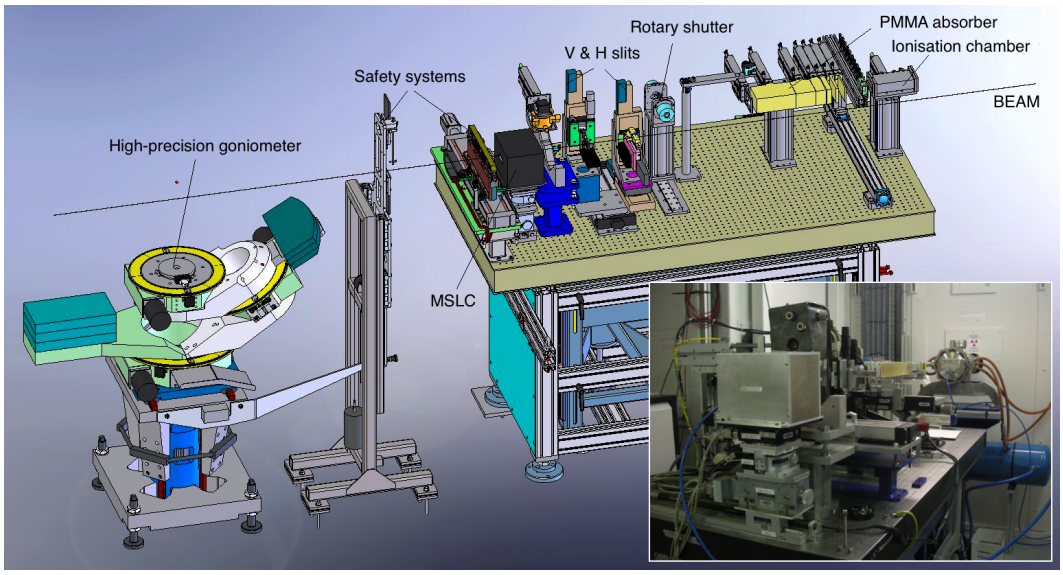

Figure 1.11: *Scheme and picture of the beam modifiers in the MRT experimental hutch (scheme courtesy of M. Renier, ESRF).*

Additional patient safety systems have been added to the set-up for forthcoming MRT clinical trials. They prevent an overdose of the patient in case of failure by using lead shielding blocks that limit the maximum irradiation dimensions [Berkvens 2011, Renier 2011].

Targets (patients or phantoms) are placed on a 3-axis Kappa-type high-precision goniometer (Huber, Germany). The mechanical accuracy of this device is in the order of 5–10 μm. The vertical dimensions of the beam at the goniometer position are very small since they are defined by the V slit aperture. In order to fill in the required vertical field size, targets are vertically scanned at constant speed (in the range of 10 to 100 mm/s). The chosen speed depends on the desired dose, beam current and vertical slit size. This scanning method is equivalent to homogeneous irradiation [Prezado 2011b].

The spatial fractionation of the beam is achieved by using two additional instruments: either a multislit collimator (MSLC) in microbeam radiation therapy (MRT), or a chopper in minibeam radiation therapy (MBRT). Thanks to the specific beam properties and these two devices, ID17 offers an ideal environment for the exploration of RT approaches based on

distinct dose delivery methods. In particular, those involving the use of intense micrometre-sized beams.

In MRT, the beam is spatially fractionated along the horizontal direction by means of a MSLC [Bräuer-Krisch 2009]. It consists of a unique 8-mm-thick block, mostly composed of tungsten carbide (86.8%, weight percentage) and Cu (12.0%). The MSLC to be used in the clinical trials will consist of a series of 50-μm-wide slits with a centre-to-centre (c-t-c) separation of 400 μm. Details on other MSLCs used in MRT, which allowed additional beam widths and c-t-c distances, can be found in the literature [Slatkin 1995a, Archer 1998, Bräuer-Krisch 2005a].

The MSLC cooling system consists of a direct flow of N_2 and a water-cooled Cu block support. The whole system is enclosed in a box with one entrance and one exit 500-μm-thick Al windows. Figure 1.12 shows a top view of the MSLC box (left) and a graphical representation of the MSLC (right).

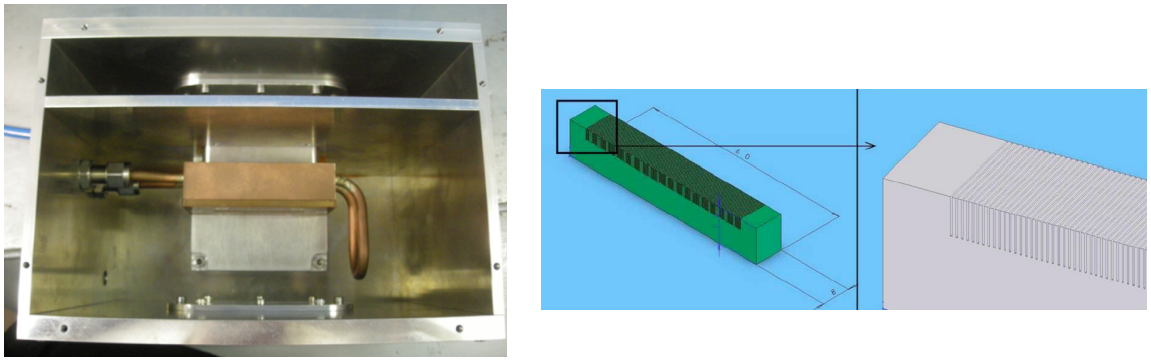

Figure 1.12: *Top view of the MSLC whole block (left) used for MRT. The slits of the MSLC can not be seen. On the right, a graphical representation of the MSLC (extracted from [Bräuer-Krisch 2009]).*

In MBRT, the vertical spatial fractionation of the beam is achieved by using a special device called white-beam chopper [Renier 2005], instead of a collimation block system. The chopper is composed of ten tungsten carbide blades. See figure 1.13.

The rotational speed of the chopper is synchronised with the vertical motion of the target. In this way, each opening of the chopper generates a horizontal beam print. The duty cycle is fixed at 50%, and thus, the time the beam is on is exactly equal to the time when it is off. For interlaced beams, the duty cycle is set to 53% in order to ensure maximum homogeneity in the interlaced region. This innovative method was preferred over a static MSLC since it offers excellent reliability and reproducibility [Prezado 2009b].

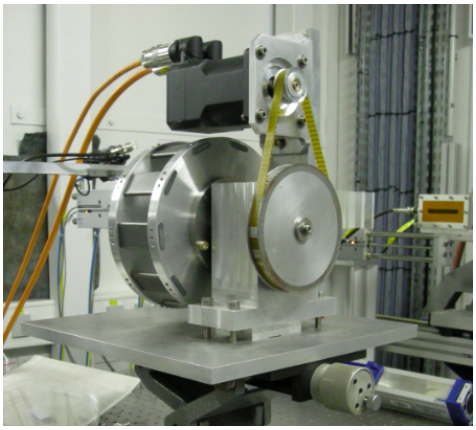

Figure 1.13: *Photograph of the white-beam chopper used for MBRT.*

1.4 Basic principles of spatially fractionated synchrotron RT techniques

As has been explained in section 1.1.3, differences in dose delivery methods (fractionation scheme, dose rate, spatial distribution, etc.) have an impact on the therapeutic index of RT treatments. This idea is the basis for the development of MRT and MBRT, whose main features in terms of beam characteristics, exploration of the dose-volume effect and potential advantages with respect to conventional methods will be explained in the following sections.

1.4.1 Beam characteristics at the patient position

MRT and MBRT irradiations present very distinct features with respect to conventional RT techniques. The x-ray source differs from medical accelerators in the method for photon generation, type and dimensions of the beam modifiers, beam intensity, energy range, etc. See figure 1.2 and section 1.3. A summary of the main MRT and MBRT beam characteristics at the patient position is:

- Submillimetric field sizes are used. The beam widths range from 25 to 100 μm in the case of MRT and from 500 to 700 μm in MBRT.
- The beam is spatially fractionated. The irradiation is performed with an array of intense quasi-parallel beams. The c-t-c distance is 200–400 μm in the case of MRT and 1200 μm in MBRT.
- The energy spectrum ranges from 27 to 600 keV with a mean energy of 99 keV. The fraction of photons with energies higher than 300 keV is very small (0.1%) [Siegbahn 2006,

Martínez-Rovira 2012a].

- Beam divergence is approximately 0.5 mrad in the horizontal direction and 0.02 mrad in the vertical one. These values are significantly lower than in a conventional linear accelerator (around 35 mrad).
- The spectral flux at the patient position is several orders of magnitude higher than any conventional x-ray generator. This leads to extremely high dose rates, which provide fast irradiations and minimise cardiosynchronous motion effects in the patient [Poncelet 1992]. In particular, the dose rate is approximately 13.4 kGy/s for the maximum electron current and a 50 μm V slit size (for a 2×2 cm^2 whole irradiation field size at 2 cm-depth in water). This, along with the low energy spectrum and the small beam divergence, allows production of sharply defined beam edges.
- The beam is highly linearly polarised in the plane of the electron orbit at the patient position (the total degree of linear polarisation equals 0.994 [Martínez-Rovira 2012a]).

The resulting dose profiles consist of a pattern of peaks and valleys, *i.e.*, with high doses along the microbeam path and low doses in the spaces between them. The minimum dose in the central region between two microbeams is named the valley dose and the dose at the centre of the microbeam is the peak dose. The ratio between the peak dose and the valley dose (peak-to-valley dose ratio, PVDR) is an important dosimetric parameter in spatially fractioned techniques, since it plays an important role in biological response [Dilmanian 2002]. The MRT dosimetric parameters depend on the incident x-ray beam energy, beam width, c-t-c distance, irradiation field size and tissue composition. Figure 1.14 shows an example of lateral dose profile. The peak and valley regions and the c-t-c distance, which refers to the separation between the centres of two consecutive peaks, are represented.

1.4.2 Exploring the limits of dose-volume effect

The use of submillimetric field sizes allows the limits of the dose-volume effect to be explored: the smaller the field size is, the higher the tolerance of the healthy tissue. This phenomenon has been known since the 50s, when Zeman and collaborators investigated the possible hazards of heavy cosmic rays in the brain of astronauts [Zeman 1959, Zeman 1961, Curtis 1967]. To this end, they irradiated mice brains with 22.5 MeV deuteron beams of several field sizes. They evaluated the threshold dose to produce necrotic lesions along the first half of the beam path (1.5 mm) within 24 days. The reconstruction of the results is represented in figure 1.15 [Zeman 1959, Zeman 1961]. The tolerance doses remain almost constant for

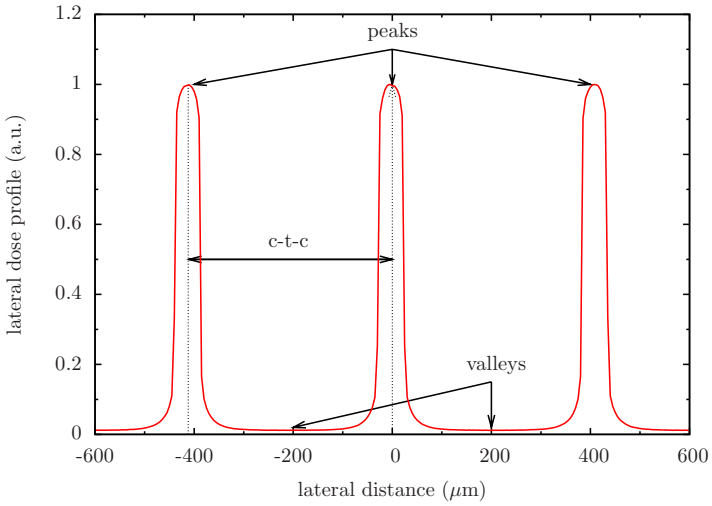

Figure 1.14: *Example of MRT dose pattern.*

field sizes larger than approximately 0.1 mm; below this value, the tolerance dose increases dramatically.

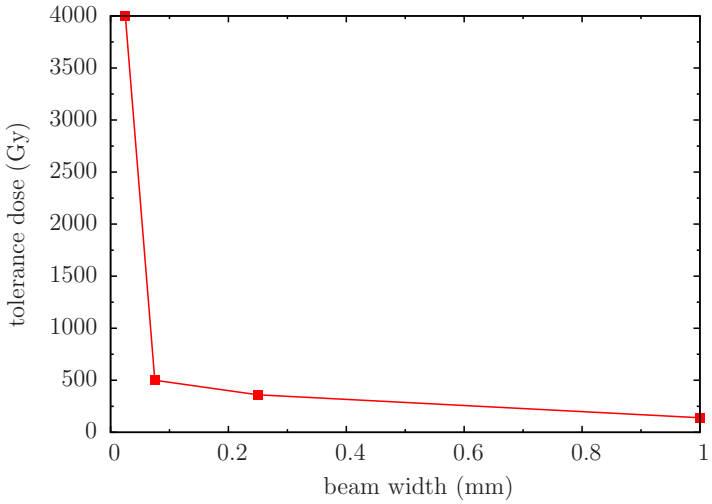

Figure 1.15: *Tolerance doses (Gy) of mice brains to irradiation with 22.5 MeV deuteron beams of several widths (mm). There is an inverse relationship between radiosensitivity and volume of tissue exposed for small volumes. This is known as the dose-volume effect [Zeman 1959, Zeman 1961, Curtis 1967].*

Figure 1.16 shows histology images of mice brains irradiated with 22.5 MeV deuteron beams with a diameter of 1 mm (entrance dose of 280 Gy) and 25 μm (4000 Gy). The results clearly indicate that there is an inverse relationship for small volumes between radiosensitivity and volume of tissue exposed. This phenomenon was also observed a few years later

in x-ray beams [Straile 1963] and, subsequently, for high-energy photons [Hopewell 2000, Lawrence 2010].

The dose-volume effect might be explained by the stem cell depletion hypothesis: for each organ, there is a critical volume that can be repopulated by a single survival stem cell that migrates from the nearby tissue to recover the tissue damaged by the radiation [Yaes 1988]. Thus, the combination of submillimetric field sizes and spatial fractionation of the dose provides a further gain in tissue sparing due to the biological repair of the microscopic lesions by the minimally irradiated contiguous cells. This leads to a shift of the NTCP curve towards higher doses, widening the therapeutic window for gliomas, as indicated by the biological studies performed so far (see section 1.5).

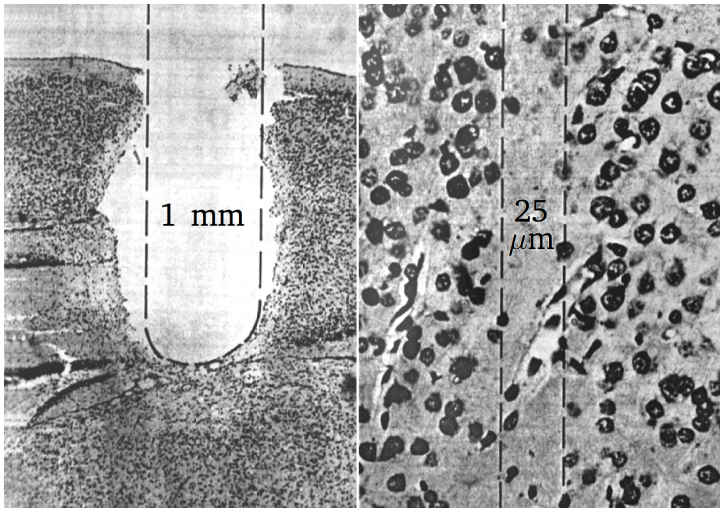

Figure 1.16: *Histology images of mice brains illustrating the dose-volume effect. On the left, complete tissue destruction is observed after irradiation with a 22.5 MeV deuteron beam of 1 mm of diameter and an entrance dose of 280 Gy. On the right, the tissue is well preserved after irradiation with a 25-μm-wide beam and an entrance dose of 4000 Gy. Extracted from [Zeman 1961].*

1.4.3 Potential advantages of MRT and MBRT with respect to conventional RT methods

Possible improvements of MRT and MBRT over the existing clinical RT and radiosurgery techniques might include:

- Superior normal tissue tolerances, allowing the use of higher and potentially curative doses.

- Small penumbras (10–40 μm) in comparison with several millimetres in radiosurgery. Hence, they are a perfect candidate for the treatment of tumours close to an organ at risk or for the treatment of illnesses such as epilepsy, Parkinson's disease, etc. with negligible secondary effects.

- A potentially more effective combination with tumour-dose enhancement agents based on high-Z elements due to the larger photoelectric cross section in the energy range of MRT and MBRT.

- MRT and MBRT might also produce a temporary disruption of the blood-brain barrier (brain capillaries that protect the central nervous system by strictly regulating the entrance of molecules from the extracellular fluid) for selective delivery of a chemotherapy drug to small areas in the brain, which can be exploited for improving the therapeutic index in an exponential way.

1.5 Microbeam radiation therapy (MRT)

MRT was conceived at the Brookhaven National Laboratory (BNL) at the National Synchrotron Light Source (NSLS), in Upton (USA) in 1992 [Slatkin 1992]. For two decades, numerous experiments have been carried out at the NSLS and, subsequently, at the ESRF, with the aim of assessing the therapeutic effectiveness of MRT. Nowadays, the use of MRT has spread to other synchrotrons around the world (Spring 8 in Japan, Canadian Light Source, Australian Synchrotron, etc.). This section will provide details on MRT preclinical trials and related Monte Carlo and experimental dosimetric studies performed up to now.

1.5.1 MRT preclinical trials

1.5.1.1 Assessment of the MRT therapeutic index

The first MRT biological experiment took place at the BNL in 1995 [Slatkin 1995b]. Synchrotron-generated 20 and 37 μm microbeams (spaced by 75 and 200 μm, respectively; 48.5 keV critical energy) were delivered to rat brains in a single exposure. No brain damage was observed in the histology for entrance doses inferior to 625 Gy.

In 1998, the technique was applied to 9L gliosarcoma-bearing rats [Laissue 1998]. This type of tumour, which is immunologically compatible with rats, is extremely radioresistant compared to other models [Barth 1998, Bencokova 2008]. The irradiation was performed with 25-μm-wide unidirectional and bidirectional arrays of microbeams (spaced by 100 μm;

312.5 and 625 Gy skin entrance doses). The results showed that MRT protocols significantly increased the survival of the animals, which was accompanied by a reduction in tumour growth after irradiation (see figure 1.17). The longest survival was observed for the 625 Gy bidirectional group, with 50% of the animals alive at day 115 (control rats died within 31 days). Furthermore, the complete ablation of the tumour was also observed in more than half of the rats. This suggested the possibility of a differential effect between healthy and tumour tissue after MRT irradiations.

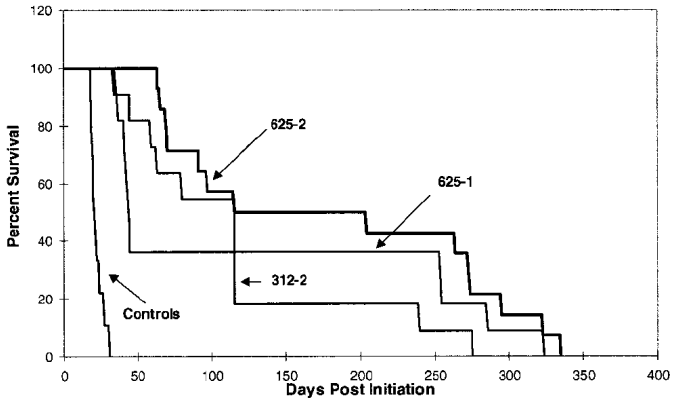

Figure 1.17: *Survival curves of 9L gliosarcoma-bearing rats after irradiation with different MRT protocols: bidirectional irradiation with entrance doses of 312.5 (named 312-2) and 625 Gy (625-2), and unidirectional irradiation with an entrance dose of 625 Gy (625-1). Extracted from [Laissue 1998].*

A series of preclinical studies continued at the NSLS and started at the ESRF [Laissue 1999] for more than 20 years. Several experiments confirmed the healthy tissue sparing capability of MRT irradiation in hindbrains of weanling piglets [Laissue 2001], rat leg skin [Zhong 2003] and in very immature tissues such as suckling rat hindbrains [Laissue 2001] or duck embryo brains *in ovo* [Dilmanian 2001]. Figure 1.18 shows a histological section of a piglet cerebellum 15 months after an MRT irradiation with an entrance dose of 300 Gy (20–30 μm-wide microbeams spaced by 200 μm). Despite the fact that some cells were killed in the beam path, no tissue destruction, haemorrhage, demyelination or locomotion problem was observed for entrance doses up to 600 Gy.

The biological basis of the healthy tissue sparing after MRT irradiations is not well understood. As has been mentioned, this effect was attributed to hyperplasia and migration of minimally irradiated endothelium and glial cells between the irradiated slices [Slatkin 1995b]. The initiation of migration, proliferation and differentiation of the progenitor glial cells could be assisted by distant bystander effects from the dying cells [Dilmanian 2007b, Kashino 2009].

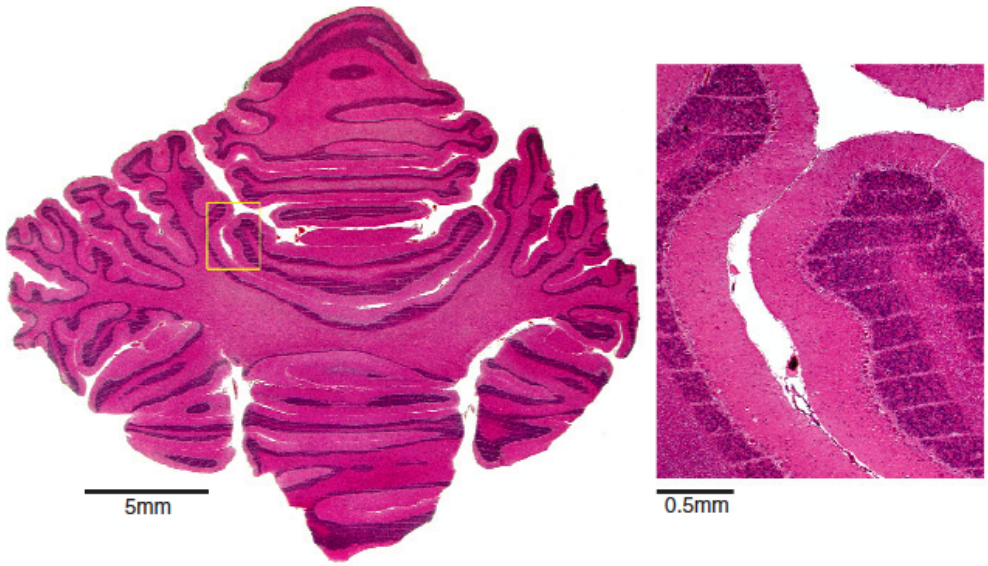

Figure 1.18: *Horizontal section of the cerebellum of a piglet 15 months after an MRT irradiation with an entrance dose of 300 Gy (20–30 μm-wide microbeams spaced by 200 μm). The beam paths are clearly visible in the histology images, but no tissue destruction is observed. Extracted from [Laissue 2001, Laissue 2007].*

Dilmanian *et al.* discovered that this sparing effect (measured by the onset of the appearance of white matter necrosis) vanishes when the valley dose approaches the tissue tolerance to seamless beams. Therefore, the brain damage threshold from MRT seemed to depend mostly on the valley dose [Dilmanian 2002].

The fast regeneration of healthy vasculature may also play a role in normal tissue recovery after an MRT irradiation. Several experiments confirmed no changes in blood volume and vascular density in normal vasculature at very high entrance doses [Serduc 2006, van der Sanden 2010]. In addition, no disruption of the blood brain barrier or significant oedema was observed and only a transient increase in the blood-barrier permeability was detected [Serduc 2006, Serduc 2008b]. The absence of important oedema may represent an important advantage of MRT with respect to other RT treatments.

The high therapeutic index of MRT has been exhaustively confirmed by the significant increase in survival time, and in some cases, tumour ablation in different kinds of tumours in rodents, such as 9L rat gliosarcoma [Laissue 1998, Dilmanian 2002, Serduc 2008a], subcutaneous murine EMT-6 carcinoma [Dilmanian 2003b], subcutaneous human squamous-cell SCCVII carcinoma [Miura 2006] and C6 and F98 gliomas [Schültke 2008]. In the latter case, object recognition tests were performed on the animals after irradiation. MRT did not seem

to affect the memory capability of the rats.

Tumour cells are not so effective in terms of a repair response to MRT irradiations as normal cells [Crosbie 2010]. However, Dilmanian *et al.* showed that the tumoricidal effect of MRT is not completely attributed to direct tumour cell lethality since 2% of clonogenic cells survived 5 min after the irradiation of 9L gliosarcoma-bearing rats (with doses that had ablated about 50% of the tumours) [Dilmanian 2002]. It was hypothesised that some other mechanisms might be the preferential effect on immature tumour vessels with respect to differentiated normal vasculature, which would result in ischemic necrosis of the tumour [Dilmanian 2002]. This was confirmed by irradiation of chick chorioallantoic membranes *ex ovo* containing immature fast growing vessels. Results showed massive damage to the microvascular plexus traversed by microbeams, while minor and reversible alterations, and thus, an uninterrupted blood flow, was observed in larger vessels [Blattmann 2005, Sabatasso 2011].

Posterior *in vivo* studies did not show any important damage to tumour vessels after MRT irradiation in 9L gliosarcoma-bearing nude mices (by using two orthogonal arrays of 25-μm-wide microbeams). In this case, the increased survival time was attributed to cytoreduction rather than early direct effects of IR on tumour vessels [Serduc 2008a]. However, recent studies with 50-μm-wide microbeams revealed loss of tumour vessel endothelia and a significant decrease in blood volume from 8 to 15 days after irradiation, with a subsequent reduction in tumour volume. The extracellular matrix and lack of endothelia could cause initial temporary irrigation to the tumours. These results confirmed the differential effect between tumour and healthy blood vessels for 50-μm-wide microbeams [Bouchet 2010].

The promising results obtained in preclinical studies have opened the door to the preparation of MRT clinical trials. The work performed on different medical physics features will be explained in sections 1.5.2 and 1.5.3.

The remarkable MRT therapeutic index shown in the preclinical trials can be further improved by optimising irradiation ballistics or by using drugs or high-Z contrast agents in combination with MRT. Both improvements have been experimentally tested and they will be described in the following subsections.

1.5.1.2 Optimisation of the MRT irradiation ballistics

Several studies were performed with the aim of finding the best balance between healthy tissue sparing and tumour control in function of microbeam parameters (microbeam width, c-t-c distance and irradiation modality).

The first work that evaluated MRT therapeutic index in function of the spacing of the

microbeams was performed by Dilmanian *et al.* [Dilmanian 2002]. In this study, the biological effects of irradiations with 27-μm-wide microbeams spaced by 50, 75 and 100 μm were assessed. These beam spacings turned out to be too small, given the observed toxicity in the normal brain. Subsequent studies revealed that a 200 μm spacing provided a higher therapeutic index than 100 μm for a single array of 25-μm-wide microbeams in 9L gliosarcoma-bearing rats [Régnard 2008b].

The effect of the microbeam width was evaluated by Serduc *et al.* [Serduc 2009a], who concluded that 50-μm-wide microbeams (spaced by 211 μm) provide the best compromise between tumour control and normal brain toxicity compared to 25 or 75 μm-wide microbeams, for the same valley doses at the centre of the tumour of 9L gliosarcoma-bearing rats. Following these observations, the irradiation conditions for forthcoming clinical trials were fixed to 50-μm-wide microbeams spaced by 400 μm. The c-t-c distance was chosen to maintain the ratio of beam spacing to beam thickness from conclusions extracted in smaller beam sizes [Régnard 2008b]. Some preclinical studies have already been performed in this configuration [Bouchet 2010, van der Sanden 2010].

In addition, new irradiation configurations were explored. Some of the first MRT experiments used two orthogonally crossed arrays of microbeams [Laissue 1998]. A further improvement of this method consisted of the crossfire of two orthogonal microbeam arrays. In this case, the microbeam spacing at the centre of the tumour is divided by two but the healthy tissue remains exposed to unidirectional irradiation [Bräuer-Krisch 2005b, Bräuer-Krisch 2005c]. High-precision irradiation methods using several entrance ports guided by synchrotron imaging methods have also been developed [Serduc 2010a, Serduc 2010b]. In parallel, preliminary work pointed at a possible advantage of using a 'temporal' fractionation of the dose [Serduc 2009b].

1.5.1.3 MRT in combination with drugs

The exploration of other methods to further improve the MRT therapeutic index include, for instance, the combination of MRT with immunotherapy. The subcoutaneous inoculation of antigenically-enhanced radiation-disabled gliosarcoma cells grown *in vitro* showed a significant increase in the survival time in 9L gliosarcoma-bearing rats [Smilowitz 2002, Smilowitz 2006]. Additionally, MRT was also successfully used in combination with drugs that produce a cytotoxic effect [Régnard 2008a] or an increase in the radiosensitivity [Schültke 2008] of tumour cells.

The latest efforts are mainly directed to an enhancement of dose deposition in the tumour by the combination of MRT with high-Z labelled-compounds. These can be selec-

tively accumulated within the tumour prior to any irradiation protocol. This idea was first proposed by Dilmanian *et al.* [Dilmanian 2007a] and applied experimentally by Régnard *et al.* [Régnard 2008a]. The injection of gadolinium compounds Gd-DTPA (resulting from the union of Gd with diethylene triamide pentaacetic acid, DTPA) in the tumour prior to MRT irradiation improved the life span of rats by a factor greater than two. This is because the probability of undergoing a photoelectric interaction increases significantly for the energy range of the MRT spectrum in the presence of high-Z contrast agents. Therefore, a localised dose enhancement in the tumour is achieved. Similar results were obtained with Au@DTDTPA-Gd. The combination of Gd and Au with a dithiolated derivative of DTPA (DTDTPA) permitted both the follow up by x-ray imaging and MRI [Alric 2008].

The use of other lanthanides with chemical properties similar to those of Gd (Z=64) can also be found in a biocompatible formulation with DTPA: holmium (Z=67), erbium (Z=68), ytterbium (Z=70) and lutetium (Z=71). Some these approaches have already been used and commercialised for medical applications [Koudelková 2003, Nawroth 2008, Yasui 2008]. Gold (Z=79) and iodine (Z=53) were also successfully used as dose enhancers in preclinical trials with kilovoltage x-rays [Adam 2005, Hainfeld 2010]. Some new nanoparticles based on Hf (Z=72), which preclude the metabolism of living organisms due to their structure, have been recently developed [NANOBIOTIX® 2012]. Finally, thallium (Z=81) is also a good candidate due to its high-Z; it has already been employed for experimental treatment of glioma-bearing rats [Ljunggren 2004].

1.5.2 Previous MC dosimetric studies in MRT

Several Monte Carlo (MC) dosimetric studies were performed to guide the aforementioned biological research. Table 1.3 shows some of the most relevant MC studies in MRT (in chronological order). The main features of the microbeams and the phantoms used for the simulations are also detailed; the studies marked in bold are related to this PhD work and they will be presented in chapter 2.

The first MC dosimetric study in MRT was performed by Slatkin *et al.* [Slatkin 1992]. Despite the fact that the importance of including electron transport was recognised in this work, dose distributions were initially computed by partially considering charged particle interactions (INHOM, EGS4 + CPE codes). Subsequently, similar simulations were repeated by other authors who used sophisticated codes which included more accurate cross sections and a single-collision electron transport approach (PSI-GEANT [Stepanek 2000]) or a mixed approach (PENELOPE [Siegbahn 2005, Siegbahn 2006] and GEANT4 [Spiga 2007] codes). Differences in PVDR values were of the order of 10–20% with respect to the first MRT MC

Table 1.3: *Some of the most relevant MC dosimetric studies in MRT (in chronological order). References in bold are part of this thesis and they will be detailed in chapter 2. 'MC code' indicates the MC code used to perform the simulations. More information on the physical models used in each version of the code can be found in the 'Reference'. 'Width' refers to the microbeam width, while 'c-t-c' indicates the spacing between microbeams. 'Field size' is the total irradiation field size. In the column 'Energy', the photon energy of the microbeams is detailed. NSLS or ESRF refers to the complete NSLS or ESRF spectrum, respectively, while specific energy values indicate monochromatic beams. The asterisks denote the level of complexity in the photon source definition (including polarisation* and beam divergence** or a complete wiggler and beamline description***). 'Phantom' indicates the main features of the phantom used in the simulations.*

Reference	MC code	width (μm)	c-t-c (μm)	Field size (cm^2)	Energy (keV)	Phantom
[Slatkin 1992]	INHOM (EGS4),CPE	25	50/100/200	1×1, 2×2, 3×3	50/100/150	water
[Company 1998]	XYZDOS (EGS4)	25/50	150/200/300	2×2, 4×4, 7×7, 12×12, 20×20	100	water/lung
[Orion 2000]	EGS4	30	100/200	6×2, 4×6	NSLS*	human head
[Stepanek 2000]	PSI-GEANT	25	50/100/200	1×1, 2×2, 3×3	50/100/150/200	water
[Felici 2005a]	EGS4	25	200	1×1, 3×3, 1×3	ESRF*/50/100/150/200	water
[Siegbahn 2006]	PENELOPE	25	50/100/200	1×1, 2×2, 3×3	ESRF	water
[Spiga 2007]	GEANT4	25/50/75	50/100/200	1×1	ESRF/50/100/150	water
[Prezado 2009a]	PENELOPE	50	200	2×2	ESRF	human head
[Nettelbeck 2009]	PENELOPE	50	410	1×1	ESRF**	water
[Martínez-Rovira 2010]	PENELOPE	50	400	2×2	ESRF	human head
[Martínez-Rovira 2011]	PENELOPE	50	400	2×2	ESRF	human head
[Martínez-Rovira 2012a]	PENELOPE	50	400	1×1, 2×2, 3×3	ESRF***	water
[Martínez-Rovira 2012b]	PENELOPE	50	400	1×1, 2×2, 3×3	ESRF***	voxelised structures

study [Slatkin 1992]. The impact on the lateral dose profiles for the different type of interactions is represented in figure 1.19.

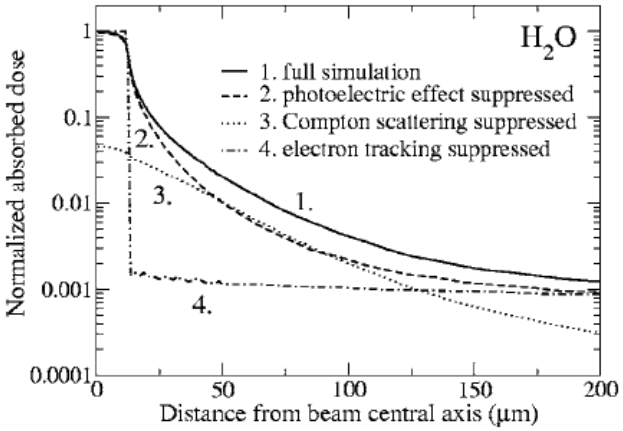

Figure 1.19: *Impact on the lateral dose profiles of suppressing different types of interactions: the photoelectric effect, Compton scattering and electron transport. The microbeam size corresponds to 25 μm. Extracted from [Siegbahn 2006].*

The important role of the low-energy physics models implemented in MC codes has been emphasised in different works [Siegbahn 2006, Spiga 2007]. In particular, significant differences were observed in the dose profiles and PVDR values obtained with GEANT4 and with PENELOPE. Deviations were mainly attributed to the cross sections and to the algorithms for tracking secondary interactions used in the GEANT4 code [Torres 2004, Spiga 2007].

Two early works (with the EGS4 code) included the real spectrum and polarisation state of the synchrotron beam in the simulations [Orion 2000, Felici 2005a], while other studies considered non-polarised monochromatic beams. A very interesting publication of De Felici *et al.* showed that the polarisation of the beam had a non-negligible effect on the dose calculations away from the centre of the microbeam array [Felici 2005a]. Since the scattering of polarised photons is now considered in the PENELOPE code (version 2008), recent MRT studies also include this feature [Martínez-Rovira 2012a, Martínez-Rovira 2012b].

The simplification of the real irradiation source geometry was a common practice among authors of theoretical MRT studies (see table 1.3). Indeed, identical, parallel, perfectly rectangular microbeams were usually considered. The dose of a single microbeam was simulated and a superposition algorithm was used to generate the dose profile of the complete array. These simplifications failed to account for the source size and shape, the beam divergence along the distance from the synchrotron source to the patient position or any geometrical and scattering effect arising from the radiation transport through the beamline.

Nettelbeck *et al.* showed, by using simple models, that these approximations could lead to inaccuracies in the valley doses, penumbral regions of dose profiles and in the PVDR values. If beam divergence was included, an increase of 26% in the penumbra region and 10% in the valley doses was observed. Furthermore, modelling of a synchrotron-distributed source rather than a point source resulted in almost 30% larger penumbral doses [Nettelbeck 2009]. See figure 1.20. Additionally, De Felici *et al.* reported that the effects induced by the fine structure of biological tissues were important for the microbeam dose deposition assessment [Felici 2005b, Felici 2007].

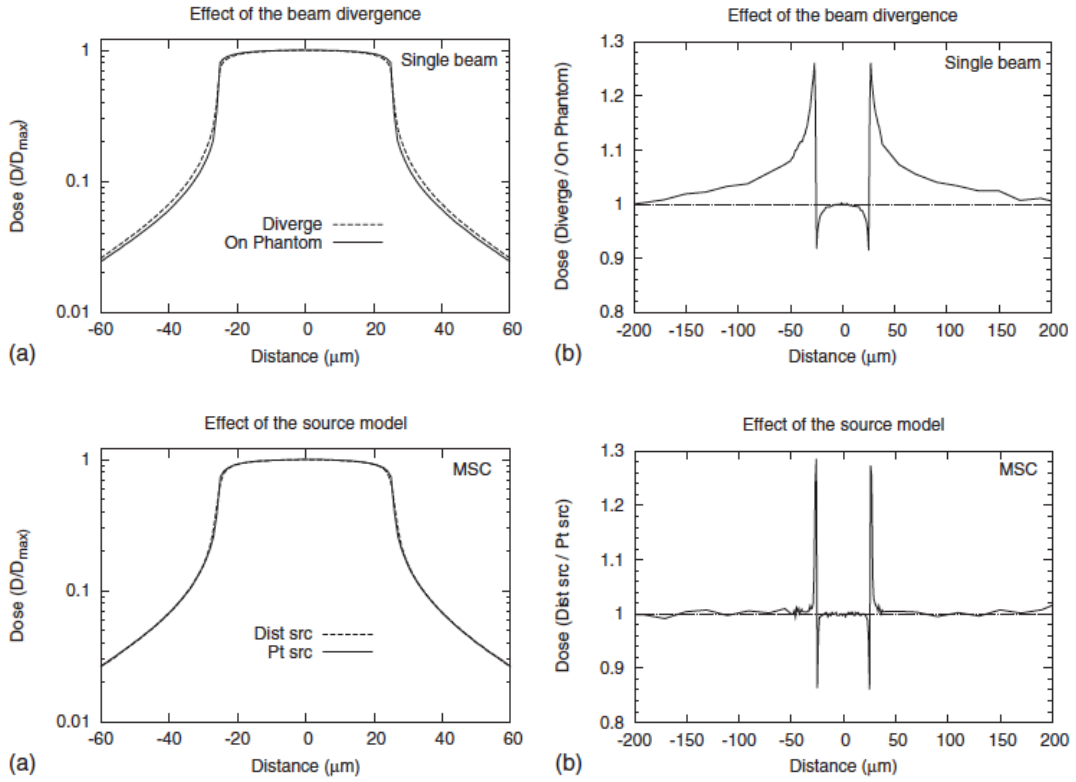

Figure 1.20: *Influence of the beam divergence (top) and source model (bottom) for a single microbeam scored between a depth of 1 and 2 cm in water. Extracted from [Nettelbeck 2009].*

All aforementioned works were performed on a water phantom. The first realistic dosimetric study of MRT dose distributions in a human head phantom was performed by Orion *et al.* [Orion 2000]. The posterior study of Prezado *et al.* [Prezado 2009a] was also devoted to the dose assessment in a human head phantom but with particular interest in the dose enhancement obtained in a Gd-loaded tumour. Other studies considered heterogeneous

phantoms for lung cancer applications [Company 1998]. It is important to point out that the use of realistic geometries is essential for correct dose assessment. For example, the valley dose in a centrally located tumour in a water phantom is around 2.8 times higher than that of a head phantom. The difference is mainly ascribed to the presence of bone. Thus, MC studies performed in this PhD considered both a realistic source model and phantom.

1.5.3 Previous experimental dosimetric studies in MRT

In parallel, several experiments based on different dosimetric systems were performed. The main challenge lies in developing a detector with a very high spatial resolution that is able to cope with the high dose rates and high doses used in MRT.

Among the different approaches, solid state detectors were the first to be explored. Rosenfeld *et al.* used a metaloxide-semiconductor field-effect transistor (MOSFET) in 'edge on' mode scanned through the beam and compared it with other experimental detector systems. The study showed the superiority of the MOSFET when mapping narrow radiation beams since the spatial resolution was mainly determined by the sensitive gate-oxide layer (1 μm in this case) [Rosenfeld 1996, Rosenfeld 1999, Kaplan 2000]. Orion *et al.* compared experimental results with MC data and they found relatively good agreement in the lateral dose fall-off of a single microbeam [Orion 2000]. Subsequent works measured experimental absolute peak and valley doses in a PMMA phantom by using a similar MOSFET; they found that experimental doses were 20% smaller than the expected MC values [Rosenfeld 2001, Bräuer-Krisch 2003]. A study of Siegbahn *et al.* found that MC simulations estimated PVDR values up to 50% higher than experimental data. The main sources of discrepancies were attributed to the energy dependence response of the MOSFET detector [Siegbahn 2009] and to the impact of the microbeams on the elements of the detector set-up, which had a high average atomic number [Rosenfeld 2005].

Thermoluminescence (TL) systems have also been used in MRT. In particular, LiF:Mg,Cu,P (MCP) powder (minimum MCP grain size: 0–45 μm). The observed differences in the PVDR values up to 20% were attributed to the detector design. The limitations of the reader might also have played a role [Ptaszkiewicz 2008].

Despite its limitations, the most suitable detector system for MRT available nowadays seems to be radiochromic films. In particular, Gafchromic® films [ISP® 2012]. These films provide high spatial resolution and enable PVDR values to be assessed. They have been successfully used to record doses in synchrotron sources and to evaluate PVDR values in MRT [Crosbie 2008, Bräuer-Krisch 2009, Nariyama 2009, Martínez-Rovira 2012a]. Although Crosbie *et al.* found some differences in the measured (films) and calculated (MC) values,

they were attributed to the simplified models used in the MC calculations [Crosbie 2008]. MC results with an accurate source model showed very good agreement with experimental data obtained with radiochromic films, as will be presented in section 2.5.

Recently, other detectors such as TL Ge-doped silica fibres [Abdul Rahman 2010], fluorescence nuclear track detectors [Bratz 2011] or high resolution optical calorimetry systems [Ackerly 2011] are under investigation. Further studies are warranted to completely characterise these detectors and evaluate their use in MRT. Silicon strip detectors have also been proposed to perform online dosimetry [Cullen 2011].

A review of the systems used or that can be potentially used for MRT can be found in [Braüer-Krisch 2010a]. Fundamentals on detector systems are beyond the scope of this work and can be found in the literature [Knoll 2000].

1.5.4 Dosimetry for forthcoming clinical trials in MRT

The success of the preclinical studies opened the way to future clinical trials in MRT at the ESRF [Renier 2008, Requardt 2010]. In order to minimise the risk, the first phase of the clinical trials will consist of the treatment of spontaneous tumours in large animals (cats and dogs) [Bräuer-Krisch 2010b]. The relatively high incidence of some cancers, similar biological behaviour, large body size, comparable responses to cytotoxic agents, and shorter overall lifespan are the factors that contribute to the advantages of this pet animal model [MacEwen 1990].

Within this framework, an important part of this PhD work was devoted to establishing accurate dosimetry in MRT. In particular, extensive work was performed both from the MC simulation and experimental dosimetry points of view. An introduction to the MC PENELOPE/penEasy code used to perform the simulations and the experimental methods employed in absolute and relative MRT dose measurements will be presented in the following sections.

1.5.4.1 The MC PENELOPE/penEasy code

PENELOPE [Baró 1995, Sempau 1997, Salvat 2008], an acronym of PENetration and Energy LOss of Positrons and Electrons in matter, is a MC simulation package that describes the coupled transport of photons, electrons and positrons in a wide energy range (from 50 eV to 1 GeV) and in arbitrary materials systems. PENELOPE, which is coded in FORTRAN, is both free and open source. It was developed at the *Universitat de Barcelona* and it is distributed by the Nuclear Energy Agency (NEA) and the Radiation Safety Information Computational

Center (RSICC) of the Oak Ridge National Laboratory (ORNL). Presently, there are more than 1500 copies of the code distributed around the world.

PENELOPE uses detailed simulation for photon transport and a mixed approach for charged particle transport. Hard electron and positron interactions are simulated individually, whereas a condensed simulation is applied for soft interactions. This classification is based on certain user-defined parameters: the cutoff energy for the production of hard inelastic events (`WCC`) and hard bremsstrahlung (`WCR`), the maximum allowed step length (`dsmax`), the average angular deflection (C_1) and the maximum average energy loss (C_2) in a single multiple-scattering step. All particles are transported until their kinetic energy is below the absorption energy (`EABS`), at which the remaining energy is locally absorbed.

PENELOPE is widely used in the medical physics field and, in particular, in dose calculations for spatially fractionated synchrotron RT techniques (see [Siegbahn 2006, Nettelbeck 2009, Prezado 2011a, Martínez-Rovira 2012a], among others). The flexibility and simplicity of the simulation code, along with the accurate physical models implemented in the package, especially for low-energy radiation transport, have made PENELOPE the best candidate for the aims of this work.

The most relevant interactions in our energy range (mean energy $\sim$ 100 keV) are Compton scattering and the photoelectric effect. Compton scattering cross sections are obtained from the relativistic impulse approximation (RIA), which accounts for Doppler broadening and binding effects. Photoelectric cross sections are interpolated from tabulations in the evaluated photon data library (EPDL) from the Lawrence Livermore National Laboratory (LLNL) [Cullen 2011].

The polarisation state of photons is also considered in the scattering events [Salvat 2008]. Polarisation is described by means of the Stokes parameters (P_1, P_2, P_3) [Fano 1954], following the convention commonly used in Quantum Mechanics [Salvat 2008]. Thus, in our set-up (see figure 1.6, right), P_3 determines linear polarisation along the horizontal and vertical axis, P_2 represents circular (right and left) polarisation and P_1 corresponds to polarisation in the lines that bisect the transversal plane. Polarisation effects are especially relevant in our case as synchrotron beams are highly linearly polarised in the electron orbit plane.

As regards electron transport, the dominant energy loss mechanism in our energy range are inelastic collisions. The description of inelastic scattering of charged particles is performed on the basis of a schematic generalised oscillator strength (GOS) model with mean excitation energies taken from ICRU Report 37 [ICRU-37 1984]. Elastic collisions of electrons, which are mainly responsible for angular deflections, are simulated by using data obtained from relativistic partial-wave calculations [Salvat 2005].

PENELOPE users can adapt a steering main program in order to define the radiation

source, the simulation parameters, the quantities of interest to be scored, variance-reduction (VR) techniques to be applied and report the final results. The modular general-purpose main program for PENELOPE named PENEASY [Sempau 2011] has been employed in this thesis. It was developed at the *Institut de Tècniques Energètiques (Universitat Politècnica de Catalunya*) and it is both free and open source.

The PENEASY code permits the dose computation in voxelised geometries as well as its superposition with objects limited by quadric surfaces. Each voxel is defined by the material index and the mass density. The code accounts for the density changes between voxels by scaling the remaining distance up to the following interaction with the inverse of the density of the voxel being traversed. See the work of Sempau *et al.* [Sempau 2011] for more information on this code.

1.5.4.2 Experimental dosimetry methods in MRT

The experimental dosimetry in MRT is divided into two parts. The first is related to the absolute dosimetry in reference conditions (seamless field), while the second consists of the dose assessment in non-reference conditions (MRT). Details of both parts are presented here.

Absolute dosimetry in reference conditions (seamless field)

The absolute dosimetry in MRT was performed by following as closely as possible the recommendations compiled in the International Atomic Energy Agency (IAEA) Technical Reports Series (TRS) 398 [IAEA-TRS-398 2005]. The 'medium x-ray energies' recommendations are associated with x-ray beams with half-value layers (HVL) greater than 2 mm of aluminium. The MRT beam fits within the medium-energy x-ray range since its aluminium HVL was found to be 16 mm [Siegbahn 2007].

In this case, the dose measurement in reference conditions (seamless irradiation field, named broad beam, hereafter) is performed at 2 g/cm^2. The reference field size was chosen to be 2×2 cm^2 instead of 10×10 cm^2 since it is closer to the field sizes that are going to be used for MRT treatments.

Cylindrical ionisation chambers (IC) with a cavity volume in the range of 0.1–1.0 cm^3 are recommended for reference dosimetry in medium-energy x-ray beams. Although the most widely used IC for absolute dosimetry is the 0.6 cm^3 Farmer®, our dosemeter of choice was the Semiflex 31010 IC (active volume of 0.125 cm^3) [PTW® 2012] due to the need to perform dose measurements for very small fields (down to 1×1 cm^2). The IC was calibrated in kilovoltage x-rays. During measurement, the reference point of the chamber (on the chamber axis at the centre of the cavity volume) was placed at the reference depth

[IAEA-TRS-398 2005].

Water is the recommended medium for measurements of absorbed dose. There should be a margin of at least 5 g/cm^2 beyond all four sides of the largest field size and 10 g/cm^2 beyond the maximum depth of measurement. Additionally, the window of the phantom should be made of plastic with a thickness of 0.2–0.5 cm. Dose measurements for horizontal beams performed with the water tank MP3-P T41029 [PTW® 2012] (dimensions: 35×45×48 cm^3; PMMA entrance window of 0.5 cm) satisfied the recommended criteria defined in [IAEA-TRS-398 2005]. The water tank was filled with distilled water. The water-equivalent thickness of the window was calculated as the product of its thickness by the density of PMMA (ρ=1.19 g/cm^3).

These measurements had to be repeated for each experiment and/or refill due to small misalignments of beamline elements or beam emittance changes that could potentially lead to differences in the dose of up to 10%. Since the accurate setting of the water tank in the Biomedical Beamline experimental area is very time consuming, RW3 (Goettingen White Water) solid-water slab phantoms (30×30×12 cm^3) [PTW® 2012] were used instead in our measurements. However, this will not be the case for dose assessment before patient treatment in forthcoming MRT clinical trials. The TRS 398 states that solid-water phantoms can be used for routine measurements provided that the relationship between dosimetry readings in water and in the solid-water phantom have been previously established [IAEA-TRS-398 2005]. In our case, a 5.7 ± 0.1% higher dose deposition in water with respect to RW3 solid-water has been measured and computed by MC simulations [Prezado 2011a]. Figure 1.21 shows both experimental set-ups.

Determination of the absorbed dose to water under reference conditions is expressed as (see [IAEA-TRS-398 2005])

$$D_{\mathrm{w,Q}} = M_{\mathrm{Q}}\, N_{D,\mathrm{w},\mathrm{Q}_0}\, K_{\mathrm{Q},\mathrm{Q}_0}, \tag{1.4}$$

where $N_{D,\mathrm{w},\mathrm{Q}_0}$ is the calibration factor in terms of absorbed dose to water for the beam quality Q_0 provided by the calibration laboratory; M_{Q} is the reading of the dosemeter corrected by influence quantities such as temperature and pressure ($K_{\mathrm{TP}} = [P_0\,(273.2+T)]/[P\,(273.2+T_0)]$, with T_0=20 °C and P_0=101.3 kPa), ionic recombination (K_s=1.000), polarity effect ($K_{\mathrm{pol}} < 0.3\%$) and electrometer calibration (K_{elec}=1.000 ± 0.5%) [PTW® 2012]; $K_{\mathrm{Q},\mathrm{Q}_0}$ is a chamber-specific factor which corrects for differences between the reference beam quality Q_0 and the actual beam quality Q. The calibration laboratory provided us with $K_{\mathrm{Q},\mathrm{Q}_0}$ values, which were obtained from measurements [Ma 1991, PTW® 2012]. The $K_{\mathrm{Q},\mathrm{Q}_0}$ value is 0.953 ± 0.031 for the closest beam quality [Prezado 2011a].

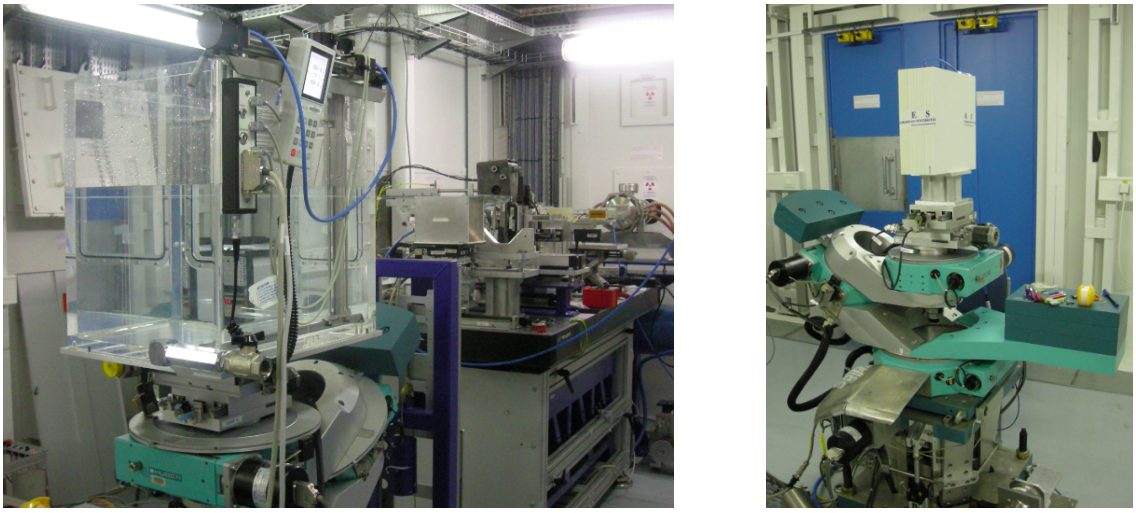

Figure 1.21: *Phantoms used in MRT experimental measurements. On the left, a monitored water tank for horizontal beams (PTW MP3-P T41029 [PTW® 2012]) full of distilled water is shown. On the right, a RW3 solid-water slab phantom [PTW® 2012] is placed on the high-precision goniometer. Inside both phantoms, the thimble Semiflex IC 31010 [PTW® 2012] is located at 2 g/cm^2.*

Standard dosimetry and reference calibration protocols assume exposure of the IC to a uniform beam. However, as has been mentioned, the vertical dimensions of the beam at the patient position are defined by the V slit size (50–800 μm). The beam is then scanned in the vertical direction at constant speed. See figure 1.22. The work of Prezado *et al.* has proved that this method is equivalent to measuring the dose deposited with uniform irradiation [Prezado 2011b].

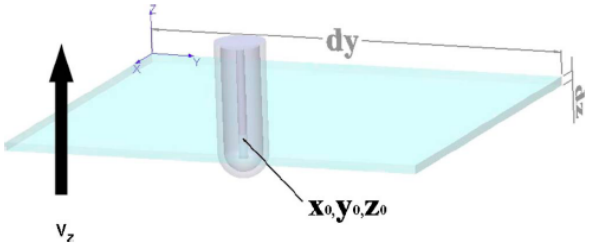

Figure 1.22: *Scheme illustrating the dosimetry configuration. Since the vertical dimensions of the beam at the patient position are very small, the IC (and the phantom) are moved at constant speed through the synchrotron beam in order to sweep the whole irradiation field size. Extracted from [Prezado 2011b].*

From these measurements, a value of dose rate $\dot{D}$ was obtained. In particular, for the maximum electron current and a V slit size of 50 μm, the dose rate was in the order of 60–70 Gy/(mA.s). The scanning goniometer velocity (v) was set considering the desired dose

(D), the value of the dose rate, the V slit size (d_{v}) and the beam current (I) as follows

$$v = \frac{\dot{D}\, I\, d_{\mathrm{v}}}{D}. \tag{1.5}$$

Dosimetry in non-reference conditions (MRT)

In order to determine the dose deposited with one microbeam (peak dose) from the absolute dose measured in the broad beam configuration, scatter factors were used [Prezado 2012a]. These factors take into account the field size dependence of dose deposition. Scatter factors have been measured experimentally by using two alternative detection systems: a large area chamber (LAC) type (Bragg Peak PTW 34070, with a diameter of 4 cm [PTW® 2012]), following the method described in the work of Sánchez-Doblado *et al.* [Sánchez-Doblado 2007], and HD-810 radiochromic films [ISP® 2012]. See section 2.6 for more information on this type of measurements.

Relative dosimetry in MRT was performed with HD-810 radiochromic films in homogeneous and heterogeneous slab-phantoms (composed of RW3 solid-water and RW3 solid-water and bone, respectively). See details of the phantoms and the obtained results in section 2.5. As has been mentioned, Gafchromic® HD-810 films [ISP® 2012] provide the high spatial resolution required to measure lateral dose profiles in MRT. Furthermore, the broad dose range (from 10 to 400 Gy) also enables PVDR values to be assessed. Additionally, the manufacturers of the HD-810 radiochromic films state that films are energy independent for photons with energies above 200 keV [ISP® 2012]; the energy dependence in the low energy range of our spectrum has been considered sufficiently small to be ignored [Muench 1991, Crosbie 2008].

For the handling and calibration of the films, the recommendations provided by Task Group 55 of the American Association of Physics in Medicine (AAPM) [Niroomand-Rad 1998] were taken into account. In particular, films were cut in pieces and the position of each film on each sheet was carefully numbered. For each dataset measurement, a group of films was then selected from the same region on the same sheet. In this way, the uncertainties arising from sheet-to-sheet uniformity (5%) were avoided and those coming from single-sheet uniformities (3.2%) were minimised.

The spatial resolution of the typical flat bed scanner used in RT is not adapted to perform dosimetry at the micron scale required in MRT. Instead, a microdensitometer (3CS Microdensitometer, J. L. Automation) was employed to read the films. See figure 1.23. This system has a wide dynamic range (it is sensitive to optical densities (OD) from 0.2 to 6) and a very high spatial resolution (around 5 μm).

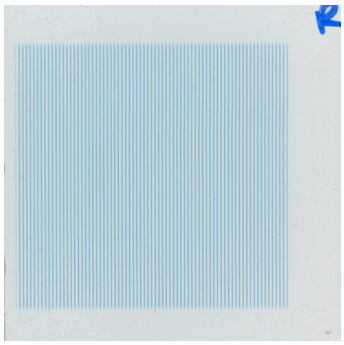

Figure 1.23: *On the left, the microdensitometer (3CS Microdensitometer, J. L. Automation) used to read the radiochromic films exposed to MRT irradiations. On the right, a piece of Gafchromic® HD-810 film after an MRT irradiation (3×3 cm² field size).*

The output of the microdensitometer is a magnitude named the pen deflection (PD), which is related somehow to the OD; this magnitude varies at any adjustment of the microdensitometer. The dose assessment at one particular point is performed by comparing the PD value of films irradiated in the broad beam configuration with a well-known dose (D_{ref}) with the PD value of the film under evaluation. An example of PD profile obtained with the microdensitometer is shown in figure 1.24. A large representative set of films irradiated with D_{ref} moving from 0 Gy to 400 Gy (at intervals of 1–2 Gy for low doses, 5 Gy for intermediate doses and 10–25 Gy for very high doses) was acquired at each experiment. Absolute peak and valley doses were adjusted to the dynamic range of the HD-810 films and they were selected to be as near as possible to the expected clinical doses.

The use of these types of systems is extremely time-consuming as the reading speed is very low (a 1 mm ×1 mm scan at 5 μm step resolution takes more than 1 hour) and the delicate optical and mechanical parts composing the microdensitometer forced us to frequently adjust it to avoid any drift in the system [Zimmer 1978, Aydarous 2001]. This meant that we had to perform short measurements of one profile (for instance 1–2 mm of the whole beam in the region of interest). For each evaluated point, the measurement was repeated at least twice on different days/run. In addition, each film was read a minimum of three times to ensure reproducibility of data.

Further information on the working principle of the microdensitometer can be found elsewhere [Swing 1998].

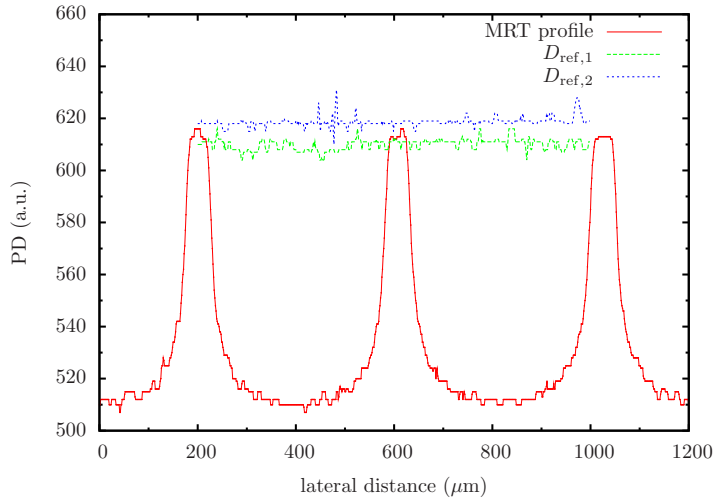

Figure 1.24: *Example of pen deflection (*PD*) profile obtained with the microdensitometer. The dose assessment is performed by comparing the* PD *value of the film under study with the* PD *value of films irradiated in the broad beam configuration with a well-known dose (D_{ref}).*

1.6 Minibeam Radiation Therapy (MBRT)

1.6.1 Introduction

The main drawback of MRT is that its widespread clinical implementation is limited nowadays due to the requirement of high dose rates. Only the high photon fluxes present in synchrotrons enable a fast irradiation process (in a fraction of a second) that prevents artifacts caused by cardiosynchronous pulsations [Poncelet 1992]. Thicker beams used in MBRT overcome these difficulties. Since the MBRT dose profiles are not as vulnerable as those of MRT to beam smearing from cardiac pulsations, high dose rates are not needed. Hence, it is conceptually possible to extend this technique by using modified x-ray equipment, creating an opportunity for its implementation at hospitals [Dilmanian 2006, Babcock 2011].

In addition, the use of higher beam energies is feasible in MBRT ($\geq$200 keV); this results in lower entrance doses to deposit the same integral dose in the tumour, despite the larger penumbral doses (penumbras are about 40 μm for a mean energy of 100 keV at 2 cm-depth in a water phantom) [Prezado 2009c]. Furthermore, the clinical implementation of the interlaced method producing an homogeneous dose in the tumour is not possible in MRT due to the higher technical precision required. These advantages triggered the exploration of MBRT as a new radiotherapeutic approach.

Since the thicker beams and spacings employed in MBRT in comparison with thin microbeams may lead to different biological effects than those observed in MRT [Uyama 2011],

experimental studies are warranted to evaluate the possible different tumour and normal tissue response between MRT and MBRT.

1.6.2 Previous clinical trials in MBRT

The first hint about the preservation of healthy tissues (rat brain and spinal cord) with thicker beams (270 μm; entrance dose of 750 Gy) was provided by Dilmanian *et al.* in 2005 [Dilmanian 2005]. However, the first experiments in MBRT were performed a few years later by the same group in unidirectional and interlaced geometries [Dilmanian 2006]. Rat spinal cords were irradiated with four 680-μm-wide minibeams with a spacing of 4 mm. Despite the fact that some healthy tissue damage was observed, an entrance dose of 400 Gy was tolerated in three out of four rats, as opposed to what happened in seamless beam irradiations. In addition, MBRT irradiations (680-μm-wide minibeams spaced by 1360 μm) of rat brains showed a 4-fold higher tolerance with respect to broad beams [Dilmanian 2006]. This tolerance is equivalent to that previously found in MRT [Dilmanian 2002]. In interlaced geometries, no significant damage was observed outside the target area at any time for entrance doses up to 120 Gy [Dilmanian 2006].

This outcome motivated the implementation of this novel technique at the ESRF ID17 Biomedical Beamline [Prezado 2009b]. Some *in vitro* [Gil 2011] and *in vivo* [Prezado 2012b] studies in white-beam MBRT have already been performed. They have showed a gain factor of three in the mean survival time of 9L gliosarcoma bearing-rats with respect to controls [Prezado 2012b]. However, additional preclinical studies need to be developed in order to completely assess the TCP and NTCP curves for this new radiotherapeutic modality. The use of MBRT with monochromatic x-rays is also being explored at the ESRF [Deman 2011, Deman 2012].

1.6.3 Previous MC and experimental dosimetric studies in MBRT

The first MC dosimetric study in white-beam MBRT was performed by Dilmanian *et al.* [Dilmanian 2006]. In this work, a series of MC simulations (EGS4 code) in a water phantom for irradiation of an array of 680-μm-wide planar minibeams spaced by 1360 μm (field sizes of 1.5$\times$1.5 and 3$\times$3 cm^2) was assessed for unidirectional and interlaced irradiation geometries. Posterior works performed calculations in a realistic voxelised human phantom (MCNPX code); in particular, dose enhancement due to the presence of contrast agents together with MBRT (680-μm-wide planar minibeams spaced by 1360 μm; field size of 2$\times$2 cm^2) was evaluated by Gokeri *et al.* [Gokeri 2010]. Additional MC calculations (PENELOPE code) in 80 keV

monochromatic MBRT were also performed [Deman 2011]. These MC studies used a simplified non-divergent irradiation source geometry.

The experimental dose assessment in white-beam [Dilmanian 2008] and monochromatic [Deman 2011] MBRT was achieved by means of polymer gel dosimetry. MC calculations showed good correlation with experimental dosimetry despite the large uncertainties (more than 15%) arising from the gel reading method. Gel dosimetry can be used to check irradiation geometries and obtain an estimation of the dose distribution. For instance, these methods were useful to prove that minibeam interlacing in the brain was possible even in anthropomorphic head phantoms, since the three-dimensional pattern of the microplanar arrays was shown not to be distorted by bone [Dilmanian 2008]. However, this method is not accurate enough for a precise dose assessment, although recently developed PRESAGE® polymers read by an optical CT scan seem to achieve a higher spatial resolution [Doran 2010, Abdul Rahman 2011].

1.6.4 Dosimetry for future preclinical trials in MBRT

In this work, MC calculations in MBRT were also performed with the PENELOPE/PENEASY code (see section 1.5.4.1).

The experimental dosimetry in reference conditions was performed as has been explained in section 1.5.4.2. The dose in non-reference conditions (MBRT) was also evaluated by means of scatter factors. They were assessed by MC simulations and measurements by using Gafchromic® HD-810 films [ISP® 2012]. See section 2.7.

The thicker beams used in MBRT allow radiochromic films to be read with a flat bed scanner (Epson Perfection V750-M Pro Scanner [EPSON® 2012]), at 1200 dpi resolution, instead of the microdensitometer. See figure 1.25. For the reading and analysis of the films, the methodology described in the work of Devic *et al.* [Devic 2005] was followed. The transmission scanner readings of the films (I) were obtained by extracting the red channel from the red-green-blue (RGB) image [Stevens 1996]. The optical density (OD) at each pixel was then calculated by

$$\mathrm{OD} = -\log_{10}\left(\frac{I - I_{\mathrm{back}}}{I_0 - I_{\mathrm{back}}}\right), \tag{1.6}$$

where I and I_0 are the readings for exposed and unexposed film pieces, respectively; and I_{back} is the zero-light transmitted intensity value.

The absorbed dose (D) at any point in the film is computed by using the calibration curve (D versus OD). In order to obtain this curve, films were irradiated in broad beam with well-

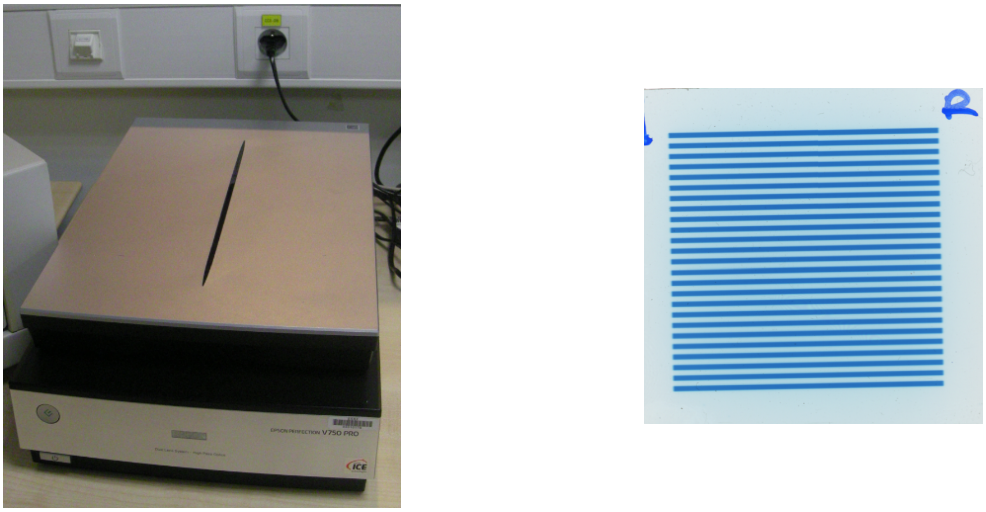

Figure 1.25: *On the left, the flat bed scanner (Epson Perfection V750-M Pro Scanner [EPSON® 2012]) used to read the radiochromic films exposed to MBRT irradiations. On the right, a piece of Gafchromic® HD-810 film for an MBRT irradiation (3×3 cm² field size).*

known doses. The dose calibration range went from 10 to 400 Gy (which is the recommended range of use for HD-810 films [ISP® 2012]). The central average OD of these films was evaluated for each dose (equation (1.6)). Figure 1.26 shows an example of calibration curve, which follows a quadratic polynomial regression, $D = c_1\,\mathrm{OD} + c_2\,\mathrm{OD}^2$, where c_i (i=1,2) are the unknown fit parameters. Each film box was calibrated separately.

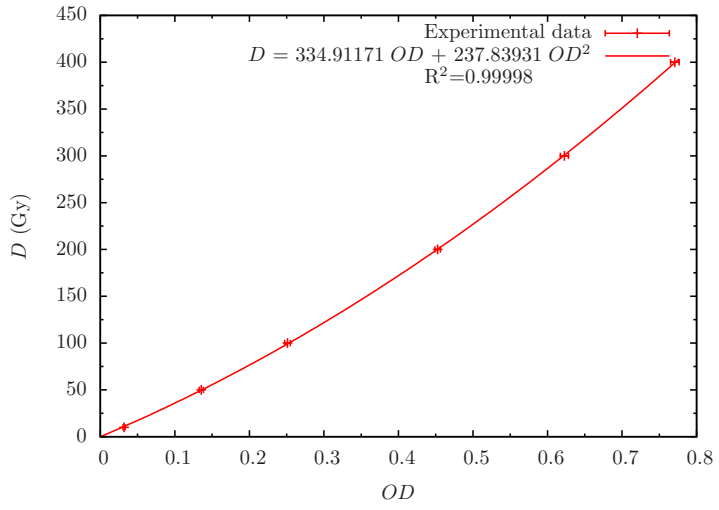

Figure 1.26: *Example of calibration curve of the Gafchromic® HD-810 films [ISP® 2012], which follows a quadratic polynomial regression $D = c_1\,\mathrm{OD} + c_2\,\mathrm{OD}^2$, with c_1=334.91171 and c_2=237.83931, and a correlation coefficient of R^2=0.99998.*

CHAPTER 2

Results

Contents

2.1 Global summary

This PhD work deals with different features related to small (micrometre-sized) field dosimetry involved in spatially fractionated synchrotron radiotherapy techniques: MRT and MBRT. MC simulations and experimental methods were used with this aim in mind.

The core of this work consisted of the development and benchmarking of a MC-based computation engine for a treatment planning system (TPS) devoted to MRT within the framework of the preparation of forthcoming MRT clinical trials. Additional achievements were the definition of safe MRT irradiation protocols, the assessment of scatter factors in MRT and the further improvement of the MRT therapeutic index by injecting a contrast agent into the tumour. Finally, a dosimetry protocol for future preclinical studies in MBRT was established.

The work performed in this thesis, which is presented in several papers published in (or submitted to) peer-reviewed journals, have provided the dosimetric tools for forthcoming MRT clinical trials in pets and the MBRT preclinical trials in small animals.

2.2 List of contributions

The results of this work are reported in the following six papers:

I.- **I. Martínez-Rovira**, J. Sempau, J. M. Fernández-Varea, A. Bravin and Y. Prezado, "Monte Carlo dosimetry for forthcoming clinical trials in x-ray microbeam radiation therapy", *Phys. Med. Biol.* **55**, 4375–4388 (2010). ***Featured article (high-interest article across IOP)***. doi:10.1088/0031-9155/55/15/012.

II.- **I. Martínez-Rovira** and Y. Prezado, "Monte Carlo dose enhancement studies in microbeam radiation therapy", *Med. Phys.* **38**, 4430–4439 (2011). doi:10.1118/1.3603189.

III.- **I. Martínez-Rovira**, J. Sempau and Y. Prezado, "Development and commissioning of a Monte Carlo photon beam model for the forthcoming clinical trials in microbeam radiation therapy", *Med. Phys.* **39**, 119–131 (2012). doi:10.1118/1.3665768.

IV.- **I. Martínez-Rovira**, J. Sempau and Y. Prezado, "Monte Carlo-based treatment planning system calculation engine for microbeam radiation therapy" (*manuscript/submitted to Med. Phys.*)

V.- Y. Prezado, **I. Martínez-Rovira** and M. Sánchez, "Scatter factors assessment in microbeam radiation therapy", *Med. Phys.* **39**, *in press* (2012).

VI.- Y. Prezado, **I. Martínez-Rovira**, S. Thengumpallil and P. Deman, "Dosimetry protocol for the preclinical trials in white-beam minibeam radiation therapy", *Med. Phys.* **38**, 5012–5020 (2011). doi:10.1118/1.3608908.

For clarity, each paper will be preceded by a brief introduction.

2.3 Paper I: Monte Carlo dosimetry protocol for forthcoming clinical trials in x-ray MRT

Introduction

When moving from MRT investigations in rodents to clinical application in humans, it is necessary to first perform a risk analysis. In particular, the definition of safe irradiation protocols is required. The identification of safe dose limits was carried out by evaluating the maximum peak and valley doses achievable in the tumour to keep the valley dose in the healthy tissue under well-known tolerances in conventional RT [Dilmanian 2002, Bentzen 2010].

As has been explained in section 1.1.2, the most common RT practice in the last 100 years is the fractionation of the dose in small doses of radiation (typically in 2 Gy per fraction) for many days. Since in MRT high doses of radiation are delivered to the tumour in one fraction, the expected biological effects and tissue tolerances will depart from values in conventional RT. In order to establish the dose equivalence between the different fractionation schemes, the concept of normalised total dose (NTD) has been used [Flickinger 1990, Joiner 2009]. The applicability of this radiobiological model in MRT will be discussed and justified in the paper [Brenner 2008, Kirkpatrick 2009].

Dose distributions in a realistic head phantom were assessed by MC simulations in several irradiation and phantom configurations, *i.e.*, for various tumour positions, skull thicknesses and c-t-c distances (PENELOPE/penEasy code, see section 1.5.4.1). The resulting physical dose was then translated to biological equivalent dose by using the aforementioned radiobiological models.

IOP PUBLISHING PHYSICS IN MEDICINE AND BIOLOGY

Phys. Med. Biol. **55** (2010) 4375–4388 doi:10.1088/0031-9155/55/15/012

Monte Carlo dosimetry for forthcoming clinical trials in x-ray microbeam radiation therapy

I Martínez-Rovira[1,2], J Sempau[2], J M Fernández-Varea[3], A Bravin[1] and Y Prezado[1]

[1] ID17 Biomedical Beamline, European Synchrotron Radiation Facility (ESRF), B.P. 220, 6 Jules Horowitz, F-38043 Grenoble Cedex, France
[2] Institut de Tècniques Energètiques, Universitat Politècnica de Catalunya, Diagonal 647, E-08028 Barcelona, Spain
[3] Facultat de Física (ECM and ICC), Universitat de Barcelona, Diagonal 647, E-08028 Barcelona, Spain

E-mail: yolanda.prezado@esrf.fr

Received 6 November 2009, in final form 4 June 2010
Published 20 July 2010
Online at stacks.iop.org/PMB/55/4375

Abstract

The purpose of this work is to define safe irradiation protocols in microbeam radiation therapy. The intense synchrotron-generated x-ray beam used for the treatment is collimated and delivered in an array of 50 μm-sized rectangular fields with a centre-to-centre distance between microplanes of 400 μm. The absorbed doses received by the tumour and the healthy tissues in a human head phantom have been assessed by means of Monte Carlo simulations. The identification of safe dose limits is carried out by evaluating the maximum peak and valley doses achievable in the tumour while keeping the valley doses in the healthy tissues under tolerances. As the skull receives a significant fraction of the dose, the dose limits are referred to this tissue. Dose distributions with high spatial resolution are presented for various tumour positions, skull thicknesses and interbeam separations. Considering a unidirectional irradiation (field size of 2×2 cm^2) and a centrally located tumour, the largest peak and valley doses achievable in the tumour are 55 Gy and 2.6 Gy, respectively. The corresponding maximum valley doses received by the skin, bone and healthy brain are 4 Gy, 14 Gy and 7 Gy (doses in one fraction), respectively, i.e. within tolerances (5% probability of complication within 5 years).

(Some figures in this article are in colour only in the electronic version)

1. Introduction

Gliomas are extremely radioresistant tumours. The high absorbed doses needed to ablate gliomas are limited by the high morbidity of the surrounding healthy tissue, especially

0031-9155/10/154375+14$30.00

in children (Kagan *et al* 1976). The average lifespan for these patients is less than 1 year, and generally no patient survives 5 years after treatment (Behin *et al* 2003). High-grade gliomas are still of poor prognostic value despite the development of many innovative therapies. Stereotactic radiosurgery (Phillips *et al* 1994), intensity-modulated radiation therapy (Cardinale *et al* 1998) and boron neutron capture therapy (Barth *et al* 2005) are some examples. The use of radiotherapy plus concomitant and adjuvant temozolomide has allowed a significant prolongation of survival (Stupp *et al* 2002, 2005, 2009). However, the outcome still remains unsatisfactory and the management of glioblastomas is mainly palliative.

One possible way to improve the therapeutic index in radiotherapy is to employ new techniques based on what is known as the dose–volume effect: the smaller the field size, the higher the tolerance of the healthy tissue (Curtis 1967). Microbeam radiation therapy (MRT) is a synchrotron radiotherapy technique that relies on this fact. Such an irradiation can be palliative or curative while causing minimal damage to the contiguous healthy tissue.

In MRT, the irradiation is carried out by means of an array of parallel x-ray microbeams (from 25 to 50 μm thick), with a centre-to-centre (c-t-c) distance between microbeams of 200 or 400 μm. The x-ray energy spectrum ranges from about 50 to 500 keV, with a mean energy around 100 keV (Siegbahn *et al* 2006). The microbeams are produced by a multi-slit collimator that spatially fractionates in the horizontal direction the beam coming from the synchrotron source (Bräuer-Krisch *et al* 2009). Targets are then vertically scanned through the microfractionated beam to deliver microplanes of x-rays. The synchrotron origin of the microbeams confers them two crucial features: negligible divergence (allowing the production of sharply defined beam edges in tissue) and high flux (enabling a fast irradiation process that prevents motion artifacts of the subject caused by cardiosynchronous pulsation).

The MRT irradiation scheme results in dose profiles consisting of a pattern of peaks and valleys, i.e. with high doses in the microbeam paths and low doses in the spaces between them (Siegbahn *et al* 2006). The minimum dose in the central region between two microbeams is named valley dose and the dose in the centre of the microbeam is the peak dose.

The ratio between the peak dose and the valley dose (peak-to-valley dose ratio, PVDR) depends on the incident x-ray beam energy, the tissue composition, the beam thickness, the c-t-c distance and the irradiation field size but it does not depend on the peak dose prescription in the tumour. Despite being an important dosimetric parameter in this type of spatially fractionated techniques, PVDR is a relative quantity and it is also necessary to have the information on both peak and valley doses.

During the last two decades, several preclinical studies have shown the sparing effect of the healthy tissue using MRT on the brain of adult rats (Slatkin *et al* 1995, Regnard *et al* 2008), suckling rats (Laissue *et al* 1999), duck embryos (Dilmanian *et al* 2001), piglets (Laissue *et al* 2001), chick-embryo chorio-amniotic membranes (Blattmann *et al* 2005) and nude mice (Serduc *et al* 2008). In parallel, it has been proven that MRT can ablate highly aggressive animal tumour models such as 9L brain gliomas (Laissue *et al* 1998, Dilmanian *et al* 2002, Smilowitz *et al* 2006), EMT-6 carcinoma (Dilmanian *et al* 2003) and SCCVII carcinoma (Miura *et al* 2006).

Dilmanian *et al* (2002) stressed the fact that MRT could cure 9L-bearing animals without killing all tumoral cells. They suggested that MRT effects might involve mechanisms other than a direct ionizing radiation effect on tumoral cells, like poor regenerative capacity of tumoral vessels after radiation exposure. Additional mechanisms such as abscopal effects may also play a role. The analysis of the results for different beam spacings from Dilmanian *et al* (2002) and Regnard *et al* (2008) suggests that a high lesion density induced by the

microbeams on tumour vasculature could be sufficient to treat brain tumours. Indeed, a decrease in microbeam spacing may increase the number of vascular lesions per unit volume.

Nevertheless, the biological mechanisms following an MRT irradiation are not yet fully understood. It has been hypothesized that the sparing effect in the healthy tissue along the beam paths is due to a rapid biological repair of the microscopic lesions by the minimally irradiated cells contiguous to the irradiated tissue slices (Slatkin *et al* 1995, Laissue *et al* 1998, Dilmanian *et al* 2001). Dilmanian *et al* (2002) have shown that the sparing effect of MRT seems to depend mostly on the valley dose. The brain-sparing effect (measured by the onset of the appearance of white matter necrosis) vanishes only when the valley dose approaches the tissue tolerance to broad beams. As for the PVDRs, the valley doses depend on the x-ray beam energy spectrum, on the spacing between microbeams, on the irradiation field size but also on the peak doses. A smaller c-t-c distance results in higher valley doses and in lower tolerances (Dilmanian *et al* 2002, Regnard *et al* 2008).

Following the success of preclinical studies, the Biomedical Beamline ID17 of the European Synchrotron Radiation Facility (ESRF) is planning to proceed towards clinical trials (Laissue *et al* 2007, Renier *et al* 2008). In this context, Monte Carlo (MC) absorbed dose calculations in realistic phantoms are needed to define irradiation protocols in MRT.

The first MC dosimetry studies in MRT were done by Slatkin *et al* (1992). The simulations were performed for 25 μm thick microbeams spaced 50, 100 or 200 μm, impinging on a 16 cm long cylindrical water phantom with a diameter of 16 cm. Subsequent works considered similar water phantoms (Stepanek *et al* 2000, De Felici *et al* 2005, Siegbahn *et al* 2006, Spiga *et al* 2007). Company and Allen (1998) calculated also the dose distribution in a tissue/lung/tissue phantom and Orion *et al* (2000) in a spherical human head phantom with a diameter equal to 17.2 cm (0.6 cm of skull and 16 cm of brain). Prezado *et al* (2009b), who investigated the dose enhancement in MRT by loading the tumour with gadolinium, have also performed the simulations in a human head phantom inspired by the one described in the work of Harling *et al* (1995).

It is important to point out that the use of realistic geometries is essential for a correct dose assessment. For example, the valley dose in a centrally located tumour in a water phantom is around 2.8 times higher than that of the head phantom considered in the present study. The difference has to be mainly ascribed to the presence of the bone.

To the best of our knowledge, the only dosimetric studies carried out in MRT using a head phantom are those of Orion *et al* (2000) and Prezado *et al* (2009b). Orion *et al* (2000) used 30 μm thick microbeams, a c-t-c distance between microplanes of 100 and 200 μm and field sizes of 3×3 and 6×6 cm^2. In Prezado *et al* (2009b), the microbeam width, the c-t-c distance and the irradiation field size were 50 μm, 200 μm and 2×2 cm^2, respectively. The PVDR value for a lateral irradiation of a centrally located tumour in Prezado *et al* (2009b) is in agreement with our results in section 3.4 and in figure 6.

None of the parameters used in previous papers are going to be employed in the forthcoming clinical trials at the ESRF. The chosen irradiation parameters have been fixed to a microbeam width of 50 μm and a c-t-c distance of 400 μm in order to reach a compromise between healthy tissue sparing and tumour eradication.

For the first time, this work presents a systematic study of the dose distribution and the corresponding conversion of absorbed dose to normalized total dose considering biological effects in a realistic head phantom with a high spatial resolution. The maximum dose prescription achievable in the tumour is evaluated in different cases by adopting the criterion of keeping the valley dose in the healthy tissue as low as possible and below tissue tolerances for a broad beam (Dilmanian *et al* 2002). In this way, safe and conservative irradiation protocols in MRT can be defined.

2. Materials and methods

2.1. Monte Carlo simulation code: PENELOPE/penEasy

The MC code PENELOPE (Salvat *et al* 2006, Sempau *et al* 1997) has been employed. PENELOPE simulates the coupled transport of photons, electrons and positrons in the energy interval from 50 eV to 1 GeV, and in arbitrary material systems. PENELOPE has been widely used in the medical physics field, see for example Sempau *et al* (2001), Torres *et al* (2004), Sempau and Andreo (2006), Fernández-Varea *et al* (2007) and Sterpin *et al* (2008) to name a few. In this work, penEasy (Sempau and Badal 2008), a structured general-purpose main program for PENELOPE, has been adopted to do the calculations.

The most relevant photon interaction mechanisms in the energy range of concern in MRT (mean energy ∼100 keV) are Compton scattering and photoelectric effect. These interactions are simulated one by one until the photon reaches an energy lower than a user-defined threshold (the absorption energy). Compton scattering is modelled by means of the relativistic impulse approximation. This formalism takes into account both Doppler broadening and binding effects of the atomic electrons. Photoelectric cross sections are interpolated from the tabulations of the Evaluated Photon Data Library (Cullen *et al* 1997). Many-body and aggregation effects are ignored and atoms are considered as independent.

Regarding electron transport, PENELOPE implements a mixed simulation algorithm in which interactions are classified into hard and soft. They are regarded as hard when the energy loss or the angular deflection of the transported particle is above certain user-defined cutoffs. Hard interactions are simulated individually. Soft interactions are simulated by resorting to multiple-scattering theories. Angular deflections are mainly caused by elastic scattering, while inelastic collisions are the dominant energy loss mechanism. Elastic scattering cross sections are calculated from relativistic partial-wave analysis (Salvat *et al* 2005). Inelastic scattering is described by means of a schematic generalized oscillator strength model with mean excitation energy values taken from the *ICRU Report 37* (ICRU 1984).

2.2. Simulation geometry and configuration

The considered head phantom is composed of slabs of skin, bone and brain, with thicknesses equal to 2 mm, 1 cm and 16 cm, respectively. The dimensions of the human brain are taken from Harling *et al* (1995).

To obtain the dose distribution for the whole field, we have adopted the following approach. First, we compute the dose distribution for a single microbeam in the head phantom. Next, for each spatial location, the dose is evaluated as the sum of the contributions of each individual microbeam to cover the desired irradiation field. In agreement with previous dosimetry works (Boudou *et al* 2005, Prezado *et al* 2009a, Prezado *et al* 2009b), a field size of 2×2 cm^2 is assumed in the simulations, which corresponds to the tumour size. In the calculations, the dose prescription is referred to as the centre of a 'virtual' tumour located at a certain depth.

Absorbed doses are tallied in voxels of 2 μm in the lateral direction of the microbeam, 1 mm in the vertical direction of the microbeam and 2 mm in depth. Doses were scored up to 2 cm away from the centre of the microbeam in the lateral direction (see figure 1).

There are different simulation parameters to be considered in PENELOPE. Users are required to define an absorption energy (`EABS`) for each particle type (γ, e$^{\pm}$) at which histories are terminated and their remaining energy is locally absorbed. Charged-particle transport also requires the setting of the following parameters: `C1`, which determines the average angular deflection between two consecutive hard elastic events; `C2`, which defines the maximum average fractional energy loss in a single multiple-scattering step; `WCC`, the cutoff energy for

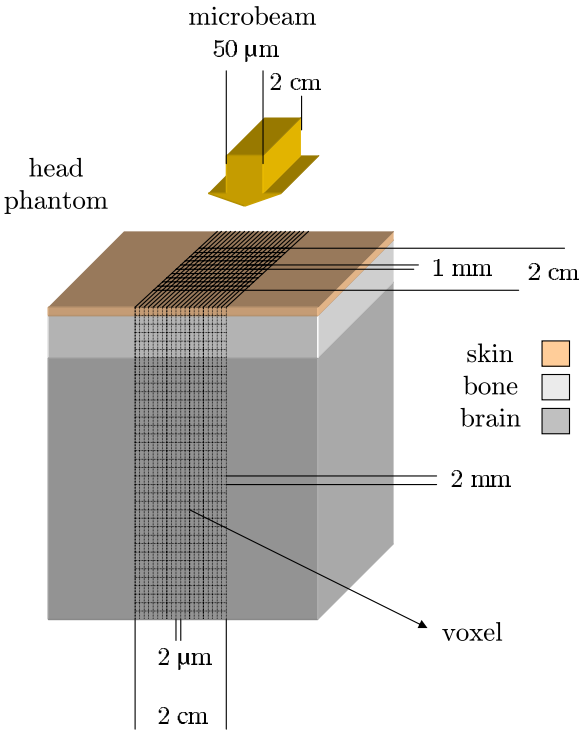

Figure 1. Scheme of the dimensions and orientation of the head phantom, as well as the voxels used to tally the dose distribution in the simulations (not to scale).

the production of hard inelastic events; `WCR`, the cutoff energy for the production of hard bremsstrahlung; and `DSMAX`, the maximum allowed step length.

In our simulations, `EABS` is set to 300 eV for all particles, to ensure that the photon mean free path and the secondary-electron range are smaller than the minimum bin width used to tally the dose distributions. `C1` and `C2` are set to 0.01, which is a very conservative value. `WCC` and `WCR` are set equal to `EABS`. Finally, the value of `DSMAX` is chosen to be one tenth of the different slab thicknesses.

Simulations are discontinued when the average statistical uncertainty is less than 0.5% (2 standard deviations). This uncertainty is calculated as an average of the uncertainties of the bins with doses above half of the maximum score.

2.3. Dose equivalence with standard fractionation schemes

Since in MRT the doses are delivered in one fraction, the expected biological effects and tissue tolerances will depart from the values in conventional radiotherapy, where the doses are typically delivered in 2 Gy/session (Emami *et al* 1991, QUANTEC 2010). To establish the equivalence of the valley dose with the standard fractionation scheme, the normalized total dose (NTD) has been evaluated from

$$\mathrm{NTD}_{2.0} = nd\left(1+\frac{d}{\alpha/\beta}\right)\left(1+\frac{2\,\mathrm{Gy}}{\alpha/\beta}\right)^{-1}, \tag{1}$$

where $\mathrm{NTD}_{2.0}$ is the NTD corresponding to the standard fractionation scheme of 2 Gy/fraction, d is the absorbed dose per fraction and n is the number of sessions. In our case, $n = 1$ and the

total dose given in one MRT fraction is $D = nd = d$. The α/β ratio is a parameter related to the biological response of the tissue under consideration and depends on its renewal capability.

Equation (1) is derived from the linear-quadratic (LQ) model (Flickinger and Kalend 1990) for the biological response to ionizing radiation, often employed to compare different fractionation schemes in conventional radiotherapy because it fits the experimental cell survival curves quite well in most cases. It is widely used to quantify the effects of radiotherapy at low and medium doses, but it might overestimate the magnitude of cell killing for doses greater than 10 Gy (Brenner 2008). Several attempts have been made to extend the LQ model to higher doses per fraction, all of them leading to the inclusion of at least one additional parameter in the formalism (Lind *et al* 2003, Guerrero and Li 2004). Unfortunately, the applicability is limited because most clinical datasets are insufficient to estimate all the parameters (Joiner and van der Kogel 2009).

There are ongoing discussions in the scientific community on the applicability of the LQ model at high doses per fraction due to the lack of clinical data (Kirkpatrick *et al* 2009). *In vivo* studies have suggested that the predictions of the LQ model are still acceptable for the design of clinical trials based on doses per fraction up to 18 Gy (Brenner 2008). *In vitro* investigations have shown that the cell survival followed the standard LQ model up to 15 Gy (Garcia *et al* 2006). Theoretical works indicate that the LQ model remains valid up to 17 Gy (Sachs *et al* 1997). As the valley dose in the present work ranges from 1 to 14 Gy in one fraction, equation (1) can be used with reasonable confidence.

The values of α/β range from 8 to 15 Gy (Steel 2002) for tumours and early responding tissues. The skin is a rapidly renewable tissue for which $\alpha/\beta = 8.8$ Gy (Turesson and Thames 1989). For late responding tissues such as the brain and the bone, the values of α/β are smaller: 2 Gy (Steel *et al* 2002) and 1.8 Gy (Overgaard 1988), respectively. In the latter cases, the dose fractionation effect and the repair mechanisms between consecutive fractions are more important than in early responding tissues, where the total absorbed dose plays a more significant role.

The valley dose is converted into $\mathrm{NTD}_{2.0}$ to assess if it is under the tolerance level for the well-established conventional radiotherapy limits, following the results by Dilmanian *et al* (2002). According to the latest published compilations of values on human patients, the tolerance doses (with a 5% probability of complication within 5 years from treatment, irradiation of one-third of the whole organ volume) are 70 Gy for the skin and 50–60 Gy for the bone (Emami *et al* 1991). In the case of the brain, a 5% risk of symptomatic radiation necrosis with the standard fractionation scheme is predicted to occur at 72 Gy (Lawrence *et al* 2010). For single fractionation radiosurgery, a clear correlation has been demonstrated between the target size and the risk of adverse events. For targets smaller than 20 mm in diameter, the maximum brain tolerance dose is higher than 24 Gy (Shaw *et al* 2000).

Emami *et al* (1991) also present the tolerance doses for 50% probability of necrosis within 5 years: >70 Gy for the skin and 65–75 Gy for the brain and the bone. The peak dose relative to this latter case has been studied as well.

3. Results and discussion

Dose distributions for various positions of a tumour, skull thicknesses and interbeam separations have been computed. The influence of these variables on the dose distributions will be presented separately. Dose is reported as absorbed dose to medium.

The valley dose presented in the figures that follow is obtained in the centre of the field since this is the location of the largest valley dose. A conservative criterion is to consider that the absorbed dose in this valley must be lower than the tolerances in conventional radiotherapy.

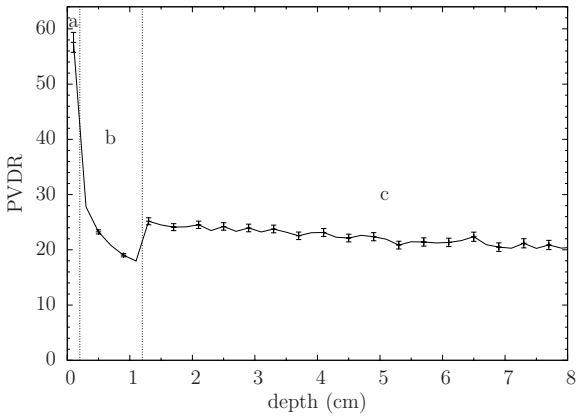

Figure 2. PVDR as a function of depth in the head phantom considering a unidirectional irradiation with 50 μm thick microbeams and a c-t-c distance of 400 μm. The three labelled areas correspond to skin (a), skull (b) and brain (c). Statistical uncertainty bars are at two standard deviations.

For this, we relied on the $NTD_{2.0}$ to establish the equivalence between the valley dose (given in one fraction) with the standard fractionation scheme of 2 Gy/fraction.

3.1. Dose distributions for a centrally located tumour

The most conservative tumour location to evaluate the absorbed dose in the healthy tissue is the centre of the brain. Using a single port irradiation, the optimum ballistics will be given by a lateral irradiation (ear-to-ear axis). With this configuration, in which the tumour centre is at a depth of 7.2 cm with respect to the skin entrance (Harling *et al* 1995), the quantity of healthy irradiated tissue is minimized.

Figure 2 shows the ratio between the peak dose and the valley dose, i.e. the PVDR, as a function of depth. The PVDR takes values around 58 in the first 2 mm (skin), but it falls off rapidly in the bone, reaching a value of 18 in the interface with the brain. This drastic reduction in bone with respect to skin is due to the increase of the fluence of photons that are Compton scattered into the valley region. These photons have a larger probability per unit mass of undergoing a photoelectric absorption in bone since its average atomic number is higher. This results in a higher local dose deposition. In the brain, the PVDR remains almost constant (PVDR $\simeq$ 25).

Figures 3 and 4 display the valley dose distribution, the peak dose distribution and the $NTD_{2.0}$ for different dose prescriptions in the centre of the tumour ranging from 40 to 65 Gy in one fraction. The maximum valley doses are 2–5 Gy in the skin, 9–17 Gy in the bone and 4–8 Gy in the brain. The maximum values of $NTD_{2.0}$ are 2–6 Gy in the skin, 30–80 Gy in the bone and 6–18 Gy in the brain. Owing to the high effective atomic number of the bone, the skull receives a substantial dose and it will be the limiting organ to establish the maximum peak dose in the tumour.

The tolerance for the bone lies between 50 and 65 Gy for a 5 % probability of complications within 5 years (Emami *et al* 1991). Therefore, from figure 4, the maximum tumour peak dose prescription achievable is 55 Gy and the corresponding valley dose in the tumour is 2.6 Gy (see figure 3 left). Considering this and the information displayed in figure 3, the maximum peak and valley doses for all the tissues can be established. The maximum skin entrance dose is 200 Gy and the maximum peak doses in the skull and the brain are 315 and 150 Gy. The corresponding valley doses in the skin, skull and brain are 4, 14 and 7 Gy, respectively. In

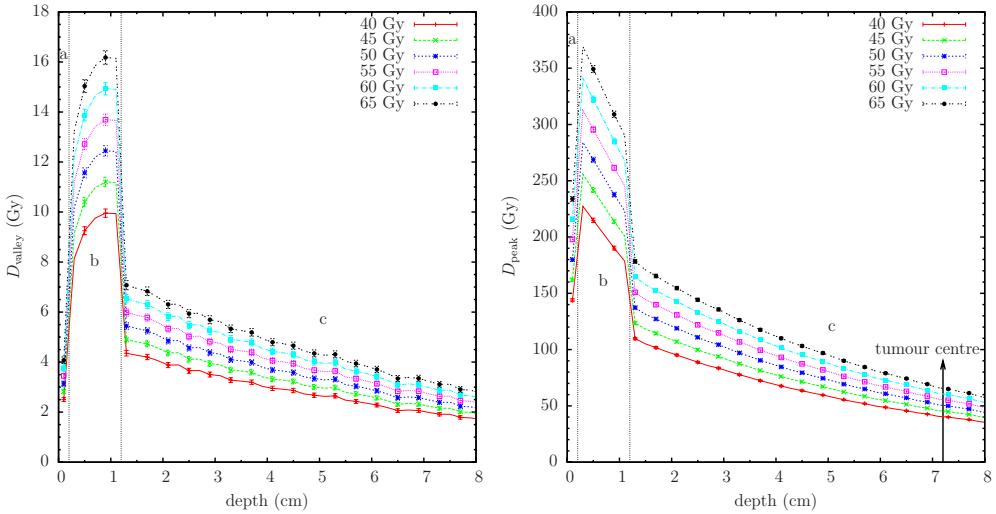

Figure 3. Valley dose (left) and peak dose (right) distributions for skin (a), skull (b) and brain (c) for the indicated peak dose prescriptions in the tumour, situated at a depth of 7.2 cm. The c-t-c distance between the 50 μm thick microbeams is 400 μm. Each curve is proportional to the tumour dose prescription.

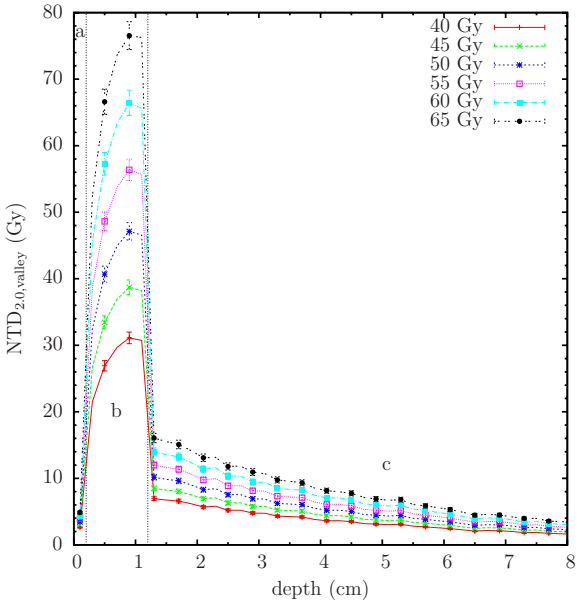

Figure 4. $NTD_{2.0}$ valley dose distribution for the different tissues: skin (a), skull (b) and brain (c) for the indicated peak dose prescriptions in the tumour, situated at a depth of 7.2 cm. The c-t-c distance between the 50 μm thick microbeams is 400 μm.

summary, if the peak dose prescription in the tumour is smaller than 55 Gy, the valley dose in the healthy tissue will be kept under tolerances. If peak doses of 62 Gy were delivered to a centrally located tumour, the 50 % probability of bone necrosis within 5 years in bone would be reached (see figure 4).

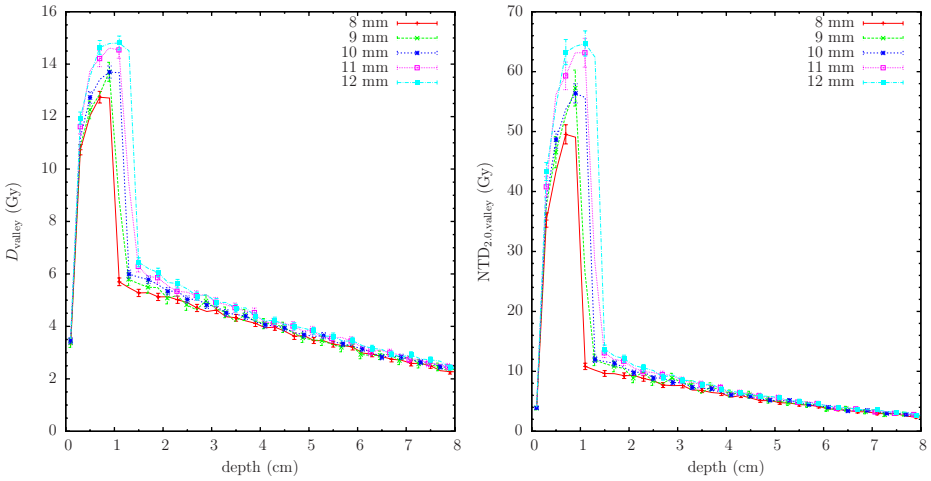

Figure 5. Absorbed dose (left) and $NTD_{2.0}$ (right) valley dose distributions for skull thicknesses ranging from 8 to 12 mm. The prescribed peak dose in the centre of the tumour, situated at a depth of 7.2 cm, is 55 Gy in one fraction. The c-t-c distance between the 50 μm thick microbeams is 400 μm.

Table 1. Maximum peak dose prescription and valley dose in the tumour in one fraction keeping the healthy tissue under tolerances (5% complication probability within 5 years) for different tumour positions.

Depth of tumour (cm)	Maximum peak dose (Gy)	Corresponding valley dose (Gy)
1.5	145	5.9
2.5	125	5.2
3.5	105	4.5
4.5	90	4.1
5.5	75	3.5
6.5	65	2.9
7.2	55	2.6

3.2. Dose distributions as a function of tumour position

The valley doses and the corresponding $NTD_{2.0}$ values have been calculated for a number of tumour positions with respect to the head surface. Table 1 lists, for several tumour locations, the maximum peak dose that can be prescribed in the tumour to keep the corresponding valley doses below healthy tissue tolerances. As can be seen, a deeper-seated tumour implies a lower maximum peak dose prescription to fulfil the requested condition.

3.3. Dose distributions as a function of bone thickness

The above calculations have been done for a skull thickness of 10 mm. However, there might be some slight variation among individuals. Figure 5 shows the valley and $NTD_{2.0}$ dose distributions for several skull thicknesses close to the value used in this work (8, 9, 11 and 12 mm). Doses were obtained for a tumour dose prescription of 55 Gy in one fraction. There are appreciable differences in the bone but there is no variation of the deposited dose as a function of depth (beyond 2 cm). It is important to point out that the difference in $NTD_{2.0}$ between considering 8 mm or 12 mm of skull is about 15 Gy. As a consequence, one should prescribe doses that are several Gy below the tissue tolerances to account for these variations.

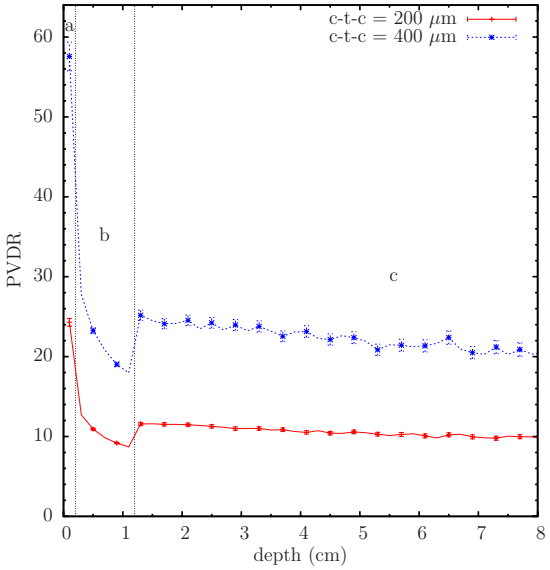

Figure 6. PVDR as a function of depth for two separations between microbeams. The dashed and solid curves correspond to c-t-c separations of 400 and 200 μm, respectively.

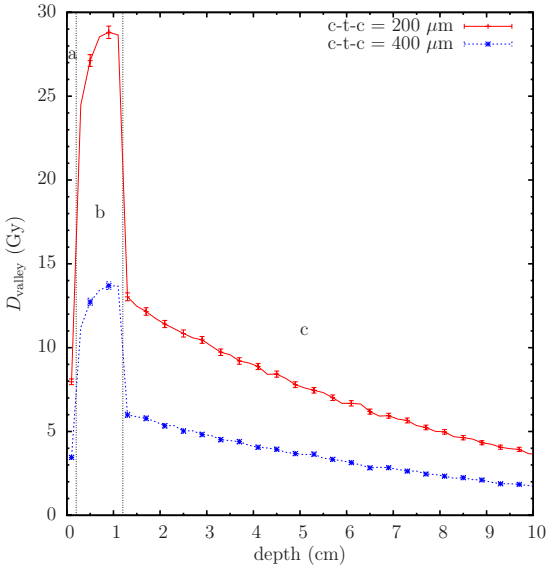

Figure 7. Valley dose distribution as a function of depth for two separations between the microbeams. The dashed and solid curves correspond to c-t-c separations of 400 and 200 μm, respectively. The prescribed peak dose in the centre of the tumour, situated at a depth of 7.2 cm, is 55 Gy in one fraction.

3.4. Dose distributions as a function of the separation between microbeams

Figure 6 compares the PVDR values for two c-t-c distances between microbeams, namely 200 and 400 μm. The PVDR for a c-t-c distance of 200 μm is lower because of the higher valley dose. Figure 7 presents the valley dose distribution corresponding to a peak dose prescription

of 55 Gy in the centre of the tumour. With a 200 μm c-t-c distance, it is possible to deliver a maximum dose of only 27 Gy in the tumour, maintaining the healthy tissue under tolerances, i.e. half than that for a c-t-c separation of 400 μm. The valley dose in a centrally located tumour is now 3.3 Gy. Therefore, to scale up the doses with respect to the ones in conventional radiosurgery, a c-t-c distance of 400 μm is recommended.

4. Conclusions

MC simulations in a human head phantom have been performed to define safe irradiation protocols for the forthcoming clinical trials in MRT. The aim of these trials is the quest for a radical treatment of gliomas, which are the most aggressive and radioresistant brain tumours. The results of this work show that it is possible to deliver a relatively large dose to the tumour and, at the same time, keep the valley dose in the healthy tissue under tolerances. In order to establish the equivalence of the valley dose (one fraction) with the standard fractionation scheme, the $NTD_{2.0}$ has been used. The maximum peak dose that can be prescribed to the tumour while sparing the surrounding normal tissue has been evaluated for various tumour positions. The skull is the organ with the largest absorbed doses. For the most conservative tumour location, i.e. in the centre of the brain, the maximum peak and valley doses accomplishable in the tumour are 55 Gy and 2.6 Gy, respectively, in one fraction and with a unidirectional irradiation. In this way, the valley dose in the healthy tissue will remain under tolerances (5% probability of complication within 5 years). A level of 50% probability of bone necrosis would be reached if the tumour were irradiated with a peak dose of 62 Gy. Although there is no data on the doses required to ablate glioma tumours in humans using MRT, existing data from conventional radiotherapy indicate that an aggressive treatment would enhance the patient lifespan.

Acknowledgments

The authors would like to thank the support given by the ESRF, in particular the help of Rainer Wilcke of the Scientific Software Group. JS acknowledges financial support from the Spanish Ministerio de Educación y Ciencia (projects no. FIS2006-07016 and FPA2009-14091-C02-01) and from the Spanish networking research center CIBER-BBN. JMFV acknowledges financial support from the Spanish Ministerio de Educación y Ciencia (projects no. FPA2006-12066 and FPA2009-14091-C02-01) and FEDER.

References

Barth R F, Coderre J A, Vicente M G H and Blue T E 2005 Boron neutron capture therapy of cancer: current status and future prospects *Clin. Cancer Res.* **11** 3987–4002

Behin A, Hoang-Xuan K, Carpentier A F and Delattre J Y 2003 Primary brain tumours in adults *Lancet Oncol.* **361** 323–31

Blattmann H *et al* 2005 Applications of synchrotron x-rays for radiotherapy *Nucl. Instrum. Methods* A **548** 17–22

Boudou C, Balosso J, Estève F and Elleaume H 2005 Monte Carlo dosimetry for synchrotron stereotactic radiotherapy of brain tumours *Phys. Med. Biol.* **50** 4841–51

Bräuer-Krisch E, Requardt H, Brochard T, Berruyer G, Renier M, Laissue J A and Bravin A 2009 New technology enables high precision multislit collimators for microbeam radiation therapy *Rev. Sci. Instrum.* **80** 074301

Brenner D J 2008 The linear-quadratic model is an appropriate methodology for determining isoeffective doses at large doses per fraction *Semin. Radiat. Oncol.* **18** 234–9

Cardinale R M, Benedict S H, Wu Q, Zwicker R D, Gaballa H E and Mohan R 1998 A comparison of three stereotactic radiotherapy techniques: ARCS vs. noncoplanar fixed fields vs. intensity modulation *Int. J. Radiat. Oncol. Biol. Phys.* **42** 431–6

Company F Z and Allen B J 1998 Calculation of microplanar beam dose profiles in a tissue/lung/tissue phantom *Med. Phys. Biol.* **43** 2491–501

Cullen D E, Hubbell J H and Kissel L 1997 *EPDL97: The evaluated photon data library, 97 version. Report UCRL-50400* vol 6 (Livermore, CA: Lawrence Livermore National Laboratory)

Curtis H J 1967 The use of a deuteron microbeam for simulating the biological effects of heavy cosmic-ray particles *Radiat. Res. Suppl.* **7** 250–7

De Felici M, Felici R, Sanchez del Rio M, Ferrero C, Bacarian T and Dilmanian F A 2005 Dose distributions from x-ray microbeam arrays applied to radiation therapy: an EGS4 Monte Carlo study *Med. Phys.* **32** 2455–63

Dilmanian F A *et al* 2001 Response of avian embryonic brain to spatially segmented x-ray microbeams *Cell. Mol. Biol. (Noisy-le-grand)* **47** 485–93

Dilmanian F A *et al* 2002 Response of rat intracranial 9 L gliosarcoma to microbeam radiation therapy *Neuro Oncol.* **4** 26–38

Dilmanian F A, Morris G M, Zhong N, Bacarian T, Hainfeld J F, Kalef-Ezra J, Brewington L J, Tammam J and Rosen E M 2003 Murine EMT-6 carcinoma: high therapeutic efficacy of microbeam radiation therapy *Radiat. Res.* **159** 632–41

Dilmanian F A, Zhong Z, Bacarian T, Benveniste H, Romanelli P, Wang R, Welwart J, Yuasa T, Rosen E M and Anschel D J 2006 Interlaced x-ray microplanar beams: a radiosurgery approach with clinical potential *Proc. Natl Acad. Sci. USA* **103** 9709–14

Emami B, Lyman J, Brown A, Coia L, Goitein M, Munzenrider J E, Shank B, Solin L J and Wesson M 1991 Tolerance of normal tissue to therapeutic irradiation *Int. J. Radiat. Oncol. Biol. Phys.* **21** 109–22

Fernández-Varea J M, Carrasco P, Panettieri V and Brualla L 2007 Monte Carlo based water/medium stopping-power ratios for various ICRP and ICRU tissues *Phys. Med. Biol.* **52** 6475–83

Flickinger J C and Kalend A 1990 Use of normalized total dose to represent the biological effect of fractionated radiotherapy *Radiother. Oncol.* **17** 339–47

Garcia L M, Leblanc J, Wilkins D and Raaphorst G P 2006 Fitting the linear-quadratic model to detailed data sets for different dose ranges *Phys. Med. Biol.* **51** 2813–23

Guerrero M and Li X A 2004 Extending the linear-quadratic model for large fraction doses pertinent to stereotactic radiotherapy *Phys. Med. Biol.* **49** 4825–35

Harling O K, Roberts K A, Moulin D J and Rogus R D 1995 Head phantoms for neutron capture therapy *Med. Phys.* **22** 579–83

ICRU 37 1984 *Stopping Powers for Electrons and Positrons ICRU Report No 37* (Bethesda, MD: ICRU)

Joiner M and van der Kogel A (ed) 2009 *Basic Clinical Radiobiology* (London: Edward Arnold)

Kagan A R, Steckel R J, Cancilla P, Juillard G and Patin T 1976 The pathogenesis of brain necrosis: time and dose parameters *Int. J. Radiat. Oncol. Biol. Phys.* **1** 729–32

Kirkpatrick J P, Brenner D J and Orton C G 2009 POINT/COUNTERPOINT: the linear-quadratic model is inappropriate to model high dose per fraction effects in radiosurgery *Med. Phys.* **36** 3381–4

Laissue J A *et al* 1998 Neuropathology of ablation of rat gliosarcomas and contiguous brain tissues using a microplanar beam of synchrotron-wiggler-generated X rays *Int. J. Cancer* **78** 654–60

Laissue J A *et al* 1999 Microbeam radiation therapy *Proc. SPIE* **3770** 38–45

Laissue J A *et al* 2001 The weanling piglet cerebellum: a surrogate for tolerance to MRT (microbeam radiation therapy) in pediatric neuro-oncology *Proc. SPIE* **4508** 65–73

Laissue J A, Blattmann H, Wagner H P, Grotzer M A and Slatkin D N 2007 Prospects for microbeam radiation therapy of brain tumours in children to reduce neurological sequelae *Dev. Med. Child. Neurol.* **49** 577–81

Lawrence Y R, Li X A, el Naqa I, Hahn C A, Marks L B, Merchant T E and Dicker A P 2010 Radiation dose–volume effects in the brain *Int. J. Radiat. Oncol. Biol. Phys.* **76** S20–7

Lind B K, Persson L M, Edgren M R, Hedlöf I and Brahme A 2003 Repairable-conditionally repairable damage model based on dual Poisson processes *Radiat. Res.* **160** 366–75

Miura M, Blattmann H, Bräuer-Krisch E, Bravin A, Hanson A L, Nawrocky M M, Micca P L, Slatkin D N and Laissue J A 2006 Radiosurgical palliation of aggressive murine SCCVII squamous cell carcinomas using synchrotron-generated x-ray microbeams *Br. J. Radiol.* **79** 71–5

Orion I, Rosenfeld A B, Dilmanian F A, Telang F, Ren B and Namito Y 2000 Monte Carlo simulation of dose distributions from a synchrotron-produced microplanar beam array using the EGS4 code system *Phys. Med. Biol.* **45** 2497–508

Overgaard M 1988 Spontaneous radiation-induced rib fractures in breast cancer patients treated with postmastectomy irradiation—a clinical radiobiological analysis of the influence of fraction size and dose–response relationships on late bone damage *Acta Oncol.* **27** 117–22

Phillips M H, Stelzer K J, Griffin T W, Mayberg M R and Winn H R 1994 Stereotactic radiosurgery: A review and comparison of methods *J. Clin. Oncol.* **12** 1085–99

Prezado Y, Fois G, Edouard M, Nemoz C, Renier M, Requardt H, Estève F, Adam J F, Elleaume H and Bravin A 2009a Biological equivalent dose studies for dose escalation in stereotactic synchrotron radiation therapy clinical trials *Med. Phys.* **36** 725–33

Prezado Y, Fois G, Le Duc G and Bravin A 2009b Gadolinium dose enhancement studies in microbeam radiation therapy *Med. Phys.* **36** 3568–74

Regnard P *et al* 2008 Irradiation of intracerebral 9 L gliosarcoma by a single array of microplanar x-ray beams from a synchrotron: balance between curing and sparing *Phys. Med. Biol.* **53** 861–78

QUANTEC 2010 Quantitative analyses of normal tissue effects in the clinic *Int. J. Radiat. Oncol. Biol. Phys.* **76** S1–160

Renier M *et al* 2008 The radiotherapy clinical trials projects at the ESRF: technical aspects *Eur. J. Radiol.* **68S** S147–50

Sachs R K, Hahnfeld P and Brenner D J 1997 The link between low-LET dose-response relations and the underlying kinetics of damage production repair misrepair *Int. J. Radiat. Biol.* **72** 351–74

Salvat F, Jablonski A and Powell C J 2005 ELSEPA—Dirac partial-wave calculations of elastic scattering of electrons and positrons by atoms, positive ions and molecules *Comput. Phys. Commun.* **165** 157–90

Salvat F, Fernández-Varea J M and Sempau J 2006 *PENELOPE-2006, A Code System for Monte Carlo Simulation of Electron and Photon Transport* (Issy-les-Moulineaux: OECD Nuclear Energy Agency)

Sempau J, Acosta E, Baró J, Fernández-Varea J M and Salvat F 1997 An algorithm for Monte Carlo simulation of coupled electron–photon transport *Nucl. Instrum. Methods* B **132** 377–90

Sempau J, Sánchez-Reyes A, Salvat F, Oulad ben Tahar H, Jiang S B and Fernández-Varea J M 2001 Monte Carlo simulation of electron beams from an accelerator head using PENELOPE *Phys. Med. Biol.* **46** 1163–86

Sempau J and Andreo P 2006 Configuration of the electron transport algorithm of PENELOPE to simulate ion chambers *Phys. Med. Biol.* **51** 3533–48

Sempau J and Badal A 2008 PenEasy, a modular main program and voxelised geometry package for PENELOPE http://www.upc.edu/inte/downloads/penEasy.htm

Serduc R *et al* 2008 Characterization and quantification of cerebral edema induced by synchrotron x-ray microbeam radiation therapy *Phys. Med. Biol.* **53** 1153–66

Shaw E, Scott C, Souhami L, Dinapoli R, Kline R, Loeffler J and Farnan N 2000 Single dose radiosurgical treatment of recurrent previously irradiated primary brain tumors and brain metastases: Final report of RTOG PROTOCOL 90-05 *Int. J. Radiat. Oncol. Biol. Phys.* **47** 291–8

Siegbahn E A, Stepanek J, Bräuer-Krisch E and Bravin A 2006 Determination of dosimetrical quantities used in microbeam radiation therapy (MRT) with Monte Carlo simulations *Med. Phys.* **33** 3248–59

Slatkin D N, Spanne P, Dilmanian F A and Sandborg M 1992 Microbeam radiation therapy *Med. Phys.* **19** 1395–400

Slatkin D N, Spanne P, Dilmanian F A, Gebbers J O and Laissue J A 1995 Subacute neuropathological effects of microplanar beams of x-rays from a synchrotron wiggler *Proc. Natl Acad. Sci. USA* **92** 8783–7

Smilowitz H M *et al* 2006 Synergy of gene-mediated immunoprophylaxis and microbeam radiation therapy for advanced intracerebral rat 9 L gliosarcomas *Neuro Oncol.* **78** 135–43

Spiga J, Siegbahn E A, Bräuer-Krisch E, Randaccio P and Bravin A 2007 The GEANT4 toolkit for microdosimetry calculations: application to microbeam radiation therapy (MRT) *Med. Phys.* **34** 4322–30

Steel G G (ed) 2002 *Basic Clinical Radiobiology* 3rd edn (London: Edward Arnold)

Stepanek J, Blattmann H, Laissue J A, Lyubimova N, Di Michiel M and Slatkin D N 2000 Physics study of microbeam radiation therapy with PSI-version of Monte Carlo code GEANT as a new computational tool *Med. Phys.* **27** 1664–75

Sterpin E, Salvat F, Cravens R, Ruchala K, Olivera G H and Vynckier S 2008 Monte Carlo simulation of helical tomotherapy with PENELOPE *Phys. Med. Biol.* **53** 2161–80

Stupp R *et al* 2002 Promising survival for patients with newly diagnosed glioblastoma multiforme treated with concomitant radiation plus temozolomide followed by adjuvant temozolomide *J. Clin. Oncol.* **20** 1375–82

Stupp R *et al* 2005 Radiotherapy plus concomitant and adjuvant temozolomide for glioblastoma *N. Engl. J. Med.* **352** 987–96

Stupp R *et al* 2009 Effects of radiotherapy with concomitant and adjuvant temozolomide versus radiotherapy alone on survival in glioblastoma in a randomised phase III study: 5-year analysis of the EORTC-NCIC trial *Lancet Oncol.* **10** 459–66

Torres J, Buades M J, Almansa J F, Guerrero R and Lallena A M 2004 Dosimetry characterization of ^{32}P intravascular brachytherapy source wires using Monte Carlo codes PENELOPE and GEANT4 *Med. Phys.* **31** 296–304

Turesson I and Thames H D 1989 Repair capacity and kinetics of human skin during fractionated radiotherapy: Erythema, desquamation, and telangiectasia after 3 and 5 years follow-up *Radiother. Oncol.* **15** 169–88

2.4 Paper II: Monte Carlo dose enhancement studies in MRT

Introduction

The remarkable therapeutic index in MRT can be further improved by the combination with enhanced absorption induced by contrast agents, as has been explained in section 1.5.1.3. The aim of this work was to assess MRT dose enhancement due to the presence of these high-Z elements.

To this end, an exhaustive MC dosimetric study using different head phantoms (human and rat), MRT irradiation configurations (MRT spectrum and monochromatic beam of 175 keV; c-t-c distances of 200 and 400 μm), several contrast agents clinically used or at the development stage (I, Gd, Ho, Er, Yb, Lu, Hf, Au and Tl) and feasible concentrations (5 and 10 mg/mL) was performed. The MRT irradiation modalities correspond to the clinical trials (MRT spectrum and c-t-c distance of 400 μm) and preclinical trials (MRT spectrum and c-t-c distance of 200 μm) settings. The monochromatic beam of 175 keV corresponds to the energy that provides the optimum balance between dose deposition in the tumour and sparing of healthy tissue [Prezado 2009a].

The optimum dose enhancer was assessed by the maximisation of the ratio between the PVDR values in healthy tissue with respect to the PVDR in the tumour and by the minimisation of bone and brain valley doses.

Monte Carlo dose enhancement studies in microbeam radiation therapy

I. Martínez-Rovira
ID17 Biomedical Beamline, European Synchrotron Radiation Facility (ESRF), B.P. 220, 6 rue Jules Horowitz, F-38043 Grenoble Cedex, France and Institut de Tècniques Energètiques, Universitat Politècnica de Catalunya, Diagonal 647, E-08028 Barcelona, Spain

Y. Prezado[a)]
ID17 Biomedical Beamline, European Synchrotron Radiation Facility (ESRF), B.P. 220, 6 rue Jules Horowitz, F-38043 Grenoble Cedex, France

(Received 24 January 2011; revised 3 June 2011; accepted for publication 3 June 2011; published 30 June 2011)

Purpose: A radical radiation therapy treatment for gliomas requires extremely high absorbed doses resulting in subsequent deleterious side effects in healthy tissue. Microbeam radiation therapy (MRT) is an innovative technique based on the fact that normal tissue can withstand high radiation doses in small volumes without any significant damage. The synchrotron-generated x-ray beam is collimated and delivered to an array of narrow micrometer-sized planar rectangular fields. Several preclinical experiments performed at the Brookhaven National Laboratory (BNL) and at the European Synchrotron Radiation Facility (ESRF) confirmed that MRT yields a higher therapeutic index than nonsegmented beams of the same characteristics. This index can be greatly improved by loading the tumor with high atomic number (Z) contrast agents. The aim of this work is to find the high-Z element that provides optimum dose enhancement.
Methods: Monte Carlo simulations (PENELOPE/penEasy) were performed to assess the peak and valley doses as well as their ratio (PVDR) in healthy tissue and in the tumor, loaded with different contrast agents. The optimization criteria used were maximization of the ratio between the PVDR values in healthy tissue respect to the PVDR in the tumor and minimization of bone and brain valley doses.
Results: Dose enhancement factors, PVDR, and valley doses were calculated for different high-Z elements. A significant decrease of PVDR values in the tumor, accompanied by a gain in the valley doses, was found in the presence of high-Z elements. This enables the deposited dose in the healthy tissue to be reduced. The optimum high-Z element depends on the irradiation configuration. As a general trend, the best outcome is provided by the highest Z contrast agents considered, i.e., gold and thallium. However, lanthanides (especially Lu) and hafnium also offer a satisfactory performance.
Conclusions: The remarkable therapeutic index in microbeam radiation therapy can be further improved by loading the tumor with a high-Z element. This study reports quantitative data on several dosimetric magnitudes in order to find the optimum contrast agent. Although the final choice of the element will also depend on possible cytotoxicity, three elements were found to be worthy of mention: gold, thallium, and lutetium. © *2011 American Association of Physicists in Medicine*. [DOI: 10.1118/1.3603189]

Key words: microbeam radiation therapy, synchrotron radiation, Monte Carlo simulations, dose enhancement

I. INTRODUCTION

A fundamental challenge in radiation-based cancer therapies is the optimization of cell killing within the tumor, while preserving surrounding healthy tissue. There are some particularly radio-resistant tumors, such as gliomas, for which radical radiation therapy treatment does not exist. The control of such tumors requires high doses, whereas the surrounding healthy tissue shows high morbidity.[1] The use of concomitant and adjuvant temozolomide and radiation therapy has enabled significant prolongation of survival.[2] However, the outcome still remains unsatisfactory in most cases.

In the quest for possible ways of improving the therapeutic index in radiation therapy (ratio of the normal tissue tolerance dose to the required dose for tumor control), a new technique that explores the limits of dose-volume effects[3,4] is under development at Biomedical Beamline ID17 of the European Synchrotron Radiation Facility (ESRF). This innovative method is called microbeam radiation therapy (MRT). MRT irradiation is carried out by using an array of parallel, extremely intense x-ray microbeams 25–75 μm-thick with a center-to-center (c-t-c) distance of 200–400 μm.

The MRT irradiation scheme results in dose profiles consisting of a pattern of peaks and valleys, i.e., with high doses in the microbeam paths and low doses in the spaces in between.[5] The dose in the central region between two microbeams is named the valley dose, while the dose at the center of the microbeam is called the peak dose. The ratio between the peak and the valley doses (peak-to-valley dose ratio, PVDR) is also an important magnitude in spatially

fractionated techniques. The PVDR depends on the incident x-ray beam energy, tissue composition, beam thickness, the c-t-c distance, and the irradiation field.[6–9] In order to spare healthy tissue, the PVDR should be high, with a valley dose as low as possible and always below the tolerance level for seamless irradiation. However, low tumor PVDR values show high lesion density, which suppress possible repair mechanisms.[9,10]

MRT has proved to offer remarkable healthy tissue sparing.[11–15] Moreover, MRT protocols have been shown to be able to ablate highly aggressive animal tumor models.[10,15–21] MRT, therefore, yields a higher therapeutic index than nonsegmented beams of a similar energy spectrum.[10,20] The outcome of MRT can be further improved by combining MRT irradiation with dose enhancers such as high-Z-labeled compounds. These can be selectively accumulated within the tumor prior to any irradiation protocol. This idea was first proposed by Dilmanian *et al.*[22] and applied experimentally by Régnard *et al.*[23] The probability of undergoing a photoelectric interaction increases significantly for the energy range of the MRT spectrum and in the presence of high-Z contrast agents. Localized tumor dose enhancement is thus achieved.

Among the high-Z elements, Gd ($Z=71$) compounds are both widely and routinely used for medical imaging as nonspecific magnetic resonance imaging contrast agents. Pilot *in vivo* experiments performed at ESRF showed an important increase in survival time when the tumor was loaded with gadolinium compounds [resulting from the union of Gd with diethylene triamine pentaacetic acid (DTPA)].[23] Gd concentrations of 5 mg/ml have been reported.[24] Due to the continuous improvement of contrast agent delivery methods and their chemistry, higher achievable concentrations are expected in the near future. Other lanthanides that have the same chemical properties as Gd can also be encountered in a biocompatible formulation by the similar complexion with DTPA. Thus, holmium ($Z=67$), erbium ($Z=68$), ytterbium ($Z=70$), and lutetium ($Z=71$) have also been evaluated as MRT dose enhancers in this study. Some of them (Ho, Er, and Lu) have already been used and commercialized for medical applications.[25,26]

Gold ($Z=79$) and iodine ($Z=53$) were also successfully used as dose enhancers in preclinical trials with kilovoltage x-rays[27,30] and numerous gold nanoparticle-based applications for solid tumor therapy are under investigation.[31,32] Au concentrations higher than 5 mg/ml have been reported in preclinical trials without any toxicity effect.[27,28] Tumor iodine concentrations up to 4–5 mg/ml are routinely obtained by intravenous administration for brain tumor imaging.[33,34] In order to maximize iodine concentration, other methods of contrast delivery may provide tumor iodine concentrations of 10–20 mg/ml.[35]

Due to its high atomic number ($Z=81$), thallium is also a good candidate for dose enhancement in MRT. This element has already been employed for experimental treatment of glioma-bearing rats.[36,37]

Some new nanoparticles based on hafnium ($Z=72$) have recently been developed[38] such as inert crystalline nanoparticles of hafnium oxide with a simple coating formulated in water for injection. The crystalline structure of the nanoparticles prevents metabolization by living organisms, so its use as a dose enhancer is promising.

Previous Monte Carlo (MC) dosimetric studies have confirmed the remarkable dose enhancement when the tumor is loaded with high-Z elements in several radiation therapy treatments (see Refs. 35,39–42), including MRT.[43,44] This work reports the first exhaustive dosimetric study using different head phantoms (human and rat), MRT irradiation configurations, several contrast agents (I, Gd, Ho, Er, Yb, Lu, Hf, Au, and Tl), and concentrations (5 and 10 mg/ml). As has been pointed out above, a concentration of 5 mg/ml within the tumor is feasible for most of the studied elements. A higher concentration of 10 mg/ml is either currently achievable or expected to be in the near future. This would offer a higher gain in dose deposition. The final aim was to evaluate the optimum high-Z element which will be used as a dose enhancer as a function of the MRT configuration. Maximization of the PVDR quotient values in healthy tissue with respect to the PVDR in the tumor and minimization of the valley doses in healthy tissue were used as the criteria.

II. MATERIALS AND METHODS

II.A. Radiation source

The ESRF is a third-generation synchrotron with a 6-GeV electron storage ring. The photon beam used in MRT is generated by a wiggler that has 21 poles, a period of 15 cm, and a maximum magnetic field of 1.6 T. The generated photon beam crosses different filters in order to eliminate low energies and other beam modifiers such as diaphragms, slits, etc. The patient position is located 42 m from the source. The final x-ray spectrum, hereafter named MRT spectrum, ranges from 50 to 600 keV, with a peak energy at 80 keV.[5]

The microbeams are generated by a multislit collimator[45] which spatially fractionates the beam in the horizontal direction. As the natural vertical aperture of the synchrotron beam is extremely small, targets are vertically scanned through the microfractionated beam to deliver microplanes of x-rays. Synchrotron microbeams possess two important features: negligible divergence and high flux. These properties allow the production of sharply defined beam edges and delivery of the dose in a fraction of a heart beat, which minimizes cardiosynchronous motion effects in the brain.[46]

II.B. Monte Carlo simulation code: PENELOPE\penEasy

The 2008 version of the MC code PENELOPE (Refs. 47 and 48) and penEasy,[49] a general-purpose main program for PENELOPE, were employed. PENELOPE allows the coupled transport of electrons, photons, and positrons to be simulated in a very wide energy range and in arbitrary materials. It has been frequently used in the medical physics field (see, for example, Refs. 50–52).

The predominant photon interactions for the energy range and materials used in this study are the photoelectric effect and Compton scattering. Figure 1 shows the attenuation

coefficients μ/ρ for these interactions in terms of incoming photon energy. The photoelectric cross sections are interpolated from tabulations in the evaluated photon data library from the Lawrence Livermore National Laboratory.[53] The photoelectric effect is especially important in bone or in a tumor loaded with a high-Z element. The Compton cross sections are obtained by using the relativistic impulse approximation, which takes into account both Doppler broadening and binding effects of atomic electrons. Many-body and aggregation effects are ignored.

II.C. Phantom description and simulation details

Two geometries were considered in the simulations: a human head phantom and a rat head phantom. The human head phantom is composed of slabs of skin (0.2 cm), skull (0.8 cm), and brain (12 cm), with a tumor located at the center of the brain. The thicknesses correspond to a lateral irradiation in order to minimize the length of irradiated healthy tissue.[54] The tumor, loaded with different contrast agents, was modeled by a 2-cm-diameter cylinder of 2 cm height. The size of the tumor was inspired by others that were published in previous dosimetry works[55,56] rather than from clinical data, which is highly dependent on type of tumor, location, etc.

The rat head phantom consists of slabs of skin (700 μm), bone (500 μm), and brain (2.6 cm). These thicknesses were extracted from MRI images.[43] A cylindrical tumor of 4 mm in height and 4 mm in diameter was placed 6.7 mm from the head surface to mimic the tumor model used in the experiments.[23]

The tumor was loaded with different elements in both phantoms: iodine ($Z=53$), gadolinium ($Z=64$), holmium ($Z=67$), erbium ($Z=68$), ytterbium ($Z=70$), lutetium ($Z=71$), hafnium ($Z=72$), gold ($Z=79$), and thallium ($Z=81$). A concentration of 5 mg/ml in the tumor was assessed for each element. In the human case, additional simulations with 10 mg/ml were performed. Several MRT configurations were evaluated for each geometry.

- MRT irradiation parameters that will be used in the forthcoming clinical trials, i.e., 50-μm-wide microbeams with a c-t-c of 400 μm and the MRT energy spectrum (hereafter referred to as $\text{MRT}_{\text{ctc400}}$).
- 175 keV monochromatic 50-μm-wide microbeams with a c-t-c of 400 μm (denoted as $175\ \text{keV}_{\text{ctc400}}$). This energy provides the optimum balance between dose deposition in the tumor and sparing of healthy tissue.[43]
- Common preclinical trial irradiation conditions: 50-μm-wide microbeams, 200 μm c-t-c distance, and MRT energy spectrum (hereafter, called $\text{MRT}_{\text{ctc200}}$).
- 175 keV monochromatic 50-μm-wide microbeams with a c-t-c distance of 200 μm ($175\ \text{keV}_{\text{ctc200}}$).

The dose computation was divided into two parts. First, the absorbed dose distribution for a single microbeam in the phantom was simulated. A simplified model in which beam divergence is not included was used. The single dose distribution was then shifted and added to the total dose distribution at each depth in order to cover the irradiation field size: $2\times 2\ \text{cm}^2$ for the human phantom and $1\times 1\ \text{cm}^2$ for the rat phantom. Although these simplifications are common practice for many authors of theoretical MRT studies,[5,7,8] it should be pointed out that these unsophisticated models have some limitations detailed in the work of Nettelbeck *et al.*[57]

For the human head phantom, doses were scored in voxels of 2 μm along the microbeam width and 2 mm in the vertical direction of the microbeam and in depth. These dimensions were reduced by half for the rat head phantom, as a higher spatial resolution was required.

The simulation parameters were the following. The absorption energies, EABS, were set to 1 keV for electrons and 0.1 keV for photons. The average angular deflection

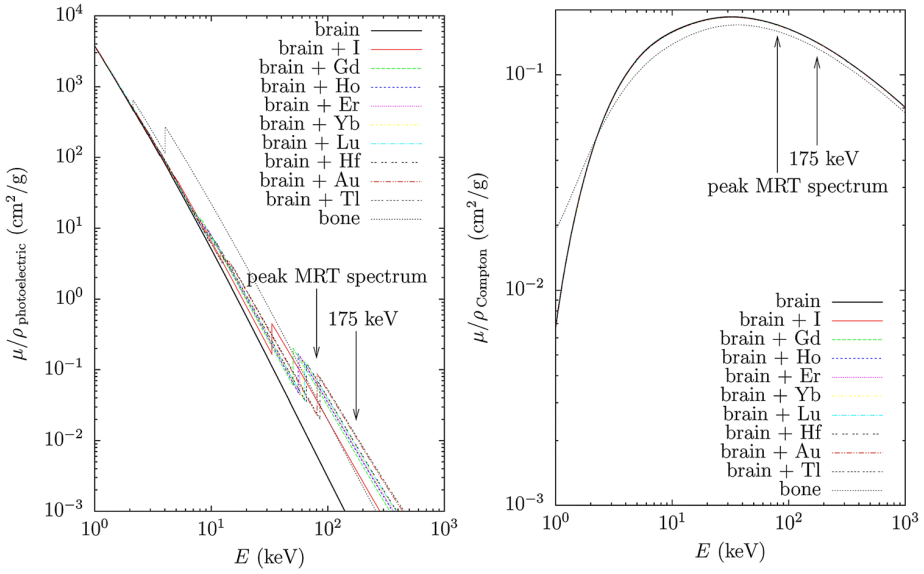

FIG. 1. Photoelectric (left) and Compton (right) attenuation coefficients for bone and the brain after being loaded with different contrast agents.[47]

between two consecutive events, C1, and the maximum average fractional energy loss in a single multiple-scattering step, C2, were fixed at 0.1. The cut-off energies for the production of hard inelastic, WCC, and hard bremsstrahlung events, WCR, were set equal to electron and photon EABS (Refs. 47 and 58). The simulations were discontinued when the average statistical uncertainty was less than 0.5% (two standard deviations, 2σ).

III. RESULTS AND DISCUSSION

In this section, dose enhancement factors (DEFs), PVDR values and valley doses (D_{valley}) in the tumor and healthy tissue are reported for several configurations, contrast agents, and concentrations in the two phantoms. The results for the different irradiation configurations in the human head phantom will be first discussed. Calculations for the rat phantom geometry will then be presented.

III.A. Dose enhancement studies on a human head phantom irradiated with an array of 50-μm-wide microbeams with a spacing of 400 μm

III.A.1. Dose enhancement factors (DEFs)

DEFs quantify the overall dose enhancement in the tumor. They are defined as the ratio of the absorbed dose in the tumor loaded with a contrast agent to the absorbed dose in the absence of any element. Table I shows the DEF values for two concentrations (5 and 10 mg/ml) of the several high-Z elements as a function of beam energy.

The photoelectric effect plays a major role for dose enhancement in the tumor in the presence of high-Z elements. Higher DEF values were obtained when using the MRT spectrum in comparison with the 175 keV monochromatic beam. This is due to the fact that the photoelectric effect cross section decreases with energy. Photoelectric absorption also increases drastically with the atomic number of the medium. For Hf, Au, and Tl, however, the DEF diminished when the MRT spectrum was used since its peak is located at the K-edge of these elements. DEF also increased with element concentration. The average ratio between energy deposited in the tumor loaded with a concentration of 10 mg/ml with respect to 5 mg/ml was 1.22 for the MRT spectrum and 1.10 for a 175 keV beam. Hence, the effect of the element concentration was enhanced when the MRT spectrum was used.

TABLE I. DEF values for different contrast media as a function of microbeam energy and element concentration in the human head phantom. Statistical uncertainty corresponds to 2σ.

		MRT spectrum		Monochromatic 175 keV	
Z	Element	5 mg/ml	10 mg/ml	5 mg/ml	10 mg/ml
53	I	1.242(1)	1.478(1)	1.063(1)	1.125(1)
64	Gd	1.298(1)	1.585(1)	1.095(1)	1.189(1)
67	Ho	1.305(1)	1.599(1)	1.104(1)	1.208(1)
68	Er	1.306(1)	1.603(1)	1.108(1)	1.215(1)
70	Yb	1.307(1)	1.603(1)	1.113(1)	1.226(1)
71	Lu	1.308(1)	1.606(1)	1.117(1)	1.232(1)
72	Hf	1.306(1)	1.602(1)	1.119(1)	1.237(1)
79	Au	1.304(1)	1.597(1)	1.138(1)	1.274(1)
81	Tl	1.301(1)	1.592(1)	1.142(1)	1.281(1)

DEF values provide a general idea of the global dose deposition gain when the tumor is loaded with a high-Z element. However, this magnitude does not offer a complete picture in the case of spatially fractionated techniques such as MRT. For this reason, other dosimetric magnitudes were evaluated.

III.A.2. PVDR assessment

As stated in Sec. I, the lower the tumor PVDR ($PVDR_{tumor}$), the higher the achievable tumor control probability. However, PVDR in healthy tissue ($PVDR_{HT}$) should remain high with the lowest possible valley dose, always below the tolerance level for seamless irradiation.[10]

Figure 2 (top) presents the PVDR values versus depth for a nonloaded tumor, called unloaded tumor. Both MRT_{ctc400} and 175 keV_{ctc400} configurations were assessed. In the first case, PVDR took values around 59 in the first 2 mm (skin) and then fell off rapidly in the bone down to a value of 19 at the interface with the brain. PVDR remained almost constant throughout the brain (20–25). For the 175 keV monochromatic beam, PVDR in the skin was approximately 80, while it decreased to 30 when it entered the brain, where it remained constant (25–30). Healthy tissue PVDR values were higher for the 175 keV monochromatic beam than for the MRT spectrum due to its higher penetration power, thus offering better tissue sparing. This is important as the aim was to study how much this sparing can be enhanced by using high-Z elements.

Figure 2 also shows the tumor PVDR values versus depth for a tumor loaded with different high-Z elements. Two configurations, MRT_{ctc400} (center) and 175 keV_{ctc400} (bottom), were assessed. The presence of high-Z contrast agents increased both the photoelectric and Compton cross sections in the peaks and in the valleys. The peak dose average gain in the tumor (10 mg/ml) was 1.5 and 1.1 for MRT_{ctc400} and 175 keV_{ctc400}, respectively. The increase in valley doses for these configurations was 2.0 and 1.6. The higher gain in valley doses rather than in the peaks was responsible for the overall reduction of PVDR values in the tumor.

Table II shows quantitative $PVDR_{tumor}$ values as a function of microbeam energy and element concentration. The lowest PVDR values were obtained in the case of the MRT spectrum. No remarkable differences were encountered among the different elements, despite the fact that they were more pronounced when the 175 keV monochromatic beam was used. The degree to which $PVDR_{tumor}$ decreased with respect to the unloaded tumor was similar for both energies and depended on the concentration. The average reduction of $PVDR_{tumor}$ was about 16% and 26% for 5 and 10 mg/ml. Therefore, we can state that the higher the concentration, the lower $PVDR_{tumor}$, which produced higher normal tissue sparing.

As explained in Sec. I, the optimum contrast media would be that which provides maximization of the quotient between PVDR in healthy tissue and PVDR in the tumor. In addition, the values of valley doses in normal tissues with respect to

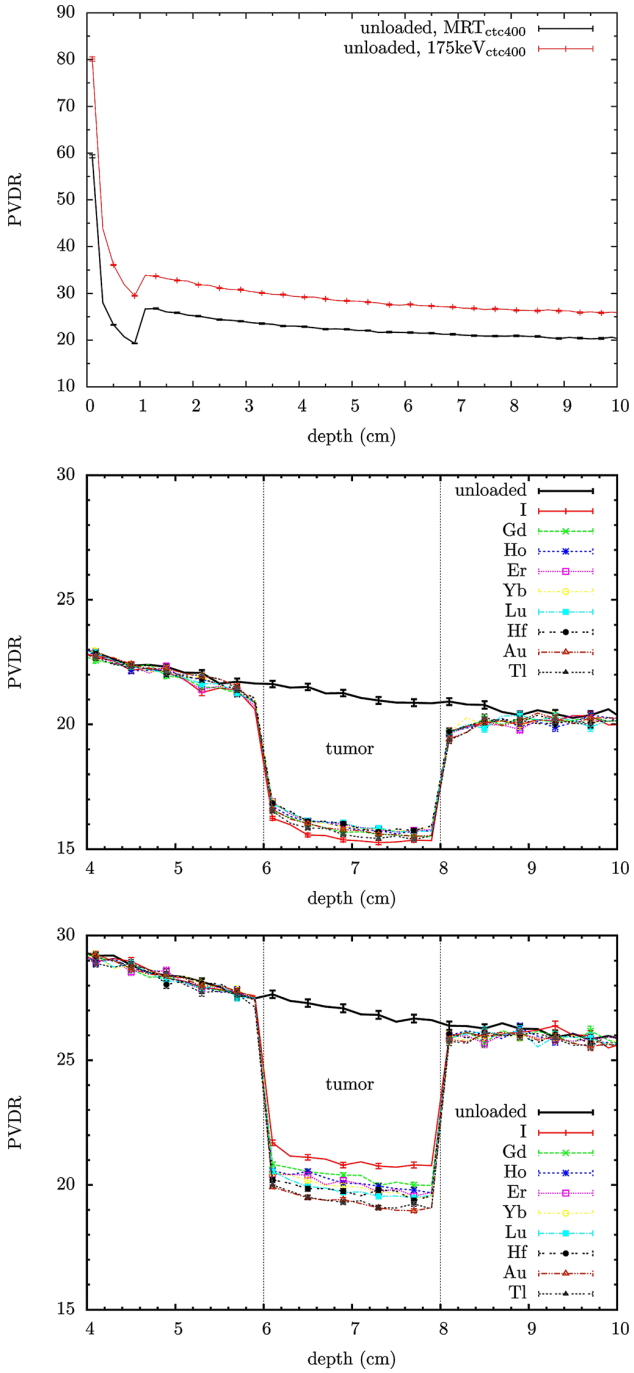

FIG. 2. PVDR values versus depth for a nonloaded (top) and loaded tumor in the human head phantom. The MRT$_{ctc400}$ (center) and 175 keV$_{ctc400}$ (bottom) irradiation configurations were assessed (c-t-c: 400 μm, field size: 2-by-2 cm^2). Each line corresponds to a different high-Z element (10 mg/ml). Statistical uncertainty bars are at 2σ.

those in the tumor must be minimized. Table III lists the maximum PVDR in the bone (PVDR$_{max\ bone}$) and the average PVDR in the brain (PVDR$_{average\ brain}$), both with respect to PVDR$_{tumor}$. When the PVDR$_{HT}$/PVDR$_{tumor}$ is higher, a major healthy tissue sparing is expected. Maximum sparing of the bone (highest PVDR$_{max\ bone}$/PVDR$_{tumor}$ ratios) was obtained with an incoming beam energy of 175 keV, since

TABLE II. PVDR$_{tumor}$ for different contrast media as a function of microbeam energy and element concentration in the human head phantom (c-t-c: 400 μm, field size: 2-by-2 cm^2). Statistical uncertainty corresponds to 2σ.

		MRT spectrum		175 keV	
Z	Element	5 mg/ml	10 mg/ml	5 mg/ml	10 mg/ml
	Unloaded	21.1(1)		26.9(2)	
53	I	17.5(1)	15.33(8)	23.6(1)	20.9(1)
64	Gd	17.7(1)	15.70(8)	22.9(1)	20.4(1)
67	Ho	17.7(1)	15.77(8)	22.8(1)	20.1(1)
68	Er	17.8(1)	15.87(8)	22.6(1)	20.0(1)
70	Yb	17.9(1)	15.88(8)	22.7(1)	19.9(1)
71	Lu	17.6(1)	15.84(8)	22.7(1)	19.7(1)
72	Hf	17.8(1)	15.82(8)	22.7(1)	19.6(1)
79	Au	17.7(1)	15.75(8)	22.3(1)	19.25(8)
81	Tl	17.6(1)	15.48(8)	22.2(1)	19.4(1)

photoelectric absorption in the bone is reduced at high energies. However, both energies provided similar gain in brain tissue sparing (PVDR$_{average\ brain}$/PVDR$_{tumor}$ were close). The elements that provide the minimum PVDR$_{tumor}$ and the maximum PVDR$_{HT}$/PVDR$_{tumor}$ values were I and Tl for the MRT spectrum and Au and Tl for the 175 keV monochromatic beam.

III.A.3. Valley dose quantification

Despite the fact that PVDR is an important parameter, it is a relative quantity. Evaluation of valley doses in healthy tissue ($D_{valley,\ HT}$) is also required as they are the most important magnitude in order to examine tissue sparing. Figure 3 shows the ratio of valley doses in healthy tissue with respect to the valley dose in the tumor for MRT$_{ctc400}$ (top) and 175 keV$_{ctc400}$ (bottom). Dose enhancement is observed in the tumor due to the increase of the photoelectric cross sections. The use of high-Z elements has led to a reduction in healthy tissue valley doses in delivering a given dose to the tumor (normalized to the tumor in Fig. 3). Bone is the tissue that receives the highest doses, so it will be the limiting organ.[9,59]

Table IV gives the quotients between the maximum valley dose in the bone ($D_{valley,\ max\ bone}$) and the average valley dose in the brain from 2 to 5 cm depth ($D_{valley,\ average\ brain}$), both with respect to the valley dose in the tumor ($D_{valley,\ tumor}$). As explained above, these quotients quantify the effective reduction in healthy tissue valley doses in the presence of high-Z elements. A total of 175 keV$_{ctc400}$ favored bone sparing while MRT$_{ctc400}$ contributed slightly more to brain preservation.

The elements that provide the best outcome were lutetium and thallium, despite the rest of lanthanide elements and hafnium offered also a satisfactory performance. The valley doses in bone and in the brain were 3.34 and 1.105 times the valley dose in the tumor for Lutetium (Lu) at a concentration of 5 mg/ml. For 175 keV$_{ctc400}$, the best results were provided by gold and thallium. Differences in performance between elements were more pronounced in this configuration. The

TABLE III. $PVDR_{max\ bone}/PVDR_{tumor}$ (left) and $PVDR_{average\ brain}/PVDR_{tumor}$ (right) as a function of microbeam energy and element concentration in the human head phantom (c-t-c: 400 μm, field size: 2-by-2 cm^2). Statistical uncertainty corresponds to 2σ.

		Bone				Brain			
		MRT spectrum		175 keV		MRT spectrum		175 keV	
Z	Element	5 mg/ml	10 mg/ml	5 mg/ml	10 mg/ml	5 mg/ml	10 mg/ml	5 mg/ml	10 mg/ml
Unloaded		1.33(1)		1.63(1)		1.110(1)		1.114(1)	
53	I	1.60(1)	1.82(1)	1.86(1)	2.10(1)	1.335(2)	1.519(2)	1.268(2)	1.427(2)
64	Gd	1.59(1)	1.78(1)	1.92(1)	2.16(1)	1.322(2)	1.484(2)	1.302(2)	1.466(2)
67	Ho	1.58(1)	1.78(1)	1.92(1)	2.19(2)	1.318(2)	1.480(2)	1.310(2)	1.486(2)
68	Er	1.58(1)	1.77(1)	1.94(1)	2.18(2)	1.312(2)	1.471(2)	1.320(2)	1.490(2)
70	Yb	1.57(1)	1.77(1)	1.94(1)	2.12(2)	1.306(2)	1.470(2)	1.317(2)	1.498(2)
71	Lu	1.59(1)	1.77(1)	1.94(1)	2.22(2)	1.324(2)	1.470(2)	1.322(2)	1.515(2)
72	Hf	1.58(1)	1.77(1)	1.93(1)	2.24(2)	1.314(2)	1.474(2)	1.313(2)	1.525(2)
79	Au	1.59(1)	1.77(1)	1.97(1)	2.27(1)	1.318(2)	1.481(2)	1.339(2)	1.553(2)
81	Tl	1.60(1)	1.80(1)	1.99(1)	2.27(2)	1.328(2)	1.507(2)	1.347(2)	1.541(2)

maximum benefit in the $D_{valley,\ HT}/D_{valley,\ tumor}$ for a loaded tumor compared to the same ratio for a nonloaded tumor was obtained at a concentration of 10 mg/ml; the average gain in the presence of high-Z elements was about 48% for MRT_{ctc400} and 32% for 175 keV_{ctc400} compared with the absence of a contrast agent.

III.A.4. Discussion

Table V gives the elements that provide the best results for each dosimetric parameter (bold letters indicate the optimum case among the irradiation configurations). The differences in performance among the high-Z elements were more pronounced for 175 keV_{ctc400} than for MRT_{ctc400} and increased with concentration. Two elements stand out in the 175 keV_{ctc400} configuration: thallium and gold. The best outcome for MRT_{ctc400} was achieved by employing thallium, together with lanthanide elements (especially, lutetium). Iodine provided a significant reduction of $PVDR_{tumor}$ that was not accompanied by an increase in the valley dose, which lost effectiveness in terms of tumor control. In the present study, only dosimetric considerations have been taken into account. Nevertheless, the possible cytotoxicity of the different contrast agents should also be considered.

III.B. Dose enhancement studies on a human head phantom irradiated with an array of 50-μm-wide microbeams with a spacing of 200 μm

Analogous calculations were performed for a c-t-c distance of 200 μm. Table VI presents PVDR values in the center of the tumor. I, Au, and Tl are the elements that provide the highest decrease in $PVDR_{tumor}$ for MRT_{ctc200}. The lanthanides and hafnium are the elements that give the best outcome in the case of 175 keV_{ctc200}, in contrast to 175 keV_{ctc400}. This is explained in Fig. 4, where the lateral dose profiles for one microbeam at the central tumor position are plotted. The K-edge energies of lanthanides are lower than those of Au/Tl. Therefore, the products of the photoelectric interactions in the presence of lanthanides have a higher kinetic energy at 100 μm. Consequently, the dose deposition in the valleys (and the decrease of $PVDR_{tumor}$) is more effective for lanthanides than it is for Au/Tl in this irradiation configuration (c-t-c of 200 μm).

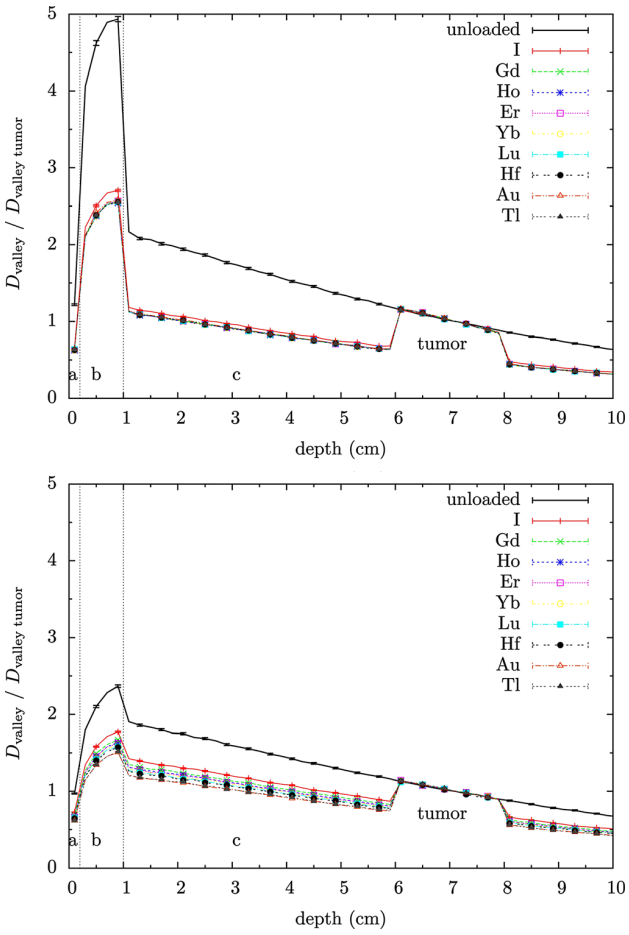

FIG. 3. Valley dose with respect to $D_{valley,\ tumor}$ versus depth in the human head phantom. The MRT_{ctc400} (top) and 175 keV_{ctc400} (bottom) irradiation configurations were assessed (c-t-c: 400 μm, field size: 2-by-2 cm^2). Each line corresponds to a tumor loaded with a different high-Z element (10 mg/ml). The three labeled areas correspond to skin (a), skull (b), and the brain (c). Statistical uncertainty bars are at 2σ.

TABLE IV. $D_{valley,\ max\ bone}/D_{valley,\ tumor}$ (left) and $D_{valley,\ average\ brain}/D_{valley,\ tumor}$ (right) as a function of microbeam energy and element concentration in the human head phantom (c-t-c: 400 μm, field size: 2-by-2 cm^2). Statistical uncertainty corresponds to 2σ.

		Bone				Brain			
		MRT spectrum		175 keV		MRT spectrum		175 keV	
Z	Element	5 mg/ml	10 mg/ml	5 mg/ml	10 mg/ml	5 mg/ml	10 mg/ml	5 mg/ml	10 mg/ml
Unloaded		4.94(3)		2.37(2)		1.632(2)		1.505(2)	
53	I	3.50(2)	2.71(2)	2.04(1)	1.77(1)	1.157(1)	0.893(1)	1.296(2)	1.130(1)
64	Gd	3.37(2)	2.55(1)	1.92(1)	1.67(1)	1.118(1)	0.849(1)	1.244(2)	1.070(1)
67	Ho	3.38(2)	2.54(2)	1.93(1)	1.64(1)	1.114(1)	0.845(1)	1.232(2)	1.047(1)
68	Er	3.40(2)	2.57(2)	1.89(1)	1.62(1)	1.121(1)	0.847(1)	1.219(1)	1.041(1)
70	Yb	3.39(2)	2.57(2)	1.89(1)	1.61(1)	1.124(1)	0.848(1)	1.218(1)	1.028(1)
71	Lu	3.34(2)	2.55(2)	1.90(1)	1.58(1)	1.109(1)	0.847(1)	1.211(1)	1.012(1)
72	Hf	3.37(2)	2.56(2)	1.90(1)	1.57(1)	1.117(1)	0.847(1)	1.218(2)	1.004(1)
79	Au	3.40(2)	2.58(1)	1.85(1)	1.506(8)	1.123(1)	0.853(1)	1.177(1)	0.959(1)
81	Tl	3.38(2)	2.55(2)	1.80(1)	1.514(9)	1.120(1)	0.843(1)	1.162(1)	0.963(1)

TABLE V. Overview of the elements providing the best outcome for each dosimetric parameter in the human head phantom (c-t-c: 400 μm, field size: 2-by-2 cm^2). Bold letters indicate the best case among the different irradiation configurations. The asterisk signals the optimum element(s) despite the fact that statistical differences are not significant (the values agree within the error bars).

		MRT spectrum		175 keV	
Parameter	Table	5 mg/ml	10 mg/ml	5 mg/ml	10 mg/ml
Maximum DEF	I	Lu	**Lu**	Tl	Tl
Minimum $PVDR_{tumor}$	II	I/Lu/Tl*	**I/Tl**	Au/Tl	Au/Tl
Maximum $PVDR_{max\ bone}/PVDR_{tumor}$	III	I/Tl*	I/Tl	Au/Tl	**Au/Tl**
Maximum $PVDR_{average\ brain}/PVDR_{tumor}$	IV	I/Tl	**I/Tl**	Au/Tl	Au/Tl
Minimum $D_{valley,\ max\ bone}/D_{valley,\ tumor}$	V	Lu*	Ho*	Au/Tl	**Au/Tl***
Minimum $D_{valley,\ average\ brain}/D_{valley,\ tumor}$	VI	Lu	**Tl***	Au/Tl	Au/Tl

Table VII presents $D_{valley,\ max\ bone}/D_{valley,\ tumor}$ and $D_{valley,\ average\ brain}/D_{valley,\ tumor}$. The 175 keV_{ctc200} irradiation configuration favors bone sparing. The two energies provided a similar gain in brain dose reduction. Values of $D_{valley,\ average\ brain}/D_{valley,\ tumor}$ less than one were observed for a contrast agent concentration of 10 mg/ml. This indicated the average valley dose deposited in the brain was lower than the one in the tumor. $D_{valley,\ HT}/D_{valley,\ tumor}$ values were significantly smaller than the ones presented for an unloaded tumor. Thus, the use of high-Z elements led to a reduction in healthy tissue valley doses in delivering a given dose to the tumor. Au and Tl were the optimum choice for MRT_{ctc200} while lutetium stand out in the 175 keV_{ctc200} configuration. Therefore, choice of the optimum element depends not only on the energy of the incoming beam but also on the c-t-c distance between microbeams.

III.C. Dose enhancement studies on a rat head phantom irradiated with an array of 50-μm-wide microbeams with a spacing of 200 and 400 μm

Analogous calculations were performed on a rat head phantom with the most relevant contrast media: lutetium, gold, and thallium with a concentration of 5 mg/ml. The average DEF values were around 1.31 for the MRT spectrum and 1.12 for the 175 keV monochromatic beam.

Table VIII shows $PVDR_{tumor}$, $PVDR_{max\ bone}/PVDR_{tumor}$, and $PVDR_{average\ brain}/PVDR_{tumor}$ (average from 3 to 4 mm) for all irradiation configurations. The best outcome was provided by Au and Tl in all configurations except for 175 keV_{ctc200}, where Lu was once again the element with minimum $PVDR_{tumor}$. The healthy tissue valley doses with respect to $D_{valley,\ tumor}$ followed the same trend as the human

TABLE VI. $PVDR_{tumor}$ for different contrast media as a function of microbeam energy and element concentration in the human head phantom (c-t-c: 200 μm, field size: 2-by-2 cm^2). Statistical uncertainty corresponds to 2σ.

		MRT spectrum		175 keV	
Z	Element	5 mg/ml	10 mg/ml	5 mg/ml	10 mg/ml
Unloaded		10.04(4)		13.81(6)	
53	I	8.27(3)	7.32(3)	10.97(4)	9.36(3)
64	Gd	8.33(3)	7.44(3)	10.30(4)	8.34(3)
67	Ho	8.34(3)	7.42(3)	10.18(4)	8.23(3)
68	Er	8.37(3)	7.44(3)	10.17(4)	8.16(3)
70	Yb	8.38(3)	7.48(3)	10.14(4)	8.20(3)
71	Lu	8.35(3)	7.45(3)	10.07(4)	8.21(3)
72	Hf	8.36(3)	7.45(3)	10.16(4)	8.24(3)
79	Au	8.24(3)	7.31(3)	10.56(4)	8.71(2)
81	Tl	8.23(3)	7.30(3)	10.66(4)	8.91(3)

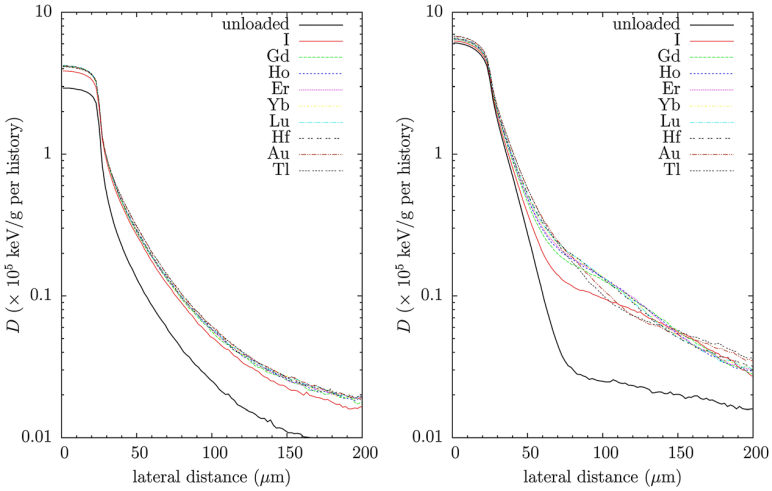

FIG. 4. Lateral dose profile of a single microbeam at the central tumor position (human head phantom) when the irradiation is performed using the MRT spectrum (left) and the 175 keV monochromatic beam (right). The different lines correspond to the different high-Z elements studied (10 mg/ml).

TABLE VII. $D_{\text{valley, max bone}}/D_{\text{valley, tumor}}$ (left) and $D_{\text{valley, average brain}}/D_{\text{valley, tumor}}$ (right) as a function of microbeam energy and element concentration in the human head phantom (c-t-c: 200 μm, field size: 2-by-2 cm^2). Statistical uncertainty corresponds to 2σ.

		Bone				Brain			
		MRT spectrum		175 keV		MRT spectrum		175 keV	
Z	Element	5 mg/ml	10 mg/ml	5 mg/ml	10 mg/ml	5 mg/ml	10 mg/ml	5 mg/ml	10 mg/ml
Unloaded		4.91(2)		3.11(1)		1.651(1)		1.526(1)	
53	I	3.42(1)	2.64(1)	2.42(1)	2.009(8)	1.151(1)	0.888(1)	1.182(1)	0.983(1)
64	Gd	3.30(1)	2.489(9)	2.231(9)	1.739(7)	1.110(1)	0.840(1)	1.092(1)	0.851(1)
67	Ho	3.38(2)	2.474(9)	2.192(9)	1.704(7)	1.104(1)	0.833(1)	1.075(1)	0.833(1)
68	Er	3.30(1)	2.471(9)	2.193(9)	1.685(6)	1.109(1)	0.832(1)	1.071(1)	0.824(1)
70	Yb	3.31(1)	2.48(1)	2.174(9)	1.682(7)	1.108(1)	0.835(1)	1.064(1)	0.821(1)
71	Lu	3.29(1)	2.472(9)	2.164(9)	1.678(6)	1.105(1)	0.832(1)	1.054(1)	0.818(1)
72	Hf	3.30(1)	2.484(9)	2.175(9)	1.679(6)	1.107(1)	0.834(1)	1.062(1)	0.820(1)
79	Au	3.27(1)	2.460(8)	2.226(9)	1.721(5)	1.099(1)	0.827(1)	1.089(1)	0.841(1)
81	Tl	3.28(1)	2.475(9)	2.228(9)	1.755(7)	1.104(1)	0.829(1)	1.090(1)	0.858(1)

TABLE VIII. PVDR dosimetric study in the tumor and healthy tissue for different contrast media as a function of microbeam energy and the c-t-c distance in the rat head phantom (field size: 1-by-1 cm^2). Statistical uncertainty corresponds to 2σ.

		MRT spectrum		175 keV	
Z	Element	400 μm	200 μm	400 μm	200 μm
		$\text{PVDR}_{\text{tumor}}$			
Unloaded		64.7(7)	25.0(2)	78.1(8)	37.7(3)
71	Lu	58.0(6)	21.6(1)	65.1(6)	22.2(1)
79	Au	57.3(6)	20.9(1)	62.8(6)	24.4(1)
81	Tl	56.7(6)	20.7(1)	62.7(6)	25.4(2)
		$\text{PVDR}_{\text{max bone}}/\text{PVDR}_{\text{tumor}}$			
Unloaded		1.40(2)	1.37(1)	1.85(3)	1.18(1)
71	Lu	1.56(2)	1.56(1)	2.22(4)	2.01(2)
79	Au	1.58(2)	1.61(2)	2.27(4)	1.82(2)
81	Tl	1.58(2)	1.62(2)	2.29(4)	1.75(2)
		$\text{PVDR}_{\text{average brain}}/\text{PVDR}_{\text{tumor}}$			
Unloaded		1.117(8)	1.105(5)	1.140(8)	1.140(6)
71	Lu	1.200(9)	1.231(5)	1.33(1)	1.743(7)
79	Au	1.215(9)	1.255(6)	1.359(9)	1.608(7)
81	Tl	1.222(9)	1.266(6)	1.356(9)	1.553(7)

TABLE IX. $D_{\text{valley, max bone}}/D_{\text{valley, tumor}}$ and $D_{\text{valley, average brain}}/D_{\text{valley, tumor}}$ for different contrast media as a function of microbeam energy and the c-t-c distance in the rat head phantom (field size: 1-by-1 cm^2). Statistical uncertainty corresponds to 2σ.

		MRT spectrum		175 keV	
Z	Element	400 μm	200 μm	400 μm	200 μm
		$D_{\text{valley, max bone}}/D_{\text{valley, tumor}}$			
Unloaded		1.12(2)	1.18(1)	0.85(1)	1.17(1)
71	Lu	0.80(1)	0.808(7)	0.68(1)	0.653(6)
79	Au	0.80(1)	0.795(7)	0.65(1)	0.707(7)
81	Tl	0.79(1)	0.793(7)	0.65(1)	0.733(7)
		$D_{\text{valley, average brain}}/D_{\text{valley, tumor}}$			
Unloaded		0.934(7)	0.943(5)	0.910(7)	0.908(5)
71	Lu	0.720(6)	0.700(4)	0.68(1)	0.584(3)
79	Au	0.719(6)	0.695(4)	0.731(6)	0.621(3)
81	Tl	0.718(6)	0.691(3)	0.729(6)	0.639(3)

head phantom, despite the fact that the brain receives equivalent doses to the skull for the rat head phantom (see Table IX).

Our Monte Carlo predicted dosimetry data from the rat head phantom were equivalent to data from the human head phantom. This equivalence may prove useful when moving from preclinical rodent studies to clinical trials in humans.

IV. CONCLUSIONS

MRT is a synchrotron radiation therapy technique with the potential to cure brain tumors. Many preclinical studies have proved that MRT is able to ablate highly aggressive tumors while sparing healthy tissue. A further improvement in its remarkable therapeutic index can be achieved by loading the tumor with a high-Z element in order to enhance the deposited dose. In this study, Monte Carlo calculations have been performed to assess the optimum high-Z element in different irradiation configurations. Maximization of the quotient between PVDR in healthy tissue and PVDR in the tumor and minimization of the valley doses in bone and the brain were used as criteria. The optimum element depends on the irradiation configuration used. The best outcome is provided by the highest Z contrast agents studied, i.e., gold and thallium. However, results obtained with lanthanide elements (in particular lutetium) or hafnium are extremely satisfactory in some configurations. Analogous data were obtained for a rat head phantom. This may be useful to transfer preclinical studies to future clinical trials in patients. In the present work, only dosimetric considerations were taken into account, but the final choice on the element and its concentration would also depend on the degree of cytotoxicity.

ACKNOWLEDGMENTS

The authors would like to thank the support given by the ESRF, in particular to A. Bravin, G. Le Duc, and E. Bräuer-Krisch from the ID17 team. Thanks to T. Nawroth (University of Mainz, Germany), S. Roux (Université Claude Bernard Lyon 1, France), O. Tillement (Université Claude Bernard Lyon 1, France), and S. Gil (Universitat Autònoma de Barcelona, Spain) for scientific discussions. Special thanks to J. Sempau (INTE, Universitat Politècnica de Catalunya, Spain) and J. M. Fernández-Varea (Universitat de Barcelona, Spain) for their continuous help in the use of PENELOPE.

[a]Electronic mail: prezado@esrf.fr

[1]A. R. Kagan, R. J. Steckel, P. Cancilla, G. Juillard, and T. Patin, "The pathogenesis of brain necrosis: Time and dose parameters," Int. J. Radiat. Oncol. Biol. Phys. **1**, 729–732 (1977).
[2]R. Stupp *et al.*, "Effects of radiotherapy with concomitant and adjuvant temozolomide versus radiotherapy alone on survival in glioblastoma in a randomised phase III study: 5-year analysis of the EORTC-NCIC trial," Lancet Oncol. **10**, 459–466 (2009).
[3]H. J. Curtis, "The use of a deuteron microbeam for simulating the biological effects of heavy cosmic-ray particles," Radiat. Res. Suppl. **7**, 258–264 (1967).
[4]Y. R. Lawrence, X. A. Li, I. El Naqa, C. A. Hahn, L. B. Marks, T. E. Merchant, and A. P. Dicker, "Radiation dose-volume effects in the brain," Int. J. Radiat. Oncol. Biol. Phys. **76**, S20–S27 (2010).
[5]E. Sieghban, J. Stepanek, E. Bräuer-Krisch, and A. Bravin, "Determination of dosimetrical quantities used in microbeam radiation therapy (MRT) with Monte Carlo simulations," Med. Phys. **33**, 3248–3259 (2006).
[6]J. Stepanek, H. Blattmann, J. A. Laissue, N. Lyubimova, M. Di Michiel, and D. N. Slatkin, "Physics study of microbeam radiation therapy with PSI-version of Monte Carlo code GEANT as a new computational tool," Med. Phys. **27**, 1664–1675 (2000).
[7]J. Spiga, E. A. Siegbahn, E. Bräuer-Krisch, P. Randaccio, and A. Bravin, "The GEANT4 toolkit for microdosimetry calculations: Application to microbeam radiation therapy (MRT)," Med. Phys. **34**, 4322–4330 (2007).
[8]Y. Prezado, S. Thengumpallil, M. Renier, and A. Bravin, "X-ray energy optimization in minibeam radiation therapy," Med. Phys. **36**, 4897–4902 (2009).
[9]I. Martínez-Rovira, J. Sempau, J. M. Fernández-Varea, A. Bravin, and Y. Prezado, "Monte Carlo dosimetry for forthcoming clinical trials in x-ray microbeam radiation therapy," Phys. Med. Biol. **55**, 4375–4388 (2010).
[10]F. A. Dilmanian *et al.*, "Response of rat intracranial 9L gliosarcoma to microbeam radiation therapy," Neuro Oncol. **4**, 26–38 (2002).
[11]J. A. Laissue *et al.*, "The weanling piglet cerebellum: A surrogate for tolerance to MRT (microbeam radiation therapy) in pediatric neuro-oncology," SPIE **4508**, 65–73 (2001).
[12]N. Zhong, G. M. Morris, T. Bacarian, E. M. Rosen, and F. A. Dilmanian, "Response of rat skin to high-dose unidirectional x-ray microbeams: A histological study," Radiat. Res. **160**, 133–142 (2003).
[13]F. A. Dilmanian, Z. Zhong, T. Bacarian, H. Benveniste, P. Romanelli, R. Wang, J. Welwart, T. Yuasa, E. M. Rosen, and D. J. Anschel, "Interlaced x-ray microplanar beams: A radiosurgery approach with clinical potential," Proc. Natl. Acad. Sci. U.S.A. **103**, 9709–9714 (2006).
[14]R. Serduc *et al.*, "Characterization and quantification of cerebral edema induced by synchrotron x-ray microbeam radiation therapy," Phys. Med. Biol. **53**, 1153–1166 (2008).
[15]A. Bouchet *et al.*, "Preferential effect of synchrotron microbeam radiation therapy on intracerebral 9L gliosarcoma vascular networks," Int. J. Radiat. Oncol. Biol. Phys. **78**, 1503–1512 (2010).
[16]P. Régnard *et al.*, "Irradiation of intracerebral 9L gliosarcoma by a single array of microplanar x-ray beams from a synchrotron: balance between curing and sparing," Phys. Med. Biol. **53**, 861–878 (2008).
[17]J. A. Laissue *et al.*, "Neuropathology of ablation of rat gliosarcomas and contiguous brain tissues using a microplanar beam of synchrotron-wiggler-generated X rays," Int. J. Cancer **78**, 654–660 (1998).
[18]H. M. Smilowitz *et al.*, "Synergy of gene-mediated immunoprophylaxis and microbeam radiation therapy for advanced intracerebral rat 9L gliosarcomas," Neuro Oncol. **78**, 135–143 (2006).
[19]R. Serduc, E. Brauer-Krisch, A. Bouchet, L. Renaud, T. Brochard, A. Bravin, J. A. Laissue, and G. Le Duc, "First trial of spatial and temporal fractionations of the delivered dose using synchrotron microbeam radiation therapy," J. Synchrotron Radiat. **16**, 587–590 (2009).
[20]F. A. Dilmanian, G. Morris, N. Zhong, T. Bacarian, J. F. Hainfeld, J. Kalef-Ezra, L. J. Brewington, J. Tammam, and E. M. Rosen, "Murine EMT-6 carcinoma: High therapeutic efficacy of microbeam radiation therapy," Radiat. Res. **159**, 632–641 (2003).
[21]M. Miura, H. Blattmann, E. Bräuer-Krisch, A. Bravin, A. L. Hanson, M. M. Nawrocky, P. L. Micca, D. N. Slatkin, and J. A. Laissue, "Radiosurgical palliation of aggressive murine SCCVII squamous cell carcinomas using synchrotron-generated X-ray microbeams," Br. J. Radiol. **79**, 71–75 (2006).
[22]F. A. Dilmanian, G. M. Morris, and J. F. Hainfeld, "Methods for implementing microbeam radiation therapy," Patent no. US 2006/0176997. Last accessed March 20, 2007.
[23]P. Régnard *et al.*, "Enhancement of survival of 9L gliosarcoma bearing rats following intracerebral delivery of drugs in combination with microbeam radiation therapy," Eur. J. Radiol. **68**, 151–155 (2008).
[24]L. S. Yasui, C. Andorf, L. Schneider, T. Kroc, A. Lennox, and K. R. Saroja, "Gadolinium neutron capture in glioblastoma multiforme cells," Int. J. Radiat. Biol. **84**, 1130–1139 (2008).
[25]M. Koudelkova, H. Vinsova, and V. Jedinakova-Krizova, "Characterisation of Ho-DTPA and Y-DTPA complexes by capillary isotachophoresis and TLC with radiometric detection," Czech. J. Phys. **53**, A769–A775 (2003).
[26]T. Nawroth *et al.*, "Nano-IRT: Indirect radiation therapy development with target nanoparticles," *Proceeding of the workshop New prospects for*

brain tumour radiotherapy: Synchrotron light and Microbeam Radiation Therapy (Grenoble, France, 2008).
[27]J. F. Hainfeld, D. N. Slatkin, and H. M. Smilowitz, "The use of gold nanoparticles to enhance radiotherapy in mice," Phys. Med. Biol. **49**, 309–315 (2004).
[28]J. F. Hainfeld, F. A. Dilmanian, Z. Zhong, D. N. Slatkin, J. A. Kalef-Ezra, and H. M. Smilowitz, "Gold nanoparticles enhance the radiation therapy of a murine squamous cell carcinoma," Phys. Med. Biol. **55**, 3045–3059 (2010).
[29]J. F. Adam, H. Elleaume, A. Joubert, M. C. Biston, A. M. Charvet, J. Balosso, J. F. Le Bas, and F. Estève, "Synchrotron radiation therapy of malignant brain glioma loaded with an iodinated contrast agent: First trial on rats bearing F98 gliomas," Int. J. Radiat. Oncol. Biol. Phys. **57**, 1413–1426 (2003).
[30]J. F. Adam, M. C. Biston, A. Joubert, A. M. Charvet, J. F. Le Bas, F. Estève, and H. Elleaume, "Enhanced delivery of iodine for synchrotron stereotactic radiotherapy by means of intracarotid injection and blood–brain barrier disruption: Quantitative iodine biodistribution studies and associated dosimetry," Int. J. Radiat. Oncol. Biol. Phys. **61**, 1173–1182 (2005).
[31]Y. Cheng, A. C. Samia, J. D. Meyers, I. Panagopoulos, B. Fei, and C. Burda, "Highly efficient drug delivery with gold nanopaticle vectors for in vivo photodynamic therapy of cancer," J. Am. Chem. Soc. **130**, 10643–10647 (2008).
[32]J. F. Hainfeld, D. N. Slatkin, F. A. Dilmanian, and H. M. Smilowitz, "Radiotherapy enhancement with gold nanoparticles," J. Pharm. Pharmacol. **60**, 977–985 (2008).
[33]R. Santos Mello, H. Callisen, J. Winter, A. R. Kagan, and A. Norman, "Radiation dose enhancement in tumors with iodine," Med. Phys. **10**, 75–78 (1983).
[34]A. Norman, M. Ingram, R. G. Skillen, D. B. Freshwater, K. S. Iwamoto, and T. Solberg, "X-ray phototherapy for canine brain masses," Radiat. Oncol. Investig. **5**, 8–14 (1997).
[35]A. V. Mesa, A. Norman, T. D. Solberg, J. J. Demarco, and J. B. Smathers, "Dose distributions using kilovoltage x-rays and dose enhancement from iodine contrast agents," Phys. Med. Biol. **44**, 1955–1968 (1999).
[36]H. Sjöholm, K. Ljunggren, R. Adeli, A. Brun, C. Ceberg, S. E. Strand, and L. G. Salford, "Necrosis of malignant gliomas after intratumoral injection of Thallium-201 in vivo in the rat," Anticancer Drugs **6**, 109–114 (1995).
[37]K. Ljunggren, X. Liu, K. Erlandsson, M. Ljungberg, L. G. Salford, and S. E. Strand, "Absorbed dose distribution in glioma tumors in rat brain after therapeutic intratumoral injection of 201Tl-chloride," Cancer Biother. Radiopharm. **19**, 562–569 (2004).
[38]Nanobiotix (www.nanobiotix.com).
[39]S. H. Cho, "Estimation of tumour dose enhancement due to gold nanoparticles during typical radiation treatments: A preliminary Monte Carlo study," Phys. Med. Biol. **50**, N163–N173 (2005).
[40]F. Verhaegen, B. Reniers, F. Deblois, S. Devic, J. Seuntjens, and D. Hristov, "Dosmetric and microdosimetric study of contrast-enhanced radiotherapy with kilovolt x-rays," Phys. Med. Biol. **50**, 3555–3569 (20005).
[41]M. Edouard, D. Broggio, Y. Prezado, F. Estève, H. Elleaume, and J. F. Adam, "Treatment plans optimization for contrast-enhanced synchrotron stereotactic radiotherapy," Med. Phys. **37**, 2445–2456 (2010).
[42]S. J. McMahon, M. H. Mendenhall, S. Jain, and F. Currell, "Radiotherapy in the presence of contrast agents: A general figure of merit and its application to gold nanoparticles," Phys. Med. Biol. **53**, 5635–5651 (2008).
[43]Y. Prezado, G. Fois, G. Le Duc, and A. Bravin, "Gadolinium dose enhancement studies in microbeam radiation therapy," Med. Phys. **36**, 3568–3574 (2009).
[44]G. Gokeri, C. Kocar, and M. Tombakoglu, "Monte Carlo simulation of microbeam radiation therapy with an interlaced irradiation geometry and Au contrast agent in a realistic head phantom," Med. Phys. Biol. **55**, 7469–7487 (2010).
[45]E. Bräuer-Krisch, H. Requardt, T. Brochard, G. Berruyer, M. Renier, J. A. Laissue, and A. Bravin, "New technology enables high precision multislit collimators for microbeam radiation therapy," Rev. Sci. Instrum. **80**, 0743011–0743016 (2009).
[46]B. P. Poncelet, V. J. Wedeen, R. M. Weisskoff, and M. S. Cohen, "Brain parenchyma motion: Measurement with cine echo-planar MR imaging," Radiology **185**, 645–651 (1992).
[47]F. Salvat, J. M. Fernández-Varea, and J. Sempau, *PENELOPE 2008, a Code System for Monte Carlo Simulation of Electron and Photon Transport* (OECD Nuclear Energy Agency, Issy-les-Moulineaux, France, 2008).
[48]J. Sempau, E. Acosta, J. Baró, J. M. Fernández-Varea, and F. Salvat, "An algorithm for Monte Carlo simulation of coupled electron-photon transport," Nucl. Instrum. Methods B **132**, 377–390 (1997).
[49]J. Sempau and A. Badal, "PenEasy, a modular main program and voxelised geometry package for PENELOPE," (http://www.upc.edu/inte/downloads/penEasy.htm).
[50]J. Sempau, A. Sánchez-Reyes, F. Salvat, H. Oulad ben Tahar, S. B. Jiang, and J. M. Fernández-Varea, "Monte Carlo simulation of electron beams from an accelerator head using PENELOPE," Phys. Med. Biol. **46**, 1163–1186 (2001).
[51]J. M. Fernández-Varea, P. Carrasco, V. Panettieri, and L. Brualla, "Monte Carlo based water/medium stopping-power ratios for various ICRP and ICRU tissues," Phys. Med. Biol. **52**, 6475–6483 (2007).
[52]B. A. Faddegon, M. Asai, J. Perl, C. Ross, J. Sempau, J. Tinslay, and F. Salvat, "Benchmarking of Monte Carlo simulation of bremsstrahlung from thick targets at radiotherapy energies," Med. Phys. **35**, 4308–4317 (2008).
[53]D. E. Cullen, J. H. Hubbell, and L. Kissel, "EPDL97: The evaluated photon data library, 97 version," Report UCRL-50400 vol. 6 (Lawrence Livermore Nation Laboratory, Livermore, 1997).
[54]O. K. Harling, K. A. Roberts, D. J. Moulin, and R. D. Rogus, "Head phantoms for neutron capture therapy," Med. Phys. **22**, 579–583 (1995).
[55]C. Boudou, J. Balosso, F. Estève, and H. Elleaume, "Monte Carlo dosimetry for synchrotron stereotactic radiotherapy of brain tumours," Phys. Med. Biol. **50**, 4841–4851 (2005).
[56]Y. Prezado, G. Fois, M. Edouard, C. Nemoz, M. Renier, H. Requardt, F. Estève, J. F. Adam, H. Elleaume, and A. Bravin, "Biological equivalent dose studies for dose escalation in stereotactic synchrotron radiation therapy clinical trials," Med. Phys. **36**, 725–733 (2009).
[57]H. Nettelbeck, G. J. Takacs, M. L. F. Lerch, and A. B. Rosenfeld, "Microbeam radiation therapy: A Monte Carlo study of the influence of the source, multislit collimator, and beam divergence on microbeams," Med. Phys. **36**, 447–456 (2009).
[58]J. Sempau and P. Andreo, "Configuration of the electron transport algorithm of PENELOPE to simulate ion chambers," Phys. Med. Biol. **51**, 3533–3548 (2006).
[59]S. M. Bentzen, L. S. Constine, J. O. Deasy, A. Eisbruch, A. Jackson, L. B. Marks, R. K. Ten Haken, and E. D. Yorke, QUANTEC: Quantitative analyses of normal tissue effects in the clinic," Int. J. Radiat. Oncol. Biol. Phys. **76**, S1–S160 (2010).

2.5 Paper III and IV: Monte Carlo-based treatment planning system calculation engine for MRT

Introduction

Accurate dose calculations in a 'virtual' model of the patient (typically extracted from computer tomography (CT) data) are required to treat patients in RT. This is done by what is called a treatment planning system (TPS).

The distinct features of MRT (beam generation, machine geometry, energy range, micrometre-sized fields, etc.) with respect to conventional linacs (see figure 1.2 and section 1.3) have required the development of a dedicated TPS. In particular, a MC-based dose calculation engine was developed and benchmarked experimentally in this thesis. It will constitute an essential tool for future MRT clinical trials.

International Reports [ICRU-24 1976, ICRU-42 1987, AAPM-85 2004] reflected that an accuracy of around ±2–5% is needed in the delivery of absorbed dose to the target volume if the eradication of the primary tumour is sought. Due to the slope of the TCP and NTCP curves, a dose error of 5% might lead to a TCP change of 10–20% and to even larger NTCP changes [AAPM-85 2004]. Since MC results yield the highest possible dose calculation accuracy [Reynaert 2007], this was the method of choice for the MRT TPS calculation engine (PENELOPE/PENEASY code, see section 1.5.4.1). A scheme of this work, which was divided into two papers (III and IV), is presented in figure 2.1.

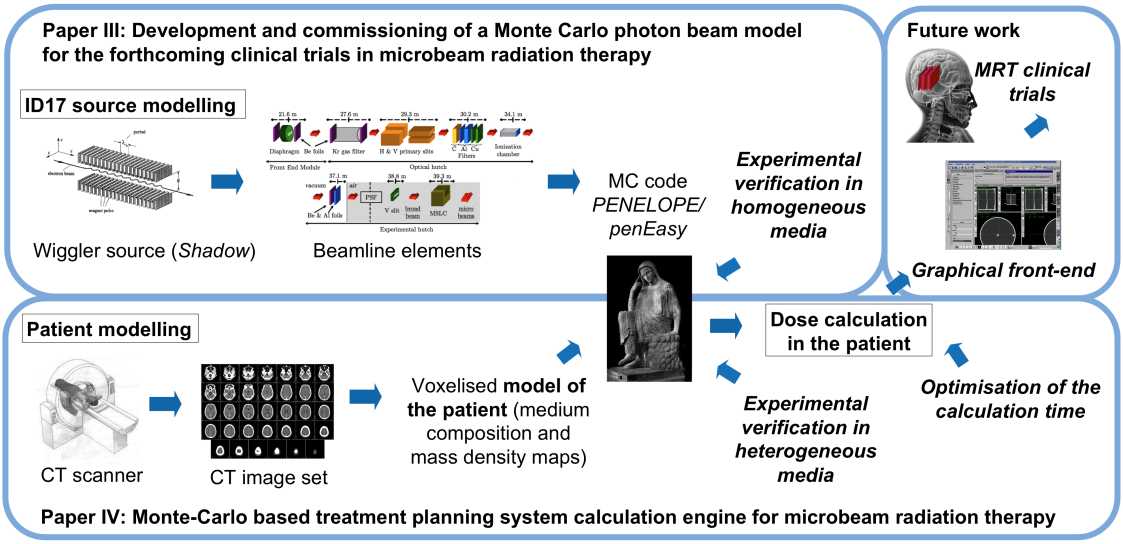

Figure 2.1: *Scheme of the MC-based TPS calculation engine for MRT.*

Whereas statistical uncertainties due to the limited number of histories can be reduced by increasing the simulation time, inaccuracies coming from approximations used in cross section libraries or in beam modelling are not always easily predictable. The first source of uncertainties is typically considered negligible [Fraass 2003]. In order to reduce the uncertainties arising from the beam model, the first objective consisted of the development of precise and realistic modelling of the radiation source (paper III), in contrast to the simplified models used in previous MC studies (see section 1.5.2). In particular, the ID17 x-ray source was modelled by the synchrotron ray-tracing code SHADOW (see section 1.3.3.1). The MC simulation code PENELOPE/PENEASY was employed to transport the photon beam from the source to the patient position through the beamline. The phase-space state variables of the particles reaching the patient position were saved in a phase-space file (PSF). The information contained in this PSF was used as an input to generate a photon beam model.

Computed dose distributions from photons sampled according to probability distributions derived from the beam model were experimentally verified by using HD-810 radiochromic films [ISP® 2012] analysed with a microdensitometer (see section 1.5.4.2). The benchmarking process (both in homogeneous and heterogeneous media) was essential in order to assess both the performance of the photon source model and the TPS calculation engine [IAEA-TRS-430 2004].

The second part (paper IV) reports the use of the photon model to perform dose calculations in a voxelised model of the patient. To this end, the decoupling of the CT image voxel grid (size in the order of mm^3) to the dose bin grid, which has micrometre-sized dimensions in the direction transversal to the microbeams, was required. Since the calculation of such small voxels demands high computation times, work on optimising the simulation efficiency was also carried out by using variance-reduction (VR) techniques and parallelisation of the simulations, among other methods.

Both publications are presented in this section.

Development and commissioning of a Monte Carlo photon beam model for the forthcoming clinical trials in microbeam radiation therapy

I. Martínez-Rovira
ID17 Biomedical Beamline, European Synchrotron Radiation Facility (ESRF), B.P. 220, 6 rue Jules Horowitz, F-38043 Grenoble Cedex, France and Institut de Tècniques Energètiques, Universitat Politècnica de Catalunya, Diagonal 647, E-08028 Barcelona, Spain

J. Sempau
Institut de Tècniques Energètiques, Universitat Politècnica de Catalunya, Diagonal 647, E-08028 Barcelona, Spain

Y. Prezado[a)]
ID17 Biomedical Beamline, European Synchrotron Radiation Facility (ESRF), B.P. 220, 6 rue Jules Horowitz, F-38043 Grenoble Cedex, France

(Received 21 June 2011; revised 7 November 2011; accepted for publication 11 November 2011; published 12 December 2011)

Purpose: A new radiotherapy technique, named microbeam radiation therapy (MRT), is under development at the ID17 Biomedical Beamline of the European Synchrotron Radiation Facility (ESRF). This innovative method is based on the fact that normal tissue can withstand high radiation doses in small volumes without any significant damage. The promising results obtained in the preclinical studies have paved the way to forthcoming clinical trials, which are currently in preparation. Highly accurate dose calculations at the treatment planning stage are required in this context. The aims of this study are the development and experimental benchmarking of a photon beam source model, which will be the core of the future MRT treatment planning system (TPS).
Methods: The ID17 x-ray source was modeled by the synchrotron ray tracing code SHADOW. The Monte Carlo (MC) simulation code PENELOPE/PENEASY was employed to transport the photon beam from the source to the patient position through all the beamline components. The phase-space state variables of the particles reaching the patient position were used as an input to generate a photon beam model. Computed dose distributions in a homogeneous media were experimentally verified by using Gafchromic® films in a solid–water phantom. Benchmarking was split into two phases. First, the lateral dose profiles and the percentage depth-dose (PDD) curves in the broad beam configuration were considered. The acceptability criteria for radiotherapy dose computations recommended by international protocols such as the Technical Reports Series 430 (TRS 430) of the International Atomic Energy Agency (IAEA) were used. Second, the analogous dosimetric magnitudes in MRT irradiations, i.e., PDD of the central microbeam and the corresponding peak-to-valley dose ratios (PVDR) were evaluated and compared with MC calculations.
Results: A full characterization of the ID17 Biomedical Beamline (ESRF) synchrotron x-ray source and the development of an accurate photon beam model were achieved in this work. Calculated and experimental dose distributions agreed to within the recommended acceptability criteria described in international codes of practice (TRS 430) for broad beam irradiations. The overall deviation in low gradient areas amounted to 2%–3%. The maximum distance-to-agreement in high gradient regions was lower than 0.7 mm. MC calculations also reproduced MRT experimental results within uncertainty bars. These results validate the photon beam model for its use in MRT radiation therapy calculations.
Conclusions: The first MC synchrotron photon beam model for MRT irradiations that reproduces experimental dose distributions in homogeneous media has been developed. This beam model will constitute an essential component of the TPS calculation engine for patient dose computation in forthcoming MRT clinical trials. [DOI: 10.1118/1.3665768]

Key words: synchrotron radiation, microbeam radiation therapy, Monte Carlo simulations, clinical trials

I. INTRODUCTION

Microbeam radiation therapy (MRT) is a new radiation therapy method that uses synchrotron radiation. This innovative technique is under development at the National Synchrotron Light Source (NSLS) in Upton, USA, and at the European Synchrotron Radiation Facility (ESRF) in Grenoble, France. The ultimate goal is the treatment of inoperable brain tumors with especial emphasis on gliomas. MRT irradiation is performed by means of an array of intense parallel x-ray microbeams (25–50 μm wide) with a 200–400 μm center-to-

center (c-t-c) distance. The microbeams are produced by a multislit collimator (MSLC), which fractionates the beam in the horizontal direction.[1] The resulting dose profiles consist of a pattern of peaks and valleys, i.e., with high doses in the microbeam paths and low doses in the spaces between them.[2] The minimum dose in the central region between two microbeams is named the valley dose and the dose at the center of the microbeam is the peak dose.

MRT has several interesting properties which seem to challenge many of the current paradigms in conventional radiation therapy. Healthy tissue exhibits an exceptional resistance to very high doses ($\geq$100 Gy) in one fraction.[3–10] In addition, malignant tissue mass appears to respond to MRT by significant growth delay and, in some cases, complete tumor ablation.[11–15] despite the small fraction of tumor mass irradiated with the high-dose microbeams.

The biological mechanisms following MRT irradiation are not yet fully understood. The preferential effect on malignant tissue has been mainly attributed to selective effects of microbeams on immature tumor vessels versus a lack of microbeam effects on the differentiated normal vasculature,[12] although other factors might be operative.[10] In addition, it has been hypothesized that the sparing effect in healthy tissue along the beam paths is due to rapid biological repair of the microscopic lesions by the minimally irradiated cells contiguous to the irradiated tissue slices.[4,12] Dilmanian *et al.*[12] showed that the sparing effect of MRT seems to depend mostly on the valley dose. The brain-sparing effect (measured by the onset of the appearance of white matter necrosis) vanishes only when the valley dose approaches the tissue tolerance to broad beams. Animal experiments carried out indicate that both valley doses and the peak-to-valley dose ratio (PVDR) are relevant parameters as regards radiobiological response.

Following the success of preclinical studies, the Biomedical Beamline ID17 of the ESRF is proceeding toward clinical trials on pets,[16,17] which, if successful, may lead to clinical administration of MRT to humans. Such an implementation demands a precise MRT dose computation.

There is strong evidence that an accuracy of $\pm$2%–5% in dose delivery is required to effectively treat certain types of cancers and to reduce complications, as reflected in the 24 and 42 reports of the International Commission on Radiation Units and Measurements (ICRU).[18,19] In order to minimize discrepancies between the calculated dose distributions at the treatment planning stage and those delivered to the patient, precise dose computation methods are required. Monte Carlo (MC) simulations are considered to be the most accurate approach[20–22] for particle transport, and thus, it will be the method used in this study. Whereas statistical uncertainties can be reduced by increasing the number of simulated histories, systematic inaccuracies coming from approximations used in physical models, geometrical descriptions, etc. are not always easily predictable. Hence, precise and realistic modeling of the radiation source is a fundamental requirement in MC radiation therapy calculations.

Simplification of the real irradiation source geometry is a common practice adopted by authors of theoretical MRT studies. Thus, identical, parallel, perfectly rectangular microbeams are usually considered.[2,23–29] The dose distribution of a single microbeam is simulated and a superposition algorithm is used in order to generate the dose profile of the complete array. These simplifications fail to account for the source size and shape, the beam divergence along the distance from the synchrotron source to the patient position or any geometrical and scattering effect arising from the radiation transport through the beamline. Nettelbeck *et al.*[30] showed, by using simple models, that these approximations can lead to inaccuracies in the valley doses, penumbral regions of dose profiles and in the PVDR. If beam divergence is included, there is an increase of 26% in the penumbra region and 10% in the valley doses.[30] Modeling of a synchrotron-distributed source rather than a point source resulted in almost a 30% larger penumbral dose.[30] In addition, the effect of linear polarization of the synchrotron beam was partially accounted for in the work of De Felici *et al.*[25] and it appeared to be non negligible. This could explain part of the discrepancies between measured and calculated valley doses presented in previous MRT studies.[28,31] In both cases, 25 μm-wide microbeams spaced by 200 μm were considered. A MOSFET detector was used in the work of Siegbahn *et al.*[28] MC simulations estimated PVDR values up to 50% higher than experimental data; the main source of discrepancies between measured and simulated doses was attributed to the energy dependence response of the MOSFET detector. The work of Crosbie *et al.*[31] presented film dosimetry compared with different MC values previously published. Differences up to 50% were also reported.

Due to the aforementioned reasons and within the framework of the forthcoming clinical trials preparation, the development of both an accurate and reliable synchrotron beam model is essential. Therefore, full characterization of the ID17 Biomedical Beamline (ESRF) photon source beam, its modeling and benchmarking with experimental data has been addressed in this work. The beam model will constitute an essential component of the calculation engine of the future MRT treatment planning system (TPS). A complete set of both MC and experimental dosimetric data for the MRT clinical trial irradiation conditions (50 μm-wide microbeams spaced by 400 μm) is reported for the first time.

II. MATERIALS AND METHODS

II.A. ESRF ID17 Biomedical Beamline source

The ESRF is a third-generation synchrotron with a 6.04 GeV electron storage ring. The x-ray source differs from medical linear accelerators in photon generation, type and dimensions of beam modifiers, intensity, energies, etc. In third-generation synchrotron sources, extremely bright synchrotron radiation is produced when the trajectories of the accelerated (relativistic) electrons are deflected at the so-called insertion devices (ID), which consist of arrays of magnets. Synchrotron radiation (SR) is emitted in a narrow cone with a typical natural opening angle of about $1/\gamma$ (rad). The Lorenz factor (γ) can be expressed as $\gamma = 1 + E/(mc^2)$, where E is the kinetic energy of the electron, m is the rest mass of the electron and c is the

TABLE I. ESRF storage ring electron beam parameters and ID17 wiggler characteristics (Ref. 33).

ESRF electron beam parameters	
Electron energy	6.04 GeV
Maximum current	0.2 A
Horizontal emittance	3.9 nm
Vertical emittance	0.039 nm
RMS horizontal source size[a]	57 μm
RMS vertical source size[a]	10.3 μm
ID17 wiggler parameters	
Magnetic field period λ_u	15 cm
Number of periods	11
Gap (for the MRT irradiation conditions)	2.48 cm
Maximum magnetic field B (gap = 2.48 cm)	1.592 T
Deflection parameter $K = 0.934B[\mathrm{T}]\lambda_u$ (cm)	22.30

[a]Root mean square (RMS) source size at the ID17 wiggler position

speed of light in vacuum. The vertical and horizontal divergences of the SR beam are $2\gamma^{-1}$ and $2K\gamma^{-1}$ (rad), respectively.[32] The deflection parameter K describes the electron motion in an ID and can be expressed as

$$K = 0.934\, B[\mathrm{T}]\lambda_u[\mathrm{cm}], \quad (1)$$

where B is the magnetic field (in T), which depends on the wiggler gap (see below), and λ_u is the magnetic field period (in cm).[32]

The ID type at the ID17 Biomedical Beamline is a wiggler. In this kind of ID, the horizontal divergence is much larger than the natural opening angle of SR (K is large) and the radiation emitted at each pole adds incoherently. Table I reports the parameters of the ESRF storage ring electron beam and of the ID17 wiggler. These characteristics determine the properties of the generated SR beam, which traverses different types of beam modifiers, such as slits, filters, etc. (see Fig. 1). The main features of the ID17 beam modifiers are reported in Table II.

Targets are placed on a three-axis Kappa-type high-precision goniometer (Huber, Germany),[17] located 40.5 m downstream from the wiggler center. The maximum achievable horizontal and vertical dimensions of the beam at the patient position are 4.1 and 0.25 cm, respectively. In order to fill the desired vertical irradiation field size, targets are vertically scanned at constant speed (in the range between 10 and 100 mm/s). The chosen speed depends on the desired dose, beam current, and vertical slit size. This scanning method is equivalent to a broad beam irradiation.[34]

The irradiation modality depends on the presence or absence of the multislit collimator.[1] If the MSLC is not in the beam path, the irradiation corresponds to a seamless field irradiation, hereafter named broad beam. If the MSLC is in the beam path, an MRT irradiation is carried out. The synchrotron high-dose rate (13 440 Gy/s for the maximum electron current) provides a fast irradiation and minimizes cardiosynchronous motion effects in the brain.[35] This, along with the low beam divergence, allows the production of sharply defined beam edges. The MRT irradiation parameters used in this study correspond to those fixed in the forthcoming MRT clinical trials, i.e., 50 μm-wide microbeams with a c-t-c of 400 μm.

II.B. Simulation codes: SHADOW and PENELOPE

Two simulation codes were used: SHADOW and PENELOPE/PENEASY. The synchrotron ray tracing code SHADOW was employed to generate particles emerging from the ID17 wiggler.[36–39] SHADOW considers wigglers as a series of pseudobending magnets. The code uses MC methods to sample photon emission along a realistic electron trajectory inside the wiggler, which includes the electron beam emittance. The ESRF and ID17 wiggler parameters (Table I) were required as an input for the simulations. The phase-space state variables of the photons exiting the ID17 wiggler, i.e., energy, spatial position, direction of flight, and polarization state were obtained as the output.

The transport of photons from the wiggler to the patient position was performed with the MC code PENELOPE v. 2008,[40,41] which allows the simulation of the coupled transport of electrons, photons, and positrons in a wide energy range and in arbitrary material systems. The two codes were directly linked by inserting a new source model into the general-purpose main program for PENELOPE named PENEASY.[42] This methodology can be easily extended to any other synchrotron source by changing the electron beam and wiggler parameters and the geometry of the beamline modifiers.

The final photon beam spectrum at the patient position exhibits a continuous distribution with a range from 27 keV

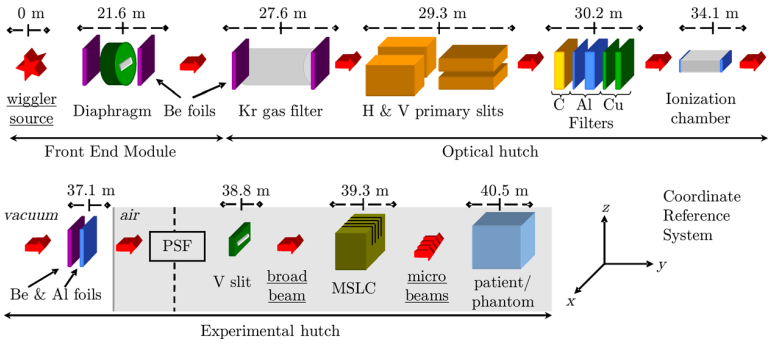

FIG. 1. Scheme of the ID17 beamline elements from the wiggler to the patient position (not to scale).

TABLE II. Description of the ID17 beamline elements.

Beamline element	Distance to wiggler	Main characteristics
Diaphragm	21.6 m	Avoidance of heat load, maximum field size definition (H × V: 2.4 × 0.15 cm^2)
Be window	Several	Separation between vacuum sections (thickness: 300–500 μm)
Kr gas filter	27.6 m	Beam attenuation
Primary slits	29.3 m	Delimitation of the field size at patient position (aperture variable)
C, Al, and Cu filters	30.2 m	Elimination of low-energy photons
Ionization chamber	34.1 m	Monitoring of the beam (Al foil of 500 μm-thick at the entrance/exit)
Al Foil	37.1 m	Separation between vacuum section and air (thickness: 500 μm)
Vertical slit	38.8 m	Delimitation of the vertical field size (50, 100, or 500 μm) before scanning
Multislit collimator[a]	39.3 m	Generation of an array of 50 μm-wide microbeams spaced by 400 μm

[a]Only in MRT irradiation modality.

to 600 keV and a mean energy of about 100 keV. The most relevant photon interaction mechanisms in this energy range are the photoelectric effect and Compton scattering. Photoelectric cross sections included in the PENELOPE code are interpolated from tabulations of the Evaluated Photon Data Library from the Lawrence Livermore National Laboratory.[43] The Compton cross section is obtained by having recourse to the relativistic impulse approximation, which takes into account both Doppler broadening and binding of the atomic electrons, but does not include many-body and aggregation effects. The scattering of polarized photons is also considered in the simulations.[40] Polarization effects will be especially relevant in our case as synchrotron beams are highly linearly polarized in the electron orbit plane. We shall describe the polarization state of electromagnetic radiation by means of the Stokes parameters (P_1, P_2, P_3),[44] following the convention commonly used in Quantum Mechanics.[40] Thus, P_3 determines linear polarization along the x and z axis, P_2 represents circular (right and left) polarization and P_1 corresponds to polarization in the lines that bisect the x-z plane.

MC simulations with the PENELOPE/PENEASY code were split into different stages. First, the transport of photons up to the vertical slit placed just before the MSLC (at 38.8 m from the wiggler center) was performed. Electron transport was not considered in this part of the simulations as secondary electrons generated from photon interactions in the various beamline elements will not reach the patient position (the range in air for a 100 keV electron is 14 cm). At the vertical slit position, a phase-space file (PSF) containing the state variables of the photons was generated for each considered horizontal field size (1, 2, and 3 cm).

The code was compiled with the Intel Fortran compiler v. 10.0 and run on a 2.9 GHz Intel Xeon Processor X5670. The simulation time needed to obtain 10^7 photons in the PSF was approximately 7 days. The fraction of photons passing through the diaphragm was 8.8%, while the fraction of particles crossing the primary slits (2 × 0.1 cm^2 field size) was 1.4%. After traversing all the beam modifiers, only 0.04% of the primary photons generated in the wiggler reached the patient position (for a 500 μm vertical slit size). Furthermore, reading particles from the PSF involved some additional processing time. Therefore, a photon source model was developed based on the phase-space distribution of the particles exiting the beamline. This model will be presented in Secs. II E and III A.

Particles sampled from our model were transported up to a water phantom to compute absorbed dose distributions. Dimensions and characteristics of the simulated water phantom are given in Sec II C. Two irradiation modalities were studied: broad beam and MRT. In the latter case, the transport of particles going through the MSLC was performed. The MSLC was carefully modeled following real proportions and chemical composition.[1] For each case, three field sizes were considered: 1 × 1, 2 × 2, and 3 × 3 cm^2. For the broad beam, doses were scored in 0.04 cm voxels in the horizontal and vertical direction of the beam and 0.1 cm in depth. The dose bin size along the horizontal direction was reduced to 5 μm for MRT irradiations.

The simulation parameters for the broad beam calculations were the following. The absorption energies, EABS, were set to 5 keV for photons and 50 keV for electrons. For charged particles, the average angular deflection in a multiple-scattering step, C1, and the maximum average fractional energy loss along that step, C2, were fixed to 0.1; the cutoff energies for the production of hard inelastic, WCC, and hard bremsstrahlung events, WCR, were set equal to electron and photon EABS, respectively.[40,45] The absorption energies in the MRT simulations were reduced to 1 keV for photons and to 10 keV for electrons to account for the reduced beam size in the x direction.

Simulations were discontinued when the average relative statistical uncertainty was less than 1% for the broad beam and less than 2.5% for the MRT simulations (2 standard deviations, 2σ). This uncertainty was calculated as a root mean square average of the uncertainties of the bins with doses above half of the maximum score.

II.C. Relative dosimetry: experimental dose distributions

Percentage depth-dose (PDD) and lateral dose profile curves were measured for several field sizes (1 × 1, 2 × 2, and 3 × 3 cm^2) and for the two irradiation configurations, i.e., broad beam and MRT.

The lateral dose profiles measurements (for broad beam) performed with a thimble ionization chamber [PTW 31010,

0.125 cm^3 (Ref. 46)] in a water tank for horizontal beams [PTW MP3-P T41029 (Ref. 46)] revealed insufficient spatial resolution for this detector system in steep dose gradient regions for the studied field sizes. In addition, the thickness of the water tank entrance window (0.5 cm of PMMA) and the external diameter of the ionization chamber prevented measurements of the PDD curves in depths shallower than 1 cm.

In contrast, Gafchromic® HD-810 films[47] provide the high spatial resolution required to measure lateral dose profiles, including the submillimetre field sizes used in MRT. The broad dose range (from 10 to 400 Gy) also enables PVDR values to be assessed. Gafchromic HD-810 films have already been used successfully to record doses in synchrotron sources[48] and to evaluate PVDR values in MRT.[31] The handling and accurate positioning of this type of radiochromic films in water is very delicate. Thus, the films were placed at different depths (from 0.3 to 10.0 cm) in a RW3 (Goettingen White Water) solid–water slab phantom of dimensions $30 \times 12 \times 30$ cm^3.[46] This phantom allowed the evaluation of PDD curves starting from the surface. Lateral dose profiles were measured up to 4 cm from the center of the field. Each measurement was performed at least twice in order to reduce experimental uncertainties.

For the handling and calibration of the films, the recommendations provided by Task Group 55 of the American Association of Physics in Medicine (AAPM) (Ref. 49) were taken into account. The dose calibration range used went from 10 to 400 Gy (that is the recommended range of use of HD-810 films.[47] The dose in broad beam was measured with a thimble ionization chamber [PTW 31010, 0.125 cm^3 (Ref. 46)] calibrated in kilovoltage x-rays. The calibration curve followed a quadratic polynomial regression $D = c_1\mathrm{OD} + c_2\mathrm{OD}^2$, where D is the dose, OD is the optical density and c_i $(i = 1,2)$ are the unknown fit parameters. Each film box used was calibrated separately. One example of this fitting was $c_1 = 334.91$ and $c_2 = 237.84$, with a correlation coefficient of $R^2 = 0.99998$.

The films receiving broad beam irradiation were analyzed with a flat bed scanner [Epson Perfection V750-M Pro Scanner (Ref. 50)] following the widely used methodology described in the work of Devic *et al.*[51] However, the spatial resolution of this scanner limited its use to performing dosimetry at the micron scale required in MRT. Instead, a microdensitometer (3CS Microdensitometer, J. L. Automation) was employed to read the films. This system has a wide dynamic range (it is sensitive to optical densities OD from 0.2 to 6) and a very high spatial resolution (around 5 μm). The dose assessment was performed by comparing the OD of films irradiated in the broad beam configuration with a well-known dose with the OD of the film under evaluation. The use of this type of system is very time-consuming as the reading speed is very low and the delicate optical and mechanical parts composing the microdensitometer forced us to frequently adjust it to avoid any drift in the system.[52,53] Further details on the working principle of the microdensitometer can be found elsewhere.[54]

For each evaluated point, the measurement was repeated at least two times in different days/run. Moreover, the films were read out a minimum of three times to ensure the reproducibility of the data. Therefore, the measurement uncertainty is taken into account nonuniformities in the films, small differences in beamline alignment in different days, etc.

II.D. Experimental validation of the Monte Carlo simulations

Benchmarking of the MC calculation engine (and especially the beam model) is an essential step toward the final development of a TPS for clinical trials in MRT. Since MRT is a complex technique, this process was divided into two steps. First, a comparison of the calculations and experimental data for broad beam irradiation was performed. Fine tuning of the modeling was then verified for MRT irradiations in a second stage.

The TPS acceptability criteria described in the TRS 430 (Ref. 55) were followed for the broad beam configuration. In particular, the method to quantify differences between MC and experimental data proposed by Venselaar *et al.*[56] was employed. Relative deviations (δ) were evaluated as

$$\delta = \frac{D_{\mathrm{MC},p} - D_{\mathrm{exp},p}}{D_{\mathrm{exp},p}}, \tag{2}$$

where $D_{\mathrm{MC},p}$ and $D_{\mathrm{exp},p}$ are the normalized calculated and experimental dose values at a certain point p, respectively. In addition, an overall confidence limit Δ was defined as

$$\Delta = |\bar{\delta}| + 1.5 s_\delta, \tag{3}$$

where $\bar{\delta}$ is the mean deviation between calculations and measurements for a number of data points p (depending on the region, see next paragraph) and s_δ is the standard deviation of the difference. The factor 1.5 represents a confidence interval of 87%.[56]

Venselaar *et al.*[56] proposed that the recommended acceptability criteria varied as a function of the region of the dose distributions since dose algorithms provide better accuracy in some zones than in others. The different regions and tolerances for homogeneous and simple irradiation geometries are listed.

- Deviations of the points beyond the maximum dose $D_{\max}$ in PDD curves are quantified by δ_1 (or Δ_1) and should take values lower than 2%.
- Deviations of points in the build-up region of PDD curves (from the phantom surface to the depth of the 90% $D_{\max}$ isodose) are described by δ_2 (or Δ_2). In the case of lateral dose profiles, δ_2 (or Δ_2) represents the points in the penumbra region (from 80 to 20% of the dose at the central axis D_{cax}). The maximum recommended deviation between MC and experimental data are 10% or 2 mm, in terms of distance-to-agreement. These values are preferably expressed in millimetres.
- The deviation of the points in the beam (excluding the three central beam axis points) in the lateral dose profiles is quantified by δ_3 (or Δ_3). The acceptability criteria recommend values lower than 3%.
- δ_4 (or Δ_4) indicates the differences between calculations and measurements for points off the geometrical beam

axis in the lateral dose profiles (less than 20% D_{cax}). Due to the inherently low accuracy of dose calculations in this region, deviations are expressed as a percentage of the central axis dose. The maximum recommended value in this case is 3%.

Fine tuning of the MC calculations for the MRT configuration was also verified experimentally by confirming that the respective uncertainty intervals overlap. The central peak and valley doses and the corresponding PVDR values were assessed for each field size at different depths. These are the most relevant dosimetric parameters in this kind of spatially fractionated techniques,[12] and thus, they represent a good estimate of MRT dose calculation performance.

II.E. Photon source characterization

Complete photon source characterization including the phase-space variables, i.e., the energy, spatial position, divergence and polarization state, of the beam at different positions in the beamline is reported in this section. This information was used to generate a photon source model, which will be presented in Sec. III A.

Figure 2 (upper part) shows the top view of the photons generated in the wiggler (left) and the beam cross section at the exit (right). The phase-space representing all possible values of position and divergence at the wiggler exit in the horizontal (x, u) and vertical (z, w) coordinates is plotted at the bottom of the same figure. The full width at half maximum (FWHM) of the distribution of photons along the x and the z coordinates is 0.280 and 0.018 cm, respectively. The phase-space distribution of wiggler radiation as a superposition of contributions from different poles is clearly visible in the (x, u) diagram, where each ellipse corresponds to one pole. In the high-brightness central region, the contribution from different poles intersects.

Photons exiting the wiggler are emitted in a continuum of energies from the infrared to the x-ray region. The highest energies are concentrated on the central part of the beam, while the low-energy content is higher in the outer beam region. The integrated spectrum over the full beam at different beamline positions is plotted in Fig. 3. The maximum photon energy is around 600 keV. Low-energy photons are absorbed by the Kr, C, Al, and Cu filters. At the patient position, the spectrum ranged from 27 to 600 keV with a peak

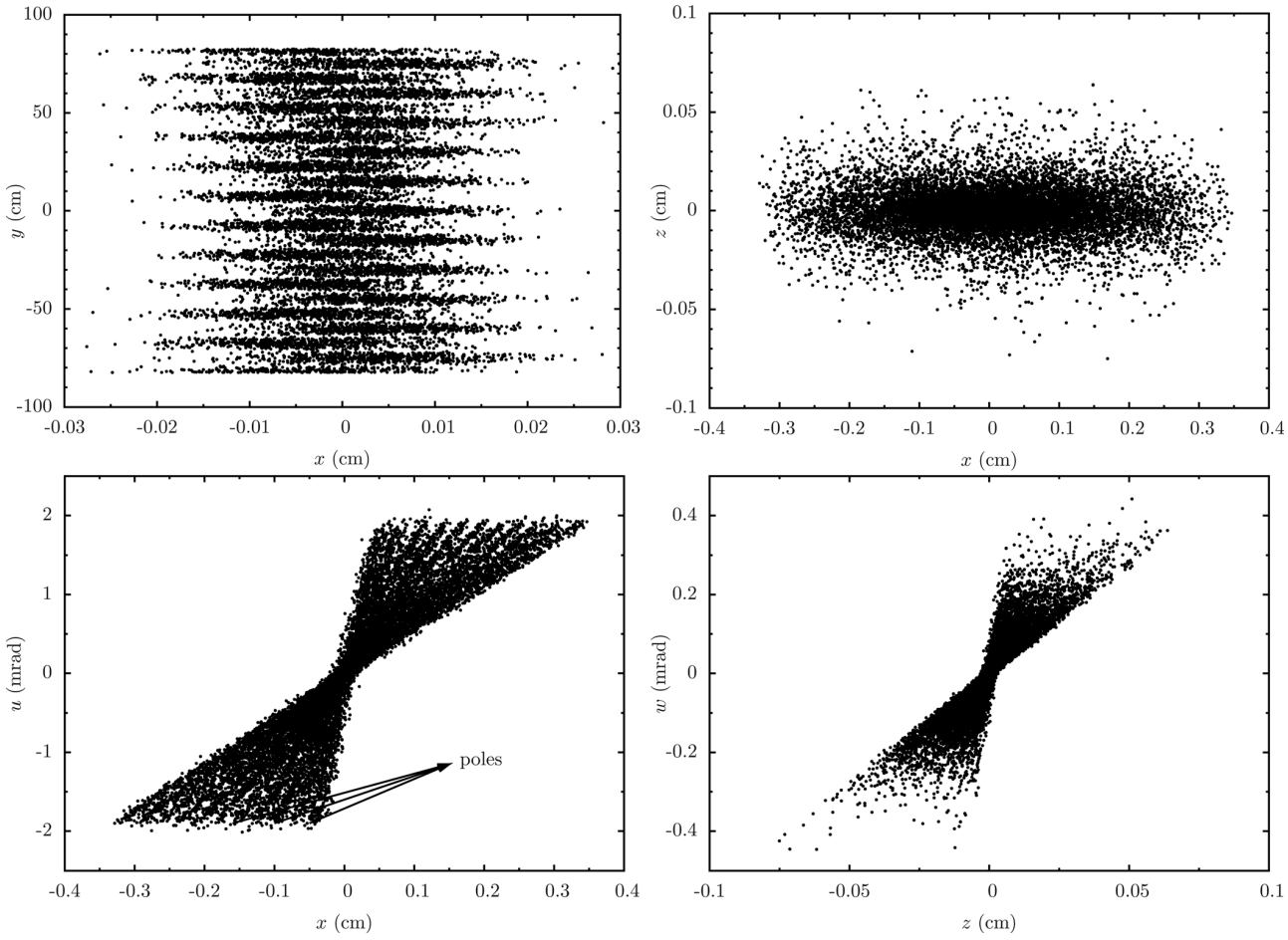

FIG. 2. Top view of the particles generated in the wiggler (top left) and beam cross section at the wiggler exit (top right). Phase-space diagrams in the horizontal (bottom left) and vertical (bottom right) coordinates at the end of the wiggler. Each point represents a photon (each plot contains 14 000 photons).

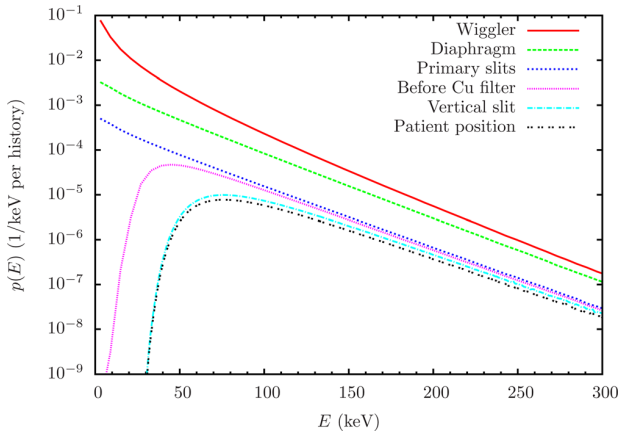

FIG. 3. Integrated spectrum obtained by MC simulation at different beamline locations: at the wiggler exit, after the first diaphragm, after the primary slits (2×0.1 cm^2 field size at the patient position), before the Cu filter, before the vertical slit position and at the patient position (500 μm vertical slit size). The final energy spectrum ranges from 27 to 600 keV with a mean energy at 99 keV. The fraction of photons with energies higher than 300 keV is very small (0.1%).

energy at 75 keV. The mean energy was 99 keV. The final fraction of photons with energies higher than 300 keV was very small (0.1%).

Another relevant property of synchrotron light is its polarization. Figure 4 shows the P_3 values in terms of the vertical divergence (w) at the patient position. Negative values correspond to a linear polarization in the horizontal plane according to our reference system. Therefore, the beam is highly linearly polarized in the horizontal direction as 95% of the photons have P_3 values between -0.98 and -1. The lowest P_3 values were encountered in the outer part of the beam.

One can quantify the degree of linear polarization (DOPL) in terms of the Stokes parameters (defined in Sec. II B) as

$$\mathrm{DOPL} = (P_1^2 + P_3^2)^{1/2}. \quad (4)$$

DOPL ranges from zero (nonlinearly polarized light) to one (completely linearly polarized light). Since the skew polarization in a wiggler is zero ($P_1 = 0$), DOPL $= |P_3|$. Table III lists

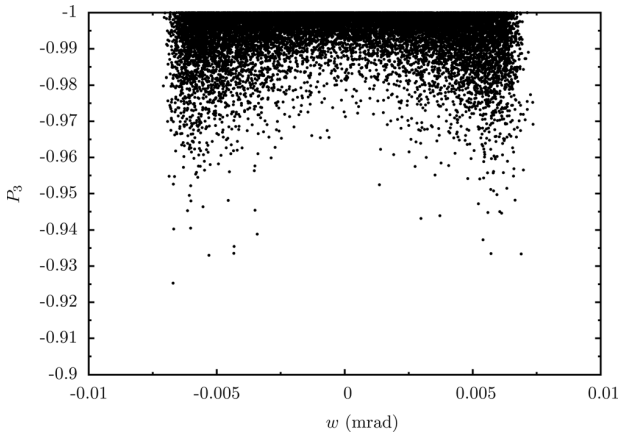

FIG. 4. P_3 values as a function of the vertical divergence (w) at the patient position for 500 μm vertical slit size. Each point corresponds to a photon.

TABLE III. DOPL at different positions in the beamline.

Position	DOPL
Wiggler	0.660
After the first diaphragm	0.952
After the primary slits (vertical field size: 0.1 cm at the patient position)	0.992
Patient position (500 μm vertical slit size)	0.994

DOPL values at different positions in the beamline. The calculated DOPL value at the wiggler exit is low (0.660) as all the photons emerging from the wiggler are considered. However, the beam modifiers progressively cut the external part of the beam and consequently, the polarization reaches a value of 0.992 after the primary slits (0.1 cm vertical field size). At the patient position, DOPL is 0.994, which indicates that the beam is highly linearly polarized along the x axis. DOPL values did not change with the horizontal field size.

Spatial beam features are modified as photons cross the different elements in the beamline. The final horizontal and vertical divergences are approximately 0.5 mrad and 0.02 mrad, respectively, for the standard MRT irradiation conditions. These values are significantly lower than in a conventional linear accelerator (around 35 mrad).

Figure 5 shows the dependence of the phase-space distributions just before the patient position, both in the horizontal and vertical direction. The probability density functions $p(x)$ and $p(z)$ (1/cm per history) are also presented in the insets, which show a homogeneous photon distribution along x and z.

The knowledge of the phase-space variables of the photons at the patient position contained in the PSF and described above allowed us to generate a photon source model (see Sec III A).

III. RESULTS AND DISCUSSION

In this section, the ID17 photon source modeling is described. Comparisons between MC computations and experimental dose distributions in homogeneous media, both for seamless and MRT irradiations, are also presented.

III.A. ID17 photon source modeling

In this section, a description of the photon beam model ("virtual source") is presented. The model was developed based on the source characterization results reported in Sec. II E.

In our model, the photon energy was sampled from the MC calculated spectrum at the patient position (see Fig. 3), which ranged from 27 to 600 keV with a mean energy of 99 keV. The high degree of polarization showed in Sec. II E indicated that the beam is extremely linearly polarized along the x axis when reaches the patient position. Therefore, a P_3 value of -1 has been considered in the calculations.

The probability distribution of the x coordinate was approximated as a uniform distribution with a width equal to the field size (from -1 to 1 cm in the example showed in

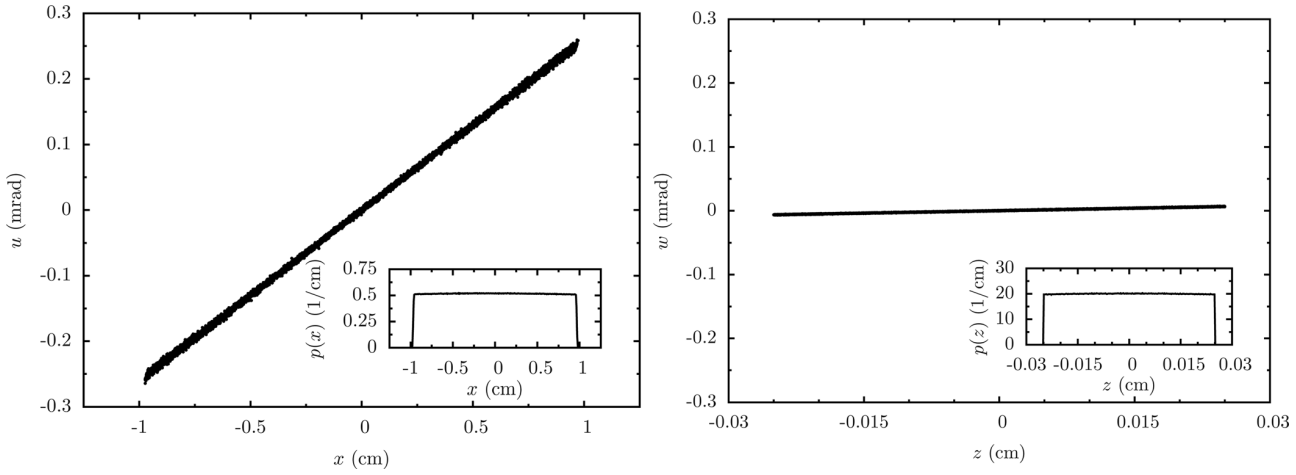

FIG. 5. Phase-space diagrams in the horizontal (left) and vertical (right) coordinates at the vertical slit position, just before the patient position (500 μm vertical slit size, 2 cm horizontal field size). Each point represents a photon. Probability density functions p(x) and p(z) (1/cm per history) are also shown in the insets.

the inset of Fig. 5). The joined distribution for position and divergence, i.e., x and u, was approximated by a straight line obtained by the linear regression $u = ax$, where $a = 0.000256(4)$ is the regression coefficient (see Fig. 5). An analogous approach was taken for the z coordinate and its associated divergence value (w), leading to a linear regression $w = bz$ with $b = 0.0002603(1)$.

In the case of MRT irradiations, particles were transported through the MLSC. The vertical scanning of the beam at the patient position was modeled by computing the vertical position as $z + d_{\text{field}}\,(\xi - 0.5)$, where d_{field} is the vertical irradiation field size and ξ is a random number uniformly distributed in the interval (0,1).

Photons sampled from our source model have been used to compute absorbed dose distributions in homogeneous media. The commissioning of this model with experimental data will be detailed in next section.

III.B. Experimental validation of the MC simulations

Photon beam model validation and MC calculation performance assessment were done by comparing the simulated dose distributions (PDD and lateral dose profiles at the patient position) with experimental data for different field sizes. As it has been explained in previous sections, the process was divided into two parts (seamless and MRT). First, the broad beam configuration was assessed. For this irradiation modality, the TPS acceptability criteria described in Sec. II D were followed.

III.B.1. Broad beam irradiation

Figure 6 (left) compares the theoretical and experimental PDD curves for seamless 1×1, 2×2, and 3×3 cm^2 field sizes. Dose values are normalized with respect to the central dose at a depth of 2 cm for a 2×2 cm^2 field size. An

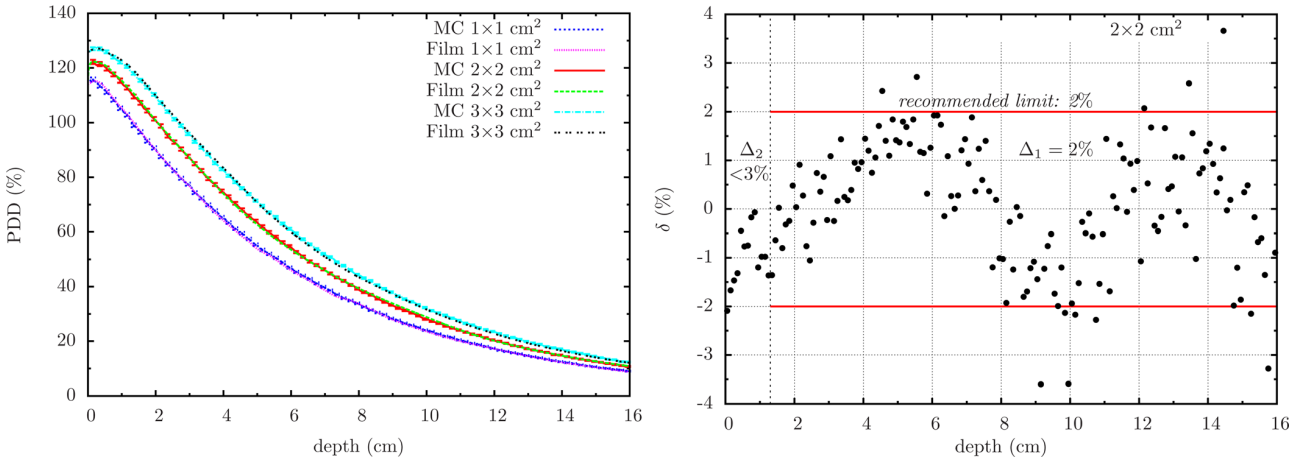

FIG. 6. Comparison of calculated (MC) and measured (Film) PDD values for 1×1, 2×2, and 3×3 cm^2 field sizes (right). Dose values are normalized with respect to the central dose at a depth of 2 cm for a 2×2 cm^2 field size. Statistical uncertainty bars are at two standard deviations. Individual deviations (δ) between experimental and MC PDD data for the reference field size (2×2 cm^2) are also presented on the left.

TABLE IV. PDD overall deviation (Δ_1 and Δ_2) values for 1×1, 2×2, and 3×3 cm^2 field sizes. Computed data were compared with the experimental PDD obtained from HD-810 Gafchromic films placed in a solid–water phantom.

Field size (cm^2)	Δ_1 (%)	Δ_2 (%)
1×1	2.9	2.4
2×2	2.0	2.9
3×3	3.0	1.8

example of the point-to-point deviations (δ) for the reference field size (2×2 cm^2) at a depth of 2 cm is also presented in Fig. 6 (right). The trend of the point-to-point deviations is similar for the 1×1 and 3×3 cm^2 field sizes. In general, δ values are contained within $\pm 2\%$. Although a few data points show high deviations, the overall deviation (Δ) between calculated and measured relative dose values is 2%–3%. Table IV shows the quantitative analysis of the deviation parameters Δ_1 and Δ_2 (%) in the PDD curves for the different field sizes. MC calculations fulfill acceptability criteria in the build-up region since differences with experimental data, which are quantified by Δ_2, are much lower than 10%. Δ_1 values, which account for the deviations of central beam axis points, slightly exceed the recommended 2%. This is probably linked to the difficulties in the measurement of the PDD curves with Gafchromic® films due to remaining air gaps between the slabs of the solid–water phantom.[57] This would also explain the oscillations in the point-to-point deviations observed in Fig. 6 (right).

Figure 7 shows the comparison between calculated and measured lateral dose profiles at a depth of 2 cm along the horizontal (H) and vertical (V) directions for the three studied field sizes. An example of the point-to-point deviations is also presented for a 2×2 cm^2 field size at a depth of 2 cm in Fig. 8. δ values are within $\pm 3\%$ in the horizontal direction and within $\pm 1\%$ in the vertical one, respectively. The maximum δ deviations are observed in the vicinity of the penumbra region. The tendency of the individual deviations is similar for the other two field sizes.

The quantitative analysis of the overall deviations was performed by evaluating the parameters Δ_2 (penumbra), Δ_3 (points in the beam), and Δ_4 (tails) of the lateral dose profiles. The average Δ_2 value was around 0.2 mm, with a maximum at 0.7 mm for the highest field sizes and depths. These values are much lower than the maximum recommended deviation (2 mm). The highest Δ_3 values were encountered for a 3×3 cm^2 field size but they never exceeded the recommended limit (3%). Δ_4 values increased as a function of depth, although they also remained within tolerances. Figure 9 shows the Δ_3 (left) and Δ_4 (right) for all the studied cases.

Deviations in the vertical profile are generally lower than in the horizontal case. As electrons are mostly moving in the x-y plane, any deviation from the ideal wiggler case produces changes in the trajectory followed by the electron beam and, consequently, in the final photon phase-space diagram (x,u). The focusing power of the wiggler along the z direction will also be affected by wiggler imperfections. However, the beam is scanned along the vertical direction at the patient position and the possible effect on beam modeling is reduced.

Other possible reasons for the deviations between experimental data and MC simulations can be found in the uncertainties of the beam modifiers characteristics (dimensions, shape or composition), in the reflection of the beam in very polished slits (not considered in the simulations), in possible small and uncontrolled misalignments in the beamline, etc. This is, of course, added to the inherent uncertainty of the experimental method and of the MC calculations.

However, calculated and experimental dose distributions agreed to within the recommended acceptability criteria described in international codes of practice. Thus, despite some deviations between MC simulations and measured data, the overall agreement is satisfactory.

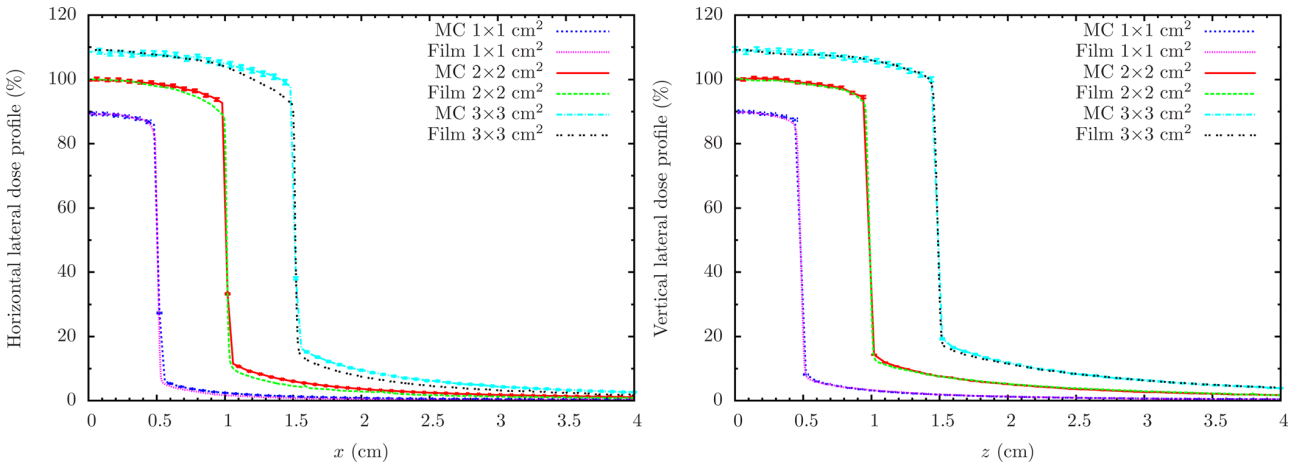

FIG. 7. Comparison of calculated (MC) and measured (Film) lateral dose profiles (at a depth of 2 cm) in the lateral (left) and vertical (right) direction, for 1×1, 2×2, and 3×3 cm^2 field sizes. Dose values are normalized with respect to the central dose at a depth of 2 cm for a 2×2 cm^2 field size. Statistical uncertainty bars are at two standard deviations.

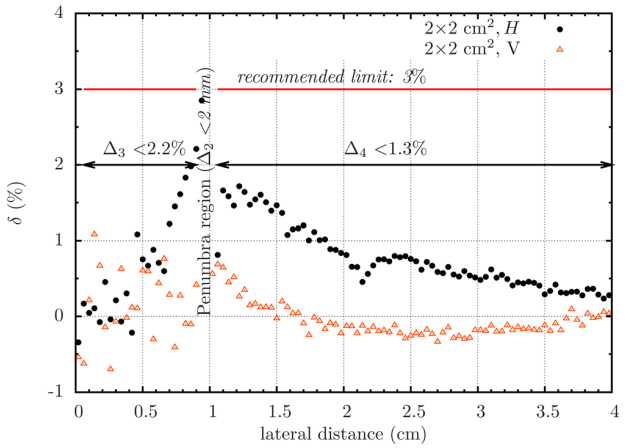

FIG. 8. Point-to-point deviations (δ) between experimental and MC lateral dose profiles (at a depth of 2 cm) in the horizontal (H) and vertical (V) direction for a 2×2 cm^2 field size.

TABLE V. Calculated (MC) and measured (Film) central microbeam PDD (%) at different depths. MRT irradiation parameters: 50 μm-wide microbeams spaced by 400 μm; three field sizes: 1×1, 2×2, and 3×3 cm^2. The normalization point is at a depth of 2 cm. Statistical uncertainty corresponds to two standard deviations.

	Central microbeam PDD (%)					
	1×1 cm^2		2×2 cm^2		3×3 cm^2	
Depth (cm)	MC	Film	MC	Film	MC	Film
0.3	132 ± 1	131 ± 9	133 ± 3	136 ± 9	132 ± 3	135 ± 9
0.5	128 ± 1	131 ± 9	127 ± 3	130 ± 9	128 ± 3	135 ± 9
1.0	118 ± 1	119 ± 8	117 ± 3	126 ± 8	117 ± 3	115 ± 8
2.0	100 ± 1	100 ± 7	100 ± 2	100 ± 7	100 ± 3	100 ± 7
4.0	71.1 ± 0.8	71 ± 6	72 ± 2	70 ± 6	72 ± 2	72 ± 6
6.0	50.9 ± 0.7	51 ± 5	51 ± 1	49 ± 5	52 ± 2	52 ± 5
8.0	36.3 ± 0.5	34 ± 5	37 ± 1	39 ± 5	37 ± 1	38 ± 5
10.0	26.0 ± 0.4	28 ± 3	26.5 ± 0.9	25 ± 3	27 ± 1	27 ± 3

III.B.2. MRT irradiation

The second phase of the benchmarking of photon beam model consisted in the comparison of MC calculations and experimental data in the MRT configuration.

Table V shows simulated (MC) and measured (Film) PDD curves of the central microbeam for different array sizes (1×1, 2×2, and 3×3 cm^2). Normalized peak dose values follow the same trend for the three field sizes (PDD values are normalized with respect to the dose at a depth of 2 cm). The maximum peak dose values are encountered near the surface (0.3 cm) and a decrease of PDD values is observed in depth.

PVDR values as a function of depth and field size are presented in Table VI. The highest PVDR values are located near the phantom surface. Then, the PVDR decreases up to a depth of 5 cm due to an increase of the fluence of photons that are Compton-scattered into the valley region. The fact that PVDR values remain almost constant in depth (beyond 5 cm) indicates that both the peaks and the valleys decrease at more or less the same rate. Moreover, a reduction of PVDR values is observed when the field size (number of beams) increases, in agreement with other authors.[58,59] For instance, PVDR in depth (beyond 5 cm) take values in the order of 15 for a field size of 1×1 cm^2, while in the case of 3×3 cm^2, the PVDR reaches values of approximately 45.

MC simulations reproduced the experimental data within the uncertainty bars, both for the peak and PVDR values. Possible deviations between experimental data and MC simulations have already been detailed in Sec III B 1. Furthermore, the experimental method for the dose assessment in MRT included the use of a microdensitometer. The problematic of using this kind of systems has already been briefly discussed in Sec. II C. Despite the inherent experimental uncertainties, the good agreement between MC calculations and experimental data in both broad beam and MRT irradiation configurations confirms the validity of our photon beam model.

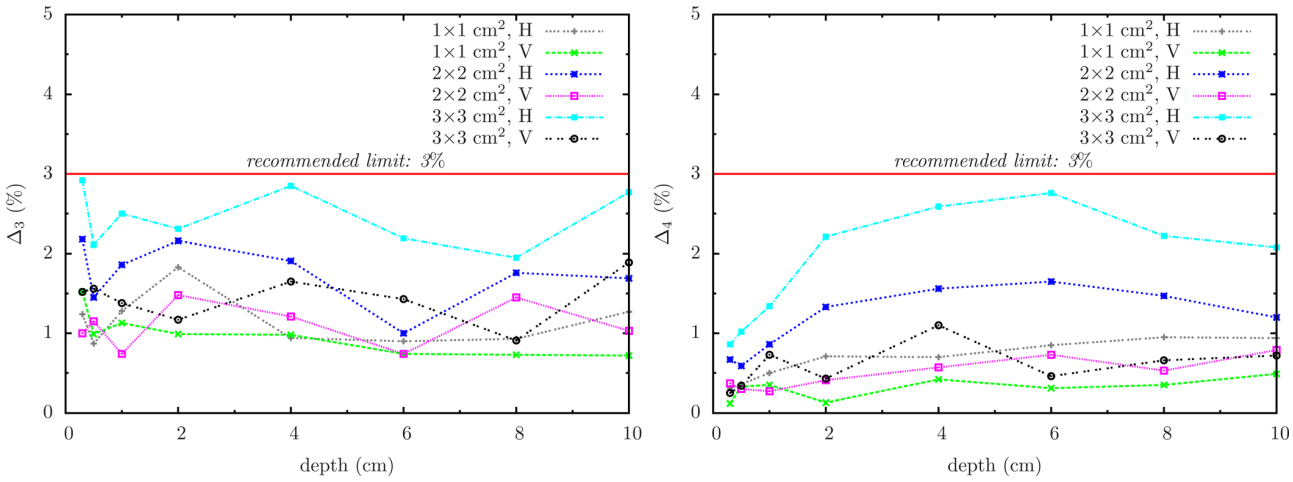

FIG. 9. Δ_3 (left) and Δ_4 (right) confidence limits versus depth for different field sizes (1×1, 2×2 and 3×3 cm^2) in the vertical (V) and horizontal (H) directions. The solid line corresponds to the maximum recommended tolerance value of 3%.

TABLE VI. Calculated (MC) and measured (Film) central PVDR at different depths. MRT irradiation parameters: 50 μm-wide microbeams spaced by 400 μm; three field sizes: 1×1, 2×2, and 3×3 cm^2. Statistical uncertainty corresponds to two standard deviations.

	PVDR					
	1×1 cm^2		2×2 cm^2		3×3 cm^2	
Depth (cm)	MC	Film	MC	Film	MC	Film
0.3	77 ± 4	69 ± 10	47 ± 4	47 ± 7	35 ± 4	33 ± 5
0.5	67 ± 3	65 ± 9	42 ± 3	38 ± 6	30 ± 4	27 ± 4
1.0	57 ± 3	51 ± 7	33 ± 3	33 ± 5	25 ± 3	22 ± 3
2.0	51 ± 3	47 ± 7	28 ± 2	28 ± 4	20 ± 2	18 ± 3
4.0	47 ± 3	44 ± 6	25 ± 2	22 ± 3	17 ± 2	13 ± 3
6.0	43 ± 3	42 ± 6	22 ± 2	20 ± 3	15 ± 2	12 ± 2
8.0	43 ± 3	40 ± 6	22 ± 3	19 ± 3	15 ± 2	13 ± 2
10.0	44 ± 4	44 ± 6	23 ± 3	19 ± 3	15 ± 3	13 ± 2

III.C. Examples of dose distributions in an homogeneous phantom

Figure 10 shows the MC dose distribution at a depth of 2 cm for an irradiation with an array of microbeams (solid line) covering an area of 1×1 cm^2. The dose profile consists in peaks and valleys, with a PVDR value of approximately 50. The small divergence of synchrotron beams and the energy range used in MRT resulted in sharp penumbras (less than 10 μm). In the same figure, the dashed line represents the simulated dose distribution obtained for an irradiation with a Gamma Knife® (GKF).[60] The main differences between both profiles are the spatial fractionation and the extreme conformality of the dose deposition in MRT in comparison with the homogeneous GFK dose distribution and its much larger penumbras.

As explained in the introduction, MRT is capable of delaying the tumor growth and, in some cases, of producing complete tumor ablation, despite the small fraction of tumor mass irradiated with the high-dose microbeams. Therefore, the spatial dose fractionation along with the high conformality (low penumbras) provide a remarkable healthy tissue sparing while tumoricidal doses are achieved. In GKF, the total doses in the target are reduced in comparison with MRT due to normal tissue radiosensitivity. In addition, the low penumbras in MRT represent a great advantage for the treatment of tumors close to an organ at risk and for avoiding serious secondary effects in healthy tissue.

In order to further increase the dose deposited in the tumor with MRT and keep the same dose in the healthy tissue, other methods can be explored. For instance, the dose enhancement with the injection of a high atomic number element prior the MRT irradiation[61] or the use of more complex MRT configurations such as crossfiring[62] or interlacing.[63]

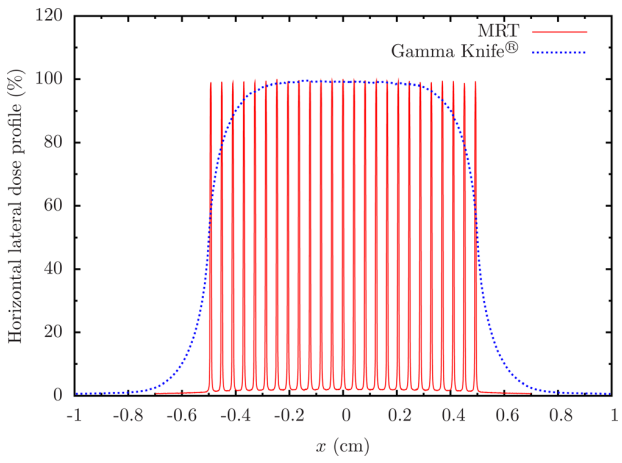

FIG. 10. Percentage lateral dose distribution at a depth of 2 cm for an irradiation with an array of microbeams (solid line) covering an area of 1×1 cm^2. The dashed line represents the dose distribution obtained for an irradiation with a Gamma Knife® (GKF) (Ref. 60).

IV. CONCLUSION

In the quest for a radical treatment of gliomas, clinical trials in MRT are under preparation at the ID17 Biomedical Beamline (ESRF). An accurate treatment planning system for dose computations in the patients was required for this purpose. Therefore, a full characterization of the synchrotron x-ray source at the ID17 (ESRF) and the development of an accurate photon beam model was carried out. The use of this beam model saves computation time. The methodology developed in this work can be easily extended to other synchrotron sources by changing the storage ring characteristics, ID parameters and geometry of the beamline modifiers.

The satisfactory agreement between calculated and measured dose distributions validates the photon beam model for its use in MRT radiation therapy calculations. This is the first published work where MRT theoretical dose maps faithfully reproduce the experimental data. The beam model developed in this study will constitute an essential component of the TPS calculation engine for patient dose computation in forthcoming MRT clinical trials at the ESRF. Future work along this line of research includes calculations in voxelized images and optimization of the computation time.

ACKNOWLEDGMENTS

The authors would like to thank the support given by the ESRF, in particular to M. Sánchez del Río and N. Canestrari from the Advanced Analysis and Modeling Unit for their invaluable help with the SHADOW code. The authors also warmly thank the ESRF for the granted beamtime and the ID17 team for technical support, especially H. Requardt. JS acknowledges partial financial support from the Spanish Ministerio de Ciencia e Innovación (project no. FPA2009-14091-C02-01) and from the Spanish Networking Research Center CIBER-BBN.

[a]Author to whom correspondence should be addressed. Electronic mail: prezado@gmail.com

[1]E. Braüer-Krisch, H. Requardt, T. Brochard, G. Berruyer, M. Renier, J. A. Laissue, and A. Bravin, "New technology enables high precision multislit collimators for microbeam radiation therapy," Rev. Sci. Instrum. **80**, 074301 (2009).

[2]I. Martínez-Rovira, J. Sempau, J. M. Fernández-Varea, A. Bravin, and Y. Prezado, "Monte Carlo dosimetry for forthcoming clinical trials in x-ray microbeam radiation therapy," Phys. Med. Biol. **55**, 4375–4388 (2010).

[3]D. Slatkin, P. Spanne, F. A. Dilmanian, J.-O. Gebbers, and J. A. Laissue, "Subacute neuropathological effects of microplanar beams of x-rays from a synchrotron wiggler," Proc. Natl. Acad. Sci. U.S.A. **92**, 8783–8787 (1995).
[4]F. A. Dilmanian *et al.*, "Response of avian embryonic brain to spatially segmented x-ray microbeams," Cell. Mol. Biol. (Noisy-le-grand) **47**, 485–493 (2001).
[5]J. A. Laissue *et al.*, "The weanling piglet cerebellum: A surrogate for tolerance to MRT (microbeam radiation therapy) in pediatric neuro-oncology," SPIE **4508**, 65–73 (2001).
[6]N. Zhong, G. M. Morris, T. Bacarian, E. M. Rosen, and F. A. Dilmanian, "Response of rat skin to high-dose unidirectional x-ray microbeams: A histological study," Radiat. Res. **160**, 133–142 (2003).
[7]F. A. Dilmanian, Z. Zhong, T. Bacarian, H. Benveniste, P. Romanelli, R. Wang, J. Welwart, T. Yuasa, E. M. Rosen, and D. J. Anschel, "Interlaced x-ray microplanar beams: A radiosurgery approach with clinical potential," Proc. Natl. Acad. Sci. U.S.A. **103**, 9709–9714 (2006).
[8]R. Serduc *et al.*, "Characterization and quantification of cerebral edema induced by synchrotron x-ray microbeam radiation therapy," Phys. Med. Biol. **53**, 1153–1166 (2008).
[9]B. Van der Sanden, E. Brauer-Krisch, E. A. Siegbahn, C. Ricard, J.-C. Vial, and J. Laissue, "Tolerance of arteries of arteries to microplanar x-ray beam beams," Int. J. Radiat. Oncol., Biol., Phys. **77**, 1545–1552 (2010).
[10]A. Bouchet *et al.*, "Preferential effect of synchrotron microbeam radiation therapy on intracerebral 9L gliosarcoma vascular networks," Int. J. Radiat. Oncol., Biol., Phys. **78**, 1503–1512 (2010).
[11]P. Régnard *et al.*, "Irradiation of intracerebral 9L gliosarcoma by a single array of microplanar x-ray beams from a synchrotron: Balance between curing and sparing," Phys. Med. Biol. **53**, 861–878 (2008).
[12]F. A. Dilmanian *et al.*, "Response of rat intracranial 9L gliosarcoma to microbeam radiation therapy," Neuro-Oncol. **4**, 26–38 (2002).
[13]F. A. Dilmanian, G. Morris, N. Zhong, T. Bacarian, J. F. Hainfeld, J. Kalef-Ezra, L. J. Brewington, J. Tammam, and E. M. Rosen, "Murine EMT-6 carcinoma: High therapeutic efficacy of microbeam radiation therapy," Radiat. Res. **159**, 632–641 (2003).
[14]M. Miura, H. Blattmann, E. Bräuer-Krisch, A. Bravin, A. L. Hanson, M. M. Nawrocky, P. L. Micca, D. N. Slatkin, and J. A. Laissue, "Radiosurgical palliation of aggressive murine SCCVII squamous cell carcinomas using synchrotron-generated x-ray microbeams," Br. J. Radiol. **79**, 71–75 (2006).
[15]H. M. Smilowitz *et al.*, "Synergy of gene-mediated immunoprophylaxis and microbeam radiation therapy for advanced intracerebral rat 9L gliosarcomas," Neuro-Oncol. **78**, 135–43 (2006).
[16]E. Braüer-Krisch, R. Serduc, E. A. Siegbahn, G. Le Duc, Y. Prezado, A. Bravin, H. Blattmann, and J. A. Laissue, "Effects of pulsed, spatially fractionated, microscopic synchrotron x-ray beams on normal and tumoral brain tissue," Mutat. Res. **704**, 160–166 (2010).
[17]M. Renier, T, Brochard, C. Nemoz, H. Requardt, E. Bräuer-Krisch, F. Estève, J. Balosso, P. Suortti, J. Baruchel, H. Elleaume, G. Berruyer, P. Berkvens, and A. Bravin, "The radiotherapy clinical trials projects at the ESRF: Technical aspects," Eur. J. Radiol. **68S**, S147–S150 (2008).
[18]International Commission on Radiation Units and Measurements, "Determination of absorbed dose in a patient irradiated by beams of X or gamma rays in radiotherapy procedures," ICRU Report No. 24 (Bethesda, MD, 1976).
[19]International Commission on Radiation Units and Measurements, "Use of computers in external beam radiotherapy procedures with high energy photons and electrons," Report No. 42 (Bethesda, MD, 1987).
[20]F. Verhaegen and J. Seuntjens, "Monte Carlo modelling of external radiotherapy photon beams," Phys. Med. Biol. **48**, R107–R164 (2003).
[21]B. Faddegon, J. Balogh, R. Mackenzie, and D. Scora, "Clinical considerations of Monte Carlo for electron radiotherapy treatment planning," Radiat. Phys. Chem. **53**, 217–227 (1998).
[22]C.-M. Ma, "Characterization of computer simulated radiotherapy beams for Monte Carlo treatment planning," Radiat. Phys. Chem. **53**, 328–344 (1998).
[23]D. N. Slatkin, P. Spanne, F. A. Dilmanian, and M. Sandborg, "Microbeam radiation therapy," Med. Phys. **19**, 1395–400 (1992).
[24]J. Stepanek, H. Blattmann, J. A. Laissue, N. Lyubimova, M. D. Michiel, and D. N. Slatkin, "Physics study of microbeam radiation therapy with PSI-version of Monte Carlo code GEANT as a new computational tool," Med. Phys. **27**, 1664–1675 (2000).
[25]M. D. Felici, R. Felici, M. S. del Rio, C. Ferrero, T. Bacarian, and F. A. Dilmanian, "Dose distribution from x-ray microbeam arrays applied to radiation therapy: An EGS4 Monte Carlo study," Med. Phys. **32**, 2455–2463 (2005).
[26]E. Siegbahn, J. Stepanek, E. Bräuer-Krisch, and A. Bravin, "Determination of dosimetrical quantities used in microbeam radiation therapy (MRT) with Monte Carlo simulations," Med. Phys. **33**, 3248–3259 (2006).
[27]J. Spiga, E. A. Siegbahn, E. Bräuer-Krisch, P. Randaccio, and A. Bravin, "The GEANT4 toolkit for microdosimetry calculations: Application to microbeam radiation therapy MRT," Med. Phys. **34**, 4322–4330 (2007).
[28]E. Siegbahn, E. Bräuer-Krisch, A. Bravin, H. Nettelbeck, M. L. F. Lerch, and A. B. Rosenfeld, "MOSFET dosimetry with high spatial resolution in intense synchrotron-generated x-ray microbeams," Med. Phys. **36**, 1128–1137 (2009).
[29]Y. Prezado, G. Fois, G. Le Duc, and A. Bravin, "Gadolinium dose enhancement studies in microbeam radiation therapy," Med. Phys. **36**, 3568–3574 (2009).
[30]H. Nettelbeck, G. J. Takacs, M. L. F. Lerch, and A. B. Rosenfeld, "Microbeam radiation therapy: A Monte Carlo study of the influence of the source, multislit collimator, and beam divergence on microbeams," Med. Phys. **36**, 447–456 (2009).
[31]J. C. Crosbie, I. Svalbe, S. M. Midgley, N. Yagi, P. A. W. Rogers, and R. A. Lewis, "A method of dosimetry for synchrotron microbeam radiation therapy using radiochromic films of different sensitivity," Phys. Med. Biol. **53** 6861–6877 (2008).
[32]J. Als-Nielsen and D. McMorrow, *Elements of Modern X-ray Physics* (John Wiley and Sons, England, 2001).
[33]European Synchrotron Radiation Facility, http://www.esrf.eu/.
[34]Y. Prezado, M. Vautrin, I. Martínez-Rovira, A. Bravin, P. Berkvens, and J. F. Adam, "Dosimetry protocol for the forthcoming clinical trials in synchrotron radiation therapy (SSRT)," Med. Phys. **38** 1709–1717 (2011).
[35]B. P. Poncelet, V. J. Wedeen, R. M. Weisskoff, and M. S. Cohen, "Brain parenchyma motion: Measurement with cine echo-planar MR imaging," Radiology **185**, 645–651 (1992).
[36]B. Lai and F. Cerrina, "SHADOW: A synchrotron radiation ray tracing program," Nucl. Instrum. Methods Phys. Res. A **246**, 337–341 (1986).
[37]B. Lai, K. Chapman, and F. Cerrina, "SHADOW: New Developments," Nucl. Instrum. Methods Phys. Res. A **266**, 544–549 (1988).
[38]K. Chapman, B. Lai, F. Cerrina, and J. Viccaro, "Modelling of undulator sources," Nucl. Instrum. Methods Phys. Res. A **283**, 88–99 (1989).
[39]M. Sánchez del Río, N. Canestrari, F. Jiang, and F. Cerrina, "SHADOW3: A new version of the synchrotron x-ray optics modelling package," J. Synchrotron Radiat. **18**, 1–9 (2011).
[40]F. Salvat, J. M. Fernández-Varea, and J. Sempau, "PENELOPE 2008, a Code System for Monte Carlo Simulation of Electron and Photon Transport" (OECD Nuclear Energy Agency, Issy-les-Molineaux, 2008).
[41]J. Sempau, E. Acosta, J. Baró, J. M. Fernández-Varea, and F. Salvat, "An algorithm for Monte Carlo simulation of coupled electron-photon transport," Nucl. Instrum. Methods Phys. Res. B **132**, 377–390 (1997).
[42]J. Sempau, A. Badal, and L. Brualla, "A PENELOPE-based system for the automated Monte Carlo simulation of clinacs and voxelized geometries—Application to far-from-axis fields," Med. Phys. **38**, 3887–3895 (2011).
[43]D. E. Cullen, J. H. Hubbell, and L. Kissel, "EPDL97: The evaluated photon data library, 97 version," Report UCRL-50400 vol 6 (Lawrence Livermore Nation Laboratory, Livermore, 1997).
[44]U. Fano, "A Stokes-parameter technique for the treatment of polarization in quantum mechanics," Phys. Rev. **93**, 121–123 (1954).
[45]J. Sempau and P. Andreo, "Configuration of the electron transport algorithm of PENELOPE to simulate ion chambers," Phys. Med. Biol. **51**, 3533–3548 (2006).
[46]PTW, http://www.ptw.de/.
[47]ISP Technologies Inc., www.ispcorp.com/.
[48]N. Nariyama, "Responses of GafChromic films for distribution of extremely high doses from synchrotron radiation," Appl. Radiat. Isot. **62**, 693–697 (2005).
[49]A. Niroomand-Rad, C. R. Blackwell, B. M. Coursey, K. P. Gall, J. M. Galvin, W. L. McLaughlin, Al. S. Meigooni, R. Nath, J. E. Rodgers, and C. G. Soares, "Radiochromic film dosimetry: Recommendations of AAPM Radiation Therapy Committee Task Group 55," Med. Phys. **25**, 2093–2115 (1998).
[50]EPSON, www.epson.com/.

[51]S. Devic, J. Seuntjens, E. Sham, E. B. Podgorsak, C. R. Schmidtlein, A. S. Kirov, and C. G. Soares, "Precise radiochromic film dosimetry using flatbed document scanner," Med. Phys. **32**, 2245–2253 (2005).
[52]K. Zimmer and G. Heltai, "Effect of properties of microdensitometers on the shape of the characteristic curve of the photographic emulsion," Spectrochim. Acta, **33B**, 417–427 (1978).
[53]A. S. Aydarous, P. J. Darley, and M. W. Charles, "A wide dynamic range, high-spatial-resolution scanning system for radiochromic dye films," Phys. Med. Biol. **46**, 1379–1389 (2001).
[54]R. E. Swing, *An Introduction to Microdensitometry* (SPIE Optical Engineering Press, Washington, 1998).
[55]International Atomic Energy Agency (IAEA), "Commissioning and quality asurance of computerized planning systems for radiation treatment of cancer," IAEA Technical Reports Series No. 430 (IAEA, Vienna, 2004).
[56]J. Venselaar, H. Welleweerd, and B. Mijnheer, "Tolerances for the accuracy of photon beam dose calculations of treatment planning systems," Radiother. Oncol. **60**, 191–201 (2001).
[57]N. Suchowerska, P. Hoban, M. Butson, A. Davison, and P. Metcalfe, "Directional dependence in film dosimetry: Radiographic and radiochromic film," Phys. Med. Biol. **46**, 1391–1397 (2001).
[58]G. Gokeri, C. Kocar, and M. Tombakoglu, "Monte Carlo simulation of microbeam radiation therapy with an interlaced irradiation geometry and an Au contrast agent in a realistic head phantom," Phys. Med. Biol. **55**, 7469–7487 (2010).
[59]Y. Prezado, S. Thengumpallil, M. Renier, and A. Bravin, "x-ray energy optimization in minibeam radiation therapy," Med. Phys. **36**, 4897–4902 (2009).
[60]www.elekta.com/.
[61]I. Martínez-Rovira and Y. Prezado, "Monte Carlo dose enhancement studies in microbeam radiation therapy," Med. Phys. **38**, 4430–4439 (2011).
[62]E. Bräuer-Krisch, H. Requardt, P. Régnard, S. Corde, E. Siegbahn, G. Le Duc, T. Brochard, H. Blattmann, J. Laissue, and A. Bravin, "New irradiation geometry for microbeam radiation therapy," Phys. Med. Biol. **50**, 3103–3111 (2005).
[63]R. Serduc, E. Bräuer-Krisch, E. A. Siegbahn, A. Bouchet, B. Pouyatos, R. Carron, N. Pannetier, L. Renaud, G. Berruyer, C. Nemoz, T. Brochard, C. Rémy, E. L. Barbier, A. Bravin, G. Le Duc, A. Depaulis, F. Estéve, and J. A. Laissue, "High-precision radiosurgical dose delivery by interlaced microbeam arrays of high-flux low-energy synchrotron x-rays," PLOS One **5**, 1–12 (2010).

Monte Carlo-based treatment planning system calculation engine for microbeam radiation therapy

I Martínez-Rovira[1,2], J Sempau[1] and Y Prezado[3]

[1] *Institut de Tècniques Energètiques, Universitat Politècnica de Catalunya (UPC), Diagonal 647, E-08028 Barcelona, Spain*

[2] *ID17 Biomedical Beamline, European Synchrotron Radiation Facility (ESRF), 6 rue Jules Horowitz B.P. 220, F-38043 Grenoble Cedex, France and*

[3] *Laboratoire Imagerie et modélisation en neurobiologie et cancérologie, Centre National de la Recherche Scientifique (CNRS), 15 rue Georges Clemenceau, F-91406 Orsay Cedex, France*

Purpose: Microbeam Radiation Therapy (MRT) is an innovative synchrotron radiotherapy technique that explores the limits of the dose-volume effect. Preclinical studies have shown that MRT irradiation (arrays of 25–75-μm-wide microbeams spaced by 200–400 μm) is able to eradicate highly aggressive animal tumor models. Furthermore, healthy tissue is preserved. These promising results have provided the basis for the forthcoming clinical trials at the ID17 Biomedical Beamline of the European Synchrotron Radiation Facility (ESRF). The first step includes irradiation of pets (cats and dogs) as a milestone before treatment of human patients. Within this context, accurate dose calculations are required. The distinct features of both beam generation and irradiation geometry in MRT with respect to conventional techniques requires the development of a specific MRT Treatment Planning System (TPS). In particular, a Monte Carlo-based calculation engine for the MRT TPS has been developed in this work. Experimental verification in heterogeneous phantoms and optimization of the computation time have also been achieved.

Methods: The PENELOPE/penEasy MC code was used to compute dose distributions from a realistic beam source model. Experimental verification was carried out by means of radiochromic films placed within heterogeneous slab-phantoms. Once validation was completed, dose computations on a virtual model of a patient, reconstructed from Computed Tomography (CT) images, were performed. To this end, decoupling of the CT image voxel grid (a few mm^3 volume) to the dose bin grid, which has micrometer dimensions in the transversal direction of the microbeams, was performed. Optimization of the simulation parameters, the use of variance-reduction (VR) techniques and other methods, such as the parallelization of the simulations, were applied in order to speed up dose computation.

Results: A good agreement between MC simulations and experimental results was achieved, even at the interfaces between two different media. Optimization of the simulation parameters and the use of VR techniques saved a significant amount of computation time (a factor of 8). Finally, parallelization of the simulations even further improved the calculation times, which reached one day for a typical irradiation case envisaged in the forthcoming clinical trials in MRT. An example of MRT treatment to a dog's head is presented, showing the performance of the calculation engine.

Conclusions: The development of the first MC-based calculation engine for the future TPS devoted to MRT has been accomplished. This will constitute an essential tool for the future clinical trials on pets at the ESRF. The MC engine is able to calculate dose distributions in micrometer-sized bins in complex voxelized CT structures in a reasonable amount of time. Minimization of the computation time by using several approaches has led to timings that are adequate for pet radiotherapy at synchrotron facilities. The next step will consist of its integration into a user-friendly graphical front-end.

Keywords: Microbeam Radiation Therapy, Monte Carlo simulations, Treatment Planning System, clinical trials

I. INTRODUCTION

Microbeam Radiation Therapy (MRT) is a synchrotron-based technique that is potentially able to widen the therapeutic window for some radioresistant tumors such as gliomas. Irradiation is carried out by means of an array of parallel x-ray 25–75-μm-wide microbeams with a center-to-center distance (c-t-c) of 200–400 μm and a mean energy of approximately 100 keV [1, 2]. The MRT irradiation scheme results in dose profiles consisting of peaks and valleys with high doses along the microbeam path and low doses between them. The central dose between two microbeams is named the valley dose, while the dose at the center of the microbeam is the peak dose. The ratio between the peak and the valley doses is called the peak-to-valley dose ratio (PVDR) and plays an important role in biological response [3].

Distinct features of MRT are the spatial fractionation of the dose and the use of submillimeter field sizes, which explore the limits of the dose-volume effect [4, 5]. This combination shifts the dose-response curve of healthy tissue towards very high doses, while growth delay or complete ablation of highly aggressive animal tumors is achieved. See [3, 6–11], among others. This has paved the way for the forthcoming MRT clinical trials at the ID17 Biomedical Beamline of the European Synchrotron Radiation Facility (ESRF) [12, 13]. For the sake of safety, the fist phases of the clinical trials will consist of the treatment of spontaneous tumors in pets, *e.g.*, cats and dogs [13].

The trials require MRT dose computations and, therefore, an adequate MRT Treatment Planning System (TPS). However, none of the commercially available TPSs is suitable in our case due to the distinct features of the MRT irradiation geometry, beam source and energy spectrum in comparison with conventional radiotherapy. Therefore, the development of an MRT TPS was needed. The calculation engine developed in this work is based on Monte Carlo (MC) simulations, which are considered to be the most accurate approach for particle transport and dose computation.

The main challenge was to calculate the absorbed dose at a micrometric scale in voxelized structures in a reasonable amount of time. In our previous work [1], complete photon source characterization was achieved. This characterization included the phase-space variables, *i.e.*, the energy, spatial position, direction of flight and polarization state, of the beam at different positions in the beamline. This information was used to generate a photon source model, which was experimentally validated in homogenous media. The use of this source model instead of phase-space files (PSF) enables the reduction of a significant amount of computation time.

In the present work, the performance of our model in heterogeneous structures is assessed. In addition, the MC code was adapted for dose calculation in micrometric bins in computed tomography (CT) images. A further reduction of computation time was achieved by optimizing the simulation parameters, by using variance-reduction (VR) techniques and parallelizing the simulations.

To our knowledge, only the work of Gokeri *et al.* [14] has dealt with dose calculation in voxelized structures in micrometer-sized bins. However, their work is on dose calculations in the presence of contrast agents rather than development of a calculation engine for MRT. Furthermore, the beam width (680 μm) and c-t-c distance (680 μm) correspond to Minibeam Radiation Therapy (MBRT), where thicker beams are used. Additionally, they used a simplified irradiation source geometry and no experimental benchmarking was performed [14]. Therefore, this is the first work where both a realistic source model and voxelized patient geometry are considered in MRT.

II. MATERIALS AND METHODS

A. ID17 Biomedical Beamline (ESRF)

The ESRF is one of the largest and brightest synchrotrons in the world. In third-generation sources, such as the ESRF, insertion devices (ID) are in-

terposed in the relativistic electron beam path to deliver extremely brilliant x-rays. At the ID17 Biomedical Beamline, the ID used is a wiggler. The emitted radiation consists of a continuum of energies ranging from the infrared to the x-ray region. Other relevant characteristics of the beam are its high degree of linear polarization in the electron orbit plane and its low divergence [1]. These synchrotron beam features allow minimization of cardiosynchronous motion effects in the brain [15] and help to define sharp beam edges.

Photons are transported approximately along 40.5 m until they reach the patient position. Several beam modifiers tune the beam along its path [1]. For instance, some filters eliminate low energies of the spectrum, while diaphragms and slits shape the beam to the desired field size. The final energy spectrum ranges from 27 to 600 keV, with a mean energy of 99 keV [1, 2]. The last element is a multislit collimator (MSLC) [16], which allows the generation of microbeams from a seamless beam. The MRT irradiation beam used in this study consisted of 50-μm-wide microbeams with a c-t-c of 400 μm (clinical settings).

Phantoms or animals are placed on a high-precision goniometer [12]. Maximum horizontal and vertical irradiation dimensions at this position are 4.1 and 0.25 cm, respectively. Wider vertical field sizes are achieved by scanning the targets at constant speed [17]. More details on the different beam modifiers and physical beam properties can be found in our previous work [1].

B. PENELOPE/penEasy code description

PENELOPE [18–20] is a MC code widely used in the medical physics field and, in particular, in dose calculations for synchrotron radiotherapy techniques [1, 2, 21–24]. This code enables the simulation of the coupled transport of photons, electrons and positrons in a very wide energy range and in arbitrary material systems.

The relevant photon interactions in MRT (mean energy $\sim$ 100 keV) are Compton scattering and the photoelectric effect. Compton scattering cross sections are obtained from the relativistic impulse approximation, which accounts for Doppler broadening and binding effects. The polarisation state of photons is considered in the scattering events [18]. Photoelectric cross sections are interpolated from tabulations in the Evaluated Photon Data Library from the Lawrence Livermore National Laboratory (LLNL) [25].

As regards electron transport, PENELOPE uses a mixed approach in which hard interactions are simulated individually whereas condensed simulation techniques are applied for soft interactions. The dominant energy loss mechanism for electrons in our energy range is inelastic collisions. The description of inelastic scattering of charged particles is performed on the basis of a schematic generalized oscillator strength (GOS) model, with mean excitation values taken from ICRU Report 37 [26]. Differential cross sections of elastic collisions of electrons, which are responsible for most angular deflections, are obtained from relativistic partial-wave calculations [27].

The simulation parameters in PENELOPE were set as follows. The absorption energies (`EABS`), at which the transport is discontinued, were set so as to ensure that the photon mean free path and the range of secondary electrons at `EABS` were both smaller than the minimum bin used to tally the dose distributions, that is, 10 keV for electrons and 1 keV for photons. In Section III B 1, optimization of these parameters is studied. Charged-particle transport involves the following parameters: the maximum average angular deflection in a multiple-scattering step (`C1`) and the maximum average fractional energy loss along that step (`C2`) were fixed to 0.1; the cut-off energies for the production of hard inelastic events (`WCC`) and hard bremsstrahlung (`WCR`) were set equal to `EABS` for electrons and photons, respectively [18, 28].

The general-purpose main program for PENELOPE, named penEasy [29], was employed in this work. The code includes different source models, tallies and the possibility of applying several VR techniques. penEasy allows dose computation in

voxelized structures, as well as their superposition with objects limited by quadric surfaces.

C. ID17 photon beam source model

A detailed simulation of photon beam transport from the wiggler source to the patient position has been described in Martínez-Rovira *et al.* [1]. The synchrotron ray tracing code SHADOW [30] was used to generate particles from the ID17 wiggler, while the PENELOPE code [18] was employed to transport the particles through the beamline. Both codes were directly linked by inserting a new source model into the penEasy program [1, 29].

As a result, a PSF with the phase-space state of the particles before the patient position was generated. This information was used to construct a 'virtual' photon beam source model. MC simulations reproduced (within uncertainty bars) the experimental peak doses and PVDR values in a water phantom for different field sizes (1×1, 2×2 and 3×3 cm^2). This source model was adopted as the input source in this work.

D. MC calculations in heterogeneous media

Particles sampled from the photon beam model described above [1] were transported up to the patient position in order to compute absorbed dose distributions in heterogeneous media. In particular, two different inhomogeneous phantoms, both composed of slabs of cortical bone (Gammex® 450 [31]) and RW3 (Goettingen White Water [32]), were considered:

- A 1-cm slab of bone followed by 10 slabs (10 cm) of RW3 solid-water phantom. This geometry corresponds to the human head phantom [22] and it will hereafter be called phantom 'A'.

- The same geometry but with the bone shifted by one centimeter, *i.e.*, 1 cm of RW3 solid-water, 1 cm of bone and 9 cm of RW3 solid-water. This phantom will be referred to as 'B'.

To accurately account for the dose deposited at the interfaces between different materials, geometric details of the detector system were also included in the simulations [33, 34].

Phantoms were irradiated in the MRT configuration (50-μm-wide microbeams with a c-t-c distance of 400 μm) and three field sizes were evaluated: 1×1, 2×2 and 3×3 cm^2. Doses were scored in 5-μm-wide bins along the transversal direction of the microbeams, 2 mm in the vertical direction and 1 mm in depth (bin volume of 10^{-5} cm^3). The average relative statistical uncertainty was computed as the root mean square of the uncertainties of the bins with doses above half the maximum score. Simulations were terminated when this uncertainty was less than 2% (two standard deviations, 2σ).

E. Experimental validation of MC calculations in heterogeneous media

Absolute central peak doses and PVDR values were evaluated experimentally for several field sizes (1×1, 2×2, 3×3 cm^2) in function of depth. The detector system used was Gafchromic® HD-810 films [33], which were placed between slabs at several depths in the two phantoms described in Section II D. Both the high spatial resolution and the broad dose range of these films make them the best candidate for MRT dose assessment. They were previously used for such delicate measurements in previous studies [1, 35].

Guidelines for handling the films provided by Task Group 55 of the American Association of Physics in Medicine (AAPM) [36] were followed. As regards calibration, the considered range went from 10 to 400 Gy. The broad beam dose was measured with a thimble ionization chamber (PTW 31010 with an active volume of 0.125 cm^3 [32]) calibrated by kilovolt x-rays. Each film box was calibrated individually.

A microdensitometer (3CS Microdensitometer, J. L. Automation) was used to read the films [37]

due to the higher resolution compared with typical flat bed scanners used for seamless irradiation in radiotherapy. The use of this kind of system is very time-consuming and delicate. Therefore, each measurement had to be repeated a minimum of three times. To our knowledge, no other system could provide more accurate measurements in the field of MRT. Further details can be found elsewhere [1, 38, 39].

F. The calculation engine of the treatment planning system for MRT

After validating our photon source model in heterogenous media, the next step consisted of optimization of computation time.

1. *Optimization of computation time*

The statistical uncertainty in MC dose calculations can be reduced by increasing the number of histories and, therefore, the computation time. However, to be able to treat patients, the time devoted to TPS calculations must be reasonably short. In order to reduce this time without compromising accuracy, several methods were examined.

The first approach was the optimization of the simulation parameters. The influence of the absorption energies of photons (`EABS`(γ)) and electrons (`EABS`(e^-)) on several dosimetric magnitudes was evaluated. In particular, `EABS`(e^-) values from 10 keV to 50 keV and `EABS`(γ) values from 1 keV to 50 keV (in steps of 5 keV) were assessed. Since the transport of particles in the human or animal body will be mainly performed in tissues with properties equivalent to water, dose distributions were initially assessed in a water phantom. Simulations were discontinued when the average relative statistical uncertainty was less than 1% (2σ).

The second optimization method consisted of employing a VR technique [18, 40], known as interaction forcing, for all photon interactions [18]. This VR method consists of increasing the probability of occurrence of the process of interest artificially by using a forcing factor (`FORCING`). This technique is implemented in the PENELOPE/penEasy code [29]. Several `FORCING` values were evaluated, from 1 to 150.

Simulations were run on the ESRF cluster [42] and were parallelized by using independent random sequences [41]. To further increase efficiency, the valley doses were computed as an average of the dose in several dose bins. This last approach was possible since valley regions are 'flat' in the central region (100 μm) between microbeams (c-t-c is 400 μm). Quantitative details on simulation times will be presented in Section III B.

2. *Calculations in voxelized structures with* PENELOPE/penEasy

To treat patients, the dose computation in voxelized structures is required. Typically, the patient model is extracted from CT images. Attenuation information in CTs is expressed in Hounsfield Units (HU). However, most MC codes do not deal with HUs, but with the mass density and material index of each CT voxel. The conversion from HUs to density and material is performed in two steps. Firstly, the mass density is obtained from a calibration curve (mass density versus HU), provided by the hospital where the CT has been obtained. Secondly, the material index of each voxel is obtained by using a classification approach, that is, by defining a mapping between HU intervals and the material index.

Due to MRT dosimetric requirements, peak and valley doses need to be measured on a micrometer-size scale. However, the penEasy code associates the dose voxel size (hereafter named 'bin') to the CT voxel size (hereafter named 'voxel') [29]. Note that the lateral voxel size is typically of the order of one or several millimeters, in other words, its dimension is much larger than the necessary dose bin size. Thus, decoupling of the two grids was performed. To this end, the corresponding tally for dose distribution in voxelized structures was modified to compute the dose in micrometer-sized bins along the transversal direction of the microbeams.

In the other two dimensions, there are no special requirements and the bin size was set to the voxel size. Additionally, a program in MATLAB® was developed to orientate the CT image along the direction of the microbeams for a given irradiation angle. This program also performs the corresponding format transformation between CT image files (typically in DICOM, Digital Imaging and Communication in Medicine, format) and the penEasy voxelized image format.

An example of a dose calculation in a dog's head will be presented in Section III C. The CT image was classified into three materials: soft tissue, bone and air. Soft tissue was identified as water with a varying mass density. This method has been used by other authors for dose calculation in clinical cases [43]. The reliability of the assimilation of soft tissue to water was assessed by evaluating the variation of peak and valley doses in function of depth for different materials (brain, fat, muscle, skin). Root-mean-relative-square differences for selected cases are less than 1%. The dog's skull composition was taken to be the same as the human skull composition in ICRU 46 [44] as there is no comprehensive reference values for pet tissues and only some data can be found in the literature [45]. The same approach was also followed by other authors in pet dose calculations [46].

III. RESULTS AND DISCUSSION

In this section, MC calculations will first be validated with experimental data in heterogeneous media. The results on the optimization of the calculation time will be then presented. Finally, the feasibility of the developed MC dose calculation engine will be shown by means of an example of an MRT treatment scenario on a dog's head.

A. Experimental validation of MC simulations in heterogeneous media

MC simulations were validated by comparing simulated central peak and PVDR dose distributions with experimental data. Our study focuses on these two magnitudes since they are the most relevant in these types of spatially fractionated techniques [3].

Table I shows simulated (MC) and experimental (film) central peak values in function of depth in the phantom 'A' (see Section II D). Values are normalized to the peak dose at a depth of 2 cm. In general, MC simulations faithfully reproduce the experimental data (within uncertainty bars), even at the interface with bone (depth of 1 cm).

Simulated (MC) and measured (film) PVDR values in function of depth in phantom 'A' are presented in Table II. Good agreement is also obtained. Maximum deviations are generally observed at the interface between the two materials. This is due to both the complexity of the measurements and the high gradient of the PVDR values in this region. PVDR values decrease in bone due to the fact that the Compton-scattered photons reaching the valley region have a larger probability of suffering photoelectric absorption. This is a consequence of the higher average atomic number of the bone with respect to RW3 solid-water. A decrease of PVDR is also observed when the field size is increased. Both trends have also been observed in previous works [22, 23]. PVDR values beyond bone heterogeneity (beyond a depth of 2 cm) are similar to those found in a homogenous phantom [1].

In order to further test the MC calculations, the central peak doses and PVDR values were evaluated in phantom 'B' (see Section II D). In this geometry, the dosimetric magnitudes could also be evaluated at the entrance of the bone. Since PVDR at depth showed no significant differences between PVDR values computed in the homogeneous phantom [1], the dose assessment in phantom 'B' only included values at the interfaces (see Table III). Peak dose values are expressed as a percentage of the dose at a depth of 3 cm (not at 2 cm) due to the presence of the interface at the reference depth. Good agreement between MC calculations and experimental data once again confirmed the performance of MC dose calculations.

TABLE I: *Calculated (MC) and measured (film) percentage depth dose along the central peak (%) in the phantom 'A'. MRT irradiation parameters: 50-μm-wide microbeams spaced by 400 μm; field sizes: 1×1, 2×2 and 3×3 cm^2. The normalization point is at a depth of 2 cm. Statistical uncertainties correspond to 2σ.*

	percentage depth dose along the central peak (%)					
depth (cm)	1×1 cm^2		2×2 cm^2		3×3 cm^2	
	MC	film	MC	film	MC	film
1.0	182 ± 2	177 ± 14	183 ± 3	178 ± 14	180 ± 3	177 ± 14
2.0	100.0 ± 0.4	100 ± 7	100.0 ± 0.8	100 ± 7	100 ± 1	100 ± 7
4.0	71.3 ± 0.3	74 ± 6	71.2 ± 0.7	67 ± 6	74 ± 1	70 ± 6
6.0	51.2 ± 0.3	53 ± 5	51.7 ± 0.5	54 ± 5	52.4 ± 0.8	54 ± 5
8.0	36.7 ± 0.2	37 ± 4	37.1 ± 0.4	37 ± 4	37.9 ± 0.7	35 ± 4

TABLE II: *Calculated (MC) versus measured (film) central PVDR at different depths in the phantom 'A'. MRT irradiation parameters: 50-μm-wide microbeams spaced by 400 μm; field sizes: 1×1, 2×2 and 3×3 cm^2. Statistical uncertainties correspond to 2σ.*

	PVDR					
depth (cm)	1×1 cm^2		2×2 cm^2		3×3 cm^2	
	MC	film	MC	film	MC	film
1.0	31 ± 2	27 ± 5	22 ± 2	18 ± 4	20 ± 2	17 ± 3
2.0	45.5 ± 0.4	43 ± 6	25.0 ± 0.3	24 ± 3	18.0 ± 0.3	18 ± 3
4.0	44.4 ± 0.4	42 ± 6	23.2 ± 0.3	20 ± 3	16.8 ± 0.3	14 ± 2
6.0	43.4 ± 0.5	44 ± 6	22.6 ± 0.4	21 ± 3	15.5 ± 0.4	14 ± 2
8.0	42.6 ± 0.6	43 ± 6	22.2 ± 0.5	22 ± 3	15.2 ± 0.4	15 ± 2

TABLE III: *Calculated (MC) and measured (film) percentage depth dose along the central peak (%) and PVDR values at different depths in the phantom 'B'. MRT irradiation parameters: 50-μm-wide microbeams spaced by 400 μm; field sizes: 1×1, 2×2 and 3×3 cm^2. The normalization point is at a depth of 3 cm. Statistical uncertainties correspond to 2σ.*

	percentage depth dose along the central peak (%)					
depth (cm)	1×1 cm^2		2×2 cm^2		3×3 cm^2	
	MC	film	MC	film	MC	film
1.0	212 ± 2	216 ± 17	212 ± 3	207 ± 17	212 ± 4	208 ± 17
2.0	183 ± 2	181 ± 14	182 ± 3	183 ± 14	178 ± 4	181 ± 14
	PVDR					
depth (cm)	1×1 cm^2		2×2 cm^2		3×3 cm^2	
	MC	film	MC	film	MC	film
1.0	35 ± 3	36 ± 7	24 ± 2	24 ± 5	19 ± 2	19 ± 4
2.0	32 ± 3	27 ± 5	21 ± 2	16 ± 3	13 ± 2	13 ± 2

B. Optimization of the calculation time

In this section, efficiency is expressed in terms of the time needed to reach a statistical uncertainty of 2% (2σ) for the dose in the central valley at 2-cm depth. Simulations were run on a 2.93 GHz Intel Xeon Processor X5670. PENELOPE/penEasy was compiled with the Intel Fortran compiler (option -O3).

1. Optimization of the absorption energies

Firstly, the influence of the different absorption energies for photons and electrons, *i.e.*, EABS(γ) and EABS(e^-), on the relevant MRT dosimetric magnitudes was studied. The evaluation was performed on an homogeneous water phantom for a 2×2 cm^2 field size. A similar study had previously been carried out by De Felici *et al.* for 50 keV monochromatic microbeams [47].

In previous MRT studies [1, 2, 21–23, 47], EABS(e^-) was fixed following the criterion that the secondary electron range had to be smaller than the half bin dimensions used to tally the dose distributions. For example, for a 5 μm bin size along the x direction, the corresponding EABS(e^-) was 10 keV since the range of a 10 keV electron in water is approximately 2.5 μm. However, this is an extremely conservative value and it can be optimized in order to gain in simulation efficiency. With this aim in mind, the variation of peak and valley depth dose curves in function of absorption energy, from 10 keV to 50 keV, in steps of 5 keV, was assessed. The dose distribution curves obtained with an EABS(e^-)=10 keV were considered as the reference values.

Average differences in the depth-dose curves along the central peak are not significant (less than 1%) for EABS(e^-) values up to 20 keV. This energy corresponds to an electron range in water of about 14 μm. Higher EABS(e^-) values lead to an overestimation of peak doses since electrons produced from photoelectric interactions in the peak region are directly absorbed at the interaction point.

Average differences in the depth-dose curves along the central valley are not statistically significant since the main dose contribution to this region arises from Compton-scattered photons in the peak region. Some differences are observed in the shoulders and penumbra region of the lateral dose profiles (see left part of Figure 1), where the electron contribution is still important. The highest EABS(e^-) results in sharper beam edges and a shorter penumbra region. For an EABS(e^-)=20 keV, the shape of the profile is not significantly altered.

In a similar way, EABS(γ) was fixed to ensure that the photon mean free path was smaller than half a bin. Typical EABS(γ) values found in the literature are 1 keV or less [1, 2, 21–23]. The mean free path for a 1 keV photon in water is 2.5 μm. This value is also very conservative since photons are mainly directed in the forward direction, where bin size is 1–2 mm. The influence on the central peak and valley doses in function of EABS(γ) values ranging from 1 keV to 50 keV, in steps of 5 keV, was assessed. The respective mean free path for these energies are 2.5 μm (EABS(γ)=1 keV) and 4.4 cm (EABS(γ)=50 keV). Dose distribution curves obtained with an EABS(γ)=1 keV were considered as the reference values.

Differences in the depth dose curves along the central valley and peak increase with EABS(γ). Deviations start to be significant (higher than 1%) at around 30 keV. This energy approximately corresponds to the energy where the Compton cross section starts to be of the same order as the photoelectric cross section in water. Photons with energies lower than 30–40 keV mainly interact by the photoelectric effect and their energy is absorbed in the nearby area. However, higher energy photons interact both by the Compton and the photoelectric effect. The valley dose depends on the balance between the number of Compton-scattered photons and the probability of absorption of these photons once they reach the valley region. For low energies (50 keV), the second factor is more important, while the first factor is dominant at higher energies (100 keV).

Figure 1 (right) presents the MRT lateral dose profiles at 2 cm in a water phantom for several EABS(γ). Despite the fact that absolute peak and valley doses depend on EABS(γ), the shape of the profile is maintained since it is mainly determined by secondary electron transport.

The same analysis was performed for the peak and valley doses at the edge of the array, where photons have a higher divergence, and the same conclusions were reached.

Table IV presents the effective reduction in computation time when EABSs are increased up

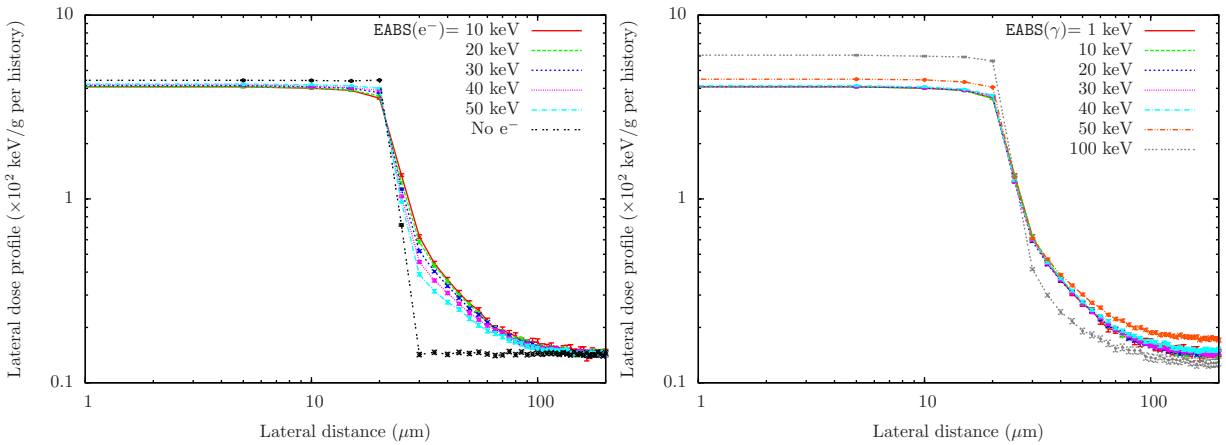

FIG. 1: *Lateral dose profile of the central microbeam at a depth of 2 cm in a water phantom for an MRT irradiation (50-μm-wide microbeams spaced by 400 μm; 2×2 cm² field size) considering different* EABS(e⁻)*, from 10 keV to 50 keV (left), and several* EABS(γ)*, from 1 keV to 100 keV (right). Statistical uncertainty bars are at 2σ.*

to a maximum that guarantees the accuracy as analyzed above, *i.e.*, EABS(e⁻)= 20 keV and EABS(γ)=30 keV. A reduction of approximately 50% in calculation time is observed when EABS(e⁻) is increased from 10 keV (reference) to 20 keV. An additional reduction of 5% is achieved when EABS(γ) changes from 1 to 30 keV. The latter reduction in computation time is less effective because a 30 keV photon will mainly interact by the photoelectric effect and it will therefore be absorbed in any case. Consequently, the two situations (EABS(γ)=1 or 30 keV for an EABS(e⁻)= 20 keV) are similar in terms of computation time.

2. *Variance reduction techniques: interaction forcing*

In order to further minimize the computation time, VR techniques were explored [18, 40]. In particular, interaction forcing was applied to photon transport. Different values of the forcing factor FORCING, by which the mean free path of interactions will be reduced, were studied. Following the results of the last section, EABS(γ) was set to 30 keV and EABS(e⁻) to 20 keV. The gain in simulation time for the several FORCING values in a water phantom is reported in Table V. The optimum FORCING value is 75, which corresponds to a mean free path of approximately 1 mm for the mean energy of the spectrum (100 keV). Therefore, each photon interacts once in each bin, which has 1 mm size in depth. At this point, computation time has been reduced by a factor of 8 with respect to the case where no VR techniques and no optimization of the simulation parameters were applied.

3. *Other methods*

The improvement in the calculation time is proportional to the number of cores used when parallelizing the simulations. Additionally, the valley dose was calculated by averaging the valley dose of several dose bins. However, the dose assessment in voxelized and more complex geometries (or for deeper tumors) required some additional time. In order to perform a good estimation of the computation time, a real irradiation geometry case would have to be evaluated.

C. Calculations in voxelized structures: MRT irradiation of a dog's head

An example of a possible treatment plan in the forthcoming clinical trials in pets is presented in this section. Coronal, axial and sagittal views of the dog's head are plotted in Figure 2 (left). Dose distributions arising from an anterior-posterior (AP) MRT irradiation (field size of 2×2 cm²) of a dog's

TABLE IV: *Simulation times for different* `EABS` *values. Efficiency is expressed in terms of the number of days to reach a statistical uncertainty of 2% (2σ) in the central valley dose in a water phantom at a depth of 2 cm. Values are normalized with respect to the simulation time for the most conservative* `EABS` *(*`EABS`*(γ)= 1 keV,* `EABS`*(e^-)= 10 keV), which corresponds to 132 days on a 2.93 GHz Intel Xeon Processor X5670. Compiler: Intel Fortran (option -O3).* `FORCING`*=75.*

`EABS`(γ) (keV)	`EABS`(e^-) (keV)	Normalized simulation time
1	10	$\equiv$ 1.00
1	20	0.50
30	20	0.45

TABLE V: *Simulation times for different* `FORCING` *values: from 0 to 150 (*`EABS`*(γ)=30 keV,* `EABS`*(e^-)=20 keV). Efficiency is expressed in terms of the number days to reach a statistical uncertainty of 2% (2σ) in the central valley dose in a water phantom at a depth of 2 cm. Values are normalized with respect to the simulation time for* `FORCING`*=0, which corresponds to 515 days on a 2.93 GHz Intel Xeon Processor X5670. Compiler: Intel Fortran (option -O3).*

`FORCING`	Normalized simulation time
1	$\equiv$ 1.0
10	0.19
25	0.16
50	0.13
75	0.12
100	0.12
150	0.14

head were assessed in all the irradiated volume. Dose is reported as absorbed dose to medium.

Figure 2 (right) represents the dose map in the dog's head obtained when the bin size is equal to the voxel size ($0.074\times0.074\times0.125$ cm^3). Typical dose distribution maps, such as isodoses, used in radiotherapy are not useful in these kinds of spatially fractionated techniques since dose homogeneity in the target is not sought. Thus, quantitative data related to the peak doses, valley doses, and the corresponding PVDR is needed for the correct assessment of the treatment. To this end, the dose was computed on the micron scale in a region of interest (ROI) of $2.2\times13.5\times2.2$ cm^3. Voxels were divided into 75 parts along the transversal direction of the microbeams, which gives a dose bin size of approximately 10 μm. Along the other two directions, the bin size corresponded to the voxel size (bin volume of approximately 0.9×10^{-5} cm^3).

Figure 3 represents the central peak (left) and valley (right) values in function of depth. Dose in the air cavities is not represented due to the large inherent statistical uncertainties and because it is not clinically relevant. The enhancement both in the peak and valley dose deposition and the corresponding reduction in the PVDR at 3, 6 and 10.5 cm-depth from the phantom surface is due to the presence of bone. PVDR in function of depth is presented in Figure 4. PVDR takes values of approximately 25 in soft tissue (water), in agreement with the results presented in Section III A and in other papers [1, 22, 23].

The lateral dose profile in a 'virtual' tumor located at a depth of 4–5 cm is represented in Figure 5 (left). The profile in the healthy bone located at a depth of 10–11 cm is also shown in Figure 5 (right). In both cases, one can clearly see the variations in the peak dose due to the distinct path traversed by the different microbeams.

Relative uncertainties in the central peak and valley doses at the tumor position are in the order of 1.2% and 1.9% (2σ), respectively. These values comply with the accuracy of $\pm$2–5% in dose delivery that is required to effectively treat certain types of cancers and to reduce complications, as reflected in the 24 and 42 reports of the International Commission on Radiation Units and Measurements (ICRU) [48, 49].

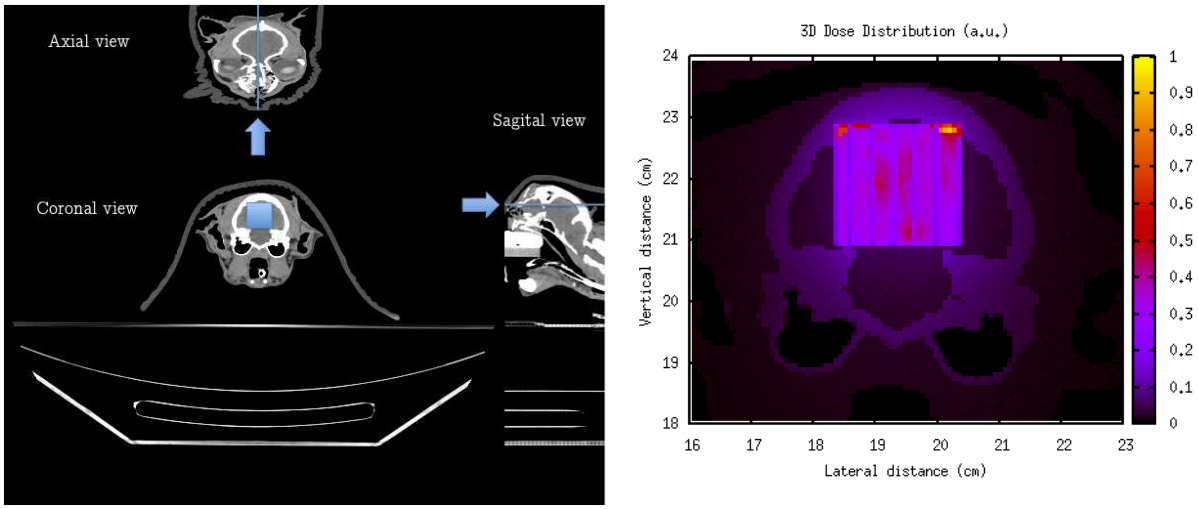

FIG. 2: *On the left, a coronal, axial and sagittal view of the irradiated dog's head. The arrow represents the beam direction (AP) and the line indicates the central part of the beam in depth. The square in the coronal view corresponds to the whole irradiation field size (2×2 cm^2). On the left, a dose map at a depth of 8 cm from the dog's head surface. MRT parameters: AP irradiation, 50-µm-wide microbeams spaced by 400 µm; field size: 2×2 cm^2.*

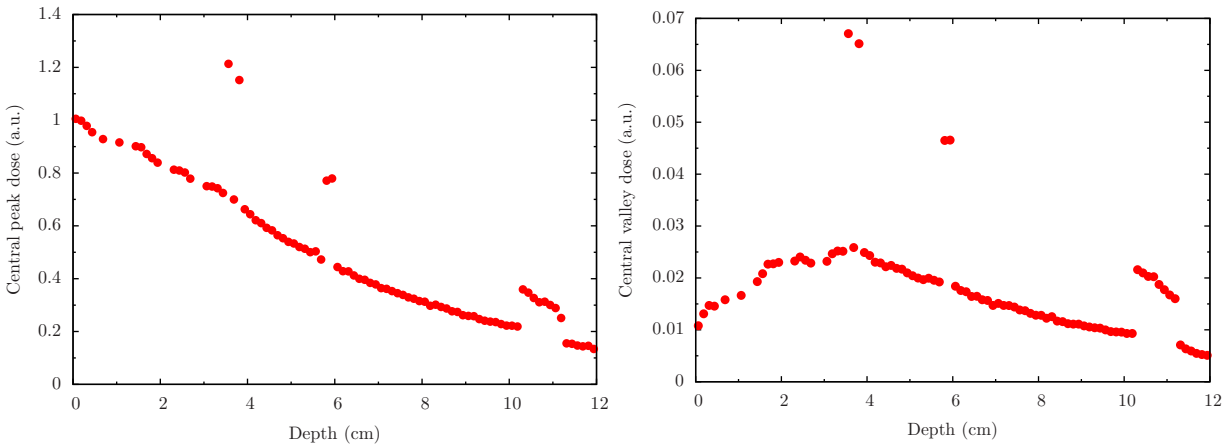

FIG. 3: *Depth dose curves along the central peak (left) and valley (right) in a dog's head. MRT parameters: AP irradiation, 50-µm-wide microbeams spaced by 400 µm; field size: 2×2 cm^2. The central part of the beam in depth is indicated by the solid lines in Figure 2 (left). Doses are normalized with respect to the central peak dose at the entrance. Statistical uncertainty bars are at two standard deviations.*

The final calculation time was less than one day (0.94 days) by using 60 cores (2.93 GHz Intel Xeon Processor X5670. Compiler: Intel Fortran, option -O3). Thus, this example confirms the feasibility of the TPS calculation engine developed for future clinical trials in MRT. The combination of the efficiency optimization methods described was enough to reduce the computation time to reasonable times for synchrotron radiation therapy on pets, *i.e.*, one day. It is important to note that the flexibility in the timings for clinical trials in synchrotrons is higher than in a pure clinical environment.

IV. CONCLUSIONS

The first MC-based calculation engine for the future treatment planning system in MRT has been developed. This will be an essential tool for future MRT clinical trials in pets. It was a non-trivial task due to the specific characteristics of an MRT irradiation.

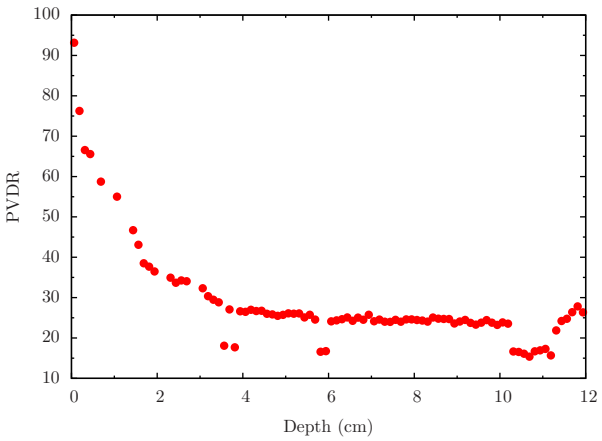

FIG. 4: *Central PVDR values in function of depth in a dog's head. MRT parameters: AP irradiation, 50-μm-wide microbeams spaced by 400 μm; field size: 2×2 cm^2. The central part of the beam in depth is indicated by the solid lines in Figure 2 (left). Statistical uncertainty bars are at two standard deviations.*

In our previous work, a photon source model was developed and verified in homogeneous phantoms. Thus, the first step of the present study included the validation of the dose calculations in heterogeneous phantoms. MC calculations reproduced the experimental peak doses and PVDR values within uncertainty bars. The following step consisted of the adaptation of the PENELOPE/penEasy code for the MRT dose calculation in micrometer-sized bins in voxelized structures. Finally, evaluation of the computation time and its minimization by means of optimization of the simulation parameters, the use of VR techniques and the parallelization of the simulations were assessed. Overall, the dose calculation time is adequate for pet radiotherapy in synchrotron facilities. An example of treatment planning scenario for AP irradiation of a dog's head has been presented, showing the performance of the developed MRT calculation engine. Future perspectives include integration of the developed MRT TPS calculation engine into a user-friendly graphical front-end.

Acknowledgments

The authors warmly thank the ESRF and the ID17 team, for support and granted beamtime. In particular, we are very grateful to H. Requardt. Thanks to G. Foerstner from the Systems and Communications group (ESRF) for her help in the use of the ESRF computing cluster. Many thanks to A. Sumova and B. Kaser-Hotz (AOI Center, Switzerland) for providing us with CT images of pets. We also acknowledge F. Pizzagalli (INSERM, Université Joseph Fourier) for discussions on image processing. JS acknowledges partial financial support from the Spanish Ministerio de Ciencia e Innovación (project no. FPA2009-14091-C02-01) and from the Spanish Networking Research Center CIBER-BBN.

[1] I. Martínez-Rovira, J. Sempau and Y. Prezado, "Development and commissioning of a Monte Carlo photon beam model for the forthcoming clinical trials in Microbeam Radiation Therapy", Med. Phys. **39**, 119–131 (2012).

[2] E. Siegbahn, J. Stepanek, E. Bräuer-Krisch and A. Bravin, "Determination of dosimetrical quantities used in microbeam radiation therapy (MRT) with Monte Carlo simulations", Med. Phys. **33**, 3248–3259 (2006).

[3] F. A. Dilmanian *et al.*, "Response of rat intracranial 9L gliosarcoma to microbeam radiation therapy", Neuro Oncol. **4**, 26–38 (2002).

[4] W. Zeman, H. J. Curtis and C. Baker, "Histopathologic effect of high-energy-particle microbeams on the visual cortex of the mouse brain", Rad. Res. **15**, 496–514 (1961).

[5] H. J. Curtis, "The use of a deuteron microbeam for simulating the biological effects of heavy cosmic-ray particles", Rad. Res. Suppl. **7**, 258–264 (1967).

[6] J. A. Laissue *et al.*, "The weanling piglet cerebellum: a surrogate for tolerance to MRT (Microbeam Radiation Therapy) in pediatric neuro-oncology", SPIE **4508**, 65–73 (2001).

[7] N. Zhong, G. M. Morris, T. Bacarian, E. M. Rosen and F. A. Dilmanian, "Response of rat skin to high-dose unidirectional x-ray microbeams: a histological study", Radiat. Res. **160**, 133–142 (2003).

[8] M. Miura, H. Blattmann, E. Bräuer-Krisch, A. Bravin, A. L. Hanson, M. M. Nawrocky, P. L.

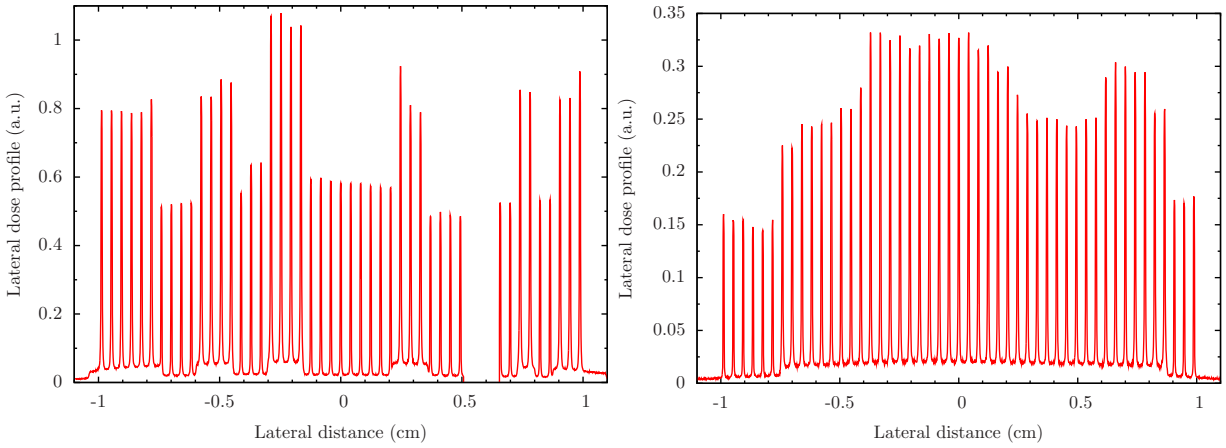

FIG. 5: *Horizontal lateral dose profile at the center of the dog's brain for a 'virtual' tumor located at a depth of 4–5 cm (left) and for the healthy bone located between 10–11 cm depth (right) from the dog surface. The central part of the beam in depth is indicated by the solid lines in Figure 2 (left). MRT parameters: AP irradiation, 50-μm-wide microbeams spaced by 400 μm; field size: 2×2 cm^2. Doses are normalized with respect to the central peak dose at the entrance. Statistical uncertainty bars are at two standard deviations.*

Micca, D. N. Slatkin and J. A. Laissue, "Radiosurgical palliation of aggressive murine SCCVII squamous cell carcinomas using synchrotron-generated X-ray microbeams", Br. J. Radiol. **79**, 71–75 (2006).

[9] P. Régnard *et al.*, "Irradiation of intracerebral 9L gliosarcoma by a single array of microplanar x-ray beams from a synchrotron: balance between curing and sparing", Phys. Med. Biol. **53**, 861–878 (2008).

[10] R. Serduc *et al.*, "Characterization and quantification of cerebral edema induced by synchrotron x-ray microbeam radiation therapy", Phys. Med. Biol. **53**, 1153–1166 (2008).

[11] A. Bouchet *et al.*, "Preferential effect of synchrotron microbeam radiation therapy on intracerebral 9L gliosarcoma vascular networks", Int. J. Radiation Oncology Biol. Phys. **78**, 1503–1512 (2010).

[12] M. Renier, T, Brochard, C. Nemoz, H. Requardt, E. Bräuer-Krisch, F. Estève, J. Balosso, P. Suortti, J. Baruchel, H. Elleaume, G. Berruyer, P. Berkvens and A. Bravin, "The radiotherapy clinical trials projects at the ESRF: Technical aspects", Eur. J. Radiol. **68S** S147–S150 (2008).

[13] E. Braüer-Krisch, R. Serduc, E. A. Siegbahn, G. Le Duc, Y. Prezado, A. Bravin, H. Blattmann and J. A. Laissue, "Effects of pulsed, spatially fractionated, microscopic synchrotron X-ray beams on normal and tumoral brain tissue", Mutation Research **704**, 160–166 (2010).

[14] G. Gokeri and C. Kocar and M. Tombakoglu, "Monte Carlo simulation of microbeam radiation therapy with an interlaced irradiation geometry and an Au contrast agent in a realistic head phantom", Phys. Med. Biol. **55**, 7469–7487 (2010).

[15] B. P. Poncelet, V. J. Wedeen, R. M. Weisskoff and M. S. Cohen, "Brain parenchyma motion: measurement with cine echo-planar MR imaging", Radiology **185** 645–651 (1992).

[16] E. Braüer-Krisch, H. Requardt, T. Brochard, G. Berruyer, M. Renier, J. A. Laissue, and A. Bravin, "New technology enables high precision multislit collimators for microbeam radiation therapy", Rev. Sci. Intrum. **80**, 074301-1–074301-6 (2009).

[17] Y. Prezado, M. Vautrin, I. Martínez-Rovira, A. Bravin, P. Berkvens and J. F. Adam, "Dosimetry protocol for the forthcoming clinical trials in synchrotron radiation therapy (SSRT)", Med. Phys. **38** 1709–1717 (2011).

[18] F. Salvat, J. M. Fernández-Varea and J. Sempau, "PENELOPE-2008, a Code System for Monte Carlo Simulation of Electron and Photon Transport" (OECD Nuclear Energy Agency, Issy-les-Molineaux, France, 2008).

[19] J. Baró, J. Sempau, J. M. Fernández-Varea and F. Salvat, "PENELOPE: An algorithm for Monte Carlo simulation of the penetration and energy loss of electrons and positrons in matter", Nucl. Instrum. Meth. B **100** 31–46 (1995).

[20] J. Sempau, E. Acosta, J. Baró, J. M. Fernández-Varea and F. Salvat, "An algorithm for Monte Carlo

simulation of coupled electron-photon transport", Nucl. Instrum. Meth. B **132** 377–390 (1997).

[21] H. Nettelbeck, G. J. Takacs, M. L. F. Lerch and A. B. Rosenfeld, "Microbeam radiation therapy: A Monte Carlo study of the influence of the source, multislit collimator, and beam divergence on microbeams", Med. Phys. **36**, 447–456 (2009).

[22] I. Martínez-Rovira, J. Sempau, J.M. Fernández-Varea, A. Bravin and Y. Prezado, "Monte Carlo dosimetry for forthcoming clinical trials in x-ray microbeam radiation therapy", Phys. Med. Biol. **55**, 4375–4388 (2010).

[23] I. Martínez-Rovira and Y. Prezado, "Monte Carlo dose enhancement studies in microbeam radiation therapy", Med. Phys. **38** 4430–4438 (2011).

[24] Y. Prezado, I. Martínez-Rovira, S. Thengumpallil and P. Deman, "Dosimetry protocol for the preclinical trials in white-beam minibeam radiation therapy", Med. Phys. **38** 5012–5020 (2011).

[25] D. E. Cullen, J. H. Hubbell and L. Kissel, "EPDL97: The evaluated photon data library, 97 version", Report UCRL-50400 vol 6 (Lawrence Livermore Nation Laboratory, Livermore, 1997).

[26] ICRU Report 37, "Stopping Powers for Electrons and Positrons" (ICRU, Bethesda, 1984)

[27] F. Salvat, A. Jablonski and C. J. Powell, "ELSEPA—Dirac partial-wave calculations of elastic scattering of electrons and positrons by atoms, positive ions and molecules", Comput. Phys. Commun. **165** 157–190 (2005).

[28] J. Sempau and P. Andreo, "Configuration of the electron transport algorithm of PENELOPE to simulate ion chambers", Phys. Med. Biol. **51**, 3533–3548 (2006).

[29] J. Sempau, A. Badal and L. Brualla, "A PENELOPE-based system for the automated Monte Carlo simulation of clinacs and vodelized geometries – Application to far-from-axis fields", Med. Phys. **38** 5887–5895 (2011).

[30] M. Sánchez del Río, N. Canestrari, F. Jiang and F. Cerrina, "SHADOW3: A new version of the synchrotron x-ray optics modelling package", J. Synchrotron Rad. **18** 1–9 (2011).

[31] Gammex, http://www.gammex.com/.

[32] PTW, http://www.ptw.de/.

[33] ISP, http://www.gafchromic.com/

[34] Z. Cai, X. Pan, D. Hunting, P. Cloutier, R. Lemay and L. Sanche, "Dosimetry of ultrasoft x-rays (1.5 keV Al_{K_α}) using radiochromatic films and colour scanners", Phys. Med. Biol. **48** 4111–4124 (2003).

[35] J. C. Crosbie, I. Svalbe, S. M. Midgley, N. Yagi, P. A. W. Rogers and R. A. Lewis, "A method of dosimetry for synchrotron microbeam radiation therapy using radiochromic films of different sensitivity", Phys. Med. Biol. **53** 6861–6877 (2008).

[36] A. Niroomand-Rad, C. R. Blackwell, B. M. Coursey, K. P. Gall, J. M. Galvin, W. L. McLaughlin, Al. S. Meigooni, R. Nath, J. E. Rodgers and C. G. Soares, "Radiochromic film dosimetry: Recommendations of AAPM Radiation Therapy Committee Task Group 55", Med. Phys. **25** 2093–2115 (1998).

[37] R. E. Swing, "An Introduction to Microdensitometry" (SPIE Optical Engineering Press, Washington, 1998).

[38] K. Zimmer and G. Heltai, "Effect of properties of microdensitometers on the shape of the characteristic curve of the photographic emulsion", Spectrochimica Acta, **33B** 417–427 (1978).

[39] A. S. Aydarous, P. J. Darley and M. W. Charles, "A wide dynamic range, high-spatial-resolution scanning system for radiochromic dye films", Phys. Med. Biol. **46** 1379–1389 (2001).

[40] A. F. Bielajew and D. W. O. Rogers, "Variance-reduction techniques in Monte Carlo Transport of Electrons and Photons". Eds. T. M. Jenkins, W. R. Nelson and A. Rindi (Plenum, New York, 1988).

[41] A. Badal and J. Sempau, "A package of Linux scripts for the parallelization of Monte Carlo simulations, Comput. Phys. Comm. **175** (2006) 440–450.

[42] European Synchrotron Radiation Facility, http://www.esrf.eu/.

[43] L. Wang and C.-S. Chui and M. Lovelock, "A patient-specific Monte Carlo dose-calculation method for photon beams", Med. Phys. **25** 867–878 (1998).

[44] International Commission on Radiation Units and Measurements, "Photon, Electron, Proton and Neutron Interaction Data for Body Tissues", Report 46, Bethesda, MD (1992).

[45] J. M. Moran, D. W. Nigg, F. J. Wheeler and W. F Bauer, "Macroscopic geometric heterogeneity effects in radiation dose distribution analysis for boron neutron capture therapy", Med. Phys. **19** 723–732 (1992).

[46] L. Padilla, C. Lee, R. Milner, A. Shahlaee and W. E. Bolch, "Canine anatomic phantom for preclini-

cal dosimetry in internal emitter therapy", J. Nucl. Med. **49** 446–452 (2008).

[47] M. De Felici and R. Felici and M. Sánchez del Río and C. Ferrero and T. Bacarian and F. A. Dilmanian, "Dose distribution from x-ray microbeam arrays applied to radiation therapy: An EGS4 Monte Carlo study", Med. Phys. **32** 2455–2463 (2005).

[48] International Commission on Radiation Units and Measurements, "Determination of Absorbed Dose in a Patient Irradiated by Beams of X or Gamma Rays in Radiotherapy Procedures", Report 24, Bethesda, MD (1976).

[49] International Commission on Radiation Units and Measurements, "Use of Computers in External Beam Radiotherapy Procedures with High Energy Photons and Electrons", Report 42, Bethesda, MD (1987).

2.6 Paper V: Scatter factors assessment in MRT

Introduction

As has been explained in section 1.5.4.2, the absolute dosimetry in MRT is divided into two steps. Firstly, the dose in reference conditions (seamless field) is measured. The conversion of the dose deposited with that broad beam is then translated to peak dose by means of scatter factors. The objective of this part of the thesis consisted of evaluating scatter factors for the MRT clinical trial settings (50-μm-wide microbeams spaced by 400 μm).

Due to the complexity of the study, the scatter factors were computed by two MC codes: PENELOPE/PENEASY (see section 1.5.4.1) and GEANT4 [GEANT4 2005]); and experimentally by using several detector systems: HD-810 radiochromic films [ISP® 2012] and a LAC chamber of 4 cm diameter [PTW® 2012].

Scatter factors assessment in microbeam radiation therapy

Y. Prezado[1], I. Martínez-Rovira[2,3] and M. Sánchez[4]

[1] *Laboratoire Imagerie et Modélisation en Neurobiologie et Cancérologie IMNC - UMR 8165, Centre National de la Recherche Scientifique (CNRS), Campus Universitaire, Bât. 440, 15 rue Georges Clemenceau 91406 Orsay cedex.*

[2] *Institut de Tècniques Energètiques Universitat Politècnica de Catalunya, Diagonal 647, E-08028 Barcelona, Spain*

[3] *ID17 Biomedical Beamline, European Synchrotron Radiation Facility (ESRF), 6, Rue Jules Horowitz B.P. 220, F-38043 Grenoble Cedex, France and*

[4] *Servicio de Radiofísica, Complejo Hospitalario de Santiago de Compostela, Rúa Choupana S/N, 15706 Santiago de Compostela, Spain.*

Purpose: The success of the preclinical studies in Microbeam Radiation Therapy (MRT) paved the way to the clinical trials under preparation at the Biomedical Beamline of the European Synchrotron Radiation Facility. Within this framework, an accurate determination of the deposited dose is crucial. With that aim, the scatter factors, which translate the absolute dose measured in reference conditions (2×2 cm^2 field size at 2 cm-depth in water) to peak doses, were assessed.

Methods: Monte Carlo (MC) simulations were performed with two different widely used codes, PENELOPE and GEANT4, for the sake of safety. The scatter factors were obtained as the ratio of the doses that are deposited by a microbeam and by a field of reference size, at the reference depth. The calculated values were compared with experimental data obtained by radiochromic (ISP HD-810) films and a PTW 34070 Large Area Chamber.

Results: The scatter factors for different microbeam field sizes assessed by the two MC codes were in agreement and reproduced the experimental data within uncertainty bars. Those correction factors were shown to be non-negligible for the future MRT clinical settings: an average 30% lower dose was deposited by a 50 μm microbeam with respect to the reference conditions.

Conclusions: For the first time the scatter factors in MRT were systematically studied. They constitute an essential key to deposit accurate doses in the forthcoming clinical trials in MRT. The good agreement between the different calculations and experimental data confirms the reliability of this challenging micrometric dose estimation.

Keywords: Synchrotron radiation, Microbeam Radiation Therapy, small-field dosimetry, scatter factors, clinical trials

I. INTRODUCTION

A major restriction to achieve a curative radiotherapy (RT) treatment for some radioresistant tumors, like gliomas, is the high morbidity of the surrounding healthy tissue. This is also the case for tumors located close to an organ at risk, such as the spinal cord. In order to overcome this limitation, small radiation fields are increasingly used in the delivery of advanced RT techniques. This is the case of intensity modulated radiotherapy (IMRT) and stereotactic radiosurgery (SRS). The purpose is to try to take advantage of the so-called dose-volume effect: the smaller the field size is, the higher the tolerances of the healthy tissues are [1, 2]. In Microbeam Radiation Therapy (MRT), a new RT approach under development at the Biomedical Beamline of the European Synchrotron Radiation Facility (ESRF), the limits of the dose-volume effect are explored. The irradiation is performed with arrays of parallel beams whose widths range from 25 to 100 μm and their center-to-center (c-t-c) distances from 200 to 400 μm (spatial fractionation of the dose). The energy spectrum has a mean energy of 99 keV [3, 4]. The dose profiles consist of a pattern of peaks and valleys, *i.e.*, with high doses in the beam paths and

low doses in the spaces between them [5]. The minimum dose in the central region between two beams is named valley dose whereas the dose in the centre of each beam is the peak dose.

The preclinical studies performed until now showed that the combination of submillimetric field sizes and a spatial fractionation of the dose leads to an exceptional normal tissue resistance to very high doses (≥100 Gy) in one fraction [6–16] combined with ablation of highly aggressive tumor models, like 9L rat glioma [17–23]. The promising results obtained in those biological investigations paved the way to the clinical trials under preparation at the ESRF [24]. In this context, a precise knowledge of the dose deposited by the microbeams (peak doses) was essential.

The use of subcentimeter field sizes presents some challenges in order the dosimetry to be accurately characterized [25]. In particular, the electronic equilibrium that exists on the central axis of larger fields breaks down for narrow fluence profiles. Absorbed dose cannot be easily calculated and/or measured unless a state of electronic equilibrium exists, which only occurs at some distance into the medium (tissue) and for large fields [25, 26]. As the irradiation field size decreases, electronic equilibrium is lost, which translates into a remarkable fall off in ionization produced in the volume. For the energy spectrum used in MRT, the majority of the secondary electrons have ranges in water longer than 40 μm. Therefore, the electronic equilibrium condition is not satisfied for the MRT sizes used (≤100 μm). Additionally, small-field dose measurements are more susceptible to geometric imprecision and to dose-averaging effects of larger detectors [27]. If accurate characterization of small-field dosimetry in SRS and IMRT requires measurements that are time consuming and error prone, the dose assessment of the micrometer-sized fields used in MRT represents a great challenge.

This work reports the first systematic assessment of the scatter factors for the MRT clinical trials settings: 50 μm-wide microbeams with a c-t-c distance of 400 μm. Due to the fact that the determination of the scatter factors is very sensitive, it was performed both by Monte Carlo (MC) simulations and by experimental measurements, for the sake of safety.

II. MATERIALS AND METHODS

A. Radiation source and microbeam generation

At ID17 Biomedical Beamline, the x-rays source is situated 40.5 meters from the patient positioning system. It consists of two wigglers with 15 cm and 12.5 cm period, respectively, and a maximum magnetic field of 1.6 T. However, only the first wiggler is used in MRT irradiations. The x-ray energy spectrum after filtering ranges from about 27 to 600 keV, with a mean energy of around 99 keV [3, 4].

The microbeams are produced when a multislit collimator spatially fractionates the beam coming from the synchrotron source [28]. Targets are then vertically scanned through the microfractionated beam to deliver microplanes of x-rays.

The animals or samples are placed in a 3-axis Kappa-type high-precision goniometer (Huber, Germany) [24]. At that position, the maximum field dimensions achievable are 2.5 mm in height and 41 mm in width, approximately. Since the beam height is very thin, the animals or phantoms are scanned vertically through the beam. It has been demonstrated that the integration of the dose rate while scanning the ionization chamber with a constant and well-known speed is equivalent to measure the dose deposited with an uniform irradiation [40].

A more detailed technical description of the beamline layout can be found elsewhere [24].

B. MC simulations

In this work, two different MC codes were used, namely, PENELOPE 2008 [29, 30] and GEANT4 [31] were employed. Both codes were previously used for dose distribution assessment in MRT [3, 32, 33, 35, 36]. The coupled transport of photons and electrons and its interactions in a wide energy

range are considered.

In PENELOPE a careful implementation of accurate low energy electron cross sections, which are of particular importance in this work, was performed. The simulation algorithm is based on a scattering model that combines numerical databases with analytical cross sections for the different interaction mechanisms and it is applicable to energies (kinetic energies in the case of electrons and positrons) from a few hundred eV to 1 GeV. It uses a mixed simulation scheme in which hard interactions are simulated collision by collision and small angular deflections and energy losses are treated in a grouped manner.

Since the working energy range is a few hundreds of keV, the most relevant interactions are photoelectric effect and Compton scattering. The photoelectric cross sections used in PENELOPE are obtained by numerical interpolation in a table extracted from the Lawrence Livermore National Laboratory (LLNL) Evaluated Photon Data Library (EPDL) [37]. PENELOPE considers bounding effects and Doppler broadening when simulating Compton interactions.

In GEANT4, the simulations are made following an analytical approach that reproduces a set of processes, originally implemented in PENELOPE. An exception is the multiple scattering process, for which GEANT4 adopts an innovative advanced model. The results are reliable for energies ranging from a few hundred eV to 1 GeV [31]. The analytical model of the Compton scattering offers two additional features with respect to the corresponding parametrized model: Doppler broadening and the atomic relaxation resulting from the vacancy generated by the primary scattering.

While PENELOPE uses a pure class II algorithm, GEANT4 employs a combination of class II (bremsstrahlung) and class I (elastic, inelastic collisions) schemes. The comparison of results from both codes reinforces the confidence in our results.

1. Simulation geometry and irradiation configuration

A homogeneous RW3 (Goettingen White Water) solid-water phantom (30×30×12 cm^3) [39] and a water tank PTW MP3-P 41029 (35×35×38 cm^3) [39]) were considered in the simulations. Several irradiation geometries were investigated:

- seamless beams of 1×1, 2×2 and 3×3 cm^2;
- a 50 μm-wide and 2 cm-high microbeam;
- arrays of 50 μm-wide microbeams with a c-t-c distance of 400 μm covering different areas: 1×1, 2×2 and 3×3 cm^2.

These field sizes are foreseen to be the most frequently used in the forthcoming clinical trials with pets.

The simulation parameters were chosen as follows. In PENELOPE, the absorption energy was set to 1 keV. In PENELOPE, the cutoff energies for the production of hard inelastic events, WCC, and for the production of hard bremsstrahlung, WCR, were set equal to the absorption energy (1 keV). The average angular deflection between two consecutive hard elastic events, C1, and the maximum average fractional energy loss in a single multiple-scattering step, C2, were selected to be 0.1. In GEANT4, low energy electromagnetic processes were used with associated data G4EMLOW6.9. The default cut value for the production of secondary particles was set to 10 nm.

Doses were scored in voxels of 5 μm along the lateral direction of the microbeams, 2 mm in the vertical direction of the microbeam and 1 mm in depth in PENELOPE. The voxel size in GEANT4 calculations was 4 μm × 4 μm × 4 mm for the microbeams case and 4×4×4 mm for broad beam irradiation. Both sizes guaranteed that no volume averaging effects were encountered.

C. Scatter factors assessment

In the forthcoming clinical trials, the absolute dosimetry will be performed following the recommendations compiled in the International Agency

of Atomic Energy (IAEA) TRS 398 Code of Practice [38]. The first step in this dosimetry methodology is to measure the dose in reference conditions (seamless irradiation field).

In agreement with the TRS 398 for medium x-ray energies, the dose measurement in reference conditions is performed with a thimble ionization chamber [39]. The cavity volume of the ionization chamber (reference point of the chamber) was placed at 2 g cm^{-2} (reference depth). The reference field size was chosen to be 2×2 cm^2. Since the average electron range in water is in the order of 100 μm for our energy spectrum, the lateral electronic equilibrium is guaranteed for that field size.

As reported in section II.A, the maximum field dimensions achievable are 2.5 mm in height and 41 mm in width. Since the beam height is very thin, the animals or phantoms are scanned vertically through the beam. The dose delivered is equivalent to the dose deposited with an uniform irradiation [40].

To determine the dose deposited with one microbeam (peak dose) from the absolute dose measured in the broad beam configuration the scatter factors were used. They take into account the different contribution from the scattered radiation as a function of the field size. Due to the low energies used and the fact that the closest collimators are around 2 m away from the patient, the collimator scatter factor is negligible [40] and only the scatter radiation originated in the phantom has a contribution. Therefore, the phantom scatter factor Sp can be assumed to be equal to the total scatter factor. Sp for one microbeam was determined as the ratio of the dose deposited in the central point of the irradiated field at 2 cm-depth in water by the microbeam and the reference field. It can be expressed mathematically as:

$$S_{\text{p, microbeam}} = \frac{D_{\text{peak, 2 cm}}}{D_{\text{reference}}} \quad (1)$$

where $S_{\text{p, microbeam}}$ is the phantom scatter factor for one microbeam, $D_{\text{peak, 2 cm}}$ refers to the dose deposited by one microbeam (peak dose) at 2 cm depth in water, $D_{\text{reference}}$ is the absolute dose deposited by a 2×2 cm^2 field size at the same depth.

Both $D_{\text{peak, 2 cm}}$ and $D_{\text{reference}}$ were assessed by MC simulations (see details in section II.B.1.) and by measurements. The experimental evaluation was performed by using two alternative types of detectors [34]:

- Gafchromic films HD 810 [41], which provide a very high spatial resolution and a wide dose range (from 10 to 400 Gy). A microdensitometer was employed to read the films following the methodology described in the work of Martínez-Rovira *et al.* [4]. The microdensitometer gives as output a magnitude named 'pen deflection' (PD). The dose assessment was performed by comparing the PD of the different films with the PD of films irradiated with a well-known dose. To assure reproducibility, each irradiation was performed at least twice and each film was analyzed several times, as described elsewhere [4].

- A large Bragg Peak chamber (PTW 34070), also called LAC (large area chamber), with a diameter of 4 cm, following the method described in the work of Sánchez-Doblado *et al.* [42]. The collected charge by the LAC corresponds to both primary and scatter radiations.

To assess the peak dose at 2 cm-depth corresponding to an array of microbeams, the equation (1) is multiplied by a factor f_{array}, which takes into account the contribution of the tails of the microbeams to the central peak. To determine the peak and valley doses at any depth the percentage depth-dose curves, and PVDR ratios are used [5].

III. RESULTS AND DISCUSSION

In this section, the scatter factors determined both by simulations (MC) and experimentally will be presented.

A. Scatter factors for different broad beam configurations

The experimental evaluation of Sp for broad field sizes ($\geq$ 1 cm^2) was performed by using a thimble ionization chamber (IC) and gafchromic films (GF). Since this is a direct and accurate measurement, the excellent match (see table I) between MC and experiment data provided a first test of the calculations performance. A 9% lower dose is deposited with a 1×1 cm^2 with respect to the reference filed size, whereas an average 10% higher dose deposition is reached with a 3×3 cm^2 field size. Those values are consistent with the output factor estimation reported in the work of Prezado *et al.* [40] for same range of energies in Stereotactic Synchrotron Radiation Therapy (SSRT). Additionally, they reflect the fact that as the field size increases, the scatter factors take higher values since the contribution of the scattered radiation to the absorbed dose also augments.

B. Scatter factor of a 50 μm-wide and 2 cm-high microbeam

Table II shows the comparison among the $S_{\text{p, microbeam}}$ values assessed by MC simulations, by GF and by the Bragg-Peak chamber (LAC) method.

There is a good agreement between the results of the two different MC codes and between the calculations and the experimental data, which permits to validate the simulations. The differences observed between the two MC values are probably due to the different algorithms used by the two codes. The experimental uncertainty bars correspond to the standard deviation of the measurements. From the results in table II, it can be concluded that the contribution of the scatter radiation to the dose deposition in the central part of the radiation field is significantly less important for a microbeam than for the reference field size. The partial loss of electronic equilibrium due to the fact that some secondary electrons have a shorter range than the field size greatly contributes the drastic decrease (30%) of the dose deposited by one microbeam.

Table III presents the calculated (PENELOPE and GEANT4) and experimental (GF) f_{array} values for some microbeam arrays to be used in the future clinical trials. The contribution of microbeams tails leads to a 3%, 5% and 8% dose increase to the central beam of 1×1, 2×2 and 3×3 cm^2 arrays, respectively. The dedicated MRT treatment planning system (TPS) under preparation [4] will be able to calculate the f_{array} for any combination of arrays using the Sp value for one microbeam (50 μm-wide and 2 cm-high) as an input.

IV. CONCLUSIONS

The enhanced tissue dose tolerance to reduced field sizes is in the origin of increased use of smaller and smaller field sizes as, for example, in radiosurgery. An extreme case of this is a new approach called MRT, a synchrotron radiotherapy technique, in which micrometer-sized (50 μm) and spatially fractionated irradiation field sizes are employed. If small field dosimetry is widely known to be highly demanding and error prone, dose assessment in MRT represents a challenge. Within the framework of clinical trials preparation, a methodology to determine dose deposited by the very small fields used in MRT was developed. Since the reference dosimetry will be performed in seamless irradiation with an IC, the assessment of the scatter factors was essential. Due to the complexity of experimental measurements, two different methods were used and the results compared to two independent MC calculations. The good agreement among all the obtained values confirmed the reliability of this method.

V. ACKNOWLEDGEMENTS

We acknowledge the European Synchrotron Radiation Facility for the granted beamtime at the ID17 Biomedical Beamline. We warmly thank P. Berkvens and E. Bräuer for scientific discussions.

TABLE I: *Scatter factors for several seamless field sizes. MC values shows an excellent agreement with the two sets of experimental data. The uncertainties correspond to one standard deviation.*

Field size (cm^2)	MC simulations	Experimental data	
		IC	GF
1×1	0.91 ± 0.05	0.89 ± 0.03	0.90 ± 0.05
3×3	1.10 ± 0.05	1.10 ± 0.03	1.09 ± 0.05

TABLE II: *Scatter factors for one 50 μm-wide and 2 cm-high microbeam. The two sets of MC values and experimental data agree well within the uncertainty bars. The uncertainties correspond to one standard deviation.*

MC simulations		Experimental data	
PENELOPE	GEANT4	GF	LAC
0.68 ± 0.04	0.75 ± 0.04	0.72 ± 0.07	0.72 ± 0.10

TABLE III: *Comparison of the MC and experimental (films) f_{array} values (GF) for some microbeams arrays. The uncertainties correspond to one standard deviation.*

Field size (cm^2)	f_{array} MC simulations		f_{array} Experimental data
	PENELOPE	GEANT4	GF
1×1	1.03 ± 0.02	1.03 ± 0.02	1.04 ± 0.08
2×2	1.05 ± 0.02	1.04 ± 0.02	1.05 ± 0.08
3×3	1.08 ± 0.02	1.05 ± 0.02	1.05 ± 0.08

[1] H.J. Curtis, "The use of a deuteron microbeam for simulating the biological effects of heavy cosmic-ray particles", Rad. Res. Suppl. **7**, 250–7 (1967).

[2] Y.R. Lawrence, X.Q. Li, I. El Naqa, *et al.*, "Radiation dose-volume effects in the brain", Int. J. Radiat. Oncol. Biol. Phys. **76**, S20–27 (2010).

[3] E.A. Siegbahn, J. Stepanek, E. Brauer-Krisch, *et al.*, "Determination of dosimetrical quantities used in microbeam radiation therapy (MRT) with Monte-Carlo simulations", Med. Phys. **33**, 3248–3259 (2006).

[4] I. Martínez-Rovira, J. Sempau and Y. Prezado, "Development and commissioning of a MC photon beam model for the forthcoming clinical trials in Microbeam radiation therapy", Med. Phys. **39**, 119–132 (2012).

[5] I. Martínez-Rovira, J. Sempau, J.M. Fernández-Varea, *et al.*, "MC dosimetry for forthcoming clinical trials in x-ray microbeam radiation therapy", Phys. Med. Biol. **55**, 4375–88 (2010).

[6] R. Serduc, P. Vérant, J.C. Vial, *et al.*, "In vivo two-photon microscopy study of short-term effects of microbeam irradiation on normal mouse brain microvasculature", Int. J. Radiat. Oncol. Biol. Phys. **64**, 1519–1527 (2006).

[7] D. Slatkin, P. Spanne, F.A. Dilmanian, *et al.*, "Subacute neuropathological effects of microplanar beams of x-rays from a synchrotron wiggler", Proc. Natl. Acad. Sci. U.S.A. **92**, 8783–8787 (1995).

[8] J.A. Laissue, N. Lyubimova, H.P. Wagner, *et al.*, "Microbeam radiation therapy", SPIE **3770**, 38–45 (1999).

[9] F.A. Dilmanian, G. Morris, G. Le Duc, *et al.*, "Response of avian embryonic brain to spatially segmented x-ray microbeams", Cell Mol Biol (Noisy-le-grand) **47**, 485–493 (2001).

[10] J.A Laissue, H. Blattmann, M. Di Michiel, *et al.*, "The weanling piglet cerebellum: a surrogate for tolerance to MRT (Microbeam Radiation Therapy) in pediatric neuro-oncology", SPIE **4508**, 65–73 (2001).

[11] N. Zhong, G.M. Morris, T. Bacarian, *et al.*, "Response of rat skin to high-dose unidirectional x-ray microbeams: a histological study", Radiat. Res. **160**, 133–142 (2003).

[12] R. Serduc, T. Christen, J. Laissue, *et al.*, "Brain tumor vessel response to synchrotron microbeam radiation therapy: a short-term in vivo study", Phys. Med. Biol. **53**, 3609–3622 (2008).

[13] R. Serduc, Y. van de Looij, G. Francony, *et al.*, "Characterization and quantification of cerebral edema induced by synchrotron x-ray microbeam radiation therapy", Phys. Med. Biol. **53**, 1153–1166 (2008).

[14] A. Bouchet, B. Lemasson, G. Le Duc, *et al.*, "Preferential effect of synchrotron microbeam radiation therapy on intracerebral 9L gliosarcoma vascular networks", Int. J. Radiat. Oncol. Biol. Phys. **78**, 1503–1512 (2010).

[15] B. Van der Sanden, E. Brauer-Krisch, E. A. Siegbahn, *et al.*, "Tolerance of arteries of arteries to microplanar x-ray beam beams", Int. J. Radiat. Oncol. Biol. Phys. **77**, 1545–1552 (2010).

[16] F.A. Dilmanian, Z. Zhong, T. Bacarian, *et al.*, "Interlaced x-ray microplanar beams: a radiosurgery approach with clinical potential", Proc. Natl. Acad. Sci. U.S.A. **103**, 9709–9714 (2006).

[17] J.A. Laissue, G. Geiser, P.O. Spanne, *et al.*, "Neuropathology of ablation of rat gliosarcomas and contiguous brain tissues using a microplanar beam of synchrotron-wiggler-generated X rays", Int. J. of Cancer **78**, 654–660 (1998).

[18] H.M. Smilowitz, H. Blattmann, E. Bräuer-Krisch, *et al.*, "Synergy of gene-mediated immunoprophylaxis and microbeam radiation therapy for advanced intracerebral rat 9L gliosarcomas", J. Neurooncol. **78**, 135–43 (2006).

[19] P. Régnard, G. Le Duc, E. Bräuer-Krisch, *et al.*, "Irradiation of intracerebral 9L gliosarcoma by a single array of microplanar x-ray beams from a synchrotron: balance between curing and sparing", Phys. Med. Biol. **53**, 861–878 (2008).

[20] F.A. Dilmanian, T. Button, G. Le Duc, *et al.*, "Response of rat intracranial 9L gliosarcoma to microbeam radiation therapy", Neuro.-Oncol. **4**, 26–38 (2002).

[21] R. Serduc, E. Bräuer-Krisch, A. Bouchet, *et al.*, "First trial of spatial and temporal fractionations of the delivered dose using synchrotron microbeam radiation therapy", J. Synchrotron Radiat. **16**, 587–590 (2009).

[22] F.A. Dilmaniann, G. Morris, N. Zhong, *et al.*, "Murine EMT-6 carcinoma: high therapeutic efficacy of microbeam radiation therapy", Radiat. Res. **159**, 632–641 (2003).

[23] M. Miura, H. Blattmann, E. Bräuer-Krisch, *et al.*, "Radiosurgical palliation of aggressive murine SCCVII squamous cell carcinomas using synchrotron-generated x-ray microbeams ", Br. J. Radiol. **79**, 71–75 (2006).

[24] M. Renier, Th. Brochard, C. Nemoz, *et al.*, "The radiotherapy clinical trials projects at the ESRF: Technical aspects", Eur. J. Radiol. **68S**, 147–150 (2008).

[25] A.J.D. Scott, A.E. Nahum, J.D. Fenwick, *et al.*, "Using a Monte Carlo model to predict dosimetric properties of small radiotherapy photon fields", Med. Phys. **35**, 4671–4684 (2008).

[26] I.J. Das, G.X. Ding and A. Ahnesjö, "Small fields: Nonequilibrium radiation dosimetry", Med. Phys. **35**, 206–215 (2008).

[27] O.A. Sauer and J. Wilbert, "Measurements of output factors for small photon beams", Med. Phys. **34**, 1983–1988 (2007).

[28] E. Bräuer-Krisch, A. Bravin, L. Zhang, *et al.*, "New technology enables high precision multislit collimators for microbeam radiation therapy", Rev. Sci. Instrum. **80**, 0743011–6 (2009).

[29] F. Salvat, J.M. Fernández-Varea and J. Sempau, "PENELOPE, a code system for MC Simulation of electron and photon transport", OECD Nuclear Energy Agency (Issy-les-Moulineaux, France), 2008 (available in PDF-format from the web at www.nea.fr).

[30] J. Sempau, E. Acosta, J. Baró, *et al.*, "An algorithm for MC simulation of coupled electron-photon transport", Nucl. Instrum. Methods B **132**, 377–390 (1997).

[31] Geant4 Collaboration, http://wwwasd.web.cern.ch/wwwasd/Geant4/.

[32] J. Spiga, E.A. Siegbahn, E. Bräuer-Krisch, *et al.*, "The Geant4 toolkit for microdosimetry calculations: Application to microbeam radiation therapy (MRT)", Med. Phys. **34**, 4322–4330 (2007).

[33] Y. Prezado, G. Fois, G. Le Duc, *et al.*, "Gadolinium dose enhancement studies in microbeam radiation therapy", Med. Phys. **36**, 3568–74 (2009).

[34] Y. Prezado, I. Martínez-Rovira, S. Thengumpallil, *et al.*, "Dosimetry protocol for the preclinical trials in white-beam Minibeam Radiation Therapy", Med. Phys. **38** 5012–5021 (2011).

[35] Y. Prezado, S. Thengumpallil, M. Renier, *et al.*, "x-ray energy optimization in minibeam radiation therapy", Med. Phys. **36**, 4897–4902 (2009).

[36] I. Martínez-Rovira and Y. Prezado, "Monte Carlo dose enhancement studies in microbeam radiation therapy", Med. Phys. **38**, 4430–4440 (2011).

[37] D.E. Cullen *et al.*, "EPDL97: The evaluated photon data library", Report UCRL-50400 vol6 (Livermore, CA: Lawrence Livermore National Laboratory) (1997).

[38] International Atomic Energy Agency (IAEA), "Absorbed dose determination in external beam radiotherapy: An International Code of Practice for Dosimetry based on Standards of Absorbed Dose to Water", IAEA Technical Reports Series 398 (Vienna: IAEA) (2005).

[39] PTW, www.ptw.de.

[40] Y. Prezado, I. Martínez-Rovira, S. Thengumpallil, *et al.*, "Dosimetry protocol for the forthcoming clinical trials in Synchrotron Stereotactic Radiation Therapy (SSRT)", Med. Phys. **38** 1709–1717 (2011).

[41] ISP, http://online1.ispcorp.com/.

[42] F. Sánchez-Doblado, G.H. Hartmann, J. Pena, *et al.*, "A new method for output factor determination in MLC shaped narrow beams", Phys. Med. **23**, 58–66 (2007).

2.7 Paper VI: Dosimetry protocol for the preclinical trials in white-beam MBRT

Introduction

The aim of this work consists of the assessment of several dosimetric features for forthcoming preclinical studies in white-beam MBRT. The first part is related to the establishment of a dosimetry protocol to ensure reproducibility in terms of dose for future MBRT biological studies in rats. The protocol is based on absorbed dose to water and inspired by the recommendations of the TRS 398 [IAEA-TRS-398 2005]. See sections 1.5.4.2 and 1.6.4. As in MRT, determination of the absorbed dose under non-reference conditions is performed by means of scatter factors, which were evaluated by MC calculations and verified experimentally.

The second part of this study deals with the experimental benchmarking of the MBRT MC simulations (PENELOPE/PENEASY CODE, see section 1.5.4.1). To this end, part of the ID17 photon source model previously defined for MRT was used (see section 2.5). The validation was carried out by using HD-810 radiochromic films [ISP® 2012] in homogeneous and heterogeneous phantoms.

Dosimetry protocol for the preclinical trials in white-beam minibeam radiation therapy

Y. Prezado[a)]
ID17 Biomedical Beamline, European Synchrotron Radiation Facility (ESRF), 6, Rue Jules Horowitz B.P.220, 38043 Grenoble, France

I. Martínez-Rovira
ID17 Biomedical Beamline, European Synchrotron Radiation Facility (ESRF), 6, Rue Jules Horowitz B.P. 220, 38043 Grenoble Cedex, France and Institut de Tècniques Energètiques, Universitat Politècnica de Catalunya, Diagonal 647, E-08028 Barcelona, Spain

S. Thengumpallil
ID17 Biomedical Beamline, European Synchrotron Radiation Facility (ESRF), 6, Rue Jules Horowitz B.P.220, 38043 Grenoble, France and Dipartimento di Fisica "E. Amaldi", Università degli Studi Roma Tre, 84, Via della Vasca Navale, 00146 Rome, Italy

P. Deman
ID17 Biomedical Beamline, European Synchrotron Radiation Facility (ESRF), 6, Rue Jules Horowitz B.P.220, 38043 Grenoble, France; INSERM, U836, Equipe 6, F-38042 Grenoble 9, France; and University Grenoble 1, F-38041 Grenoble, France

(Received 15 April 2011; revised 8 June 2011; accepted for publication 17 June 2011; published 11 August 2011)

Purpose: In the quest of a curative radiotherapy treatment for gliomas, new delivery modes are being explored. At the Biomedical Beamline of the European Synchrotron Radiation Facility, a new spatially fractionated technique, called minibeam radiation therapy (MBRT), is under development. The aims of this work were to assess different dosimetric aspects and to establish a dosimetry protocol to be applied in the forthcoming animal (rat) studies in order to evaluate the therapeutic index of this new radiotherapy approach.
Methods: Absolute dosimetry was performed with a thimble ionization chamber (PTW semiflex 31010) whose center was positioned at 2 g cm^{-2} depth. To translate the dose measured in broad beam configuration to the dose deposited with a minibeam, the scatter factors were used. Those were assessed by using the Monte Carlo simulations and verified experimentally with Gafchromic films and a Bragg Peak chamber. The comparison of the theoretical and experimental data were used to benchmark the calculations. Finally, the dose distributions in a rat phantom were evaluated by using the validated Monte Carlo calculations.
Results: The absolute dosimetry in broad beam configuration was measured in reference conditions. The dose rate was in the range between 168 and 224 Gy/min, depending on the storage ring current. A scatter factor of 0.80 ± 0.04 was obtained. Percentage depth dose and lateral profiles were evaluated both in homogenous and heterogeneous slab phantoms. The general good agreement between Monte Carlo simulations and experimental data permitted the benchmark of the calculations. Finally, the peak doses in the rat head phantom were assessed from the measurements in reference conditions. In addition, the peak-to-valley dose ratio values as a function of depth in the rat head were evaluated.
Conclusions: A new promising radiotherapy approach is being explored at the ESRF: Minibeam Radiation Therapy. To assess the therapeutic index of this new modality, in vivo experiments are being planned, for which an accurate knowledge of the dosimetry is essential. For that purpose, a complete set of measurements and Monte Carlo simulations was performed. The first dosimetry protocol for preclinical trials in minibeam radiation therapy was established. This protocol allows to have reproducibility in terms of dose for the different biological studies. [DOI: 10.1118/1.3608908]

Key words: synchrotron radiation, minibeam radiation therapy, dosimetry, Monte Carlo simulations

I. INTRODUCTION

Conventional radiation therapy, a major treatment modality for cancers, can prove ineffective at times. Its failure appears to be primarily related to constraints on delivering a curative radiation dose due to the critical morbidity of normal tissues. Despite intensive research and development work in conformal radiotherapy, there are still some radioresistant tumors, like gliomas, for which a radical treatment is usually not

feasible at hospitals. This limitation is especially severe in children, due to the high risk of complications in the development of the central nervous system. The management of tumors close to an organ of risk, like the spinal cord, is also restrained.

This is the motivation for the development of two new radiotherapy techniques at the Biomedical Beamline of the European Synchrotron Radiation Facility (ESRF): microbeam radiation therapy (MRT) and, more recently, minibeam radiation therapy (MBRT). These techniques present two distinct features with respect to the conventional radiotherapy methods that allow to shift the normal tissue tolerances to higher doses:

(1) Submillimetric field sizes are used, exploring the limits of what is called dose-volume effect: the smaller the field size is, the higher the tolerances of the healthy tissues are.[1,2] The beam width range from 25 to 100 μm in the case of MRT and from 500 to 700 μm in MBRT. The use of those extremely thin beam widths, at least one order of magnitude thinner than the ones used in radiosurgery, may permit a rapid increase in healthy tissue tolerances.
(2) The dose is spatially fractionated: very high doses ($\geq$100 Gy) are delivered in one fraction by using intense x-rays parallel beams. The interbeam separation is 200 or 400 μm in the case of MRT and 600 μm in MBRT. The dose profiles consist of a pattern of peaks and valleys, *i.e.*, with high doses in the beam paths and low doses in the spaces between them.[3] The minimum dose in the central region between two beams is named valley dose and the dose in the center of the beam is the peak dose. The different widths and spacings in MRT and MBRT might lead to dissimilar biological effects, which need to be evaluated.

In MRT the combination of submillimetric field sizes and a spatial fractionation of the dose leads to an exceptional normal tissue resistance to very high doses ($\geq$100 Gy) in one fraction.[4–14] In addition, MRT rendered significant tumor growth delay and, in some cases, complete tumor ablation.[15–21] This was despite the small fraction of the tumor mass irradiated with the high dose microbeams, fact that appear to challenge many of the current paradigms in conventional radiation therapy. The preferential effect on malignant tissues has been mainly attributed to selective effects of microbeams on immature tumor vessels versus lack of microbeam effects on the differentiated normal vasculature,[18] although other factors might be operative. Aimed at the tumor volume, the microbeams interact in tissue, delivering a lethal radiation dose to endothelial cells lying directly in their path, *i.e.*, peak regions. In normal tissue, the well-preserved vasculature in the valley regions seemed to ensure the rapid regeneration of directly irradiated blood vessels. It is therefore essential that the valley dose is kept to the minimum to ensure the preservation of normal tissue architecture[18] and the survival of sufficient cells needed for healthy tissue repair. Based on these assumptions, the effectiveness of MRT is determined by the peak-to-valley dose ratio (PVDR). Therefore, PVDR is a relevant dosimetric parameter in spatially fractionated techniques.[3,18]

The main drawback of MRT is that its widespread clinical implementation is limited nowadays due to the requirement of high dose rates, only available at synchrotrons. This is due to the fact that since microbeams are closely packed, it is important that the tissue/target does not move during the irradiation due to the cardiosynchronous pulsations.[22] The thicker beams used in MBRT, a new radiotherapy approach, overcome those difficulties. The dose profiles of minibeams are not as vulnerable as the ones of microbeams to beam smearing from cardiac pulsations, and therefore high dose rates are not needed. Hence, it is conceptually possible to extend this technique by using modified x-ray equipment, creating an opportunity for its implementation at hospitals. In addition, the use of higher beam energies in MBRT ($\geq$200 keV (Ref. 23)) than in MRT is feasible,[24] resulting in a lower entrance dose to deposit the same integral dose in the tumor. Those advantages triggered the exploration of this new radiotherapeutic approach.

Since the thicker beams and spacings employed in MBRT in comparison with the thin microbeams may lead to different biological effects than the ones observed in MRT,[25] experimental studies are warranted to evaluate the possible different tumor and normal tissue responses to MBRT with respect to MRT and the other radiotherapy methods. Functional tissue deterioration rather than direct cellular damage in the beam path may be involved in MBRT.[25] The results of the first animal experiments performed at Brookhaven National Laboratory indicate that the thicker beams used in MBRT still provide a remarkable healthy tissue tolerances.[14] This outcome paved the way to the implementation of this novel technique at the ESRF ID17 Biomedical Beamline.[26] MBRT might offer a good compromise between providing a good healthy tissue sparing and having the possibility of being extended outside synchrotron sources with a cost-effective equipment. Preclinical studies with small animals are being planned at the ESRF in order to assess the tumor control and normal tissue complication probability curves for this new therapeutic modality.

The precise knowledge of the doses in the preclinical studies is crucial in order to extract valid conclusions for the future possible clinical trials, like the assessment of dose-response of healthy tissues or tumor control probability curves. For that reason an extensive set of measurements and Monte Carlo (MC) simulations were performed in different phantoms. The agreement between the calculations and the experimental data allowed the benchmarking of the MC dosimetry. Finally, the first dosimetry protocol to be used in the preclinical trials was established and it will be described, hereafter.

II. MATERIALS AND METHODS

II.A. Radiation source and minibeams patterns generation

At ID17 Biomedical Beamline, the x-rays source consists in two wigglers with 15 and 12.5 cm period, respectively, and a maximum magnetic field of 1.6 T. In MBRT studies only the first wiggler is used. It is located 40.5 m from the patient positioning system and delivers high intensity

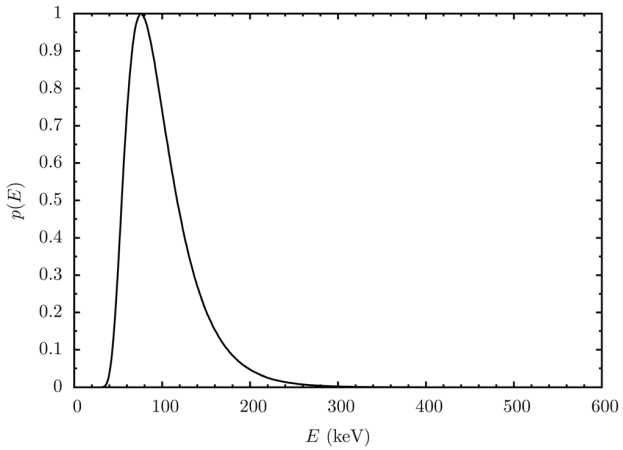

FIG. 1. Energy spectrum at the goniometer (patient) position at ID17 Biomedical Beamline, extracted from Ref. 27.

kilovoltage energy x-ray beams. The x-ray energy spectrum after filtering ranges from about 50 to 600 keV, with a mean energy around 99 keV.[27] The energy spectrum (Fig. 1) and beam divergence at the sample position was assessed from a complete modeling of the beamline and benchmarked with experimental data.[27]

The animals or samples are placed in a three-axis Kappa-type high-precision goniometer (Huber, Germany).[28] See Fig. 2. At that position, the maximum field dimensions achievable are 2.5 mm in height and 41 mm in width, approximately. Since the beam height is very thin, the animals or phantoms are scanned vertically through the beam.[29]

An original method was developed and tested at the ESRF ID17 Biomedical Beamline to produce the minibeam patterns. It utilizes a specially developed high-energy white-beam chopper whose action is synchronized with the vertical motion of the target moving at constant speed. Each opening of the chopper generates a horizontal beam print. The method offers an excellent reliability and allows for an easy control of all the parameters which are essential for the general safety of the treatment.[26]

A more detailed technical description of the beamline layout can be found elsewhere.[28]

II.B. Monte Carlo simulations

The MC code PENELOPE 2008 (Refs. 30–32) and penEasy,[33] a structured general-purpose main program for PENELOPE, were adopted to perform the calculations. In this code, the coupled transport of photons and electrons and its interactions in a wide energy range are considered. The main advantage of this code is a careful implementation of accurate low energy electron cross sections, which are of particular importance in this work. The simulation algorithm is based on a scattering model that combines numerical databases with analytical cross section models for the different interaction mechanisms and it is applicable to energies (kinetic energies in the case of electrons and positrons) from a few hundred electron volts to 1 GeV. PENELOPE uses a mixed simulation scheme in which hard interactions are simulated collision by collision and small angular deflections and energy losses are treated in a grouped manner (the thresholds depend on the simulation parameters).

Since the working energy range is a few hundreds of kilo electron volts the most relevant interactions are photoelectric effect and Compton scattering. The photoelectric cross sections used in PENELOPE are obtained by interpolation in a numerical table that was extracted from the Lawrence Livermore National Laboratory (LLNL) evaluated photon data library (EPDL).[34] Regarding Compton scattering, PENELOPE considers bounding effects and Doppler broadening when simulating Compton interactions. This code has been widely used in the medical physics field, see for example Refs. 35, 36 and in particular for the dose distribution assessment in MRT and MBRT.[3,23,24,37,38]

II.B.1. Simulation geometry and irradiation configuration

Three geometries were considered in the simulations:

(1) A homogeneous RW3 (Goettingen White Water) solid-water phantom ($30 \times 30 \times 12$ cm^3).[39]
(2) A heterogeneous slab phantom ($20 \times 20 \times 5$ cm^3) consisting of one slab of bone equivalent material (1 cm thick), two muscle equivalent slabs and two others of RW3 (1 cm-thick each one).[40]
(3) A rat head phantom consisting in layers of skin (700 μm), bone (500 μm), and brain (2.6, 5.2, and 2 cm thickness in lateral, anterior–posterior, and craneo-caudal axis, respectively). See Fig. 3. Those thicknesses were extracted from MRI images.[23]

Two irradiation geometries were investigated: a unidirectional array (600 μm wide minibeams with a center-to-center

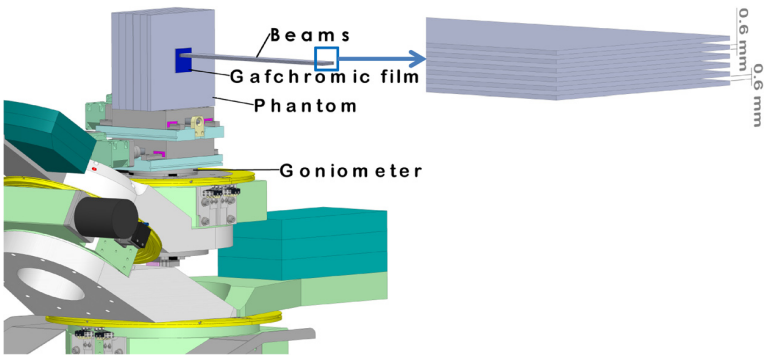

FIG. 2. Scheme of the irradiation setup. The samples are positioned on top of a high-precision goniometer whose vertical translation allows to cover the desired field size.

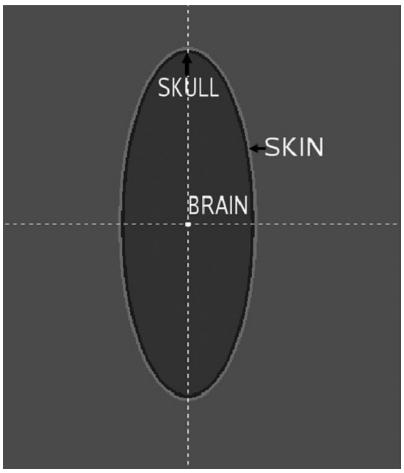

FIG. 3. Coronal view of the rat head phantom. The thickness of the skin (700 μm), the skull (500 μm) and the brain (2.6 and 5.2 cm in the lateral and anterior–posterior directions, respectively) were extracted from MRI images Ref. 23.

(c-t-c) distance of 1200 μm), and two orthogonal arrays, one of them in the lateral direction (right to left), the other in the craneo-caudal axis. The two arrays intersected in the target position such that the peaks of one of them fill the valleys of the other. This permitted to achieve a quasi-homogeneous dose distribution in the target. A beam width of 640 μm and a c-t-c distance of 1120 μm were found to provide a homogenous dose distribution in a rat head phantom. Further details will be given in Sec. III B. In the rat, the target was the central plane of the tumor position. At the Biomedical Beamline (ESRF) the tumor is usually inoculated at caudate nucleus (9 mm anterior to the ear-bars, *i.e.*, at bregma site, 3.5 mm lateral to the midline, 5.5 mm depth from the skull).[41,42]

The dose computation was divided into two parts. The absorbed dose distribution for a single minibeam in the phantom was simulated first. Then, at each depth, the single dose distribution was shifted and added to the total dose distribution in order to cover the irradiation field sizes: 1×1, 2×2, and 3×3 cm^2. Only the 1×1 cm^2 field size was evaluated in the rat head phantom.

The absorption energy was set to 50 keV for electrons and 5 keV for photons. The cutoff energies for the production of hard inelastic events, WCC, and for the production of hard bremsstrahlung, WCR were set equal to the absorption energy for electrons and photons, respectively. The average angular deflections between two consecutive hard elastic events, C1, and the maximum average fractional energy loss in a single multiple-scattering step, C2, were selected to be 0.1.

Doses were scored in voxels of 50 μm along the lateral direction of the microbeams, 2 mm in the vertical direction of the microbeam and 1 mm in depth. These dimensions were reduced to 25 μm $\times$ 1 mm $\times$ 0.07 mm for the rat head phantom as a higher spatial resolution was required.

The average statistical uncertainty in the simulations was 0.5% (two standard deviations).

II.C. Dosimetry protocol

This protocol describes a methodology for dosimetry in MBRT preclinical studies. It is based on absorbed dose to water and inspired by the recommendations compiled in the IAEA TRS 398 Code of Practice.[43] The main advantage of this methodology is that biological studies can be made on the basis of uniform dosimetry procedures. The different points of this protocol are described hereafter.

II.C.1. Dosimetry equipment

Following the recommendations of the TRS 398 for medium x-ray energies, the dose measurement in reference conditions (see Sec. II C 2) was performed with a semiflex PTW 30010 thimble ionization chamber (0.125 cm^3).[39] As reported in Sec. II A, the maximum field dimensions achievable are 2.5 mm in height and 41 mm in width. Since the beam height is very thin, the animals or phantoms are scanned vertically through the beam. It has been demonstrated that the integration of the dose rate, while scanning the ionization chamber with a constant and well known speed is equivalent to measure the dose deposited with a uniform irradiation.[29]

The experimental evaluation of the peak dose was performed by using two altenative type of detectors:

- Gafchromic films HD 810,[44] which provide a very high spatial resolution and a wide dose range (from 10 to 400 Gy). This permits to measure peak and valley doses. A widely used flat bed scanner (EPSON Perfection V750 PRO) was used to analyze the dose deposition in the films following the methodology described in the work by Devic *et al.*[45]
- A large Bragg Peak chamber (PTW 34070), also called as large area chamber (LAC), with a diameter of 4 cm. The collected charge corresponds to both primary and scatter radiations.

Dose measurements were performed both in the homogeneous RW3 (Goettingen White Water) solid-water and the heterogeneous phantoms[39] described in Sec. II B. The use of the RW3 instead of water to perform the dosimetry was due to several practical aspects. First, very small misalignments of any element of the beamline or beam emittance changes can lead to differences in dose of up to 10%. Therefore the dose must be measured before each experiment and/or refill of the storage ring. An accurate setting of a water tank in the experimental area at the Biomedical Beamline is very time-consuming. Another reason to use a solid-water phantom is that the handling and accurate positioning of the Gafchromic films to be used in relative dosimetry is very delicate in water. Since the MC simulations were performed in solid-water phantoms and the correlation between the dose deposited in the RW3 and the rat head phantom was established, developing a protocol based on solid-water phantom measurements does not lead to a lack of consistency. In addition, the code of practice TRS 398 (Ref. 43) states that solid-water phantoms could be used for routine measurements provided that the relationship between dosimetry readings in water

and in the solid-water phantom has been established. A 5.7% ± 0.1% higher dose deposition in water with respect to RW3 was encountered both by comparing experimental measurements and MC simulations. Consequently, to develop a protocol for preclinical work based on measurements in a solid-water phantom is justified.

II.C.2. Determination of absorbed dose under reference conditions

The first step in this dosimetry methodology is to measure the dose in reference conditions. Following the recommendations of the TRS 398 (Ref. 43) for medium x-ray energies, the center of the cavity volume of the ionization chamber (reference point of the chamber) was placed at 2 g cm^{-2} (reference depth). The reference field size was chosen to be 2×2 cm^2. Since at the working range of energies the average range of the electrons is less than 100 μm, the lateral electronic equilibrium is guaranteed for that field size. The phantom material was chosen to be RW3 for the reasons explained in Sec. II C 1.

The absorbed dose in the solid-water phantom is then obtained by using the following expression:

$$D_{\mathrm{sw},Q} = M_Q N_{D,\mathrm{sw},Qo} K_{Q,Qo} \quad (1)$$

where $N_{D,\mathrm{sw},Qo}$ is the calibration factor for the beam quality Qo in water provided by the calibration laboratory,[46] corrected by the 5.7% ± 0.1% difference in dose deposition in water with respect to RW3. M_Q is the reading of the dosimeter with the reference point of the chamber positioned at the reference depth and corrected for the influence quantities like temperature and pressure (K_{TP}), ionic recombination (K_s), polarity effect (K_{pol}), and electrometer calibration (K_{elec}). $K_{Q,Qo}$ is a chamber-specific factor which corrects for differences between the reference beam quality Qo and the actual beam quality being used Q. Since the Bragg–Gray theory cannot be applied in our case (the secondary electron range is around 10 μm, much smaller than the detector volume[47]), it is recommended to obtain $K_{Q,Qo}$ from measurements. The calibration laboratory has provided us with the calibration factor in ^{60}Co and some correction factors $K_{Q,Qo}$, around 4%, for different x-ray beam qualities close to our spectrum. The $K_{Q,Qo}$ value for the closest spectrum (140 kV, 0.5 mm Cu) is 0.953 ± 0.031.

II.C.3. Determination of absorbed dose under nonreference conditions

II.C.3.a. Peak dose: assessment of the scatter factors. To translate the absolute dose measured in the broad beam configuration to the dose deposited with a minibeam (peak dose), the scatter factors were used. They take into account the different contribution from the scattered radiation as a function of the field size. Due to the low energies used and the fact that the closest collimators are around 2 m away from the patient, the collimator scatter factor is negligible[29] and only the scatter radiation originated in the phantom will have a contribution. Therefore, the phantom scatter factor S_p can be assumed to be equal to the total scatter factor. S_p was determined as the ratio of the dose deposited in the central point of the irradiated field at 2 cm-depth in water by the minibeam and the reference field. Hence, the peak dose at 2 cm-depth in the solid-water phantom can be determined as:

$$D_{\mathrm{peak,2\,cm}} = D_{\mathrm{reference}} \times S_{\mathrm{p}} \times f_{\mathrm{array}} \quad (2)$$

where $D_{\mathrm{peak,2cm}}$ refers to the dose deposited by one minibeam (peak dose) at 2 cm depth in water, $D_{\mathrm{reference}}$ is the absolute dose deposited by a 2×2 cm^2 field size at the same depth, S_{p} is the phantom scatter factor for one minibeam and f_{array} is a factor that takes into account the contribution of the tails of the minibeams to the central peak when an array is used. S_{p} and f_{array} were assessed by using MC simulations and verified experimentally by using two different methods:

- The ratio of the dose deposited at 2 cm-depth in the RW3 phantom with a 2×2 cm^2 and a 600 μm × 2 cm field was assessed by using Gafchromic films.[44]
- The method described in the work of Sánchez-Doblado *et al.*[48] were followed by employing the LAC described in Sec. II C 1.

II.C.3.b. Relative dosimetry: dose distributions. The depth dose curves were assessed by placing Gafchromic films in the central axis of the phantom which was previously aligned with the beam axis. The lateral profiles were evaluated by irradiating films with different field sizes at different depths. As it has already been stated in the introduction, different biological studies suggest that PVDR is a very relevant dosimetric parameter in spatially fractionated techniques.[3,18] Therefore, PVDR values were studied.

II.C.3.c. Absorbed dose in the rat head phantom. Absolute peak dose at 1 cm-depth (middle line of the brain) in the rat head phantom ($D_{\mathrm{peak,1cm,rat}}$) is obtained from the peak dose at 2 cm-depth in the solid-water phantom ($D_{\mathrm{peak,2\ cm}}$), see Eq. (2), by means of a precalculated (MC) calibration factor ($f_{\mathrm{swater,rat}}$), as expressed by the following equation:

$$D_{\mathrm{peak,\,1\,cm,\,rat}} = D_{\mathrm{peak,\,2\,cm}} \times f_{\mathrm{swater,\,rat}}. \quad (3)$$

The dose at any other point within the rat head phantom can be evaluated by means of the percentage depth dose curves (PDD) and PVDR values.

III. RESULTS

In this section, absolute dosimetry (reference conditions) performed with the protocol described in Sec. II C and the relative dose distributions will be reported. The comparison of the experimental data with MC simulations was used to benchmark the calculations. Dose distributions in the rat head phantom will also be presented.

III.A. Absolute dosimetry

A value of $\dot{D}_{\mathrm{reference}} = 67.2\,\mathrm{Gy/s/mA}$ was obtained for an electron beam current in the storage ring of 189.41 mA. The range of dose rate went from 168 Gy/min for a beam current

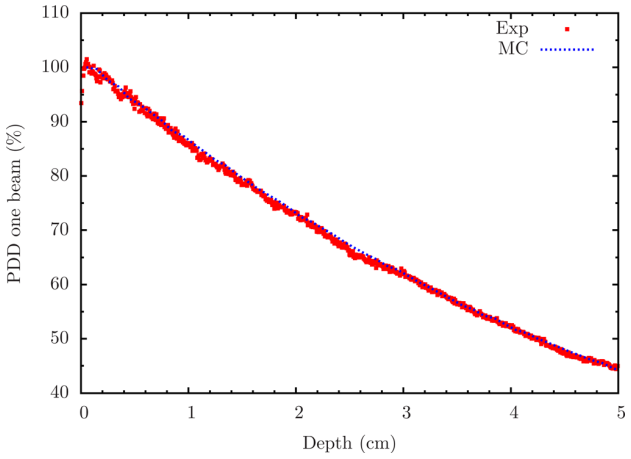

FIG. 4. Experimental (points) and MC PDD (dashed lines) curves for the central minibeam of an array covering an area of 2×2 cm^2.

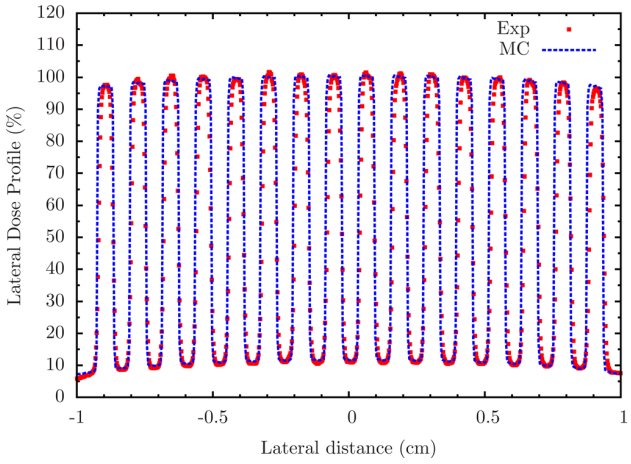

FIG. 5. Experimental (points) and MC (dashed lines) lateral dose profiles at 2 cm-depth for a field size of 2×2 cm^2.

of 150 mA to 224 Gy/min for a beam current of 200 mA, that is to say, one order of magnitude higher than the 6 Gy/min achievable in Rapid Arc (Ref. 49) or VMAT machines.[50]

The peak dose at 2 cm-depth in water was then obtained from $D_{\text{reference}}$ by using Eq. (2). S_p was assessed by using MC simulations (0.80 ± 0.04) and verified with experimental data as described in Sec. II C. A value of 0.77 ± 0.06 was obtained by using Gafchromic films, whereas the LAC chamber method provided a value of 0.82 ± 0.08. Therefore a good agreement was achieved. The correction factor f_{array} amounted to 1.09 ± 0.02.

III.B. Relative dosimetry: dose distributions

In this section, the experimental dose distributions obtained when the slabs phantoms (both homogenous and heterogeneous) were irradiated with a unilateral array of minibeams were compared with MC simulations. In addition, the quality of the interlaced configuration was assessed by using Gafchromic films.

III.B.1. Dose distributions in solid-water phantoms

The PDD and lateral dose profiles were evaluated both experimentally and theoretically (MC) for different field sizes (1×1, 2×2, and 3×3 cm^2).

Figure 4 depicts the PDD curves for the central minibeam of an array covering an area of 2×2 cm^2. A good agreement between calculations and experimental data was obtained, the global difference being lower than 2%. A satisfactory match was also achieved for the 1×1 and 3×3 cm^2 field sizes. A small buildup (around 800 μm) in the PDD was observed and consistent with the results of Prezado *et al.*[29]

Figure 5 shows how the MC simulations reproduce the experimental lateral dose profile at 2 cm-depth assessed by Gafchromic films. Systematic comparisons of theoretical and experimental PVDR values at different depths and several field sizes for the homogenous phantom were performed (see Table I).

Calculations and experimental data agreed within the error bars (corresponding to extended uncertainty, $k = 2$). PVDR values diminished as a function of depth, rapidly in the first centimeter and very smoothly after 2 cm-depth. A descend of PVDR values was also observed when the field size (number of beams) augmented, in agreement with other works.[24,51] The smaller the field sizes were, the more important the decrease in PVDR was, since the tails of the extreme minibeams in the array contribute more to the central valley than in larger field sizes.

Table II shows the satisfactory match of the theoretical and experimental data in a heterogeneous phantom for

TABLE I. Experimental (Exp) and theoretical (MC) PVDR values for different field sizes as a function of depth in a homogenous solid-water phantom.

	PVDR 1×1 cm^2		PVDR 2×2 cm^2		PVDR 3×3 cm^2	
Depth (cm)	MC	Exp	MC	Exp	MC	Exp
0.3	23.4 ± 0.2	21.7 ± 2.2	14.04 ± 0.07	15.2 ± 1.6	10.6 ± 0.1	11.3 ± 1.2
0.5	20.6 ± 0.2	17.4 ± 1.8	12.24 ± 0.06	12.8 ± 1.2	9.33 ± 0.08	9.8 ± 1.0
1.0	17.4 ± 0.2	17.5 ± 1.8	10.05 ± 0.05	9.6 ± 1.0	7.65 ± 0.07	8.1 ± 0.8
2.0	15.4 ± 0.1	16.1 ± 1.6	8.44 ± 0.04	9.3 ± 1.0	6.29 ± 0.05	6.9 ± 0.6
4.0	14.0 ± 0.1	15.1 ± 1.6	7.38 ± 0.04	8.6 ± 0.8	5.23 ± 0.05	5.9 ± 0.6
6.0	13.4 ± 0.1	12.8 ± 1.2	6.94 ± 0.04	7.5 ± 0.8	4.85 ± 0.05	5.4 ± 0.6
8.0	12.9 ± 0.2	12.7 ± 1.2	6.67 ± 0.04	6.7 ± 0.6	4.56 ± 0.05	5.1 ± 0.6

TABLE II. Experimental (Exp) and simulated (MC) PVDR values in a heterogeneous phantom, consisting in 1 cm of bone equivalent material, 2 cm of muscle equivalent slabs, and 2 cm of RW3.

	PVDR 1×1 cm^2		PVDR 2×2 cm^2		PVDR 3×3 cm^2	
Depth (cm)	MC	Exp	MC	Exp	MC	Exp
1.0	12.02 ± 0.09	11.0 ± 1.1	7.45 ± 0.07	7.4 ± 0.7	5.94 ± 0.06	5.9 ± 0.6
2.0	13.6 ± 0.1	13.9 ± 1.4	7.50 ± 0.08	8.1 ± 0.8	5.54 ± 0.06	6.4 ± 0.6
3.0	14.1 ± 0.2	13.8 ± 1.4	7.59 ± 0.09	7.8 ± 0.8	5.59 ± 0.06	6.2 ± 0.6
4.0	14.5 ± 0.2	14.0 ± 1.4	7.8 ± 0.1	8.1 ± 0.8	5.66 ± 0.07	6.2 ± 0.6

several depths. Just after the bone (at 1 cm-depth), PVDR values fell with respect to the homogenous case. Their decrease was more important the smaller the field size was. This PVDR reduction in bone is due to the increase of the fluence of photons that are Compton scattered into the valley region. These photons have a larger probability per unit mass of undergoing a photoelectric absorption in bone since its average atomic number is higher. This results in a higher local dose deposition.[3] The PVDR in depth (4 cm) were similar to the ones obtained in the homogenous one (the absolute peak doses being different in the two cases).

The general good agreement between calculations and experimental data achieved permitted to validate the simulations, which showed their performance even in the presence of heterogeneities.

In order to study, the quality of the interlacing at the approximately the tumor position in a rat head phantom, the dose distributions at 1 cm-depth in the solid-water phantom were measured with Gafchromic films. Figure 6 shows that the dose distribution fulfills the requirements to be considered as homogeneous: the dose in the target fitted within 95%–107% of the prescribed dose.[52]

III.C. Dose distributions in a rat head phantom

Absolute peak dose at 1 cm-depth in the rat head phantom irradiated with an array of eight minibeams covering a 1×1 cm^2 field size was determined by using Eq. (3). The dose at any other point within the rat head phantom can be evaluated by means of the PDD and PVDR values. Figures 7 and 8 depict the PDD curves and PVDR, respectively, as a function of depth. An enhanced dose deposition in the bone can be clearly observed in the PDD due to its higher effective atomic number. In parallel, the PVDR falls off rapidly in the bone as it was explained in Sec. III B 1. In the central part of the brain the PVDR remain almost constant. The same trend was observed in other MRT studies.[3]

Regarding the interlaced configuration, it was determined that a factor 1.12 higher dose in the target was obtained with respect to peak dose in a unidirectional array at the same position. This value was obtained by dividing the calculated dose deposited in the central part of the dose profiles in the interlaced and unidirectional configurations. This factor (1.12) should be taken into account in the dose prescriptions.

IV. CONCLUSIONS

Minibeam radiation therapy is an innovative synchrotron radiation therapy technique with potential of application outside synchrotron sources. Biological studies are planned to evaluate the therapeutic effectiveness of this new approach. For that purpose, a reliable and reproducible dosimetry protocol is essential. In this context, a complete set of measurements and MC calculations were performed on solid-water phantoms and in a rat head phantom for the first time. The spatial dose distributions, depth dose curves and lateral

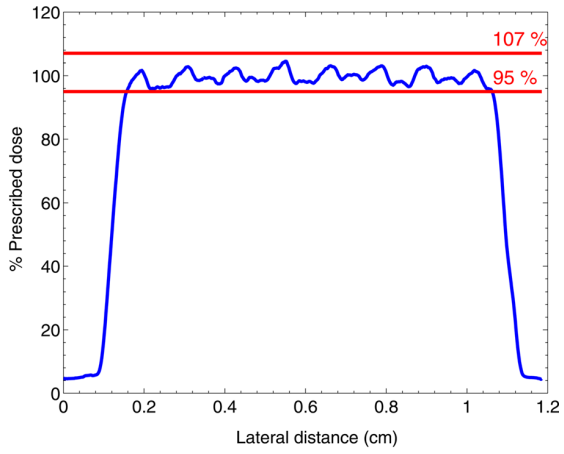

FIG. 6. Dose distribution at 1 cm-depth for an interlaced configuration measured by using the Gafchromic films. The dose distribution fits within the recommended limits (Ref. 52).

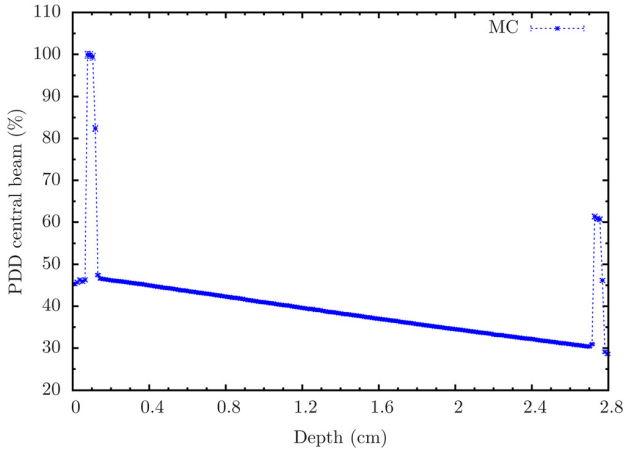

FIG. 7. PDD for the central minibeam in the rat head phantom. An enhancement of dose deposition is observed in the bone due to its high effective atomic number.

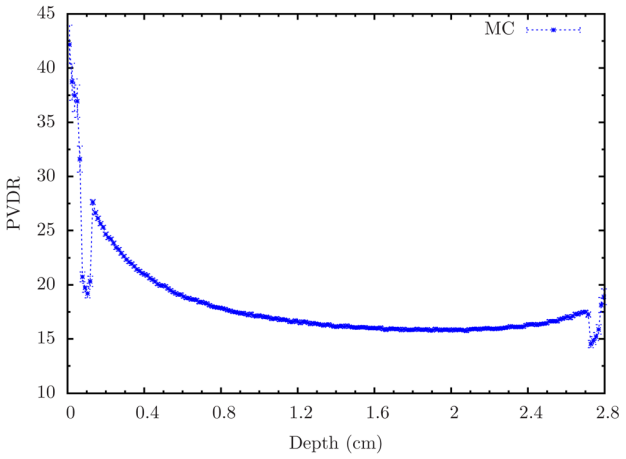

FIG. 8. PVDR values as a function of depth in the rat head phantom.

profiles, were evaluated. The satisfactory agreement between theoretical and experimental values allowed to validate the MC simulations, that had proven their performance not only for homogenous medium but also in presence of heterogeneities. This permitted to establish the first dosimetry protocol to guide the foreseen preclinical studies with small animals. The reproducibility and reliability of this protocol is a relevant feature to perform those biological studies aiming to assess dose-response curves for normal tissue complication probability (NTCP) and tumor control probability (TCP), with the goal of determining the possible therapeutic window for this new radiotherapy modality.

ACKNOWLEDGMENTS

The authors warmly thank ID17 Biomedical Beamline (ESRF) for the granted beamtime and specially M. Renier and C. Nemoz for support in the realization of the experiments.

[a]Electronic mail: prezado@gmail.com

[1]H. J. Curtis, "The use of a deuteron microbeam for simulating the biological effects of heavy cosmic-ray particles," Radiat. Res. Suppl. **7**, 250–257 (1967).
[2]Y. R. Lawrence, X. Q. Li, I. El Naqa, C. A. Hahn, L. B. Marks, T. E. Merchant, and A. P. Dicker, "Radiation dose-volume effects in the brain," Int. J. Radiat. Oncol. Biol. Phys. **76**, S20–S27 (2010).
[3]I. Martínez-Rovira, J. Sempau, J. M. Fernández-Varea, A. Bravin, and Y. Prezado, "MC dosimetry for forthcoming clinical trials in x-ray microbeam radiation therapy," Phys. Med. Biol. **55**, 4375–4388 (2010).
[4]R. Serduc *et al.*, "In vivo two-photon microscopy study of short-term effects of microbeam irradiation on normal mouse brain microvasculature," Int. J. Radiat. Oncol. Biol. Phys. **64**, 1519–1527 (2006).
[5]D. Slatkin, P. Spanne, F. A. Dilmanian, J. O. Gebbers, and J. A. Laissue, "Subacute neuropathological effects of microplanar beams of x-rays from a synchrotron wiggler," Proc. Natl. Acad. Sci. U.S.A. **92**, 8783–8787 (1995).
[6]J. A. Laissue *et al.*, "Microbeam radiation therapy," Proc. SPIE **3770**, 38–45 (1999).
[7]F. A. Dilmanian *et al.*, "Response of avian embryonic brain to spatially segmented x-ray microbeams," Cell Mol. Biol. (Noisy-le-grand) **47**, 485–493 (2001).
[8]J. A. Laissue *et al.*, "The weanling piglet cerebellum: a surrogate for tolerance to MRT (Microbeam Radiation Therapy) in pediatric neuro-oncology," Proc. SPIE **4508**, 65–73 (2001).
[9]N. Zhong, G. M. Morris, T. Bacarian, E. M. Rosen, and F. A. Dilmanian, "Response of rat skin to high-dose unidirectional x-ray microbeams: a histological study," Radiat. Res. **160**, 133–142 (2003).
[10]R. Serduc *et al.*, "Brain tumor vessel response to synchrotron microbeam radiation therapy: a short-term in vivo study," Phys. Med. Biol. **53**, 3609–3622 (2008).
[11]R. Serduc *et al.*, "Characterization and quantification of cerebral edema induced by synchrotron x-ray microbeam radiation therapy," Phys. Med. Biol. **53**, 1153–1166 (2008).
[12]A. Bouchet *et al.*, "Preferential effect of synchrotron microbeam radiation therapy on intracerebral 9L gliosarcoma vascular networks," Int. J. Radiat. Oncol. Biol. Phys. **78**, 1503–1512 (2010).
[13]B. Van der Sanden, E. Brauer-Krisch, E. A. Siegbahn, C. Ricard, J. C. Vial, and J. Laissue, "Tolerance of arteries of arteries to microplanar x-ray beam beams," Int. J. Radiat. Oncol. Biol. Phys. **77**, 1545–1552 (2010).
[14]F. A. Dilmanian *et al.*, "Interlaced x-ray microplanar beams: a radiosurgery approach with clinical potential," Proc. Natl. Acad. Sci. U.S.A. **103**, 9709–9714 (2006).
[15]J. A. Laissue *et al.*, "Neuropathology of ablation of rat gliosarcomas and contiguous brain tissues using a microplanar beam of synchrotron-wiggler-generated x rays," Int. J. Cancer **78**, 654–660 (1998).
[16]H. M. Smilowitz *et al.*, "Synergy of gene-mediated immunoprophylaxis and microbeam radiation therapy for advanced intracerebral rat 9L gliosarcomas," J. Neurooncol. **78**, 135–43 (2006).
[17]P. Régnard *et al.*, "Irradiation of intracerebral 9L gliosarcoma by a single array of microplanar x-ray beams from a synchrotron: balance between curing and sparing," Phys. Med. Biol. **53**, 861–878 (2008).
[18]F. A. Dilmanian *et al.*, "Response of rat intracranial 9L gliosarcoma to microbeam radiation therapy," Neuro Oncol. **4**, 26–38 (2002).
[19]R. Serduc, E. Brauer-Krisch, A. Bouchet, L. Renaud, T. Brochard, A. Bravin, J. A. Laissue, and G. Le Duc, "First trial of spatial and temporal fractionations of the delivered dose using synchrotron microbeam radiation therapy," J. Synchrotron Radiat. **16**, 587–590 (2009).
[20]F. A. Dilmanian *et al.*, "Murine EMT-6 carcinoma: high therapeutic efficacy of microbeam radiation therapy," Radiat. Res. **159**, 632–641 (2003).
[21]M. Miura *et al.*, "Radiosurgical palliation of aggressive murine SCCVII squamous cell carcinomas using synchrotron-generated x-ray microbeams," Br. J. Radiol. **79**, 71–75 (2006).
[22]B. P. Poncelet, V. J. Wedeen, R. M. Weisskopf, and M. S. Cohen, "Brain parenchyma motion: measurement with cine echo-planar MR imaging," Radiology **85**, 645–651 (1992).
[23]Y. Prezado, G. Fois, G. Le Duc, and A. Bravin, "Gadolinium dose enhancement studies in microbeam radiation therapy," Med. Phys. **36**, 3568–74 (2009).
[24]Y. Prezado, S. Thengumpallil, M. Renier, and A. Bravin, "X-ray energy optimization in minibeam radiation therapy," Med. Phys. **36**, 4897–4902 (2009).
[25]A. Uyama, T. Kondoh, K. Nariyama, K. Umetani, M. Fukumoto, K. Shinoharad, and E. Kohmuraa, "A narrow microbeam is more effective for tumor growth suppression than a wide microbeam: an in vivo study using implanted human glioma cells," J. Synchrotron Radiat. **18**, 671–678 (2011).
[26]Y. Prezado, M. Renier, and A. Bravin, "A new method of creating minibeam patterns for synchrotron radiation therapy: a feasibility study," J. Synchrotron Radiat. **16**, 582–586 (2009).
[27]I. Martínez-Rovira, J. Sempau, and Y. Prezado, "Development and commissioning of a MC photon beam model for the forthcoming clinical trials in Microbeam radiation therapy" (submitted).
[28]M. Renier *et al.*, "The radiotherapy clinical trials projects at the ESRF: technical aspects," Eur. J. Radiol. **68S**, S147–S150 (2008).
[29]Y. Prezado, M. Vautrin, I. Martínez-Rovira, A. Bravin, F. Estève, H. Elleaume, P. Berkvens, and J. F. Adam, "Dosimetry protocol for the forthcoming clinical trials in synchrotron stereotactic radiation therapy (SSRT)," Med. Phys. **38**, 1709–1717 (2011).
[30]F. Salvat, J. M. Fernández-Varea, and J. Sempau, *PENELOPE, a code system for MC Simulation of electron and photon transport*, OECD Nuclear Energy Agency, Issy-les-Moulineaux-France, 2003 Available in PDF-format from the web at www.nea.fr.
[31]J. Sempau, E. Acosta, J. Baró, J. M. Fernández-Varea, and F. Salvat, "An algorithm for MC simulation of coupled electronphoton transport," Nucl. Instrum. Methods B **132**, 377–390 (1997).
[32]F. Salvat, J. M. Fernández-Varea, and J. Sempau, *PENELOPE, a code system for MC Simulation of electron and photon transport* (OECD Nuclear Energy Agency, Issy-les-Moulineaux-France, 2003), Available in PDF-format from the web at www.nea.fr.
[33]J. Sempau and A. Badal, "PenEasy, a modular main program and voxelised geometry package for PENELOPE," (2008), http://www.upc.edu/inte/downloads/penEasy.htm

[34]D. E. Cullen, J. H. Hubbell, and L. Kissel, "EPDL97 the evaluated data library, 097 version," Report No. UCRL-50400, 6 (Lawrence Livermore National Laboratory, Livermore (USA), 1997).
[35]J. Sempau, A. Sánchez-Reyes, F. Salvat, H. Oulad ben Tahar, S. B. Jiang, and J. M. Fernández-Varea, "Monte Carlo simulation of electron beams from an accelerator head using PENELOPE," Phys. Med. Biol. **46**, 1163–86 (2001).
[36]J. Torres, M. J. Buades, J. F. Almansa, R. Guerrero, and A. M. Lallena, "Dosimetry characterization of 32P intravascular brachytherapy source wires using MC codes PENELOPE and GEANT4," Med. Phys. **31**, 296–304 (2004).
[37]E. A. Siegbahn, J. Stepanek, E. Brauer-Krisch, and A. Bravin, "Determination of dosimetrical quantities used in microbeam radiation therapy (MRT) with Monte-Carlo simulations," Med. Phys. **33**, 3248–3259 (2006).
[38]J. Spiga, E. A. Siegbahn, E. Brauer-Krisch, P. Randaccio, and A. Bravin, "The GEANT4 toolkit for microdosimetry calculations: application to microbeam radiation therapy (MRT)," Med. Phys. **34**, 4322–4330 (2007).
[39]www.ptw.de.
[40]www.gammex.com.
[41]N. Kobayashi, N. Allen, N. R. Clendenon, and L. W. Ko, "An improved rat brain-tumor model," J. Neurosurg. **53**, 808–815 (1980).
[42]G. Paxinos and C. Watson, *The Rat Brain in Stereotaxic Coordinates*, 4th ed. (Academic, New York, 1986).
[43]International Atomic Energy Agency "Absorbed dose determination in external beam radiotherapy: an international code of practice for dosimetry based on standards of absorbed dose to water," IAEA Technical Reports Series 398 (IAEA, Vienna, 2005).
[44]ISP advanced materials, http://online1.ispcorp.com/.
[45]S. Devic, J. Seuntjens, E. Sham, E. B. Podgorsak, C. Ross Schmidtlein, A. S. Kirov, and G. Soares, "Precise radiochromic film dosimetry using a flat-bed document scanner," Med. Phys. **32**, 2245–2253 (2005).
[46]www.ptw.de/ssdlcalibration.html.
[47]C. M. Ma and A. E. Nahum, "Bragg-Gray theory and ion chamber dosimetry for photon beams," Phys. Med. Biol. **36**, 413–428 (1991).
[48]F. Sánchez-Doblado, G. H. Hartmann, J. Pena, J. V. Rosello, G. Russiello, and D. M. Gonzalez-Castaño, "A new method for output factor determination in MLC shaped narrow beams," Phys. Med. **23**, 58–66 (2007).
[49]C. Clifton, P. Zhang, Y. Archambauld, J. Bocanek, G. Tang, and T. LoSasso," Commissioning and quality assurance of rapidarc radiotherapy delivery system," Int. J. Rad. Oncol. Biol. Phys. **72**, 575–581 (2008).
[50]V. Fleygelman, G. Zhang, and C. Stevens, "Initial dosimetric evaluation of SmartArc—A novel VMAT treatment planning module implemented in a multi-vendor delivery chain," J. Appl. Clin. Med. Phys. **11**, 1–14 (2010).
[51]G. Gokeri, C. Kocar, and M. Tombakoglu, "MC simulation of microbeam radiation therapy with an interlaced irradiation geometry and an Au contrast agent in a realistic head phantom," Phys. Med. Biol. **55**, 7469–7487 (2010).
[52]International Commission on Radiation Units and Measurements, "Prescribing, Recording, and Reporting Photon Beam Therapy," ICRU Report 50 (International Commission on Radiation Units and Measurements, Bethesda, 1993).

CHAPTER 3

Discussion and Conclusions

Synchrotron radiation is an innovative tool in the biomedical research field and, in particular, for the treatment of some radioresistant tumours. Within this context, two spatially fractionated radiotherapy techniques have been under development at the ID17 ESRF, namely, microbeam radiation therapy and, more recently, minibeam radiation therapy. Both techniques explore the limits of the dose-volume effect by the use of submillimetre field sizes in combination with the spatial fractionation of the dose.

Preclinical trials in MRT performed during the last two decades showed an exceptional healthy tissue tolerance accompanied by the eradication of some highly aggressive animal tumour models. Thus, the next step in the development of the MRT program includes the application of this therapy to pets as a safe intermediate step before treatment of human beings.

This thesis has been mainly devoted to the assessment of several small (micrometre-sized) field dosimetry features involved in the preparation of forthcoming MRT clinical trials by means of Monte Carlo calculations and experimental measurements. The main conclusions are:

- Safe irradiation protocols have been defined for forthcoming clinical trials in MRT. MC studies in combination with radiobiological models showed that it is possible to deliver a relatively large dose to the tumour (peak and valley doses of 55 Gy and 2.6 Gy, respectively, for a centrally located tumour) and, at same time, keep the valley dose in healthy tissue within tolerances. The increase in the dose deposited to the tumour with respect to conventional radiosurgery (20–25 Gy) might probably lead to an enhancement of the patient lifespan.

- The remarkable therapeutic index in MRT can be further improved by combination with the enhanced absorption induced by contrast agents. The choice of the element depends on the degree of cytotoxicity (not studied in this work), on the dosimetric parameter evaluated and on the irradiation modality. However, in general, three elements stand out with respect to the others: Au, Tl and Lu. The use of these contrast agents

in future clinical trials would lead to a reduction in normal tissue valley doses (on average 48% less with respect to the absence of high-Z elements) for a given dose to the tumour.

- A MC-based treatment planning system calculation engine devoted to MRT has been developed. The first part included the complete characterisation and modelling of the ID17 synchrotron photon beam. The beam model was successfully validated for MRT calculations with experimental measurements both in homogeneous and heterogeneous phantoms. The second part consisted of the adaptation and optimisation of a MC code for dose calculation at the micron scale in a CT voxelised model of the patient in a reasonable amount of time (less than one day). Its performance has been proved with a typical MRT clinical example. The development of this MC computation engine constitutes a key tool for future MRT clinical trials in pets.

- For the first time, scatter factors for the MRT clinical trials settings were accurately and systematically assessed. This important and challenging step would enable the absolute dose measured in reference conditions to be converted to peak doses in MRT.

A new promising radiotherapy approach is being explored at the ESRF: MBRT. The larger field sizes and associated c-t-c distances involved in this technique overcome the inherent limitations of the clinical implementation of MRT, which nowadays can be only carried out in synchrotrons. However, the different irradiation parameters can lead to dissimilar biological effects with respect to MRT. In order to assess the therapeutic index of this new modality, *in vivo* experiments are being planned at the ESRF.

Therefore, several dosimetric features were also evaluated in order to establish a MBRT dosimetry protocol to guide the foreseen preclinical studies and to evaluate reproducibility in terms of dose. The protocol includes the determination of the absorbed dose under reference conditions, the assessment of the scatter factors and the final experimental verification of the MC calculations.

The objectives achieved within the framework of this thesis have provided the dosimetric tools for forthcoming MRT clinical trials in pets and MBRT preclinical trials in small animals.

Future perspectives

Future work could include the final integration of the MRT calculation engine into a user-friendly graphical front-end. Some attempts have already been done in order to link the

programs developed during this PhD with the graphical front-end platform named VIRTUOS [Bendl 1993]. The commissioning of the whole system should be performed as well [IAEA-TECDOC-1540 2007].

The methodology developed in this work allows the MRT TPS calculation engine to be easily adapted with little or no programming to other MRT synchrotron sources, to be used for dose calculation in presence of contrast agents or for MBRT.

Improvements in the accuracy of MC calculations would need to consider the inclusion of the effects induced by the fine structure of biological tissues, which seems to have a non-negligible effect [Felici 2005b, Felici 2007].

However, the most challenging work continues to be further development of dose detection systems and improvement of radiobiology knowledge. A more accurate measurement (better than 3%) of the dosimetric magnitudes in MRT would enable complete dose characterisation. Thus, intensive research is being carried out to find a detector with high spatial resolution able to cope with the high dose rates and high doses used in MRT.

Additionally, a prerequisite to plan a radiotherapy session is to know the susceptibility to radiation damage of the various kinds of normal cells. Due to the very distinct irradiation features of MRT and MBRT with respect to conventional methods, there is no specific data on healthy tissue tolerances and on radiobiological models for these kinds of techniques. Further knowledge on these topics would allow an accurate assessment of the therapeutic index of these innovative methods to be performed. These models could be implemented in the TPS to perform a biological optimisation of the irradiations.

If the MRT clinical trials were successful (first in animals and then in humans), MRT could be a good alternative in pediatric neurooncology [Dilmanian 1997, Laissue 2007], where other kinds of treatments are unsafe and can cause unacceptable risks of long-term neurological disability [Rilliet 2000, Mueller 2009]. Additionally, other possible applications of MRT are being explored; for instance, in the treatment of brain disorders [Anschel 2011, Romanelli 2011] or vascular malformations [Dilmanian 2003a].

Bibliography

[AAPM-85 2004] AAPM-85. *Tissue inhomogeneity corrections for megavoltage photon beams*. Technical report, American Association of Physicist in Medicine, Madison, United States of America, 2004.

[Abdul Rahman 2010] A. T. Abdul Rahman, D. A. Bradley, S. J. Doran, T. Brochard, E. Bräuer-Krisch and A. Bravin. *The thermoluminescence response of Ge-doped silica fibres for synchrotron microbeam radiation therapy dosimetry*. Nucl. Instr. Methods Phys. Res. A, vol. 619, p. 167–170, 2010.

[Abdul Rahman 2011] A. T. Abdul Rahman, E. Bräuer-Krisch, T. Brochard, J. Adamovics, S. K. Clowes, D. Bradley and S. J. Doran. *Sophisticated test objects for the quality assurance of optical computed tomography scanners*. Phys. Med. Biol., vol. 56, p. 4177–4199, 2011.

[ACCURAY® 2012] ACCURAY®. http://www.accuray.com/, 2012.

[Ackerly 2011] T. Ackerly, J. C. Crosbie, A. Fouras, G. J. Sheard, S. Higgins and R. A. Lewis. *High resolution optical calorimetry for synchrotron microbeam radiation therapy*. JINST, vol. 6, p. P03003–1–P03003–11, 2011.

[ACS 2011] ACS. *Cancer facts and figures 2011*. Technical report, American Cancer Society, Atlanta, United States of America, 2011.

[Adam 2005] J.-F. Adam, M. C. Biston, A. Joubert, A. M. Charvet, J.-F. Le Bas, F. Estève and H. Elleaume. *Enhanced delivery of iodine for synchrotron stereotactic radiotherapy by means of intracarotid injection and blood-brain barrier disruption: quantitative iodine biodistribution studies and associated dosimetry*. Int. J. Radiat. Oncol. Biol. Phys., vol. 61, p. 1173–1182, 2005.

[Adam 2008] J.-F. Adam, M. C. Biston, J. Rousseau, C. Boudou, A. M. Charvet, J. Balosso, F. Estève and H. Elleaume. *Heavy element enhanced synchrotron stereotactic radiotherapy as a promising brain tumour treatment*. Physica Medica, vol. 24, p. 92–97, 2008.

[Adam 2011] J.-F. Adam, J. Balosso, L. Bobyk, A.-M. Charvet, P. Deman, M. Edouard, H. Elleaume, F. Estève, J.-F. Le Bas, J. Rousseau, R. Serduc, M. Vautrin, T. Chabrol, A. Depaulis, B. Pouyatos, J. Baruchel, P. Berkvens, G. Berruyer, A. Bouchet, E. Bräuer-Krisch, A. Bravin, T. Brochard, D. Dallery, G. Le Duc, C. Nemoz, I. Martínez-Rovira, Y. Prezado, M. Renier, H. Requardt, M. Benkebil and J. Laissue. *Radiation therapy using synchrotron radiation: preclinical studies toward clinical trials*. Synchr. Rad. News, vol. 24, p. 8–12, 2011.

[Alric 2008] C. Alric, R. Serduc, C. Mandon, J. Taleb, G. le Duc, A. Le Meur-Herland, C. Billotey, P. Perriat, S. Roux and O. Tillement. *Gold nanoparticles designed for combining dual modality imaging and radiotherapy*. Gold Bulletin, vol. 41, p. 90–97, 2008.

[Als-Nielsen 2001] J. Als-Nielsen and D. McMorrow. Elements of modern x-ray physics. John Wiley and Sons, Chichester, United Kingdom, 2001.

[Amdur 1992] R. J. Amdur, K. J. Kalbaugh, L. M. Ewald, J. T. Parsons, W. M. Mendenhall, F. J. Bova and R. R. Million. *Radiation therapy for skin cancer near the eye: kilovoltage x-rays versus electrons*. Int. J. Radiat. Oncol. Biol. Phys., vol. 23, p. 769–779, 1992.

[Anschel 2011] D. A. Anschel, A. Bravin and P. Romanelli. *Microbeam radiosurgery using synchrotron-generated submillimetric beams: a new tool for the treatment of brain disorders*. Neurosurg. Rev., vol. 34, p. 133–142, 2011.

[Archer 1998] D. W. Archer. *Collimator for producing an array of microbeams - US Patent No. 5771270*, 1998.

[Aydarous 2001] A. S. Aydarous, P. J. Darley and M. W. Charles. *A wide dynamic range, high-spatial-resolution scanning system for radiochromic dye films*. Phys. Med. Biol., vol. 46, p. 1379–1389, 2001.

[Babcock 2011] K. Babcock, N. Sidhu, V. Kundapur and K. Ali. *Collimator design for experimental minibeam radiation therapy*. Med. Phys., vol. 38, p. 2192–2197, 2011.

[Barnes 2012] P. Barnes, J. K. Cockcroft, S. Jacques and M. Vickers. *How do synchrotrons work?* http://pd.chem.ucl.ac.uk/, 2012.

[Baró 1995] J. Baró, J. Sempau, J. M. Fernández-Varea and F. Salvat. PENELOPE*: an algorithm for Monte Carlo simulation of the penetration and energy loss of electrons and positrons in matter*. Nucl. Instr. Methods Phys. Res. B, vol. 100, p. 31–46, 1995.

[Barth 1998] R. F. Barth. *Rat brain tumor models in experimental neuro-oncology: the 9L, C6, T9, F98, RG2 (D74), RT-2 and CNS-1 gliomas*. J. Neurooncol., vol. 36, p. 91–102, 1998.

[Barth 2005] R. F. Barth, J. A. Coderre, M. G. H. Vicente and T. E. Blue. *Boron neutron capture therapy of cancer: current status and future prospects*. Clin. Cancer Res., vol. 11, p. 3987–4002, 2005.

[Baruchel 2008] J. Baruchel, P. Bleuet, A. Bravin, P. Coan, E. Lima, A. Madsen, W. Ludwig, P. Pernot and J. Susini. *Advances in synchrotron hard x-ray based imaging*. C. R. Physique, vol. 9, p. 624–641, 2008.

[Bencokova 2008] Z. Bencokova, J. Balosso and N. Foray. *Radiobiological features of the anti-cancer strategies involving synchrotron x-rays*. J. Synchrotron Radiat., vol. 15, p. 74–85, 2008.

[Bendl 1993] R. Bendl, J. Pross and W. Schlegel. VIRTUOS - *A program for VIRTUal radiOtherapy Simulation*. In H. U. Lemke, K. Inamura, C. C. Jaffe and R. Felix, editors, Computer Assisted Radiology. Proc. International Symposium CAR 93, volume 676–682, p. 822–823. Springer, 1993.

[Bentzen 2010] S. M. Bentzen, L. S. Constine, J. O. Deasy, A. Eisbruch, A. Jackson, L. B. Marks, R. K. Ten Haken and E. D. Yorke. *Quantitative analyses of normal tissue effects in the clinic (QUANTEC)*. Int. J. Radiat. Oncol. Biol. Phys., vol. 76, p. S1–S160, 2010.

[Berkvens 2011] P. Berkvens. *Académie royale des Sciences, des Lettres et des Beaux-Arts de Belgique Meeting, April 5*, 2011.

[Blattmann 2005] H. Blattmann, J.-O. Gebbers, E. Bräuer-Krisch, A. Bravin, G. Le Duc, W. Burkard, M. Di Michiel, V. Djonov, D. N. Slatkin, J. Stepanek and J. A. Laissue. *Applications of synchrotron x-rays to radiotherapy*. Nucl. Instr. Methods Phys. Res. A, vol. 548, p. 17–22, 2005.

[Bouchet 2010] A. Bouchet, B. Lemasson, G. le Duc, C. Maisin, E. Bräuer-Krisch, E. A. Siegbahn, L. Renaud, E. Khalil, C. Rémy, C. Poillot, A. Bravin, J. A. Laissue, E. L. Barbier and R. Serduc. *Preferential effect of synchrotron microbeam radiation therapy on intracerebral 9L gliosarcoma vascular networks*. Int. J. Radiat. Oncol. Biol. Phys., vol. 78, p. 1503–1512, 2010.

[Boudou 2005] C. Boudou, J. Baloso, F. Estève and H. Elleaume. *Monte Carlo dosimetry for stereotactic synchrotron radiation therapy of brain tumors*. Phys. Med. Biol., vol. 50, p. 4841–4851, 2005.

[Brahme 1981] A. Brahme and D. Reistad. *Microtrons for electron and photon radiotherapy*. IEEE Trans. Nucl. Sci., vol. 28, p. 1880–1883, 1981.

[Brahme 2004] A. Brahme. *Recent advances in light ion therapy*. Int. J. Radiat. Oncol. Biol. Phys., vol. 58, p. 603–616, 2004.

[Bratz 2011] J. A. Bratz, G. J. Sykora, E. Bräuer-Krisch and M. S. Akselrod. *Imaging and dosimetry of synchrotron microbeam with aluminum oxide fluorescent detectors*. Radiat. Meas., vol. 46, p. 1936–1939, 2011.

[Bräuer-Krisch 2003] E. Bräuer-Krisch, A. Bravin, M. Lerch, A. Rosenfeld, J. Stepanek, M. Di Michiel and J. A. Laissue. *MOSFET dosimetry for microbeam radiation therapy at the European Synchrotron Radiation Facility*. Med. Phys., vol. 30, p. 583–589, 2003.

[Bräuer-Krisch 2005a] E. Bräuer-Krisch, A. Bravin, L. Zhang, E. Siegbahn, J. Stepanek, H. Blattmann, D. N. Slatkin, J.-O. Gebbers, M. Jasmin and J. A. Laissue. *Characterization of a tungsten/gas multislit collimator for microbeam radiation therapy at the European Synchrotron Radiation Facility*. Rev. Sci. Instrum., vol. 76, p. 064303–1–064303–7, 2005.

[Bräuer-Krisch 2005b] E. Bräuer-Krisch, H. Requardt, P. Régnard, S. Corde, E. Siegbahn, G. Le Duc, T. Brochard, H. Blattmann, J. Laissue and A. Bravin. *New irradiation geometry for microbeam radiation therapy*. Phys. Med. Biol., vol. 50, p. 3103–3111, 2005.

[Bräuer-Krisch 2005c] E. Bräuer-Krisch, H. Requardt, P. Régnard, S. Corde, E. A. Siegbahn, G. Le Duc, H. Blattmann, J. Laissue and A. Bravin. *Exploiting geometrical irradiation possibilities in MRT application*. Nucl. Instr. Methods Phys. Res. A, vol. 548, p. 69–71, 2005.

[Bräuer-Krisch 2009] E. Bräuer-Krisch, H. Requardt, T. Brochard, G. Berruyer, M. Renier, J. A. Laissue and A. Bravin. *New technology enables high precision multislit collimators for microbeam radiation therapy*. Rev. Sci. Instrum., vol. 80, p. 074301–1–074301–6, 2009.

[Braüer-Krisch 2010a] E. Braüer-Krisch, A. Rosenfeld, M. Lerch, M. Petasecca, M. Akselrod, J. Sykora, J. Bartz, M. Ptaszkiewicz, P. Olko, A. Berg, M. Wieland, S. Doran, T. Brochard, A. Kamlowski, G. Cellere, A. Paccagnella, E. A. Siegbahn, Y. Prezado, I. Martínez-Rovira, A. Bravin, L. Dusseau and P. Berkvens. *Potential high resolution dosimeters for MRT*. AIP Conf. Proc., vol. 1266, p. 89–97, 2010.

[Bräuer-Krisch 2010b] E. Bräuer-Krisch, R. Serduc, E. A. Siegbahn, G. Le Duc, Y. Prezado, A. Bravin, H. Blattmann and J. A. Laissue. *Effects of pulsed, spatially fractionated, microscopic synchrotron x-ray beams on normal and tumoral brain tissue*. Mutat. Res., vol. 704, p. 160–166, 2010.

[Bravin 2011] A. Bravin and P. Suortti. *The contribution of the ESRF to biomedical science: from nano to humans*. Synchr. Rad. News, vol. 24, p. 34–38, 2011.

[Brenner 2008] D. J. Brenner. *The linear-quadratic model is an appropriate methodology for determining isoeffective doses at large doses per fraction*. Semin. Radiat. Oncol., vol. 18, p. 234–239, 2008.

[Brown 1983] G. Brown, K. Halback, J. Harris and H. Winick. *Wiggler and undulator magnets - A review*. Nucl. Instr. Methods Phys. Res. A, vol. 208, p. 65–77, 1983.

[CBTRUS 2011] CBTRUS. *Primary brain and central nervous system tumors diagnosed in the United States in 2004-2007*. Technical report, Central Brain Tumor Registry of the United States, Hinsdale, United States of America, 2011.

[Chapman 1989] K. Chapman, B. Lai and F. Cerrina. *Modelling of undulator sources*. Nucl. Instr. Methods Phys. Res. A, vol. 283, p. 88–99, 1989.

[Clarke 2004] J. A. Clarke. The science and technology of undulators and wigglers. Oxford University Press, Oxford, United Kingdom, 2004.

[Combs 2005] S. E. Combs, V. Widmer, C. Thilmann, H. Hof, J. Debus and D. Schulz-Ertner. *Stereotactic radiosurgery (SRS): treatment option for recurrent glioblastoma multiforme (GBM)*. Cancer, vol. 104, p. 2168–2173, 2005.

[Company 1998] F. Z. Company and B. J. Allen. *Calculation of microplanar beam dose profiles in a tissue/lung/tissue phantom*. Phys. Med. Biol., vol. 43, p. 2491–2501, 1998.

[Coutard 1934] H. Coutard. *Principles of x-ray therapy of malignant diseases*. Lancet Oncol., vol. 224, p. 1–8, 1934.

[Crook 2011] J. Crook. *The role of brachytherapy in the definitive management of prostate cancer*. Cancer Radiother., vol. 15, p. 230–237, 2011.

[Crosbie 2008] J. C. Crosbie, I. Svalbe, S. M. Midgley, N. Yagi, P. A. W. Rogers and R. A. Lewis. *A method of dosimetry for synchrotron microbeam radiation therapy using radiochromic films of different sensitivity*. Phys. Med. Biol., vol. 53, p. 6861–6877, 2008.

[Crosbie 2010] J. C. Crosbie, R. L. Anderson, K. Rothkamm, C. M. Restall, L. Cann, S. Ruwanpura, S. Meachem, N. Yagi, I. Svalbe, R. A. Lewis, B. R. G. Williams and P. A. W. Rogers. *Tumor cell response to synchrotron microbeam radiation therapy differs markedly from cells in normal tissues*. Int. J. Radiat. Oncol. Biol. Phys., vol. 77, p. 886–894, 2010.

[Cullen 2011] A. Cullen, M. Lerch, M. Petasecca and A. Rosenfeld. *Monte Carlo modelling of a silicon strip detector for microbeam radiation therapy*. Radiat. Meas., vol. 46, p. 1646–1649, 2011.

[Curtis 1967] H. J. Curtis. *The use of a deuteron microbeam for simulating the biological effects of heavy cosmic-ray particles*. Radiat. Res., vol. 7, p. S250–S257, 1967.

[Dawson 2006] L. A. Dawson and M. B. Sharpe. *Image-guided radiotherapy: rationale, benefits and limitations*. Lancet Oncol., vol. 7, p. 848–858, 2006.

[Deman 2011] P. Deman, M. Vautrin, V. Stupar, E. L. Barbier, H. Elleaume, F. Estève and J.-F. Adam. *Monochromatic minibeam radiotherapy: theoretical and experimental dosimetry for preclinical treatment plans*. Phys. Med. Biol., vol. 56, p. 4465–4480, 2011.

[Deman 2012] P. Deman, M. Vautrin, M. Edouard, V. Stupar, L. Bobyk, R. Farion, H. Elleaume, C. Remy, E. L. Barbier, F. Estève and J.-F. Adam. *Monochromatic minibeams radiotherapy: from healthy tissue sparing effect studies towards first experimental glioma bearing rats therapy*. Int. J. Radiat. Oncol. Biol. Phys., *in press*, 2012.

[Devic 2005] S. Devic, J. Seuntjens, E. Sham, E. B. Podgorsak, C. R. Schmidtlein, A. S. Kirov and C. G. Soares. *Precise radiochromic film dosimetry using flat-bed document scanner*. Med. Phys., vol. 32, p. 2245–2253, 2005.

[Dilmanian 1997] F. A. Dilmanian, X. Y. Wu, X. Huang, M. Kershaw, B. Ren, D. N. Slatkin, K. Trandem, R. Menk, W. C. Thomlinson and Z. Zhong. *Microbeam irradiation of duck embryo brains: relevance to microbeam radiation therapy (MRT) of brain tumors in infants. 1996 NSLS BNL 52517*. Technical report, National Synchrotron Light Source, Upton, United States of America, 1997.

[Dilmanian 2001] F. A. Dilmanian, G. M. Morris, G. Le Duc, X. Huang, B. Ren, T. Bacarian, J. C. Allen, J. Kalef-Ezra, I. Orion, E. M. Rosen, T. Sandhu, P. Sathé, X. Y. Wu, Z. Zhong and H. L. Shivaprasad. *Response of avian embryonic brain to spatially segmented x-ray microbeams*. Cell. Mol. Biol., vol. 47, p. 485–493, 2001.

[Dilmanian 2002] F. A. Dilmanian, T. M. Button, G. Le Duc, N. Zhong, L. A. Pena, J. A. L. Smith, S. R. Martinez, T. Bacarian, J. Tammam, B. Ren, P. M. Farmer, J. Kalef-Ezra, P. L. Micca, M. M. Nawrocky, J. A. Niederer, F. P. Recksiek, A. Fuchs and E. M. Rosen. *Response of rat intracranial 9L gliosarcoma to microbeam radiation therapy*. Neurooncol., vol. 4, p. 26–38, 2002.

[Dilmanian 2003a] F. A. Dilmanian, J. Kalef-Ezra, M. J. Petersen, G. Bozios, J. Vosswinkel, F. Giron, B. Ren, R. Yakupov and G. Antonakopoulos. *Could X-ray microbeams inhibit angioplasty-induced restenosis in the rat carotid artery?* Cardiovasc. Radiat. Med., vol. 4, p. 139–145, 2003.

[Dilmanian 2003b] F. A. Dilmanian, G. M. Morris, N. Zhong, T. Bacarian, J. F. Hainfeld, J. Kalef-Ezra, L. J. Brewington, J. Tammam and E. M. Rosen. *Murine EMT-6 carcinoma: high therapeutic efficacy of microbeam radiation therapy*. Radiat. Res., vol. 159, p. 632–641, 2003.

[Dilmanian 2005] F. A. Dilmanian, Y. Qu, S. Liu, C. D. Cool, J. Gilbert, J. F. Hainfeld, C. A. Kruse, J. Laterra, D. Lenihan, M. M. Nawrocky, G. Pappas, C.-I. Sze, T. Yuasa, N. Zhong, Z. Zhong and J. W. McDonald. *X-ray microbeams: tumor therapy and central nervous system research*. Nucl. Instr. Methods Phys. Res. A, vol. 548, p. 30–37, 2005.

[Dilmanian 2006] F. A. Dilmanian, Z. Zhong, T. Bacarian, H. Benveniste, P. Romanelli, R. Wang, J. Welwart, T. Yuasa, E. M. Rosen and D. J. Anschel. *Interlaced x-ray microplanar beams: a radiosurgery approach with clinical potential*. Proc. Natl. Acad. Sci. USA, vol. 103, p. 9709–9714, 2006.

[Dilmanian 2007a] F. A. Dilmanian, G. M. Morris and J. F. Hainfeld. *Methods for implementing microbeam radiation therapy - US Patent No. 7194063*, 2007.

[Dilmanian 2007b] F. A. Dilmanian, Y. Qu, L. E. Feinendegen, L. A. Peña, T. Bacarian, F. A. Henn, J. Kalef-Ezra, S. Liu, Z. Zhong and J. W. McDonald. *Tissue sparing effect on x-ray microplanar beams particularly in the CNS: is a bystander effect involved?* Exp. Hematol., vol. 35, p. 69–77, 2007.

[Dilmanian 2008] F. A. Dilmanian, P. Romanelli, Z. Zhong, R. Wang, M. E. Wagshul, J. Kalef-Ezra, M. J. Maryanski, E. M. Rosen and D. J. Anschel. *Microbeam radiation therapy: tissue dose penetration and BANG-gel dosimetry of thick-beams' array interlacing*. Eur. J. Radiol., vol. 68, p. S129–S136, 2008.

[Doran 2010] S. J. Doran, T. Brochard, J. Adamovics, N. Krstajic and E. Bräuer-Krisch. *An investigation of the potential of optical computed tomography for imaging of synchrotron-generated x-rays at high spatial resolution*. Phys. Med. Biol., vol. 55, p. 1531–1547, 2010.

[ELEKTA® 2012] ELEKTA®. http://www.elekta.com/, 2012.

[Elith 2011] C. Elith, S. E. Dempsey, N. Findlay and H. M. Warren-Forward. *An introduction to the intensity-modulated radiation techniques (IMRT), Tomotherapy and VMAT*. Journal of Medical Imaging and Radiation Sciences, vol. 42, p. 37–43, 2011.

[Elleaume 1999] H. Elleaume, A. M. Charvet, P. Berkvens, G. Berruyer, T. Brochard, Y. Dabin, M. C. Dominguez, A. Draperi, S. Fiedler, G. Goujon, G. Le Duc, M. Mattanet, C. Nemoz, M. Perez, R. Renier, C. Schulze, P. Spanne, P. Suortti, W. Thomlinson, F. Estève, B. Bertrand and J.-F. Le Bas. *Instrumentation of the ESRF medical imaging facility*. Nucl. Instr. Methods Phys. Res. A, vol. 428, p. 513–527, 1999.

[EPSON® 2012] EPSON®. http://www.epson.com/, 2012.

[ESRF 2012] ESRF. *European Synchrotron Radiation Facility*. http://www.esrf.eu/, 2012.

[Fano 1954] U. Fano. *A Stokes-parameter technique for the treatment of polarization in quantum mechanics*. Phys. Rev., vol. 93, p. 121–123, 1954.

[Felici 2005a] M. De Felici, R. Felici, M. Sánchez del Río, C. Ferrero, T. Bacarian and F. A. Dilmanian. *Dose distribution from x-ray microbeam arrays applied to radiation therapy: an* EGS4 *Monte Carlo study*. Med. Phys., vol. 32, p. 2455–2463, 2005.

[Felici 2005b] M. De Felici, A. Tartari, A. Taibi, M. Gambaccini, R. Felici, A. Bravin, C. Ferrero and S. Finet. *Effects induced by the fine structure of biological tissues on microbeam dose deposition: a numerical study*. Nucl. Instr. Methods Phys. Res. A, vol. 548, p. 59–64, 2005.

[Felici 2007] M. De Felici, R. Felici, C. Ferrero, A. Bravin, A. Tartari and M. Gambaccini. *Monte Carlo assessment of peak-to-valley dose ratio for MRT*. Nucl. Instr. Methods Phys. Res. A, vol. 580, p. 489–492, 2007.

[Ferlay 2010] J. Ferlay, H. R. Shin, F. Bray, D. Forman, C. Mathers and D. M. Parkin. *Cancer incidence and mortality worldwide. IARC CancerBase 10*. Technical report, International Agency for Research on Cancer, Lyon, France, 2010.

[Flickinger 1990] J. C. Flickinger and A. Kalend. *Use of normalized total dose to represent the biological effect of fractionated radiotherapy*. Radiother. Oncol., vol. 17, p. 339–347, 1990.

[Fraass 2003] B. A. Fraass, J. Smathers and J. Deye. *Summary and recommendations of a National Cancer Institute workshop on issues limiting the clinical use of Monte Carlo calculation algorithms for megavoltage external beam radiation therapy*. Med. Phys., vol. 30, p. 3206–3216, 2003.

[Fuller 2007] C. D. Fuller, M. Choi, B. Forthuber, S. J. Wand, N. Rajagiriyil, B. J. Salter and M. Fuss. *Standard fractionation intensity modulated radiation therapy (IMRT) of primary and recurrent glioblastoma multiforme*. Radiat. Oncol., vol. 2, p. 26–32, 2007.

[Gerber 2008] D. E. Gerber and T. A. Chan. *Recent advances in radiation therapy*. Am. Fam. Physician, vol. 78, p. 1254–1262, 2008.

[Gil 2011] S. Gil, S. Sarun, A. Biete, Y. Prezado and M. Sabés. *Survival analysis of F98 glioma rat cells following minibeam or broad beam synchrotron radiation therapy*. Radiat. Oncol., vol. 6, p. 1–9, 2011.

[Gokeri 2010] G. Gokeri, C. Kocar and M. Tombakoglu. *Monte Carlo simulation of microbeam radiation therapy with an interlaced irradiation geometry and Au contrast agent in a realistic head phantom*. Phys. Med. Biol., vol. 55, p. 7469–7487, 2010.

[Green 1976] G. K. Green. *Spectra and Optics of Synchrotron Radiation. BNL 50522*. Technical report, Brookhaven National Laboratory, Upton, United States of America, 1976.

[Hainfeld 2010] J. F. Hainfeld, F. A. Dilmanian, Z. Zhong, D. N. Slatkin, J. A. Kalef-Ezra and H. M. Smilowitz. *Gold nanoparticles enhance the radiation therapy of a murine squamous cell carcinoma*. Phys. Med. Biol., vol. 55, p. 3045–3059, 2010.

[Halperin 2006] E. C. Halperin. *Particle therapy and treatment of cancer*. Lancet Oncol., vol. 7, p. 676–685, 2006.

[Hetch 2001] E. Hetch. Optics. Addison Wesley, Boston, United States of America, 4th edition, 2001.

[Holthusen 1936] H. Holthusen. *Erfahrungen über die Verträglichkeitsgrenze für Röntgenstrahlen und deren Nutzanwendung zur Verhütung von Schäden*. Strahlentherapie, vol. 57, p. 254–269, 1936.

[Hopewell 2000] J. W. Hopewell and K.-R. Trott. *Volume effects in radiobiology as applied to radiotherapy*. Radiother. Oncol., vol. 56, p. 283–288, 2000.

[IAEA-TECDOC-1540 2007] IAEA-TECDOC-1540. *TECDOC-1540. Specification and acceptance testing of radiotherapy treatment planning systems*. Technical report, International Atomic Energy Agency, Vienna, Austria, 2007.

[IAEA-TRS-398 2005] IAEA-TRS-398. *TRS-398. Absorbed dose determination in external beam radiotherapy: an international code of practice for dosimetry based on standards of absorbed dose to water*. Technical report, International Atomic Energy Agency, Vienna, Austria, 2005.

[IAEA-TRS-430 2004] IAEA-TRS-430. *TRS-430. Commissioning and quality assurance of computerized planning systems for radiation treatment of cancer*. Technical report, International Atomic Energy Agency, Vienna, Austria, 2004.

[IAEA-TRS-461 2008] IAEA-TRS-461. *TRS-461. Relative biological effectiveness in ion beam therapy*. Technical report, International Atomic Energy Agency, Vienna, Austria, 2008.

[ICRU-24 1976] ICRU-24. *Determination of absorbed dose in a patient irradiated by beams of x or gamma rays in radiotherapy procedures*. Technical report, International Commission on Radiation Units and Measurements, Bethesda, United States of America, 1976.

[ICRU-37 1984] ICRU-37. *Stopping powers for electrons and positrons*. Technical report, International Commission on Radiation Units and Measurements, Bethesda, United States of America, 1984.

[ICRU-42 1987] ICRU-42. *Use of computers in external beam radiotherapy procedures with high energy photons and electrons*. Technical report, International Commission on Radiation Units and Measurements, Bethesda, United States of America, 1987.

[IMRTGroup 2001] IMRTGroup. *Intensity-modulated radiotherapy: current status and issues of interest*. Int. J. Radiat. Oncol. Biol. Phys., vol. 51, p. 880–914, 2001.

[ISP® 2012] ISP®. http://www.ispcorp.com/, 2012.

[Jackson 1998] J. D. Jackson. Classical electrodynamics. John Wiley and Sons, New York, United States of America, 3rd edition, 1998.

[Joiner 2009] M. Joiner and A. van der Kogel, editors. Basic clinical radiobiology. Hodder Arnold, London, United Kingdom, 3rd edition, 2009.

[Kaplan 2000] G. I. Kaplan, A. B. Rosenfeld, B. J. Allen, J. T. Booth, M. G. Carolan and A. Holmes-Siedle. *Improved spatial resolution by MOSFET dosimetry of an x-ray microbeam*. Med. Phys., vol. 27, p. 239–244, 2000.

[Kashino 2009] G. Kashino, T. Kondoh, N. Nariyama, K. Umetani, T. Ohigashi, K. Shinohara, A. Kurihara, M. Fukumoto, H. Tanaka, A. Maruhashi, M. Suzuki, Y. Kinashi, Y. Liu, S.-I. Masunaga, M. Watanabe and K. Ono. *Induction of DNA double-strand breaks and cellular migration through bystander effects in cells irradiated with the slit-type microplanar beam of the Spring-8 synchrotron*. Int. J. Radiat. Oncol. Biol. Phys., vol. 74, p. 229–236, 2009.

[Kazem 1995] I. Kazem. *One hundred years of radiation therapy: a tribute*. N. J. Med., vol. 92, p. 719–721, 1995.

[Khan 2010] F. M. Khan, editor. The physics of radiation therapy. Lippincott Williams and Wilkins, Philadelphia, United States of America, 4th edition, 2010.

[Kim 2008] Y. Kim and W. Tomé. *Optimization of radiotherapy using biological parameters*. Cancer Treat. Res., vol. 139, p. 257–278, 2008.

[Kirkpatrick 2009] J. P. Kirkpatrick, D. J. Brenner and C. G. Orton. *POINT/COUNTERPOINT: the linear-quadratic model is inappropriate to model high dose per fraction effects in radiosurgery*. Med. Phys., vol. 36, p. 3381–3384, 2009.

[Knoll 2000] G. F. Knoll, editor. Radiation detection and measurement. John Wiley and Sons, New York, United States of America, 3rd edition, 2000.

[Koudelková 2003] M. Koudelková, H. Vinšová and V. Jedináková-Křížová. *Characterization of Ho-DTPA and Y-DTPA complexes by capillary isotachophoresis and TLC with radiometric detection*. Czech. J. Phys., vol. 53, p. A769–A775, 2003.

[Lai 1986] B. Lai and F. Cerrina. SHADOW*: a synchrotron radiation ray tracing program*. Nucl. Instr. Methods Phys. Res. A, vol. 246, p. 337–341, 1986.

[Lai 1988] B. Lai, K. Chapman and F. Cerrina. SHADOW*: new developments*. Nucl. Instr. Methods Phys. Res. A, vol. 266, p. 544–549, 1988.

[Laissue 1998] J. A. Laissue, G. Geiser, P. O. Spanne, F. A. Dilmanian, J.-O. Gebbers, M. Geiser, X.-Y. Wu, M. S. Makar, P. L. Micca, M. M. Nawrocky, D. D. Joel and D. N. Slatkin. *Neuropathology of ablation of rat gliosarcomas and contiguous brain tissues using a microplanar beam of synchrotron-wiggler-generated x rays*. Int. J. Cancer, vol. 78, p. 654–660, 1998.

[Laissue 1999] J. A. Laissue, N. Lyubimova, H.-P. Wagner, D. W. Archer, D. N. Slatkin, M. Di Michiel, C. Nemoz, M. Renier, E. Bräuer, P. O. Spanne, J.-O. Gebbers, K. Dixon and H. Blattmann. *Microbeam radiation therapy*. Proc. SPIE, vol. 3770, p. 38–45, 1999.

[Laissue 2001] J. A. Laissue, H. Blattmann, M. Di Michiel, D. N. Slatkin, N. Lyubimova, R. Guzman, W. Zimmermann, S. Birrer, T. Bley, P. Kircher, R. Stettler, R. Fatzer, A. Jaggy, H. M. Smilowitz, E. Bräuer, A. Bravin, G. Le Duc, C. Nemoz, M. Renier, W. Thomlinson, J. Stepanek and H.-P. Wagner. *The weanling piglet cerebellum: a surrogate for tolerance to MRT (microbeam radiation therapy) in pediatric neuro-oncology*. Proc. SPIE, vol. 4508, p. 65–73, 2001.

[Laissue 2007] J. A. Laissue, H. Blattmann, H. P. Wagner, M. A. Grotzer and D. N. Slatkin. *Prospects for microbeam radiation therapy of brain tumours in children to reduce neurological sequelae*. Dev. Med. Child. Neurol., vol. 49, p. 577–581, 2007.

[Larsson 1983] B. Larsson. *Potentialities of synchrotron radiation in experimental and clinical radiation surgery*. Acta Radiol., vol. 365, p. S58–S64, 1983.

[Lawrence 2010] Y. R. Lawrence, X. A. Li, I. El Naqa, C. A. Hahn, L. B. Marks, T. E. Merchant and A. P. Dicker. *Radiation dose-volume effects in the brain*. Int. J. Radiat. Oncol. Biol. Phys., vol. 15, p. S20–S27, 2010.

[Ljunggren 2004] K. Ljunggren, X. Liu, K. Erlandsson, M. Ljungberg, L. G. Salford and S. E. Strand. *Absorbed dose distribution in glioma tumors in rat brain after therapeutic intratumoral injection of ^{201}Tl-chloride*. Cancer Biother. Radiopharm., vol. 19, p. 562–569, 2004.

[Ma 1991] C.-M. Ma and A. E. Nahum. *Bragg-Gray theory and ion chamber dosimetry for photon beams*. Phys. Med. Biol., vol. 36, p. 413–428, 1991.

[MacEwen 1990] E. G. MacEwen. *Spontaneous tumors in dogs and cats: models for the study of cancer biology and treatment*. Cancer Metastasis Rev., vol. 9, p. 125–136, 1990.

[Martin 2010] A. Martin and A. Gaya. *Stereotactic body radiotherapy: a review*. Clin. Oncol., vol. 22, p. 157–172, 2010.

[Martínez-Rovira 2010] I. Martínez-Rovira, J. Sempau, J. M. Fernández-Varea, A. Bravin and Y. Prezado. *Monte Carlo dosimetry for forthcoming clinical trials in x-ray microbeam radiation therapy*. Phys. Med. Biol., vol. 55, p. 4375–4388, 2010.

[Martínez-Rovira 2011] I. Martínez-Rovira and Y. Prezado. *Monte Carlo dose enhancement studies in microbeam radiation therapy*. Med. Phys., vol. 38, p. 4430–4439, 2011.

[Martínez-Rovira 2012a] I. Martínez-Rovira, J. Sempau and Y. Prezado. *Development and commissioning of a Monte Carlo photon beam model for the forthcoming clinical trials in Microbeam Radiation Therapy*. Med. Phys., vol. 39, p. 119–131, 2012.

[Martínez-Rovira 2012b] I. Martínez-Rovira, J. Sempau and Y. Prezado. *Monte Carlo-based treatment planning system calculation engine for microbeam radiation therapy*. *Submitted to* Med. Phys., 2012.

[Mesa 1999] A. V. Mesa, A. Norman, T. D. Solberg, J. J. Demarco and J. B. Smathers. *Dose distributions using kilovoltage x-rays and dose enhancement from iodine contrast agents*. Phys. Med. Biol., vol. 44, p. 1955–1968, 1999.

[Miura 2006] M. Miura, H. Blattmann, E. Bräuer-Krisch, A. Bravin, A. L. Hanson, M. M. Nawrocky, P. L. Micca, D. N. Slatkin and J. A. Laissue. *Radiosurgical palliation of aggressive murine SCCVII squamous cell carcinomas using synchrotron-generated x-ray microbeams*. Br. J. Radiol., vol. 79, p. 71–75, 2006.

[Mueller 2009] S. Mueller and S. Chang. *Pedriatic brain tumors: current treatment strategies and future therapeutic approaches*. Neurotherapeutics, vol. 6, p. 570–586, 2009.

[Muench 1991] P. J. Muench, A. S. Meigooni, R. Nath and W. L. McLaughlin. *Photon energy dependence of the sensitivity of radiochromic film and comparison with silver halide film and LiF TLDs used for brachytherapy dosimetry*. Med. Phys., vol. 18, p. 769–775, 1991.

[NANOBIOTIX® 2012] NANOBIOTIX®. http://www.nanobiotix.com/, 2012.

[Nariyama 2009] N. Nariyama, T. Ohigashi, K. Umetani, K. Shinohara, H. Tanaka, A. Maruhashi, G. Kasino, A. Kurihara, T. Kondob, M. Fukumoto and K. Ono. *Spectromicroscopic film dosimetry for high-energy microbeam from synchrotron radiation*. Appl. Radiat. Isot., vol. 67, p. 155–159, 2009.

[Nawroth 2008] T. Nawroth, N. Glube, T. Peters, P. Buch, K. Buch, P. Langguth, B. Pairet, H. Decker, D. Bickes-Kelleher, P. Vaupel, M.A. Konerding, H. Schmidberger, C. Alexiou, R. Gähler, B. Lauss, M. Jentschel, R. P. May, S. Corde, P. Boesecke, A. Bravin and G. Le Duc. *Nano-IRT: indirect radiation therapy development with target nanoparticles*. Proc. SYRAD Workshop, ESRF, Grenoble, France, 2008.

[Nettelbeck 2009] H. Nettelbeck, G. J. Takacs, M. L. F. Lerch and A. B. Rosenfeld. *Microbeam radiation therapy: a Monte Carlo study of the influence of the source, multislit collimator and beam divergence on microbeams*. Med. Phys., vol. 36, p. 447–456, 2009.

[Niederlaender 2006] E. Niederlaender. *Causes of death in the EU. KS-NK-06-010-EN-N*. Technical report, Eurostat, 2006.

[Niroomand-Rad 1998] A. Niroomand-Rad, C. R. Blackwell, B. M. Coursey, K. P. Gall, J. M. Galvin, W. L. McLaughlin, Al. S. Meigooni, R. Nath, J. E. Rodgers and C. G. Soares. *Radiochromic film dosimetry: recommendations of AAPM Radiation Therapy Committee Task Group 55 (AAPM Report No. 63)*. Med. Phys., vol. 25, p. 2093–2115, 1998.

[Niyazi 2011] M. Niyazi, A. Siefert, S. B. Schwarz, U. Ganswindt, F.-W. Kreth, J.-C. Tonn and C. Belka. *Therapeutic options for recurrent malignant glioma*. Radiother. Oncol., vol. 98, p. 1–14, 2011.

[Orion 2000] I. Orion, A. B. Rosenfeld, F. A. Dilmanian, F. Telang, B. Ren and Y. Namito. *Monte Carlo simulation of dose distributions from a synchrotron-produced microplanar beam array using the* EGS4 *code system*. Phys. Med. Biol., vol. 45, p. 2497–2508, 2000.

[Papiez 2008] L. Papiez and R. Timmerman. *Hypofractionation in radiation therapy and its impact*. Med. Phys., vol. 35, p. 112–118, 2008.

[Phillips 1994] M. H. Phillips, K. J. Stelzer, T. W. Griffin, M. R. Mayberg and H. R. Winn. *Stereotactic radiosurgery: a review and comparison of methods*. J. Clin. Oncol., vol. 12, p. 1085–1099, 1994.

[Podgorsak 2005] E. B. Podgorsak, editor. Radiation oncology physics: a handbook for teachers and students. International Atomic Energy Agency, Vienna, Ausrtria, 2005.

[Polgár 2009] C. Polgár and T. Major. *Current status and perspectives of brachytherapy for breast cancer*. Int. J. Clin. Oncol., vol. 14, p. 7–24, 2009.

[Poncelet 1992] B. P. Poncelet, V. J. Wedeen, R. M. Weisskoff and M. S. Cohen. *Brain parenchyma motion: measurement with cine echo-planar MR imaging*. Radiology, vol. 185, p. 645–651, 1992.

[Prezado 2009a] Y. Prezado, G. Fois, G. Le Duc and A. Bravin. *Gadolinium dose enhancement studies in microbeam radiation therapy*. Med. Phys., vol. 36, p. 3568–3574, 2009.

[Prezado 2009b] Y. Prezado, M. Renier and A. Bravin. *A new method of creating minibeam patterns for synchrotron radiation therapy: a feasibility study*. J. Synchrotron Radiat., vol. 16, p. 582–586, 2009.

[Prezado 2009c] Y. Prezado, S. Thengumpallil, M. Renier and A. Bravin. *X-ray energy optimization in minibeam radiation therapy*. Med. Phys., vol. 36, p. 4897–4902, 2009.

[Prezado 2011a] Y. Prezado, I. Martínez-Rovira, S. Thengumpallil and P. Deman. *Dosimetry protocol for the preclinical trials in white-beam minibeam radiation therapy*. Med. Phys., vol. 38, p. 5012–5020, 2011.

[Prezado 2011b] Y. Prezado, M. Vautrin, I. Martínez-Rovira, A. Bravin, F. Estève, H. Elleaume, P. Berkvens and J.-F. Adam. *Dosimetry protocol for the forthcoming clinical trials in synchrotron radiation therapy (SSRT)*. Med. Phys., vol. 38, p. 1709–1717, 2011.

[Prezado 2012a] Y. Prezado, I. Martínez-Rovira and M. Sánchez. *Scatter factors assessment in microbeam radiation therapy*. Med. Phys., *in press*, vol. 39, 2012.

[Prezado 2012b] Y. Prezado, S. Sarun, S. Gil, P. Deman, A. Bouchet and G. Le Duc. *Increase of lifespan for glioma bearing rats by using minibeam radiation therapy*. J. Synchrotron Radiat., vol. 19, p. 60–65, 2012.

[Ptaszkiewicz 2008] M. Ptaszkiewicz, E. Bräuer-Krisch, M. Klosowski, L. Czopyk and P. Olko. *TLD dosimetry for microbeam radiation therapy at the European Synchrotron Radiation Facility*. Radiat. Meas., vol. 43, p. 990–993, 2008.

[PTW® 2012] PTW®. http://www.ptw.de/, 2012.

[Régnard 2008a] P. Régnard, E. Bräuer-Krisch, I. Tropès, J. Keyriläinen, A. Bravin and G. Le Duc. *Enhancement of survival of 9L gliosarcoma bearing rats following intracerebral delivery of drugs in combination with microbeam radiation therapy*. Eur. J. Radiol., vol. 68, p. S151–S155, 2008.

[Régnard 2008b] P. Régnard, G. Le Duc, E. Bräuer-Krisch, I. Tropès, E. A. Siegbahn, A. Kusak, C. Chair, H. Bernard, D. Dallery, J. A. Laissue and A. Bravin. *Irradiation of intracerebral 9L glioscarcoma by a single array of microplanar x-ray beams from synchrotron: balance between curing and sparing*. Phys. Med. Biol., vol. 53, p. 861–878, 2008.

[Renier 2002] M. Renier, T. Brochard, C. Nemoz and W. Thomlinson. *A white-beam fast-shutter for microbeam radiation therapy at the ESRF*. Nucl. Instr. Methods Phys. Res. A, vol. 479, p. 656–660, 2002.

[Renier 2005] M. Renier, S. Fiedler, C. Nemoz, H. Gonzalez, G. Berruyer and A. Bravin. *A mechanical chopper with continuously adjustable duty cycle for a wide x-ray beam*. Nucl. Instr. Methods Phys. Res. A, vol. 548, p. 111–115, 2005.

[Renier 2008] M. Renier, T. Brochard, C. Nemoz, H. Requardt, E. Bräuer, F. Estève, J. Balosso, P. Suortti, J. Baruchel, H. Elleaume, G. Berruyer, P. Berkvens and A. Bravin. *The radiotherapy clinical trials projects at the ESRF: technical aspects*. Eur. J. Radiol., vol. 68, p. S147–S150, 2008.

[Renier 2011] M. Renier. *Académie royale des sciences, des lettres et des beaux-arts de Belgique Meeting, April 5*, 2011.

[Requardt 2010] H. Requardt, A. Bravin, Y. Prezado, E. Bräuer-Krisch, M. Renier, T. Brochard, P. Berkvens, F. Estève, H. Elleaume, J.-F. Adam, H. Blattmann, J. A. Laissue, B. Kazer-Hotz, C. Nemoz and G. Berruyer. *The clinical trials program at the ESRF Biomedical Beamline ID17: status and remaining steps*. AIP Conf. Proc., vol. 1234, p. 161–164, 2010.

[Reynaert 2007] N. Reynaert, S. C. van der Marck, D. R. Schaart, W. van der Zee, C. van Vliet-Vroegindeweij, M. Tomsej, J. Jansen, B. Heijmen, M. Coghe and C. De Wagter. *Monte Carlo treatment planning for photon and electron beams*. Radiat. Phys. Chem., vol. 76, p. 643–686, 2007.

[Rilliet 2000] B. Rilliet and O. Vernet. *Gliomas in children: a review*. Childs Nerv. Syst., vol. 16, p. 735–741, 2000.

[Romanelli 2011] P. Romanelli, E. Fardone, E. Bräuer-Krisch, Y. Prezado and A. Bravin. *A concise review of the emerging applications of synchrotron-generated microbeams in the treatment of brain disorders*. Peeremed, http://www.peeremed.com/, 2011.

[Rosenfeld 1996] A. B. Rosenfeld, G. I. Kaplan, M. G. Carolan, B. J. Allen, R. Maughan, M. Yudelev, C. Kota and J. Corderre. *Simultaneous macro and micro dosimetry with MOSFETs*. IEEE Trans. Nucl. Sci., vol. 43, p. 2693–2700, 1996.

[Rosenfeld 1999] A. B. Rosenfeld, G. I. Kaplan, T. Kron, B. J. Allen, A. Dilmanian, I. Orion, B. Ren, M. L. F. Lerch and A. Holmes-Siedle. *MOSFET dosimetry of an x-ray microbeam*. IEEE Trans. Nucl. Sci., vol. 46, p. 1774–1780, 1999.

[Rosenfeld 2001] A. B. Rosenfeld, M. L. F. Lerch, T. Kron, E. Bräuer-Krisch, A. Bravin, A. Holmes-Siedle and B. J. Allen. *Feasibility study of online high-spatial-resolution MOSFET dosimetry in static and pulsed x-ray radiation fields*. IEEE Trans. Nucl. Sci., vol. 48, p. 2061–2068, 2001.

[Rosenfeld 2005] A. B. Rosenfeld, E. A. Siegbahn, E. Bräuer-Krisch, A. Holmes-Siedle, M. L. F. Lerch, A. Bravin, I. M. Cornelius, G. J. Takacs, N. Painuly, H. Nettelbeck and T. Kron. *Edge-on face-to-face MOSFET for synchrotron microbeam dosimetry: MC modeling*. IEEE Trans. Nucl. Sci., vol. 52, p. 2562–2569, 2005.

[Sabatasso 2011] S. Sabatasso, J. A. Laissue, R. Hlushchuk, W. Graber, A. Bravin, E. Bräuer-Krisch, S. Corde, H. Blattmann, G. Gruber and V. Djonov. *Microbeam radiation-induced tissue damage depends on the stage of vascular maturation*. Int. J. Radiat. Oncol. Biol. Phys., vol. 80, p. 1522–1532, 2011.

[Salvat 2005] F. Salvat, A. Jablonski and C. J. Powell. ELSEPA - *Dirac partial-wave calculations of elastic scattering of electrons and positrons by atoms, positive ions and molecules*. Comput. Phys. Commun., vol. 165, p. 157–190, 2005.

[Salvat 2008] F. Salvat, J. M. Fernández-Varea and J. Sempau. PENELOPE-2008, a code system for Monte Carlo simulation of electron and photon transport. OECD - Nuclear Energy Agency, Issy-les-Molineaux, France, 2008.

[Sánchez del Río 2011] M. Sánchez del Río, N. Canestrari, F. Jiang and F. Cerrina. SHADOW3*: a new version of the synchrotron x-ray optics modelling package*. J. Synchrotron Radiat., vol. 18, p. 708–716, 2011.

[Sánchez-Doblado 2007] F. Sánchez-Doblado, G. H. Hartmann, J. Pena, J. V. Roselló, G. Russiello and D. M. González-Castaño. *A new method for output factor determination in MLC shaped narrow beams*. Phys. Med., vol. 23, p. 58–66, 2007.

[Schültke 2008] E. Schültke, B. H. J. Juurlink, K. Ataelmannan, J. Laissue, H. Blattmann, E. Bräuer-Krisch, A. Bravin, J. Minczewska, J. Crosbie, H. Taherian, E. Frangou, T. Wysokinsky, L. D. Chapman, R. Griebel and D. Fourney. *Memory and survival after microbeam radiation therapy*. Eur. J. Radiol., vol. 68, p. S142–S146, 2008.

[Sempau 1997] J. Sempau, E. Acosta, J. Baró, J. M. Fernández-Varea and F. Salvat. *An algorithm for Monte Carlo simulation of coupled electron-photon transport*. Nucl. Instr. Methods Phys. Res. B, vol. 132, p. 377–390, 1997.

[Sempau 2011] J. Sempau, A. Badal and L. Brualla. *A* PENELOPE*-based system for the automated Monte Carlo simulation of clinacs and voxelized geometries - application to far-from-axis fields*. Med. Phys., vol. 38, p. 5887–5895, 2011.

[Serduc 2006] R. Serduc, P. Vérant, J.-C. Vial, R. Farion, L. Rocas, C. Rémy, T. Fadlallah, E. Bräuer, A. Bravin, J. Laissue, H. Blattmann and B. van der Sanden. *In vivo two-photon microscopy study of short-term effects of microbeam irradiation on normal mouse brain microvasculature*. Int. J. Radiat. Oncol. Biol. Phys., vol. 64, p. 1519–1527, 2006.

[Serduc 2008a] R. Serduc, T. Christen, J. Laissue, R. Farion, A. Bouchet, B. van der Sanden, C. Segebarth, E. Bräuer-Krisch, G. Le Duc, A. Bravin, C. Rémy and E. L. Barbier. *Brain*

tumor vessel response to synchrotron microbeam radiation therapy: a short-term in vivo study. Phys. Med. Biol., vol. 53, p. 3609–3622, 2008.

[Serduc 2008b] R. Serduc, Y. van de Looij, G. Francony, O. Verdonck, B. van der Sanden, J. Laissue, R. Farion, E. Bräuer-Krisch, E. A. Siegbahn, A. Bravin, Y. Prezado, C. Segebarth, C. Rémy and H. Lahrech. *Characterization and quantification of cerebral edema induced by synchrotron x-ray microbeam radiation therapy*. Phys. Med. Biol., vol. 53, p. 1153–1166, 2008.

[Serduc 2009a] R. Serduc, A. Bouchet, E. Bräuer-Krisch, J. A. Laissue, J. Spiga, S. Sarun, A. Bravin, C. Fonta, L. Renaud, J. Boutonnat, E. A. Siegbahn, F. Estève and G. Le Duc. *Synchrotron microbeam radiation therapy for rat brain tumor palliation - influence of the microbeam width at constant valley dose*. Phys. Med. Biol., vol. 54, p. 6711–6724, 2009.

[Serduc 2009b] R. Serduc, E. Bräuer-Krisch, A. Bouchet, L. Renaud, T. Brochard, A. Bravin, J. A. Laissue and G. Le Duc. *First trial of spatial and temporal fractionations of the delivered dose using synchrotron microbeam radiation therapy*. J. Synchrotron Radiat., vol. 16, p. 587–590, 2009.

[Serduc 2010a] R. Serduc, G. Berruyer, T. Brochard, M. Renier and C. Nemoz. *In vivo pink-beam imaging and fast alignment procedure for rat brain lesion microbeam radiation therapy*. J. Synchrotron Radiat., vol. 17, p. 325–331, 2010.

[Serduc 2010b] R. Serduc, E. Bräuer-Krisch, E. A. Siegbahn, A. Bouchet, B. Pouyatos, R. Carron, N. Pannetier, L. Renaud, G. Berruyer, C. Nemoz, T. Brochard, C. Rémy, E. L. Barbier, A. Bravin, G. Le Duc, A. Depaulis, F. Estève and J. A. Laissue. *High-precision radiosurgical dose delivery by interlaced microbeam arrays of high-flux low-energy synchrotron x-rays*. PLoS ONE, vol. 5, p. 1–12, 2010.

[Siegbahn 2005] E. A. Siegbahn, E. Bräuer-Krisch, J. Stepanek, H. Blattmann, J. A. Laissue and A. Bravin. *Dosimetric studies of microbeam radiation therapy (MRT) with Monte Carlo simulations*. Nucl. Instr. Methods Phys. Res. A, vol. 548, p. 54–58, 2005.

[Siegbahn 2006] E. A. Siegbahn, J. Stepanek, E. Bräuer-Krisch and A. Bravin. *Determination of dosimetrical quantities used in microbeam radiation therapy (MRT) with Monte Carlo simulations*. Med. Phys., vol. 33, p. 3248–3259, 2006.

[Siegbahn 2007] E. A. Siegbahn. *Dosimetry for synchrotron x-ray microbeam radiation therapy*. Phd Thesis, Technischen Universität München, 2007.

[Siegbahn 2009] E. A. Siegbahn, E. Bräuer-Krisch, A. Bravin, H. Nettelbeck, M. L. F. Lerch and A. B. Rosenfeld. *MOSFET dosimetry with high spatial resolution in intense synchrotron-generated x-ray microbeams*. Med. Phys., vol. 36, p. 1128–1137, 2009.

[Slatkin 1992] D. N. Slatkin, P. Spanne, F. A. Dilmanian and M. Sandborg. *Microbeam radiation therapy*. Med. Phys., vol. 19, p. 1395–1400, 1992.

[Slatkin 1995a] D. N. Slatkin, F. A. Dilmanian, M. M. Nawrocky, P. Spanne, J.-O. Gebbers, D. W. Archer and J. A. Laissue. *Design of a multislit, variable width collimator for microplanar beam radiotherapy*. Rev. Sci. Instrum., vol. 66, p. 1459–1460, 1995.

[Slatkin 1995b] D. N. Slatkin, P. Spanne, F. A. Dilmanian, J.-O. Gebbers and J. A. Laissue. *Subacute neuropathological effects of microplanar beams of x-rays from a synchrotron wiggler*. Proc. Natl. Acad. Sci. USA, vol. 92, p. 8783–8787, 1995.

[Smilowitz 2002] H. M. Smilowitz, J. A. Coderre, M. M. Nawrocky, W. Tu, A. Pinkerton, G. H. Jahng, N. Gebbers and D. N. Slatkin. *The combination of x-ray mediated radiosurgery and gene-mediated immunoprophylaxis for advanced intracerebral gliosarcomas in rats*. J. Neurooncol., vol. 57, p. 9–18, 2002.

[Smilowitz 2006] H. M. Smilowitz, H. Blattmann, E. Bräuer-Krisch, A. Bravin, M. Di Michiel, J.-O. Gebbers, A. L. Hanson, N. Lyubimova, D. N. Slatkin, J. Stepanek and J. A. Laissue. *Synergy of gene-mediated immunoprophylaxis and microbeam radiation therapy for advanced intracerebral rat 9L gliosarcomas*. J. Neurooncol., vol. 78, p. 135–143, 2006.

[Spiga 2007] J. Spiga, E. A. Siegbahn, E. Bräuer-Krisch, R. Randaccio and A. Bravin. *The* GEANT4 *toolkit for microdosimetry calculations: application to microbeam radiation therapy (MRT)*. Med. Phys., vol. 34, p. 4322–4330, 2007.

[Stepanek 2000] J. Stepanek, H. Blattmann, J. A. Laissue, N. Lyubimova, M. Di Michiel and D. N. Slatkin. *Physics study of microbeam radiation therapy with PSI-version of Monte Carlo code* GEANT *as a new computational tool*. Med. Phys., vol. 27, p. 1664–1675, 2000.

[Stevens 1996] M. A. Stevens, J. R. Turner, R. P. Hugtenburg and P. H. Butler. *High-resolution dosimetry using radiochromic film and a document scanner*. Phys. Med. Biol., vol. 41, p. 2357–2365, 1996.

[Straile 1963] W. E. Straile and H. B. Chase. *The use of elongate microbeams of x-rays for simulating the effects of cosmic rays in tissues: a study of wound healing and hair follicle regeneration*. Radiat. Res., vol. 18, p. 65–75, 1963.

[Stupp 2005] R. Stupp, W. P. Mason, M. J. van den Bent, M. Weller, B. Fisher, M. J. Taphoorn, K. Belanger, A. A. Brandes, C. Marosi, U. Bogdahn, J. Curschmann, R. C. Janzer, S. K. Ludwin, T. Gorlia, A. Allgeier, D. Lacombe, J. G. Cairncross, E. Eisenhauer and R. O. Mirimanoff. *Radiotherapy plus concomitant and adjuvant temozolomide for glioblastoma*. N. Engl. J. Med., vol. 352, p. 987–996, 2005.

[Stupp 2009] R. Stupp, M. E. Hegi, W. P. Mason, M. J. van den Bent, M. J. Taphoorn, R. C. Janzer, S. K. Ludwin, A. Allgeier, B. Fisher, K. Belanger, P. Hau, A. A. Brandes, J. Gijtenbeek, C. Marosi, C. J. Vecht, K. Mokhtari, P. Wesseling, S. Villa, E. Eisenhauer,

T. Gorlia, M. Weller, D. Lacombe, J. G. Cairncross and R. O. Mirimanoff. *Effects of radiotherapy with concomitant and adjuvant temozolomide versus radiotherapy alone on survival in glioblastoma in a randomised phase III study: 5-year analysis of the EORTC-NCIC trial*. Lancet Oncol., vol. 10, p. 459–466, 2009.

[Suortti 2003] P. Suortti and W. Thomlinson. *Medical applications of synchrotron radiation*. Phys. Med. Biol., vol. 48, p. R1–R35, 2003.

[Swing 1998] R. E. Swing. An introduction to microdensitometry. SPIE Optical Engineering Press, Washington, United States of America, 1998.

[GEANT4 2005] GEANT4. *v. 8.0, Physics Reference Manual*. http://geant4.cern.ch/, 2005.

[Thomadsen 2005] B. Thomadsen, M. Rivard and W. Butler, editors. Brachytherapy physics. Medical Physics Publishing, Madison, United States of America, 2nd edition, 2005.

[Thomlinson 2005] W. Thomlinson, P. Suortti and D. Chapman. *Recent advances in synchrotron radiation medical research*. Nucl. Instr. Methods Phys. Res. A, vol. 543, p. 288–296, 2005.

[Thompson 2009] A. C. Thompson, D. Attwood, E. Gullikson, M. Howells, K.-J. Kim, J. Kirz, J. Kortright, I. Lindau, Y. Liu, P. Pianetta, A. Robinson, J. Scotfield, J. Underwood, G. Williams and H. Winick. X-ray data booklet. Lawrence Berkeley National Laboratory, Berkeley, United States of America, 3rd edition, 2009.

[Torres 2004] J. Torres, M. J. Buades, J. F. Almansa, R. Guerrero and A. M. Lallena. *Dosimetry characterization of ^{32}P intravascular brachytherapy source wires using Monte Carlo codes* PENELOPE *and* GEANT4. Med. Phys., vol. 31, p. 296–304, 2004.

[Uyama 2011] A. Uyama, T. Kondoh, N. Nariyama, K. Umetani, M. Fukumoto, K. Shinohara and E. Kohmura. *A narrow microbeam is more effective for tumor control growth suppression than a wide microbeam: an in vivo study using implanted human glioma cells*. J. Synchrotron Radiat., vol. 18, p. 671–678, 2011.

[van der Sanden 2010] B. van der Sanden, E. Bräuer-Krisch, E. A. Siegbahn, C. Ricard, J.-C. Vial and J. Laissue. *Tolerance of arteries to microplanar x-ray beams*. Int. J. Radiat. Oncol. Biol. Phys., vol. 77, p. 1545–1552, 2010.

[Wen 2008] P. Y. Wen and S. Kesari. *Malignant gliomas in adults*. N. Engl. J. Med., vol. 359, p. 492–507, 2008.

[Wille 2001] K. Wille. The physics of particle accelerators, an introduction. Oxford University Press, Oxford, United Kingdom, 2001.

[Willers 2006] H. Willers and K. D. Held. *Introduction to clinical radiation biology*. Hematol. Oncol. Clin. North Am., vol. 20, p. 1–24, 2006.

[Yaes 1988] R. J. Yaes and A. Kalend. *Local stem cell depletion model for radiation myelitis*. Int. J. Radiat. Oncol. Biol. Phys., vol. 14, p. 1247–1259, 1988.

[Yamamoto 2008] T. Yamamoto, K. Nakai and A. Matsumura. *Boron neutron capture therapy for glioblastoma*. Cancer Lett., vol. 262, p. 143–152, 2008.

[Yasui 2008] L. S. Yasui, C. Andorf, L. Schneider, T. Kroc, A. Lennox and K. R. Saroja. *Gadolinium neutron capture in glioblastoma multiforme cells*. Int. J. Radiat. Biol., vol. 84, p. 1130–1139, 2008.

[Zeman 1959] W. Zeman, H. J. Curtis, E. L. Gebhard and W. Haymaker. *Tolerance of mouse-brain tissue to high-energy deuterons*. Science, vol. 130, p. 1760–1761, 1959.

[Zeman 1961] W. Zeman, H. J. Curtis and C. P. Baker. *Histopathologic effect of high-energy-particle microbeams on the visual cortex of the mouse brain*. Radiat. Res., vol. 15, p. 496–514, 1961.

[Zhong 2003] N. Zhong, G. M. Morris, T. Bacarian, E. M. Rosen and F. A. Dilmanian. *Response of rat skin to high-dose unidirectional x-ray microbeams: a histological study*. Radiat. Res., vol. 160, p. 133–142, 2003.

[Zimmer 1978] K. Zimmer and G. Heltai. *Effect of properties of microdensitometers on the shape of the characteristic curve of the photographic emulsion*. Spectrochim. Acta B, vol. 33, p. 417–427, 1978.